

**Aging Induced Evolution of the Fatigue Behavior and Microstructure
of Sn-Ag-Cu Lead Free Solders**

by

Nianjun Fu

A dissertation submitted to the Graduate Faculty of
Auburn University
in partial fulfillment of the
requirements for the Degree of
Doctor of Philosophy

Auburn, Alabama
August 5, 2017

Keywords: lead free solders, aging, fatigue behavior,
solder microstructure, fatigue damage accumulation

Copyright 2017 by Nianjun Fu

Approved by

Jeffrey C. Suhling, Chair, Quina Distinguished Professor of Mechanical Engineering
Hareesh V. Tippur, McWane Professor of Mechanical Engineering
Peter Schwartz, Professor of Mechanical Engineering
Michael J. Bozack, Professor of Physics

Abstract

Solder joints in electronic assemblies are often subjected to cyclic (positive/negative) mechanical strains and stresses. Such exposures can occur in variable temperature application environments or during accelerated life thermal cycling tests used for qualification. Cyclic loading leads to damage accumulation, crack initiation, crack propagation, and eventually to fatigue failure. On the microscopic level, aging leads to solder microstructural changes such as the coarsening of phases and grains. These microstructural changes are closely tied to the damage that occurs during cyclic mechanical loading.

In the first part of this investigation, the effects of aging on the cyclic stress-strain and fatigue behavior of Sn-Ag-Cu (SAC) lead free solders have been studied. Cylindrical uniaxial lead free solder test specimens (SAC305 and SAC405) have been prepared and subjected to cyclic stress/strain loading for different aging conditions. Prior to testing, the specimens were aged (preconditioned) at 125 °C or 25 °C for various aging times up to one year. It has been observed that aging degrades the mechanical fatigue properties, and those degradations are much more significant at the first few days of aging. The effects of testing temperature, strain rate, and strain range on the cyclic stress-strain behavior of SAC305 lead free solder have also been examined, and the effects of aging on the cyclic stress-strain behavior have been quantified for the first time for different testing temperatures, strain rates, and plastic strain ranges.

In the second part of this work, Scanning Electron Microscopy (SEM) has been utilized to examine aging induced microstructural changes occurring within lead free solders. Unlike

many prior studies, fixed regions in the solder cross-sections were monitored throughout the aging process, rather than examining different samples and/or different regions after the various aging exposures. Nanoindentation marks were added to the cross-sections at certain locations to facilitate locating the fixed regions of interest in subsequent microscopy observations. After preparation, the samples were aged at $T = 125\text{ }^{\circ}\text{C}$, and the microstructures were observed and recorded in the selected regions after various aging exposures using SEM. With this approach, time-lapse imagery of the microstructure evolution in a particular region of a solder joint has been recorded as a function of the aging time. When placed together sequentially, these images can be used as frames to create experimentally recorded movies of the microstructural evolution in SAC solders exposed to aging. This approach has allowed the visualization of phenomena such as the coalescence and migration of intermetallic compounds (IMCs) and the coarsening of β -Sn dendrites. The aging induced changes in number of IMCs, total area of all IMCs, average particle area, and average particle diameter have been quantified for several fixed regions in the solder samples.

Finally, the effects of mechanical cycling on the cyclic stress-strain behavior and constitutive behavior of SAC305 lead free solder in fatigue testing have been explored. At the same time, effects of fatigue cycling on solder microstructure have been studied using SEM and polarized light microscope. The goal of this portion of the work was to better understand damage accumulation that occurs in the solder material during fatigue testing.

Acknowledgments

I would like to express my sincere gratitude to my advisor Dr. Jeffrey C. Suhling for the continuous support and guidance of my research work. Also, I would like to thank the rest of my dissertation committee: Dr. Hareesh V. Tippur, Dr. Peter Schwartz, and Dr. Michael J. Bozack, for their encouragement and insightful discussions. I would also like to thank Dr. Sa'd Hamasha for serving as the university reader of this dissertation.

My sincere appreciation goes to China Scholarship Council (CSC) for the financial support during my Ph. D. studies. I also appreciate the cooperation, discussions and friendship that from all my co-workers and friends, especially Dr. Jordan Roberts, Dr. Muhannad Mustafa, Jing Zou, Sudan Ahmed, Quang Nguyen, Jing Wu, Md Mahmudur Chowdhury, Yan Chen, and Sinan Su.

Last but not the least, I would like to thank my parents Xinxu Fu and Xinzhi Yang, my sister Nianwen Fu, as well as my girlfriend Hui Xu for supporting me spiritually on my research and life in general all the time.

Table of Contents

Abstract.....	ii
Acknowledgments.....	iv
Table of Contents.....	v
List of Tables	ix
List of Figures.....	xi
CHAPTER 1 INTRODUCTION	1
1.1 Sn-Ag-Cu Lead Free Solders	1
1.2 Effects of Aging on Solder Mechanical Properties.....	4
1.3 Effects of Aging on Solder Microstructure.....	8
1.4 Various Influential Factors on Solder Mechanical Behavior.....	12
1.5 Effects of Thermo-Mechanical Cycling on Solder Microstructure	15
1.5.1 Recrystallization Phenomenon.....	15
1.5.2 Precipitate Coarsening	17
1.5.3 Crack Initialization and Propagation	18
1.5.4 TMC on Mechanical Properties of Lead Free Solders.....	19
1.5.5 Summary of the Effects of TMC on Solder Microstructure	20
1.6 Objectives of This Research	21
1.7 Organization of the Dissertation	22
CHAPTER 2 EXPERIMENTAL PROCEDURE.....	24

2.1	Introduction.....	24
2.2	Sample Preparation Procedure.....	24
2.3	Mechanical Testing.....	28
2.4	Empirical Models and Data Analysis	31
2.5	Microstructural Study	36
2.6	Summary and Discussion.....	39
CHAPTER 3 AGING INDUCED EVOLUTION OF THE CYCLIC STRESS-STRAIN BEHAVIOR OF LEAD FREE SOLDERS.....		41
3.1	Introduction.....	41
3.2	Cyclic Stress-Strain Response	42
3.3	Evolution of the Hysteresis Loop with Aging	45
3.4	Breakdown of the Evolution	54
3.5	Effects of Aging on Solder Microstructure.....	67
3.6	Summary and Discussion.....	70
CHAPTER 4 CYCLIC STRESS-STRAIN BEHAVIOR: EFFECTS OF AGING, TEMPERATURE, STRAIN RATE, AND PLASTIC STRAIN RANGE		72
4.1	Introduction.....	72
4.2	Effects of Test Temperature.....	73
4.3	Effects of Strain Rate	79
4.4	Effects of Plastic Strain Range	84
4.5	Summary and Discussion.....	89
CHAPTER 5 INVESTIGATION OF AGING INDUCED EVOLUTION OF THE MICROSTRUCTURE OF SAC305 LEAD FREE SOLDER		91
5.1	Introduction.....	91
5.2	Disadvantages of the Conventional Procedure	92

5.3	Aging Induced Solder Microstructural Evolution.....	96
5.4	Discussions on the Coarsening of IMCs with Aging.....	108
5.5	Quantitative Analysis of Aging Induced Evolution of IMCs	109
5.6	Summary and Discussion.....	125
CHAPTER 6 EVOLUTION OF SOLDER MECHANICAL BEHAVIOR AND MICROSTRUCTURE DURING FATIGUE TESTING.....		127
6.1	Introduction.....	127
6.2	Evolution of Cyclic Stress-Strain Behavior During Fatigue Testing.....	128
6.3	Evolution of Constitutive Behavior During Fatigue Testing.....	133
6.4	Effects of Fatigue Cycling on Solder Microstructure	136
6.4.1	Cycling on IMCs and Dendrite Structure	136
6.4.2	Recrystallization of Sn Grains	141
6.4.3	Fatigue Cracks	145
6.5	Summary and Discussion.....	146
CHAPTER 7 ESTABLISH BETTER CAPABILITY FOR FATIGUE TESTING IN OUR LABORATORY		148
7.1	Introduction.....	148
7.2	Current MT-210 Microtester.....	149
7.3	Instron 5948 Tester	151
7.4	Own Designed Microtester	159
7.5	Summary and Discussion.....	162
CHAPTER 8 SUMMARY AND CONCLUSIONS.....		163
8.1	Literature Review.....	163
8.2	Experimental Procedure.....	165

8.3 Aging Induced Evolution of the Cyclic Stress-Strain Behavior of Lead Free Solders	166
8.4 Cyclic Stress-Strain Behavior: Effects of Aging, Temperature, Strain Rate, and Plastic Strain Range	167
8.5 Investigation of Aging Induced Evolution of the Microstructure of SAC305 Lead Free Solder	168
8.6 Evolution of Solder Mechanical Behavior and Microstructure During Fatigue Testing.....	169
8.7 Establish Better Capability for Fatigue Testing in Our Laboratory.....	170
8.8 Recommendations for Future Work.....	170
REFERENCES	172
APPENDIX A DIMENSIONAL DRAWINGS FOR DESIGNED FIXTURES.....	185
A.1 Fixtures for MT-210 Microtester	185
A.2 Fixtures for Instron 5948 Tester and New Microtester.....	188
APPENDIX B AGING INDUCED MICROSTRUCTURAL EVOLUTION IN OTHER SELECTED REGIONS.....	190
B.1 RF SAC305 (Region 2, Aging at T = 125 °C)	190
B.2 RF SAC305 (Region 3, Aging at T = 125 °C)	194
B.3 WQ SAC305 (Region 2, Aging at T = 125 °C).....	198

List of Tables

3.1	Determination of Loop Areas, Plastic Strain Ranges, and Peak Stresses (WQ SAC305, Aging at 125 °C)	57
3.2	Determination of Loop Areas, Plastic Strain Ranges, and Peak Stresses (RF SAC305, Aging at 125 °C)	59
3.3	Determination of Loop Areas, Plastic Strain Ranges, and Peak Stresses (WQ SAC405, Aging at 125 °C)	61
3.4	Determination of Loop Areas, Plastic Strain Ranges, and Peak Stresses (RF SAC305, Aging at 25 °C)	63
3.5	Empirical Model Material Constants	67
4.1	Effects of Test Temperature on Cyclic Stress-Strain Behavior (No Aging)	74
4.2	Effects of Aging and Temperature on Cyclic Stress-Strain Behavior	79
4.3	Effects of Aging and Strain Rate on Cyclic Stress-Strain Behavior.....	84
4.4	Effects of Aging and Strain Range on Cyclic Stress-Strain Behavior.....	89
5.1	Effects of Aging on IMC Particles at 125 °C (Aging Increment: 1 Hour; RF SAC305).....	120
5.2	Effects of Aging on IMC Particles at 125 °C (Aging Increment: 1 Hour; WQ SAC305).....	121
5.3	Effects of Aging on IMC Particles at 125 °C (Aging Increment: 1 Day; RF SAC305).....	121
5.4	Effects of Aging on IMC Particles at 125 °C (Aging Increment: 1 Day; WQ SAC305).....	121
5.5	Effects of Aging on IMC Particles at 125 °C (Aging Increment: 10 Days; RF SAC305).....	122
5.6	Effects of Aging on IMC Particles at 125 °C (Aging Increment: 10 Days; WQ SAC305).....	122

6.1	Cycling Induced Changes of Loop Area, Plastic Strain Range, and Peak Stress	131
6.2	Cycling Induced Changes of Mechanical Properties	135
6.3	Cycling Induced Changes of Creep Strain Rate	135
7.1	Major Parts of the MT-210 Tester	149
7.2	Technical Specifications for Load Cell 67M25A3 (25L65).....	150
7.3	Technical Specifications for LCK-S-2-P Linear Motor.....	151
7.4	Performance Specifications for the Instron 5948 Tester.....	153
7.5	Design Criteria for the New Tester.....	158
7.6	Performance Specifications of the New Tester (with LS-270 Linear Stage).....	160
7.7	Technical Specifications for OMEGA LCMHD-50 Load Cell	161

List of Figures

1.1 Ternary Phase Diagram for Sn-Ag-Cu System [17].....	3
1.2 Typical Microstructure of SAC Lead Free Solders	3
1.3 Variation of Elastic Modulus of β -Sn with Grain Orientation [22].....	4
1.4 Drop of Stress-Strain Curve of SAC305 Solder with Increased Aging [64].....	7
1.5 Effects of Aging on the Uniaxial Fatigue Life of SAC105 Solder [79].....	8
1.6 Effects of Room Temperature (RT) Aging on the Microstructure of Sn-3.9Ag-0.6Cu Lead Free Solder, (Comparing Two Different Samples) [29].....	9
1.7 (a) Proeutectic Grain Size, (b) Ag ₃ Sn Particle Size, (c) Proeutectic Colony Size, and (d) Eutectic Channel Width as a Function of Aging Time During Isothermal Aging at 150 °C [102].....	11
1.8 Effects of Aging on the Microstructure of SAC105 Bulk Solder at 150 °C, (Studying on a Fixed Region) [103].....	12
1.9 Effects of Testing Temperature on Fatigue Life of 96.5Sn-3.5Ag [55].....	14
1.10 Effects of Frequency on Fatigue Life of 99.3Sn-0.7Cu [115].....	14
1.11 EBSD Orientation Maps for SAC305 Solder Joints (Left to Right: As-Reflowed, 1400 Cycles, and 3000 Cycles) [125].....	16
1.12 Cross-Polarized Light Micrographs for SAC305 Solder Joints, Recrystallization Induced by TMC [131].....	16
1.13 SEM Micrographs for a SAC305 Solder Joint after 500 TMF Cycles from 0 °C to 100 °C, (a) Non-Recrystallized Region, and (b) Recrystallized Region [131].....	17
1.14 Polarized Light Micrographs from Cross-Section of the Interconnection after Power Cycling (Left: 1000 Cycles; Right: 3000 Cycles) [130].....	18
1.15 Global Elastic Moduli as a Function of Number of Thermal Cycles [136].....	20
2.1 Specimen Preparation Hardware.....	26

2.2	Water Quenching Profile	27
2.3	Solder Reflow Temperature Profiles for SAC (105/205/305/405).....	27
2.4	Heller 1800EXL Reflow Oven	27
2.5	Cylindrical Uniaxial Test Specimen	28
2.6	MT-210 Testing System with Solder Sample.....	29
2.7	3-D Models of the Gripping Fixtures for Cylindrical Specimens.....	30
2.8	Specimen Gripping Fixtures	30
2.9	The Fracture of Cylindrical Specimens in Fatigue Testing (1, 3: Gripping Area; 2: Gage Area).....	31
2.10	Development of Hysteresis Loop During Cyclic Stress-Strain or Fatigue Testing	31
2.11	Typical Solder Stress-Strain Curve [16].....	33
2.12	Typical Solder Creep Curve [63].....	33
2.13	Solder Stress-Strain Curves and Empirical Model	34
2.14	Determination of Plastic Strain Range and Peak Stress.....	36
2.15	JEOL JSM-7000F Field Emission SEM.....	37
2.16	Various Signals at Different Depths Within the Sample [139].....	37
2.17	Example Region of Interest and Nanoindentation Locating Markers	39
2.18	Zeiss Axio Imager 2 Polarized Light Microscope	39
3.1	The First 10 Hysteresis Loops for a WQ SAC305 Sample (No Aging).....	43
3.2	The Changes of Loop Area with Cycles for WQ SAC305 from 5 Tests (No Aging)	44
3.3	The Cyclic Stress-Strain Behavior for WQ SAC305 from 5 Tests (No Aging).....	44
3.4	Hysteresis Loops for Cyclic Stress-Strain Testing of WQ SAC305 (Aging at 125 °C).....	48
3.5	Aging Induced Evolution of Hysteresis Loop for WQ SAC305 (Aging at 125 °C).....	48
3.6	Hysteresis Loops for Cyclic Stress-Strain Testing of RF SAC305 (Aging at 125 °C).....	50

3.7	Aging Induced Evolution of Hysteresis Loop for RF SAC305 (Aging at 125 °C).....	50
3.8	Hysteresis Loops for Cyclic Stress-Strain Testing of WQ SAC405 (Aging at 125 °C).....	52
3.9	Aging Induced Evolution of Hysteresis Loop for WQ SAC405 (Aging at 125 °C).....	52
3.10	Hysteresis Loops for Cyclic Stress-Strain Testing of RF SAC305 (Aging at 25 °C).....	54
3.11	Aging Induced Evolution of Hysteresis Loop for RF SAC305 (Aging at 25 °C).....	54
3.12	Variation of Loop Area with Aging (WQ SAC305, Aging at 125 °C).....	57
3.13	Variation of Plastic Strain Range with Aging (WQ SAC305, Aging at 125 °C).....	58
3.14	Variation of Peak Stress with Aging (WQ SAC305, Aging at 125 °C).....	58
3.15	Variation of Loop Area with Aging (RF SAC305, Aging at 125 °C).....	59
3.16	Variation of Plastic Strain Range with Aging (RF SAC305, Aging at 125 °C)	60
3.17	Variation of Peak Stress with Aging (RF SAC305, Aging at 125 °C)	60
3.18	Variation of Loop Area with Aging (WQ SAC405, Aging at 125 °C).....	61
3.19	Variation of Plastic Strain Range with Aging (WQ SAC405, Aging at 125 °C).....	62
3.20	Variation of Peak Stress with Aging (WQ SAC405, Aging at 125 °C).....	62
3.21	Variation of Loop Area with Aging (RF SAC305, Aging at 25 °C).....	63
3.22	Variation of Plastic Strain Range with Aging (RF SAC305, Aging at 25 °C)	64
3.23	Variation of Peak Stress with Aging (RF SAC305, Aging at 25 °C)	64
3.24	Evolutions of Loop Area with Aging Time (WQ and RF SAC305, WQ SAC405, Aging at 125 °C)	66
3.25	Evolutions of Loop Area with Aging Time (RF SAC305, Aging at 125 °C and 25 °C)....	66
3.26	Comparison of RF and WQ SAC305 Microstructures Without Aging (Left: RF SAC305; Right: WQ SAC305, 1000X).....	68
3.27	Comparison of RF and WQ SAC305 Microstructures Without Aging (Left: RF SAC305; Right: WQ SAC305, 2000X).....	68
3.28	Aging Induced Microstructural Evolution of WQ SAC305 (Aging at 125 °C).....	69

3.29 Aging Induced Microstructural Evolution of RF SAC305 (Aging at 125 °C)	70
4.1 Effects of Test Temperature on Cyclic Stress-Strain Curves (No Aging).....	74
4.2 Drop of Loop Area with Increased Test Temperature (No Aging)	75
4.3 Increase of Plastic Strain Range with Increased Test Temperature (No Aging)	75
4.4 Drop of Peak Stress with Increased Test Temperature (No Aging)	76
4.5 Effects of Aging and Temperature on Loop Area	77
4.6 Effects of Aging and Temperature on Plastic Strain Range	78
4.7 Effects of Aging and Temperature on Peak Stress	78
4.8 Effects of Strain Rate on Cyclic Stress-Strain Curves (No Aging)	80
4.9 Increase of Loop Area with Increased Strain Rate (No Aging).....	81
4.10 Drop of Plastic Strain Range with Increased Strain Rate (No Aging).....	81
4.11 Increase of Peak Stress with Increased Strain Rate (No Aging).....	82
4.12 Effects of Aging and Strain Rate on Loop Area	82
4.13 Effects of Aging and Strain Rate on Plastic Strain Range.....	83
4.14 Effects of Aging and Strain Rate on Peak Stress	83
4.15 Effects of Strain Range on Cyclic Stress-Strain Curves (No Aging)	85
4.16 Increase of Loop Area with Increased Strain Range (No Aging).....	86
4.17 Increase of Plastic Strain Range with Increased Strain Range (No Aging).....	86
4.18 Increase of Peak Stress with Increased Strain Range (No Aging).....	87
4.19 Effects of Aging and Strain Range on Loop Area	87
4.20 Effects of Aging and Strain Range on Plastic Strain Range.....	88
4.21 Effects of Aging and Strain Range on Peak Stress	88
5.1 Comparison of RF SAC305 Microstructures in Three Different Regions	93

5.2 Aging Led to Coarser IMC Particles (Left: No Aging; Right: 6-Hour Aging)	94
5.3 Aging Led to Finer IMC Particles (Left: No Aging; Right: 7-Hour Aging)	94
5.4 Aging Increased the Subgrain Size (Left: No Aging; Right: 6-Hour Aging).....	94
5.5 Aging Decreased the Subgrain Size (Left: No Aging; Right: 1-Month Aging)	95
5.6 Aging Weakened the Dendrite Structure (Left: No Aging; Right: 6-Hour Aging)	95
5.7 Aging Strengthened the Dendrite Structure (Left: No Aging; Right: 3-Hour Aging).....	95
5.8 Non-Aged SAC305 Microstructures.....	97
5.9 Aging Induced Microstructural Evolution of WQ SAC305 by SEM Microscopy (Aging at T = 125 °C, up to 11 Hours)	102
5.10 Aging Induced Microstructural Evolution of RF SAC305 by SEM Microscopy (Aging at T = 125 °C, up to 11 Hours)	106
5.11 Aging Induced Coarsening of IMCs (Aging at 125 °C; Aging Increment: 1 Day)	107
5.12 Aging Induced Coarsening of IMCs (Aging at 125 °C; Aging Increment: 10 Days).....	108
5.13 Sub-Region for Quantitative Analysis of Aging Effects on IMCs	110
5.14 Aging Induced Evolution of IMCs at 125 °C (Aging Increment: 1 Hour; RF SAC305; Top: Gray-Scale Image, Bottom: Binary Image)	111
5.15 Aging Induced Evolution of IMCs at 125 °C (Aging Increment: 1 Hour; WQ SAC305; Top: Gray-Scale Image, Bottom: Binary Image)	112
5.16 Aging Induced Evolution of IMCs at 125 °C (Aging Increment: 1 Day; RF SAC305)	114
5.17 Aging Induced Evolution of IMCs at 125 °C (Aging Increment: 1 Day; WQ SAC305)	115
5.18 Aging Induced Evolution of IMCs at 125 °C (Aging Increment: 10 Days; RF SAC305).....	117
5.19 Aging Induced Evolution of IMCs at 125 °C (Aging Increment: 10 Days; WQ SAC305).....	119
5.20 Variation of Number and Average Diameter of IMC Particles with Aging Time at 125 °C (Aging Increment: 1 Hour, RF SAC305).....	122

5.21 Variation of Number and Average Diameter of IMC Particles with Aging Time at 125 °C (Aging Increment: 1 Hour, WQ SAC305).....	123
5.22 Variation of Number and Average Diameter of IMC Particles with Aging Time at 125 °C (Aging Increment: 1 Day, RF SAC305).....	123
5.23 Variation of Number and Average Diameter of IMC Particles with Aging Time at 125 °C (Aging Increment: 1 Day, WQ SAC305).....	124
5.24 Variation of Number and Average Diameter of IMC Particles with Aging Time at 125 °C (Aging Increment: 10 Days, RF SAC305).....	124
5.25 Variation of Number and Average Diameter of IMC Particles with Aging Time at 125 °C (Aging Increment: 10 Days, WQ SAC305).....	125
6.1 Typical Uniaxial Fatigue Test.....	130
6.2 Cycling Induced Evolution of Hysteresis Loop.....	130
6.3 Variation of Loop Area with Cycling.....	131
6.4 Variation of Plastic Strain Range with Cycling.....	132
6.5 Variation of Peak Stress with Cycling.....	132
6.6 Cycling Induced Evolution of Stress-Strain Curve.....	134
6.7 Cycling Induced Evolution of Creep Curve.....	135
6.8 Microstructural Evolution of RF SAC305 During Fatigue Testing (500X).....	140
6.9 Elemental Mapping of Cycled Microstructure.....	140
6.10 Evolution of Sn Grains During Fatigue Testing Using Polarized Light Microscope.....	145
6.11 Fatigue Cracks in the Microstructure that Cycled for 1200 Cycles (Right: Polarized Light Image; Left: Optical Image).....	146
7.1 JR3 Multi-Axis Load Cell.....	150
7.2 Instron 5948 Universal Microtester.....	152
7.3 3-D Models of the Designed Fixtures for Instron 5948 Tester.....	155
7.4 Assembly of the Fixtures.....	155

7.5 Schematic of the Gripping and Dimensions of the Groove	156
7.6 Instron 5948 Microtester with the Fixtures.....	156
7.7 Uniaxial Fatigue Life of WQ SAC305 (Using Instron 5948 with Designed Fixtures)	157
7.8 Compatible with MT-210 Microtester Fixtures (Set-up for Cylindrical Specimens).....	158
7.9 Compatible with MT-210 Microtester Fixtures (Set-up for Flat Specimens).....	158
7.10 Compatible with MT-210 Microtester Shear Fatigue Fixtures [79]	158
7.11 PI LS-270 Linear Stage.....	161
7.12 OMEGA LCMHD-50 Tension/Compression Load Cell	161

CHAPTER 1

INTRODUCTION

1.1 Sn-Ag-Cu Lead Free Solders

Solders have been used as the interconnecting material in electronic assemblies to provide both electrical and mechanical connections between components. The conventional eutectic or near eutectic Sn-Pb solder has been extensively used in the electronics industry due to its outstanding solderability and reliability [1]. However, the lead solders have been prohibited in many countries despite their advantages, this is because lead is a toxic element and it is detrimental to both the environment and the human body [2-8]. Therefore, efforts have been made to eliminate lead in electronics and search for the lead free solder alloys. Lee [3] outlined some features that the lead free solder candidates should have: similar melting temperature to the standard lead solders, good wetting ability, good electrical and mechanical properties, nontoxicity, and low cost. Sn-Ag, Sn-Ag-Cu, and other alloys containing elements like Sn, Ag, Cu, Bi, In, and Zn have been identified as the promising lead free solders for replacing the conventional eutectic lead solder [1]. Among these candidates, Sn-Ag-Cu (SAC) lead free solder series are the most widely used lead free solders in the industry at present [9].

Compared with the 96.5Sn-3.5Ag binary eutectic alloy, near eutectic SAC solder alloys have relatively low melting temperatures, and they have better mechanical and manufacturability properties than other lead free solders. The addition of Cu in the SAC alloys contributes to lowering melting temperature and improving the wettability [10]. The composition and melting

temperature of the ternary eutectic SAC solder have been investigated by many researchers. Initially, it was reported that the eutectic composition of the SAC solder system was Sn-3.6Ag-1.5Cu [11] or Sn-4.7Ag-1.7Cu [12]. Recent studies tend to agree that the eutectic point of SAC solder is close to Sn-3.5Ag-0.9Cu (3.5 wt. % Ag, 0.9 wt. % Cu and the balance 95.6 wt. % Sn), and its melting point is around 217.2 °C [13-15]. There are a variety of other SAC alloys being used, including the SACN05 series (SAC105, SAC205, SAC305 and SAC405), near eutectic SAC alloys (SAC387, SAC396, and SAC357), and some other alloys (SAC3810, SAC3595, SAC0307, and SAC107) that used in special applications such as elevated temperature application, drop and shock optimization, etc. [16].

Figure 1.1 shows the ternary phase diagram for the SAC lead free solder series [17]. The near eutectic SAC solidifies into three phases, i. e., β -Sn (primary phase), Ag_3Sn and Cu_6Sn_5 . Figure 1.2 shows a typical microstructure of SAC lead free solders. It consists of β -Sn dendrites surrounded by interdendritic eutectic regions incorporating a fine dispersion of Ag_3Sn and Cu_6Sn_5 intermetallic particles in β -Sn. The volume fraction of Ag_3Sn IMCs is much higher than that of Cu_6Sn_5 IMCs in SAC solder microstructures. It has been reported that the IMC particles have higher strength than the bulk material [18, 19], and the dendrite structure can effectively pin and block movement of dislocations and therefore improve solder mechanical behavior [20, 21].

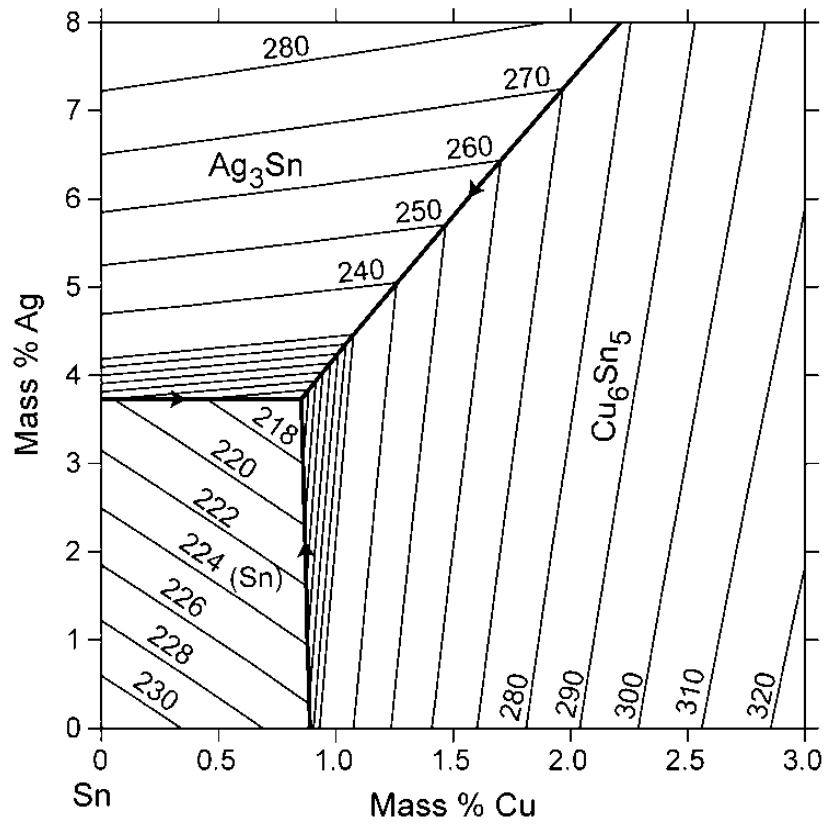


Figure 1.1 - Ternary Phase Diagram for Sn-Ag-Cu System [17]

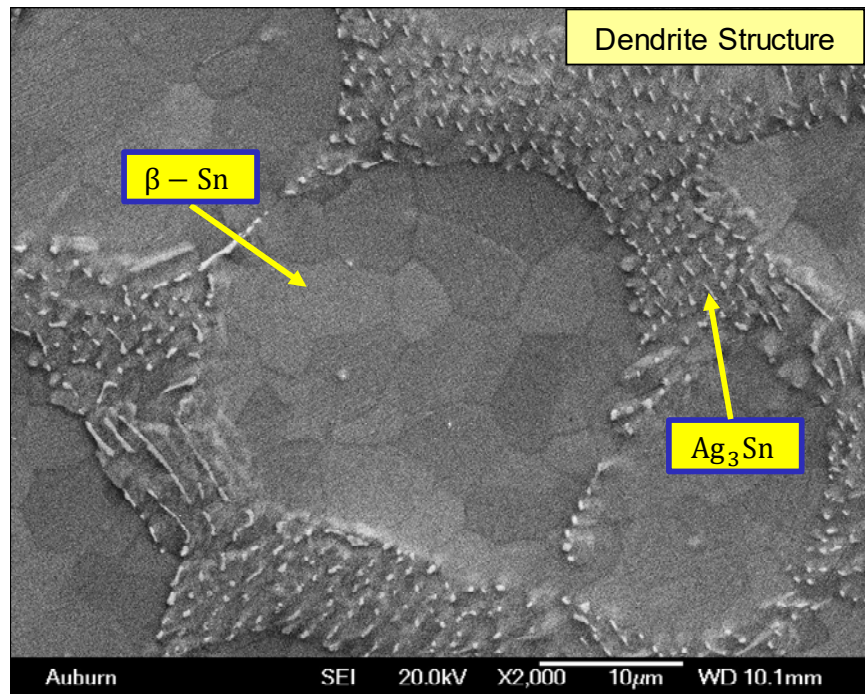


Figure 1.2 - Typical Microstructure of SAC Lead Free Solders

For the SAC lead free solders, the properties of Sn dominate their behavior as Sn has a very high weight percentage. Sn has a Body-Center Tetragonal (BCT) crystal structure with lattice parameters $a = b = 5.83\text{\AA}$ and $c = 3.18\text{\AA}$. Therefore, it is highly anisotropic in mechanical properties such as elastic modulus and hardness. In other words, the mechanical properties of Sn are highly dependent on the grain orientation. As shown in Figure 1.3, the elastic modulus of Sn is 67.6 GPa in the (001) direction, while it is only 23.6 GPa in the (100) direction [22]. Also, Sn is highly thermally anisotropic: the coefficients of thermal expansion (CTE) in the principal directions at 30 °C are $\alpha[100] = \alpha[010] = 16.5 \times 10^{-6}\text{ }^{\circ}\text{C}^{-1}$ and $\alpha[001] = 32.4 \times 10^{-6}\text{ }^{\circ}\text{C}^{-1}$ [23].

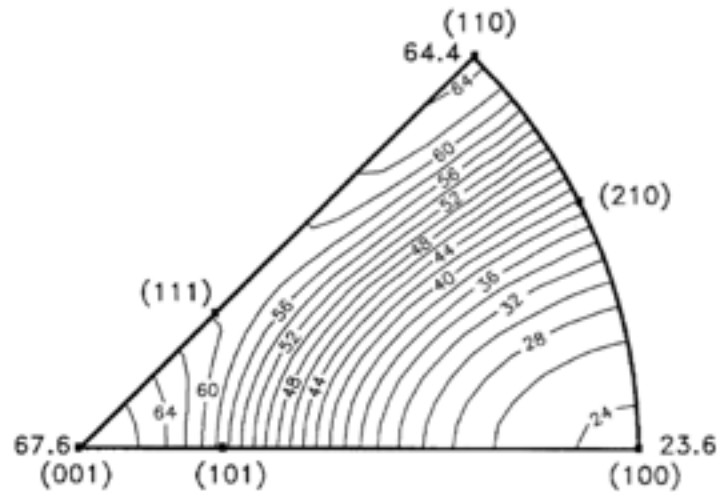


Figure 1.3 - Variation of Elastic Modulus of β -Sn with Grain Orientation [22]

1.2 Effects of Aging on Solder Mechanical Properties

Aging has a strong effect on mechanical properties of lead free solders, as they have high homologous temperatures in most product applications. Due to the low melting temperatures of solder materials, their homologous temperatures are high even in room temperature environments. Take SAC solders for example, their homologous temperatures are 0.61 at room

temperature, and it is greater than 0.5 at which creep is considered critical [16]. Ma, et al. [1] reviewed the mechanical properties of lead free solders and found large data discrepancies in the literature. For instance, at room temperature, the elastic modulus of SAC lead free solders ranges from 30 to 54 GPa, while the ultimate tensile strength and yield stress are in the range of 30 - 60 MPa and 20 - 47 MPa, respectively. They believe aging plays a significant role in the data discrepancies in the literature.

The effects of aging were first investigated on lead solders by Medvedev, et al. [24] and Lampe, et al. [25], and they reported significant degradations of mechanical properties caused by room temperature aging. As the world transitions to lead free soldering, more and more studies have been focusing on the effects of aging on lead free solders. Miyazawa and Ariga [26, 27] reported that Sn-Pb, Sn-Ag and Sn-Zn eutectic solder materials experienced significant hardness degradation and microstructural coarsening after being aged at room temperature for 1000 hours. Ding and coworkers [28] observed a quick softening effect on Sn-3.5Ag solder samples after exposing the samples at 180 °C for 120 hours. Xiao, et al. [29] studied the effects of both room temperature aging and elevated temperature aging (180 °C) on SAC396 solder, and found the tensile strength loss was 25% for 35-day room temperature aging and 33% for 9-day elevated temperature aging. Similarly, aging induced degradations in tensile properties [30-35] and creep properties [36-38] of lead free solders have been reported by many researchers.

The cyclic stress-strain behavior of solder materials has been studied extensively in the past [39-57]. For example, several researchers [39-46] have developed fatigue life prediction models for solder alloys under thermal cycling or thermomechanical fatigue loading. Hall [47-48] measured deformations and stress-strain hysteresis experimentally during the thermal cycling of a leadless ceramic chip carrier (LCC) mounted to an organic PCB. For lead free solders,

Raeder and co-workers [53] have explored thermomechanical deformation behavior of Sn-Bi eutectic solder under fatigue loading, and the findings were quantified using the plastic strain energy density. In addition, Dusek, et al. [54] have investigated the cyclic stress-strain behavior and hysteresis loop evolution for SAC lead free solders during isothermal fatigue at several different temperatures ($T = 24, 30, 60, \text{ and } 125 \text{ }^\circ\text{C}$). They reported that the number of cycles to failure increases with higher temperatures for the same stress level, and attributed this to the use of slow cycling, where creep and stress relaxation play dominant roles. Kanchanomai, et al. [55] have performed uniaxial fatigue tests on Sn-Ag solder, while Pang and coworkers [56] have performed uniaxial fatigue tests on SAC387 lead free solder. Andersson, et al. [57] compared the fatigue properties of bulk lead-free solder specimens to those found for solder joints. While aging effects have been studied in some detail on the solder constitutive behavior such as stress-strain and creep, there have been few prior studies on the effects of aging on solder cyclic stress-strain or fatigue behavior [58-60].

Our research center (Center for Advanced Vehicle and Extreme Environment Electronics, CAVE³) has been studying the effects of aging on various mechanical properties of lead free solders and has found that aging is universally detrimental to solder constitutive and failure behaviors. In particular, large degradations have been observed in creep behavior [61-65], thermal cycling reliability [66-70], Anand model parameters [69-70], nanoindentation joint modulus and hardness [71-73], high strain rate mechanical properties [74], uniaxial cyclic stress-strain curves and fatigue life [75, 76], and shear cyclic stress-strain curves and fatigue life [77, 78]. For example, it has been found that elevated temperature aging ($100 \text{ }^\circ\text{C}$) led to dramatic changes of the stress-strain curve of SAC305 solder, especially during the first few days of aging, as shown in Figure 1.4 [64]. Mustafa [79] systematically studied the effects of aging on

the fatigue life of lead free solders and proposed modified fatigue models that includes aging effects. Flat uniaxial test specimens (3 mm × 0.5 mm × 30 mm) were used to determine the uniaxial fatigue life of SAC solders in his study. Figure 1.5 shows the effects of aging on uniaxial fatigue life of SAC105 solder, and it is clear that aging decreases solder fatigue life. However, it has been found that the failure of flat specimens was often due to buckling, and the determined uniaxial fatigue life is much shorter than that from other researchers [55, 57, 80-84]. Therefore, micro-cylinder shaped specimens have been introduced in this study to solve the problem of buckling, and more details will be discussed in later chapters.

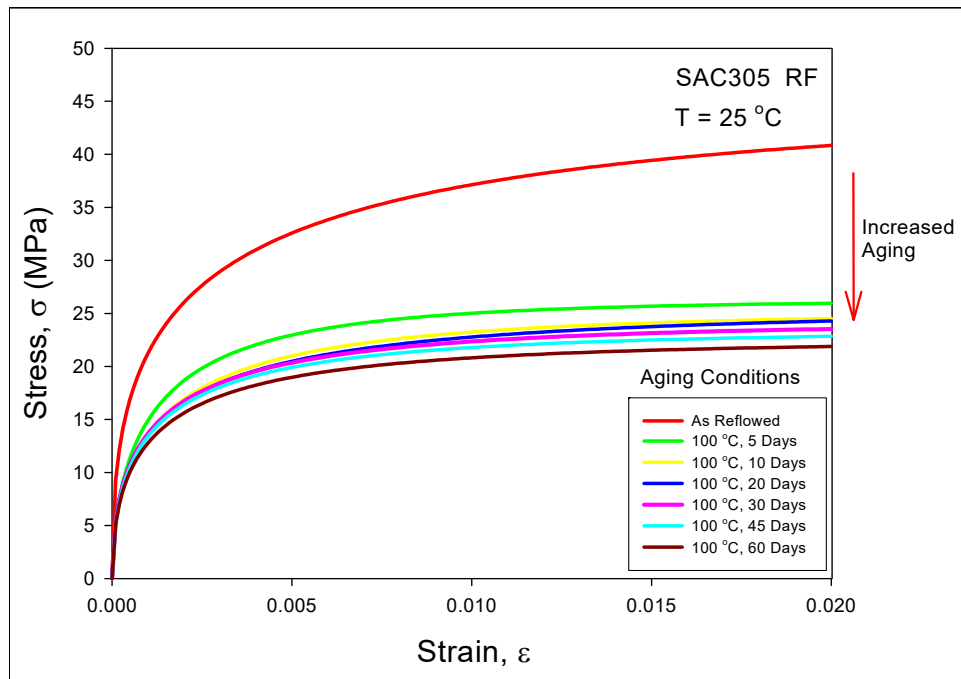


Figure 1.4 - Drop of Stress-Strain Curve of SAC305 Solder with Increased Aging [64]

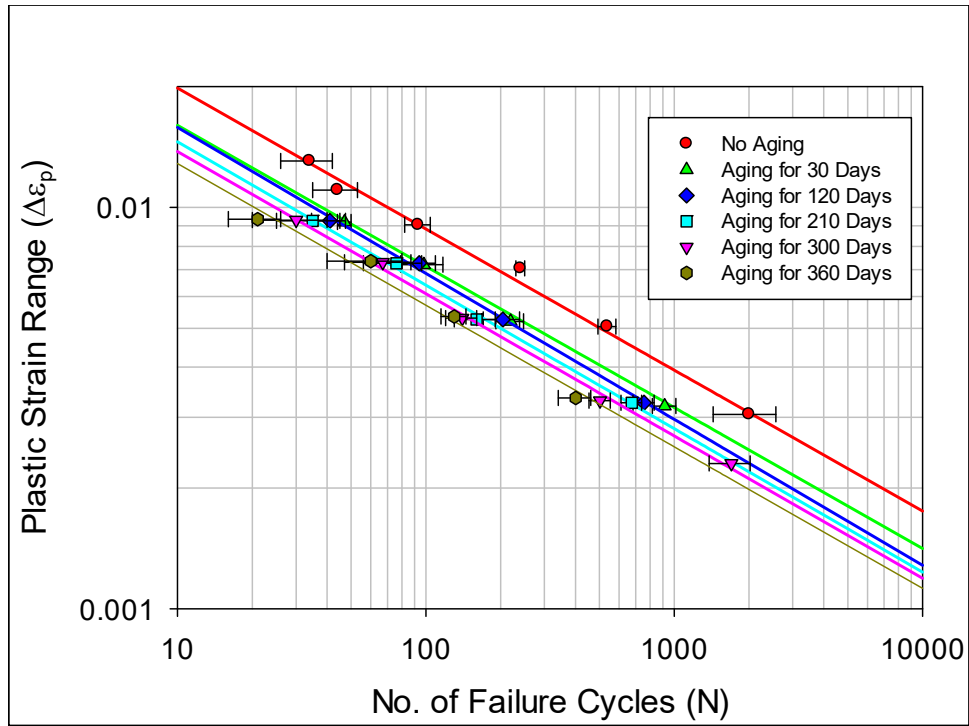


Figure 1.5 - Effects of Aging on the Uniaxial Fatigue Life of SAC105 Solder [79]

1.3 Effects of Aging on Solder Microstructure

The changes in solder mechanical behavior are a result of the evolution of the solder microstructure that occurs during aging. Many researchers have studied effects of aging on the evolution of solder microstructure, and several examples are listed in references [29, 85-104]. The most well-known and widely observed changes are coarsening of the Ag_3Sn and Cu_6Sn_5 IMCs present in the eutectic regions between β -Sn dendrites. Several researchers [89, 92, 94, 95, 99-104] have also used empirical models to describe the growth of IMC particles or layers as a function of aging temperature and aging time. For example, Dutta, et al. [89, 94, 99] studied the microstructural coarsening of Sn-Ag based solders during thermal-mechanical cycling (TMC) and reported that TMC results in both static and strain-enhanced coarsening. Thus, they proposed a model to describe the growth of Ag_3Sn IMC particles during TMC, and the static coarsening part (solely isothermal aging) is given by

$$d_p^3 - d_{p_0}^3 \approx (8K \frac{C_{eq}}{T} D_{sol})t \quad (1.1)$$

where d_p is the diameter of Ag_3Sn particles at any instant during aging and d_{p_0} is the initial particle diameter. K is the static coarsening constant, and C_{eq} and D_{sol} are the equilibrium solubility and diffusivity of the solute Ag in Sn . T is the aging temperature and t is the aging time. In many studies on the effects of aging on solder microstructure, observations were made on two different solder joints (one non-aged and one aged). For example, Xiao, et al. [29] investigated the effects of aging on the microstructure of Sn-3.9Ag-0.6Cu lead free solder, and found that the microstructure changed remarkably after aging at room temperature for 35 days by comparing two different samples, as shown in Figure 1.6. However, the comparisons made were often qualitative in nature since the two microstructures were from different samples and could not be directly compared.

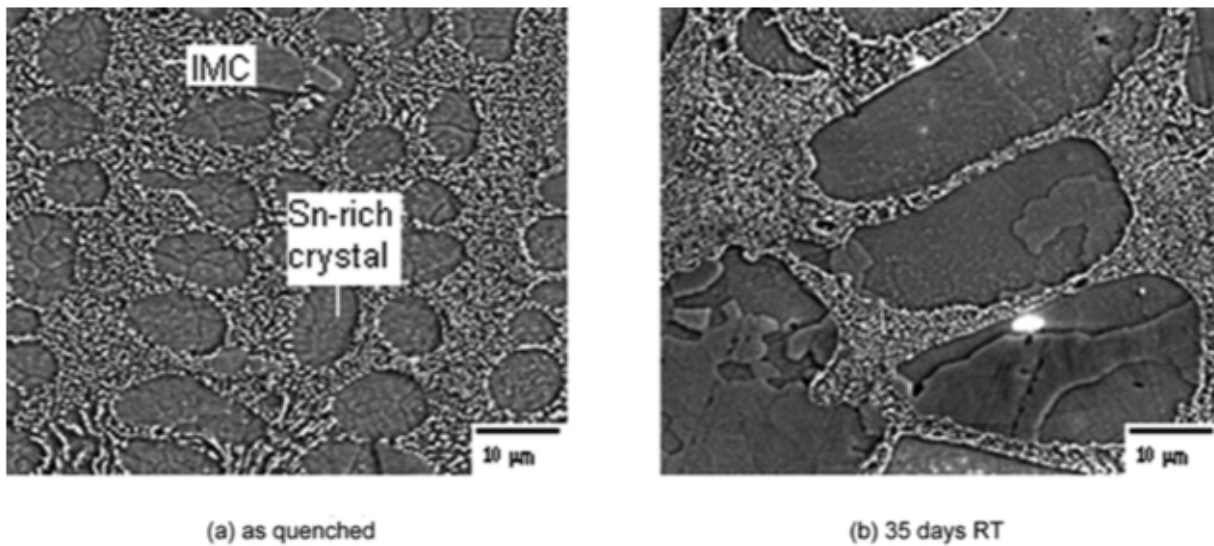


Figure 1.6 - Effects of Room Temperature (RT) Aging on the Microstructure of Sn-3.9Ag-0.6Cu Lead Free Solder, (Comparing Two Different Samples) [29]

There are limited investigations that have involved the monitoring of evolving microstructure in a fixed region in a single solder sample [85, 90, 93, 100, 102]. For example, Choi and Lee [85] made photographs of growing intermetallic layers at the boundary between a Sn-Ag solder joint and the copper bonding pad. Ubachs, et al. [90] made experimental observations of aging-induced Sn-Pb solder microstructure evolution, and compared their results to predictions made with two-dimensional diffusion simulations. Telang and coworkers [93] made before and after grain boundary maps in fixed regions in pure-Sn and Sn-Ag samples subjected to high temperature aging at 150 °C. Similarly, Kumar, et al. [100] and Sahaym, et al. [102] observed changes to the IMC particles occurring within fixed regions in SAC105 and SAC305 solder joints exposed to aging at 150 °C for 100 - 300 hours. To obtain quantitative data and develop models, observations of a large set of IMC particles were made before and after aging, and average particle size and subgrain size were measured and plotted, as shown in Figure 1.7 [102]. Figure 1.8 illustrates the microstructural changes of SAC105 bulk solder that occurred in a fixed region during isothermal aging at 150 °C, and the coarsening of IMC particles is obvious [103].

Other changes in the SAC solder microstructure have also been observed to occur during aging, but they are not well characterized and their effects on mechanical behavior and reliability are not well understood. These include changes in size/shape of the β -Sn dendrites, growth of pure Sn subgrains within the β -Sn dendrites, migration of IMC particles to subgrain boundaries, changes in Sn grain orientation, etc.

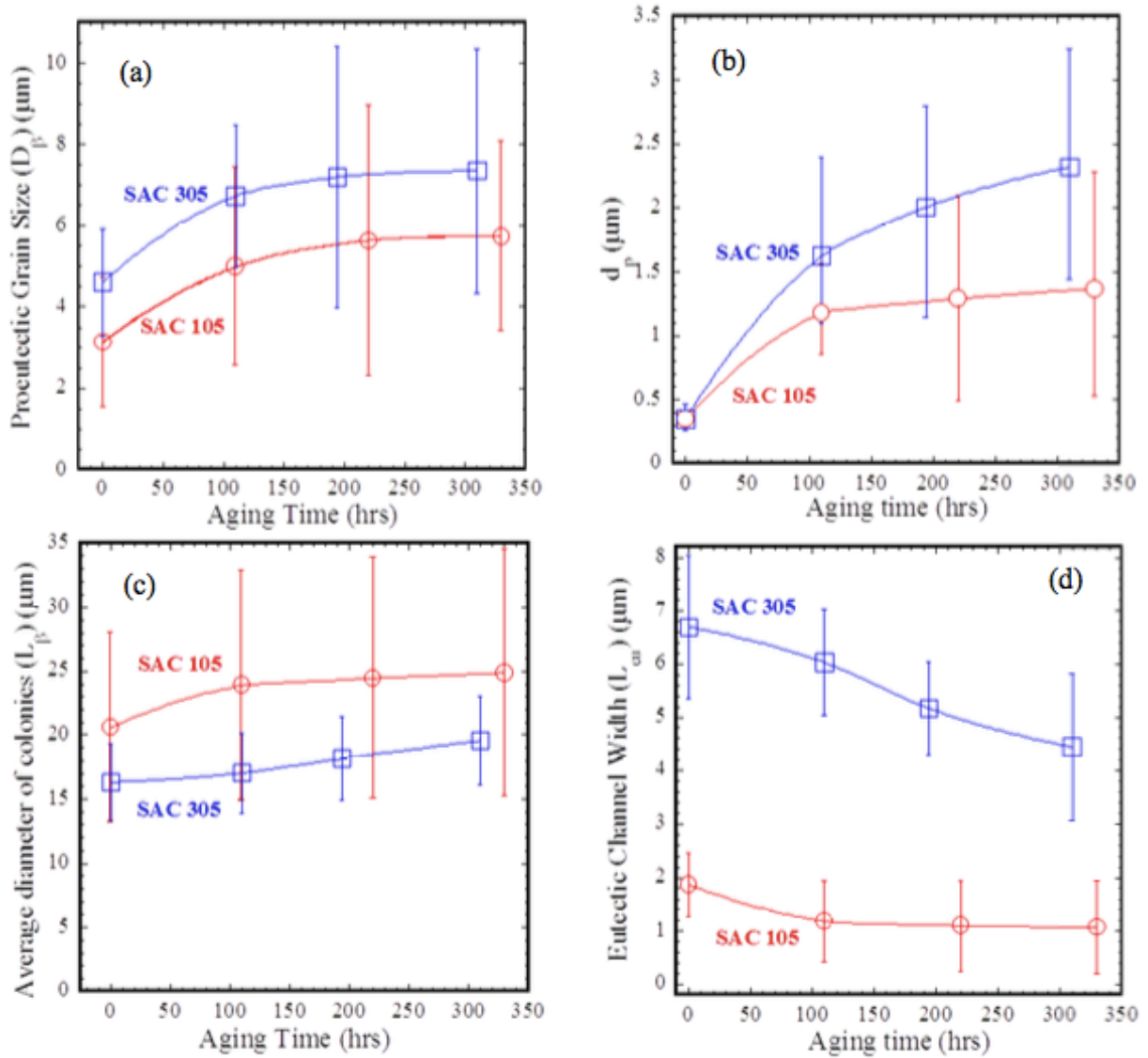


Figure 1.7 - (a) Proeutectic Grain Size, (b) Ag_3Sn Particle Size, (c) Proeutectic Colony Size, and (d) Eutectic Channel Width as a Function of Aging Time During Isothermal Aging at 150 °C [102]

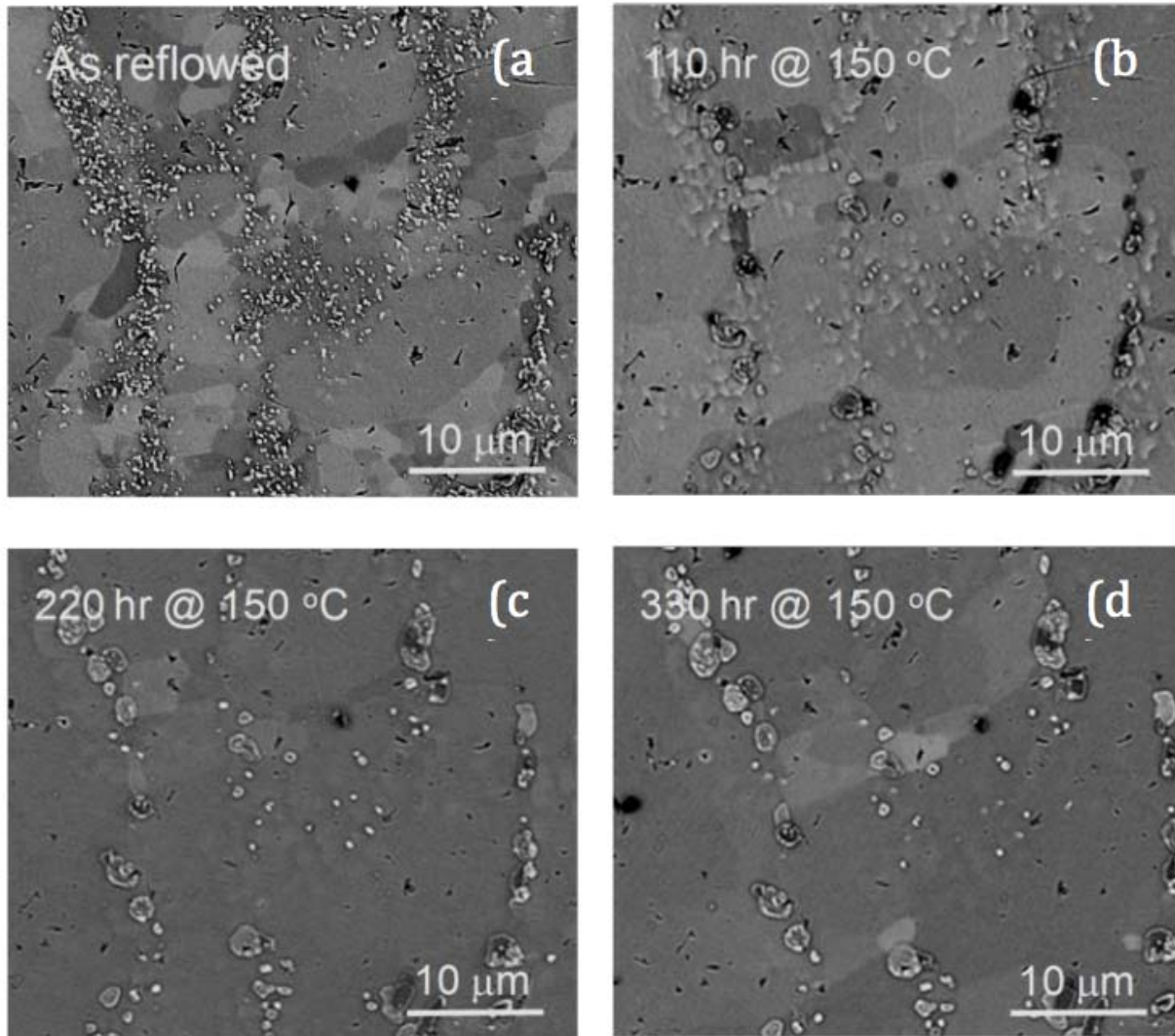


Figure 1.8 - Effects of Aging on the Microstructure of SAC105 Bulk Solder at 150 °C, (Studying on a Fixed Region) [103]

1.4 Various Influential Factors on Solder Mechanical Behavior

Apart from aging, there are many other parameters such as cooling rate, strain rate (frequency) and testing temperature that can influence the mechanical behavior of solder materials, and a better understanding of the effects of aging and those parameters on solder mechanical behavior is critical to resolving the large discrepancies in solder mechanical testing data found in the literature.

Different solidification profiles (cooling rates) result in different initial microstructures of a solder test specimen, which will dramatically influence the results of any mechanical test performed on that material. Typically, fast cooling rates lead to a finer initial lead free solder microstructure and then enhance its mechanical properties [105-110]. Kim, et al. [105] studied the effects of cooling rate on the microstructure and tensile properties of SAC lead free solders. They found that slow cooling rate led to additional large primary Ag_3Sn platelets in the Sn-3.5Ag-0.7Cu and Sn-3.9Ag-0.6Cu microstructures, which resulted in a decrease in tensile strength and elongation. Liang, et al. [108] compared the macro/micro-structure and mechanical properties of SAC387 solder samples that were solidified at different rates, and they reported that fast cooling rate results in the decrease of Sn dendrite arm spacing and the enhancement of solder creep resistance. Similarly, Basit, et al. [109, 110] compared the effects of two solidification profiles (reflow and water quenching) on the tensile properties of SAC lead free solders, and found that fast cooling (water quenching) results in finer solder microstructure and better mechanical properties.

As solder materials are viscoplastic, their mechanical properties are highly rate and temperature dependent. For materials that exhibit viscoplastic behavior, Anand [111] proposed a unified plastic/creep constitutive model that establishes a relationship between flow stress and plastic strain, with strain rate and ambient temperature as parameters. In finite element simulations, this model has been widely used to represent material behavior of lead free solders. Typically, when tested at lower temperatures or higher strain rates, solder test specimens exhibit better mechanical properties [45, 55, 57, 80, 81, 112-119]. For instance, Figure 1.9 shows the effects of testing temperature on fatigue life of 96.5Sn-3.5Ag lead free solder [55], while Figure 1.10 illustrates the effects of frequency (strain rate) on fatigue life of 99.3Sn-0.7Cu solder [115].

The fatigue life data in Figure 1.9 and Figure 1.10 are represented using Coffin-Manson model and Morrow model, respectively. In addition, some researchers proposed modified fatigue models to include the effects of test frequency or strain rate [45, 55, 80, 112, 113, 115, 117, 119].

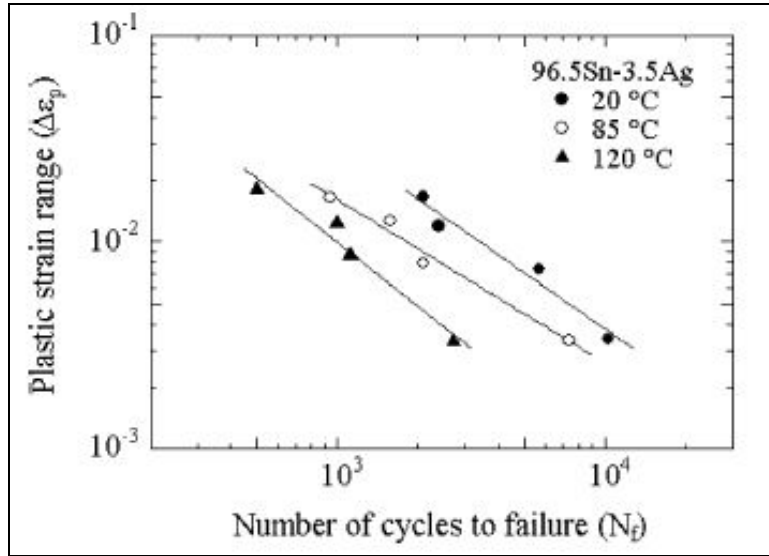


Figure 1.9 - Effects of Testing Temperature on Fatigue Life of 96.5Sn-3.5Ag [55]

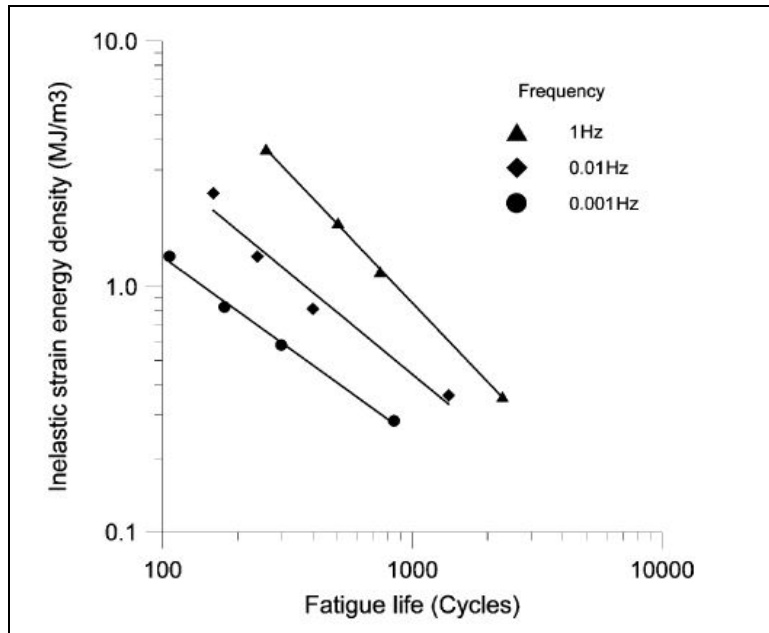


Figure 1.10 - Effects of Frequency on Fatigue Life of 99.3Sn-0.7Cu [115]

1.5 Effects of Thermo-Mechanical Cycling on Solder Microstructure

The effects of thermo-mechanical cycling (TMC) on the microstructure of eutectic Sn-Pb solder joints have been explored by several researchers [120-125]. The most reported change on the solder microstructure induced by TMC is phase coarsening. For lead free solders, the most reported microstructural changes during TMC are the recrystallization of β -Sn and the precipitate coarsening.

1.5.1 Recrystallization Phenomenon

Recrystallization is the formation of a new grain structure by the formation and migration of grain boundaries with misorientation angle greater than 10-15°, which is driven by the stored deformation energy [126]. Chen, et al. [125] used orientation imaging microscopy (OIM) and SEM to study the evolution of solder microstructure in Sn-Ag-Cu and mixed solder interconnects during thermo-mechanical cycling (0 - 100 °C). Figure 1.11 shows the EBSD orientation maps for SAC305 lead free solder joints at different cycling conditions. Recrystallization phenomenon was observed in the cycled microstructures of SAC305 solder joints. Many small subgrains were found in the recrystallized region, and the subgrain size increased after 3000 thermal cycles. Also, the recrystallized region expanded significantly with increased thermal cycling. Berthou, et al. [127] studied the failure mechanism of SAC solder joint during thermo-mechanical fatigue. They found that Sn recrystallization occurred in the regions where stress accumulation was high, and the formation of small size grains was observed in those regions. According to [128, 129], the recrystallization during thermal fatigue is caused by thermal strain and elevated temperature in the highly-strained regions, which leads to the development of fatigue cracks in the recrystallized regions.

Yin, et al. [131] studied the microstructure evolution of SAC305 lead free solder during thermo-mechanical cycling (-40 °C to 125 °C). As shown in Figure 1.12, the grain recrystallization was found in the region close to the corners after 500 cycles (indicated by the arrows). After 1000 cycles, grain boundaries can be discerned across the pad region, and it was a result of the recrystallization. After 2000 cycles, a slight size increase of the recrystallized regions and the formation of grain boundaries with high misorientation angles have been found. They also explored the recrystallization mechanism based on the EBSD analysis. The recrystallization can be divided into two regimes, the formation of new grains and the growth of those grains. They suggested that continuous subgrain formation and rotation is the mechanism of Sn recrystallization, and it does not go through a “nucleation” stage.

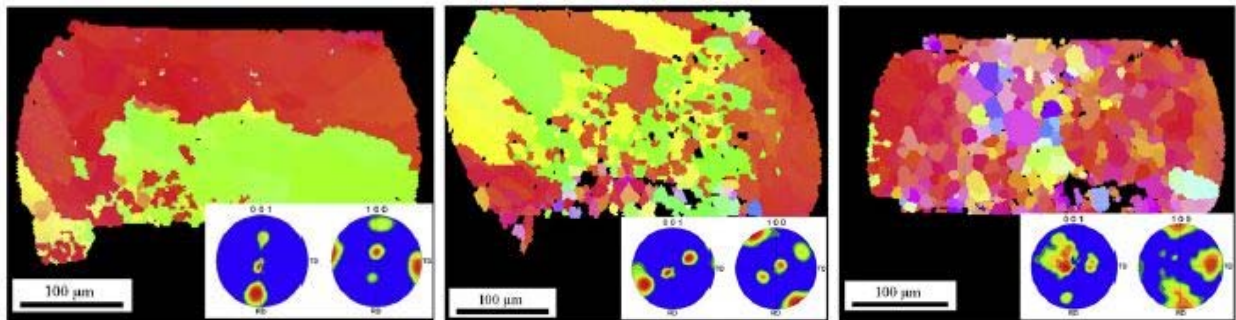


Figure 1.11 - EBSD Orientation Maps for SAC305 Solder Joints (Left to Right: As-Reflowed, 1400 Cycles, and 3000 Cycles) [125]

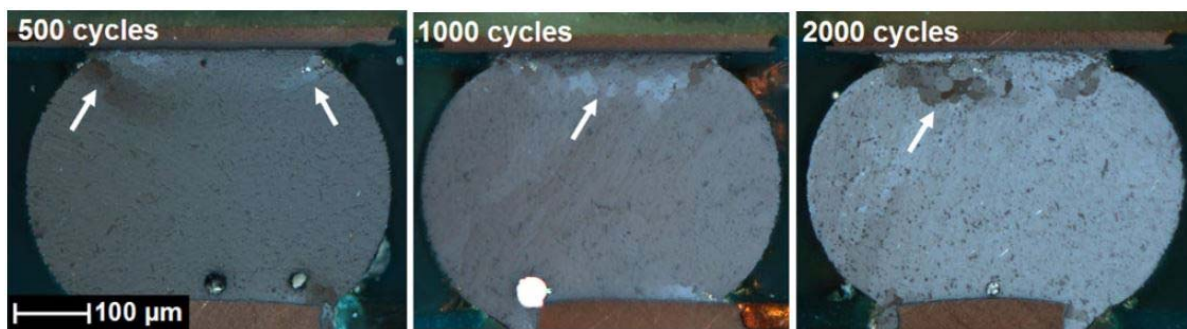


Figure 1.12 - Cross-Polarized Light Micrographs for SAC305 Solder Joints, Recrystallization Induced by TMC [131]

1.5.2 Precipitate Coarsening

Another commonly observed change of solder microstructure induced by thermo-mechanical cycling is precipitate coarsening. The coarsening of Ag_3Sn intermetallic compound (IMC) particles that occurred in the recrystallized region during TMC has been reported in [94, 99, 125, 131-133]. For example, Figure 1.13 shows the microstructures of a SAC305 solder joint after being thermally cycled ($0\text{ }^\circ\text{C}$ to $100\text{ }^\circ\text{C}$) for 500 times [131]. It is clear that the IMC particles (Ag_3Sn and Cu_6Sn_5) were larger and fewer in the recrystallized region than those in the non-recrystallized region. Also, they found that the recrystallization was always accompanied by the coarsening of IMCs in the same area. Qi, et al. [133] studied the effects of thermal-shearing cycling on the coarsening of Ag_3Sn IMCs in SAC305 solder. They found that the Ag_3Sn particles in the cycled microstructure were nearly spherical, and the average diameter of the particles increased from $1.07\text{ }\mu\text{m}$ to $1.36\text{ }\mu\text{m}$ after 200 thermal cycles between $25\text{ }^\circ\text{C}$ and $125\text{ }^\circ\text{C}$. Dutta, et al. [94, 99] studied the coarsening kinetics of Ag_3Sn particles in Sn-Ag-based lead free solder during TMC, and proposed a model to predict the radius of the precipitate particles at any instant.

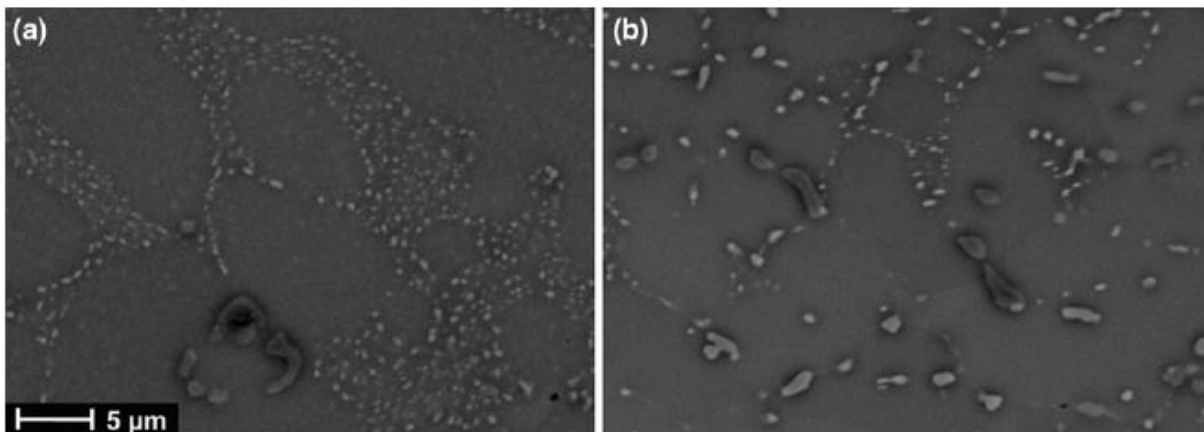


Figure 1.13 - SEM Micrographs for a SAC305 Solder Joint after 500 TMC Cycles from $0\text{ }^\circ\text{C}$ to $100\text{ }^\circ\text{C}$, (a) Non-Recrystallized Region, and (b) Recrystallized Region [131]

1.5.3 Crack Initialization and Propagation

Laurila, et al. [130] investigated the microstructure evolution and failure mechanism of lead free solder interconnections during power cycling. Figure 1.14 shows the microstructures after being power cycled for 1000 and 3000 cycles using polarized light microscope, and the recrystallization phenomenon and fatigue cracks have been observed. Some cracks were observed to propagate along the boundaries between grains in the recrystallized region. Actually, the cracks tended to nucleate at those boundaries and then propagate in an intergranular manner, as less energy consumption was required. After power cycling the specimen for 3000 cycles, the recrystallized region became larger and cracks grew further into the solder interconnection. Similar findings have been reported in [125, 127, 131].

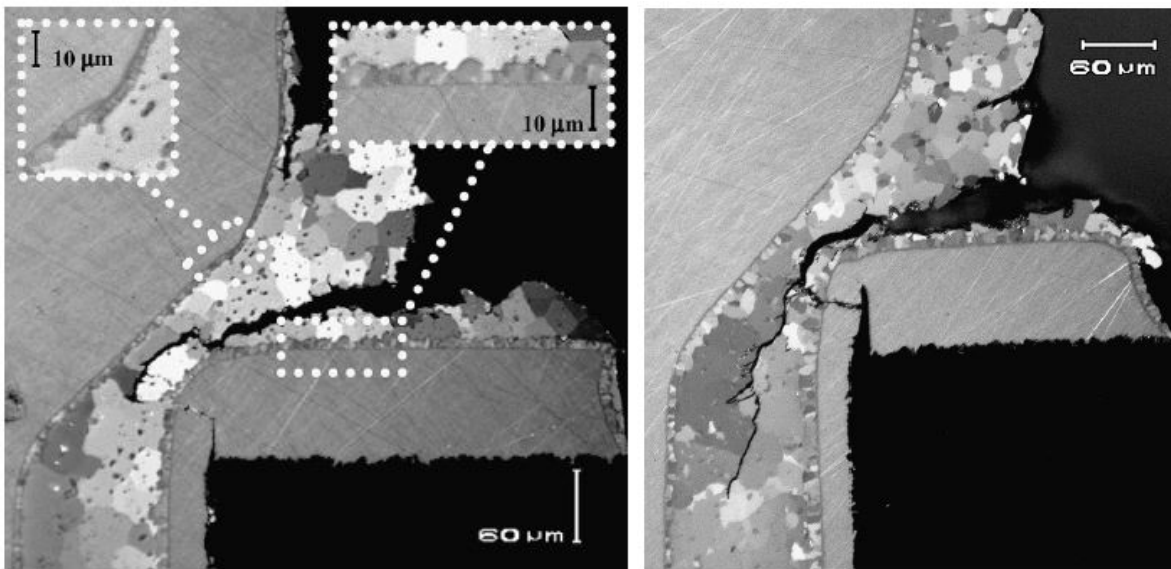


Figure 1.14 - Polarized Light Micrographs from Cross-Section of the Interconnection after Power Cycling (Left: 1000 Cycles; Right: 3000 Cycles) [130]

According to [134], there are three key factors that govern the evolution of fatigue damage in SAC solder interconnections during TMC: thermal mismatches in the assembly materials, intrinsic thermal mismatches caused by Sn anisotropy and the mechanical constraints

by the Cu pad. They found that the fatigue damage occurred during TMC was correlated with the regions where stresses were high, and the damage initiated at grain boundaries. They also conducted a study on the microstructure evolution of lead free solder sample during purely mechanical fatigue cycling [135]. They found that microcracks mainly formed on interfaces between the persistent slip bands and the eutectic regions, which is different than their findings from mechanically unconstrained thermal fatigue testing. Furthermore, Shang and coworkers [81] studied the initiation and growth of fatigue cracks in lead free solders. In the dendritic microstructures, the cyclic loading results in the initiation of fatigue crack along the dendrite boundary or in the β -Sn matrix. They found the crack initiation mechanism is different for low frequency loading and high frequency loading. When the loading frequency is low, the fatigue cracks have the tendency to initiate along the Sn dendrites. While the cracks tend to initiate along the subgrain boundaries in the Sn matrix under high frequency loading. In addition, the crack growth path is mainly intergranular if it is time-dependent, or mainly transgranular if it is cycle-dependent.

1.5.4 TMC on Mechanical Properties of Lead Free Solders

Chen, et al. [132] reported that the hardness of SAC305 decreased by about 39% and 20%, respectively, in the recrystallized and non-recrystallized regions after 2815 thermal cycles between 0 °C and 100 °C. Dutta and coworkers [94, 99] studied the effects of TMC induced microstructural coarsening on the creep behavior of lead free solders. They reported that the creep rate increases with the precipitate size proportionately when the stresses are low. On the other hand, precipitate coarsening changes the threshold stress for particle-limited creep when the stresses are high. Erinc, et al. [136] found the global elastic modulus was dropping for the three SAC405 samples of different thickness as the thermal cycling progressed (-40 °C to 125

°C), as shown in Figure 1.15. Furthermore, a significant reduction in board-level drop reliability with increased thermal cycling was reported in [137].

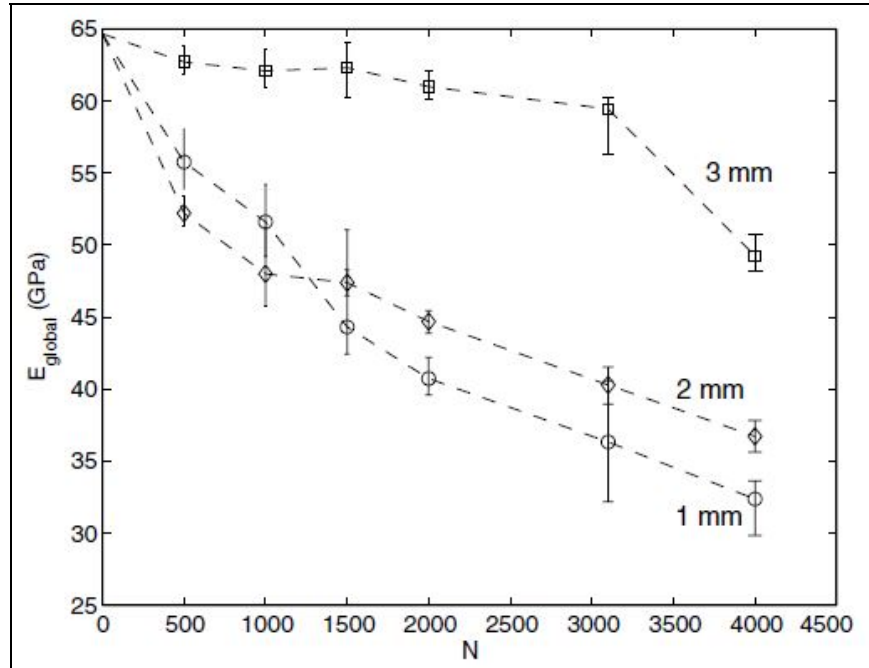


Figure 1.15 - Global Elastic Moduli as a Function of Number of Thermal Cycles [136]

1.5.5 Summary of the Effects of TMC on Solder Microstructure

- (1) Several useful experimental techniques have been used to explore solder microstructural changes during TMC, such as Scanning Electron Microscopy (SEM), Orientation Imaging Microscopy (OIM), and polarized light microscopy;
- (2) Thermo-mechanical cycling tends to result in recrystallization of β -Sn in the region where stresses or strains are high, and the recrystallized region expands as the cycling progresses;
- (3) Thermo-mechanical cycling also leads to the coarsening of IMC particles, and the coarsening is severer in the recrystallized region;

- (4) Generally, the fatigue crack initiates at the Sn grain boundaries in the recrystallized region, and then propagates along the boundaries between recrystallized grains;
- (5) Thermo-mechanical cycling leads to the degradations of various mechanical properties of lead free solders.

1.6 Objectives of This Research

This research mainly concentrates on the effects of aging on the microstructure and the cyclic stress-strain or fatigue behavior of Sn-Ag-Cu (SAC) lead free solders. Also, some work will be done to better understand the damage accumulation that occurs in SAC solders during fatigue testing. The general objectives of this research are:

- (1) Introduce cylindrical uniaxial solder test specimens in the cyclic or fatigue testing to solve the problem of buckling during compression, and then design gripping fixtures for those specimens;
- (2) Characterize and quantify effects of aging on the cyclic stress-strain behavior of SAC solders over a wide range of aging times;
- (3) Study the effects of strain rate, test temperature and strain range on the solder cyclic stress-strain behavior;
- (4) Quantify the effects of aging on solder cyclic stress-strain behavior for different strain rates, test temperatures and plastic strain ranges;
- (5) Investigate aging induced evolution of solder microstructure in fixed regions using SEM, and then create the first experimentally recorded movies of the microstructural evolution with aging;
- (6) Monitor the coarsening of IMC particles during aging in identical regions, and quantitatively analyze the coarsening using image analysis methods;

(7) Explore the evolution of solder microstructure, constitutive behavior and cyclic stress-strain behavior of SAC305 solder during fatigue testing;

(8) Establish better capability for fatigue testing in our laboratory.

1.7 Organization of the Dissertation

The research is presented in the following chapters:

Chapter 1. Introduction to and literature review on SAC lead free solders, effects of aging on solder mechanical properties and microstructure, effects of thermo-mechanical cycling on solder microstructure, etc.;

Chapter 2. Description of sample preparation procedure, experimental equipment, empirical models and data analyses;

Chapter 3. Study on the effects of aging on the cyclic stress-strain behavior (hysteresis loop area, peak stress and plastic strain range) of SAC lead free solders, and the examination of several parameters such as aging time, aging temperature, silver content, and solidification profile;

Chapter 4. Characterization of the effects of test temperature, strain rate and plastic strain range on solder cyclic stress-strain behavior, and quantification of the aging effects for different test temperatures, strain rates and plastic strain ranges;

Chapter 5. Visualization of the evolution of solder microstructure during aging in fixed regions, and quantitative analyses of aging induced coarsening of IMC particles such as the increase of average particle diameter;

Chapter 6. Investigation of the evolution of constitutive behavior (stress-strain and creep), cyclic stress-strain behavior and microstructure of SAC305 during fatigue testing;

Chapter 7. Improvement of the capability for fatigue testing in our laboratory by developing the Instron 5948 universal tester and designing a new fatigue tester based on the current MT-210 microtester;

Chapter 8. Summary and conclusions of the dissertation, and recommendations for future work.

CHAPTER 2

EXPERIMENTAL PROCEDURE

2.1 Introduction

A unique sample preparation procedure has been used to produce rectangular cross-section specimens in the lab. As mentioned earlier, the thin flat specimens tend to buckle during compression in fatigue testing. In order to prevent buckling, the circular cross-section specimens are introduced, and fixtures are designed to grip the cylindrical specimens. The mechanical testing was performed using a tension/torsion thermo-mechanical test system. After testing, empirical models were utilized to represent the stress-strain, creep, and cyclic stress-strain experimental data. For the microstructural analysis, the solder cross-sectional specimens were polished and then the microstructures were examined using SEM or polarized light microscope.

2.2 Sample Preparation Procedure

Solder uniaxial samples are often fabricated by machining of bulk solder material, or by melting of solder paste in a mold. These methods have several disadvantages as discussed in [61-65]. In the current study, we have avoided the issues present with machining or molding samples by using a novel procedure where solder uniaxial test specimens are formed in high precision glass tubes using a vacuum suction process. Unlike prior studies that used rectangular cross-section glass tubes [61-65, 75-78], glass tubes with circular cross-sections were adopted in

this work to produce cylindrical specimens that are more resistant to buckling during the compression portions of cyclic stress-strain testing.

Buckling is the bending of a slender element when subjected to compression, which leads to a sideways deflection. If buckling occurs during fatigue testing, it can be told from the test sample, corresponding hysteresis loop and cycles to failure. According to Euler formula, the maximum axial load a long, slender, ideal column can carry without buckling is

$$F = \frac{\pi^2 EI}{(KL)^2} \quad (2.1)$$

where, E is elastic modulus, I is area moment of inertia of the column cross-section, L is the unsupported length of the column, and K is column effective length factor and the value is 0.5 for both ends fixed. The area moment of inertia for rectangular cross-sections is

$$I = \frac{bh^3}{12} \quad (2.2)$$

where, b and h are the width and height of the cross-section, respectively. While the area moment of inertia for circular cross-sections is

$$I = \frac{\pi d^4}{64} \quad (2.3)$$

where d is the diameter of the cross-section. Therefore, the resistance to buckling can be significantly improved by using the cylindrical specimens in proper size.

The solder is first melted in a quartz crucible using a pair of circular heating elements (see Figure 2.1). A thermocouple is attached on the crucible and a temperature control module is used to direct the melting process. One end of the glass tube is inserted into the molten solder, and suction is applied to the other end via a rubber tube connected to the house vacuum system. The suction forces are controlled through a regulator on the vacuum line so that only a desired

amount of solder is drawn into the tube. The specimens are then cooled to room temperature using a user-selected cooling profile (can be the same as actual solder joints). Both water quenched (WQ) and reflowed (RF) lead free solder specimens were studied in this work. Typical temperature versus time plots for water quenching and reflow profile cooling of the test samples are shown in Figure 2.2 and Figure 2.3, respectively. The water quenching profile represents an extreme condition that yields an extremely fine microstructure due to the fast cooling rate, which results in the upper limits of the various mechanical properties. For the reflow profile cooling, the glass tube assemblies are first cooled to room temperature by water quenching, and then subjected to the temperature profile shown in Figure 2.3 using a reflow oven (9 zone Heller 1800EXL, see Figure 2.4). The reflow profile yields microstructures similar to those found in actual solder joints used in the industry.

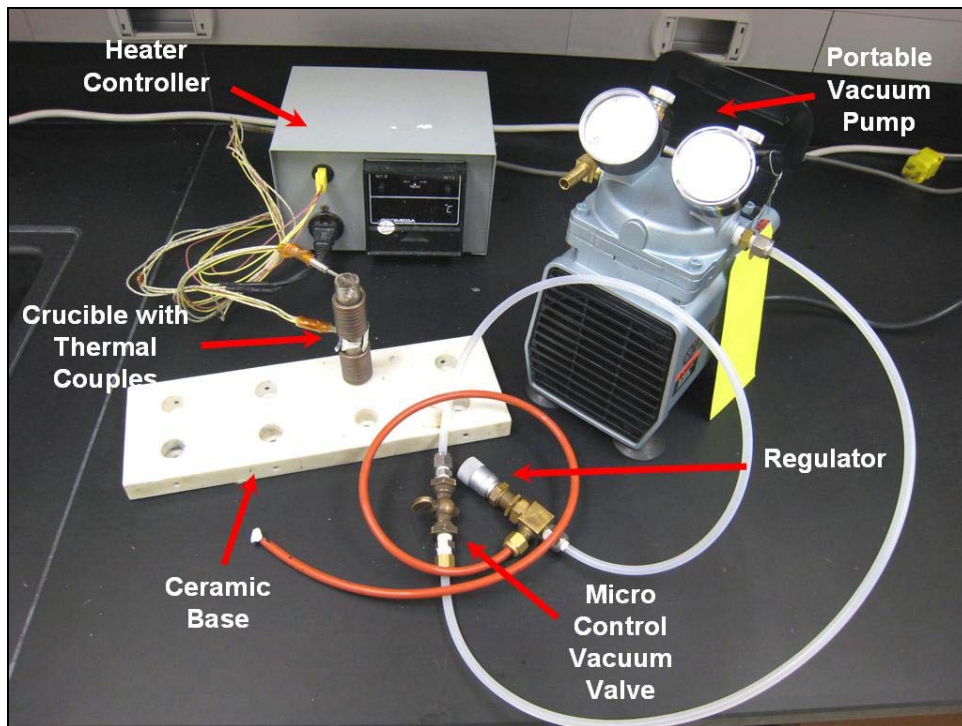


Figure 2.1 - Specimen Preparation Hardware

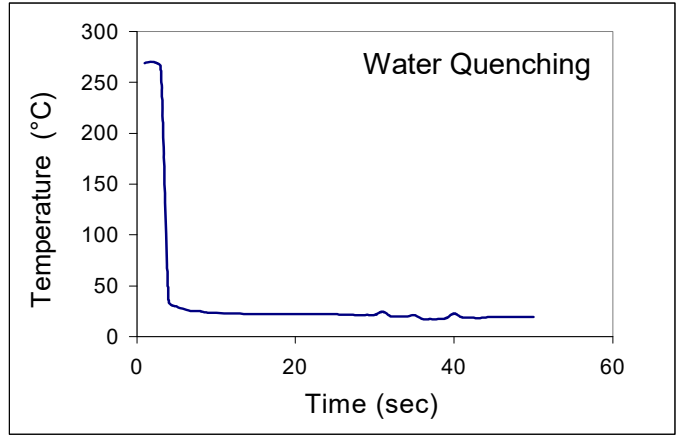


Figure 2.2 - Water Quenching Profile

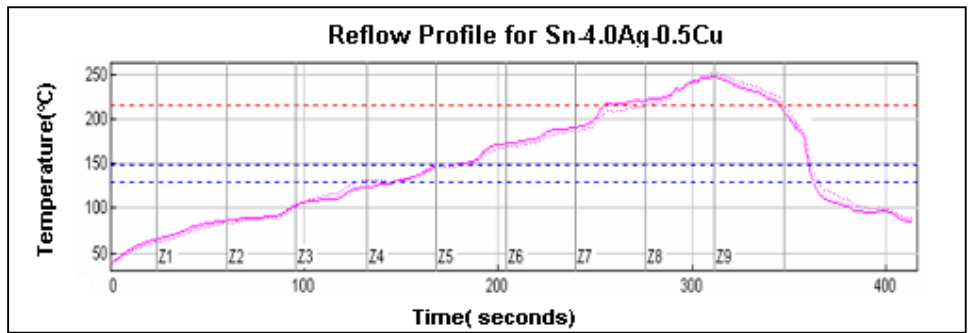


Figure 2.3 - Solder Reflow Temperature Profiles for SAC (105/205/305/405)



Figure 2.4 - Heller 1800EXL Reflow Oven

Typical cylindrical glass tube assemblies filled with solder and a final extracted specimen are shown in Figure 2.5. The solder samples can be easily pulled out from the tubes due to the differential expansions that occur when cooling the low CTE glass tube and higher CTE solder alloy. The described sample preparation procedure yielded repeatable samples with controlled cooling profile (i.e. microstructure), oxide free surface, and uniform dimensions. Sample cross-sectioning has shown that the microstructure of any given sample was consistent throughout the volume of the sample, and the repeatable sample microstructures were obtained from sample to sample for a given solidification temperature profile. With proper experimental techniques, samples with no flaws and voids were generated.

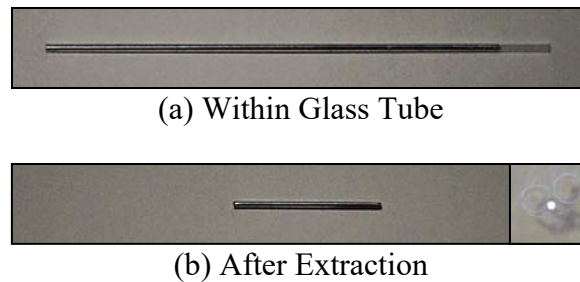


Figure 2.5 - Cylindrical Uniaxial Test Specimen

2.3 Mechanical Testing

The MT-210 tension/torsion thermo-mechanical test system from Wisdom Technology, Inc., shown in Figure 2.6 was used to perform the tensile, creep, and cyclic stress-strain testing in this work. The system provides an axial displacement resolution of 0.1 micron, and universal 6-axis load cell was utilized to simultaneously monitor three forces and three moments during sample mounting and testing. Use of the pictured heating chamber allowed samples to be tested up to +200 °C. In order to grip the cylindrical specimens properly, gripping fixtures with V-shaped grooves were designed and introduced as shown in Figure 2.7 and Figure 2.8. The

dimensional drawings of those fixtures are shown in Appendix A.1. After introducing the cylindrical specimens and gripping fixtures, we have solved many problems such as buckling during compression, specimen breaks in the grip, and slippage during testing. Figure 2.9 shows the fracture of cylindrical specimens in fatigue testing and there was no buckling in the gage areas.

During the cyclic stress-strain or fatigue testing, cyclic stress-strain curves (also called hysteresis loops) are developed. Figure 2.10 illustrates the development of hysteresis loops. The left picture shows the movement of the microtester crosshead, while the right picture shows a typical cyclic stress-strain response. The specimen is load free at the initial position A. The start of the test pulls the specimen to position B, and it is the same as tensile testing at this point. Unlike tensile testing, the movement is reversed at position B and the specimen is compressed to position C. Then direction of the movement is reversed again and the specimen is pulled back to position B. In this way, cyclic stress-strain curves or hysteresis loops are developed.

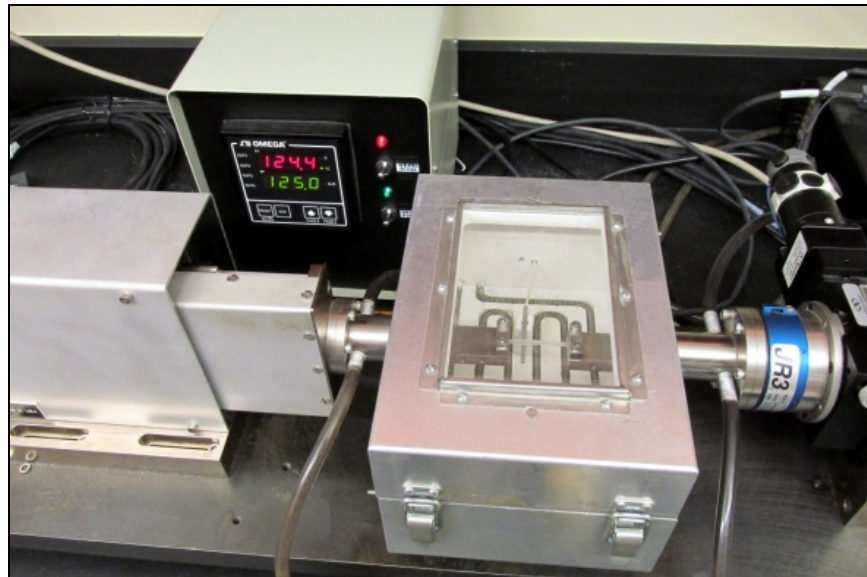


Figure 2.6 - MT-210 Testing System with Solder Sample

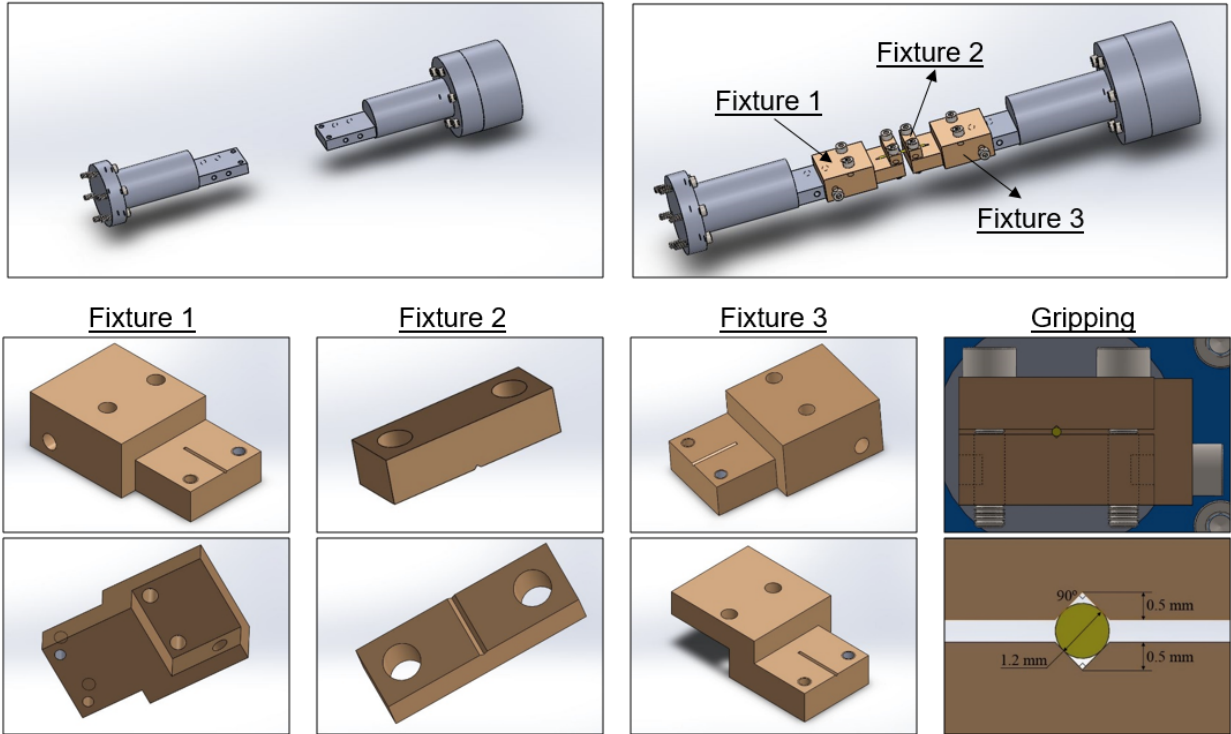
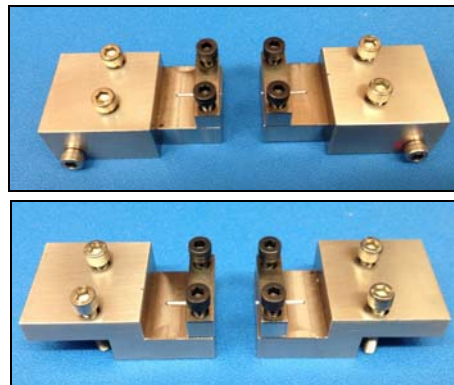


Figure 2.7 - 3-D Models of the Gripping Fixtures for Cylindrical Specimens



(a) Front & Rear Views of the Fixtures



(b) Testing System with the Fixtures

Figure 2.8 - Specimen Gripping Fixtures

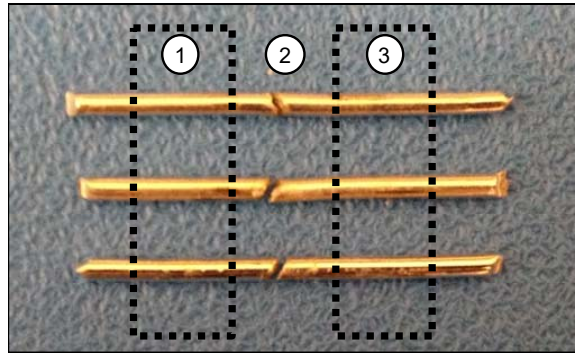


Figure 2.9 - The Fracture of Cylindrical Specimens in Fatigue Testing
(1, 3: Gripping Area; 2: Gage Area)

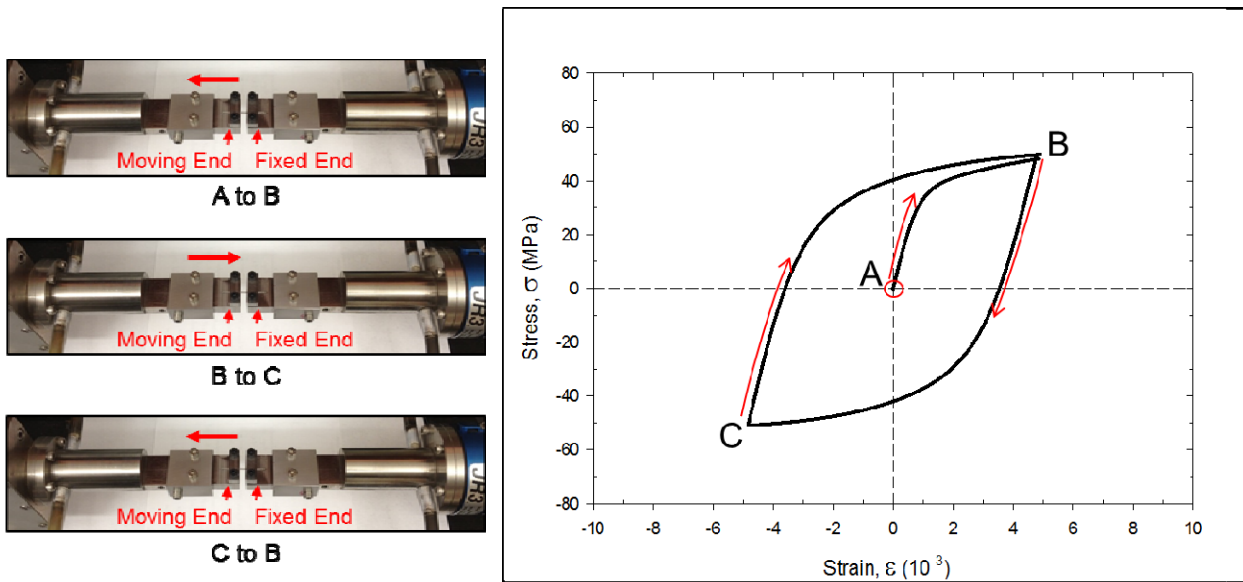


Figure 2.10 - Development of Hysteresis Loop During Cyclic Stress-Strain or Fatigue Testing

2.4 Empirical Models and Data Analysis

The axial stress and axial strain during testing were calculated from the measured applied force and crosshead displacement using

$$\sigma = \frac{F}{A} \quad \varepsilon = \frac{\Delta L}{L} = \frac{\delta}{L} \quad (2.4)$$

where σ is the uniaxial stress, ε is the uniaxial strain, F is the measured uniaxial force, A is the original cross-sectional area, δ is the measured crosshead displacement, and L is the specimen gage length (initial length between the grips).

For tensile testing, Mustafa, et al. [75] proposed a four-parameter hyperbolic tangent model (Eq. (2.5)) to represent the experimental stress-strain data.

$$\sigma = C_1 \tanh(C_2 \varepsilon) + C_3 \tanh(C_4 \varepsilon) \quad (2.5)$$

where C_1, C_2, C_3, C_4 are material constants to be determined through regression fitting of the model to experimental data. From the recorded stress-strain curve, mechanical properties such as effective elastic modulus E , yield stress σ_Y (YS) and ultimate tensile strength σ_u (UTS) can be determined, as illustrated in Figure 2.11. E is the initial slope of the stress-strain curve, and σ_Y is set at the standard 0.2% plastic strain. σ_u is taken to be the maximum stress in the stress-strain data. Solder materials are viscoplastic and their properties are rate and temperature dependent.

As shown in Figure 2.12, the typical solder creep curve can be divided into three stages, and the secondary (steady-state) region is often characterized by a long duration that is nearly linear. The constant slope is called secondary creep rate and is a key parameter used in finite element simulations for the prediction of solder reliability. For solder creep experiments, the four-parameter Burger's (spring-dashpot) model was found to fit the primary and secondary creep regions very well [63]:

$$\varepsilon = \varepsilon(t) = k_0 + k_1 t + k_2 \left(1 - e^{-k_3 t}\right) \quad (2.6)$$

From the strain versus time curve under constant stress, the "steady state" secondary creep rate (constant k_1) can be obtained.

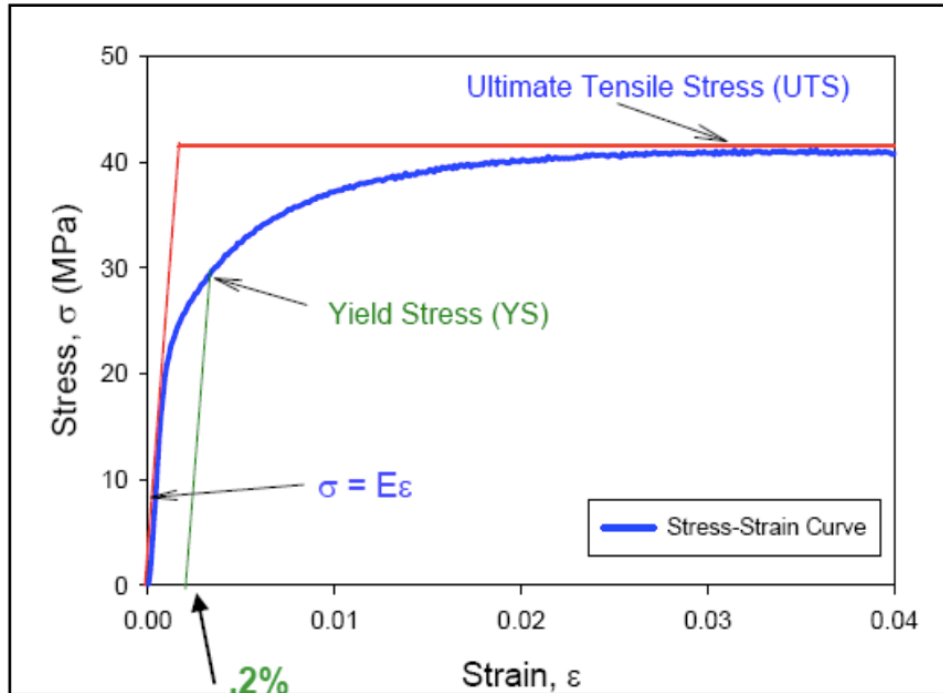


Figure 2.11 - Typical Solder Stress-Strain Curve [16]

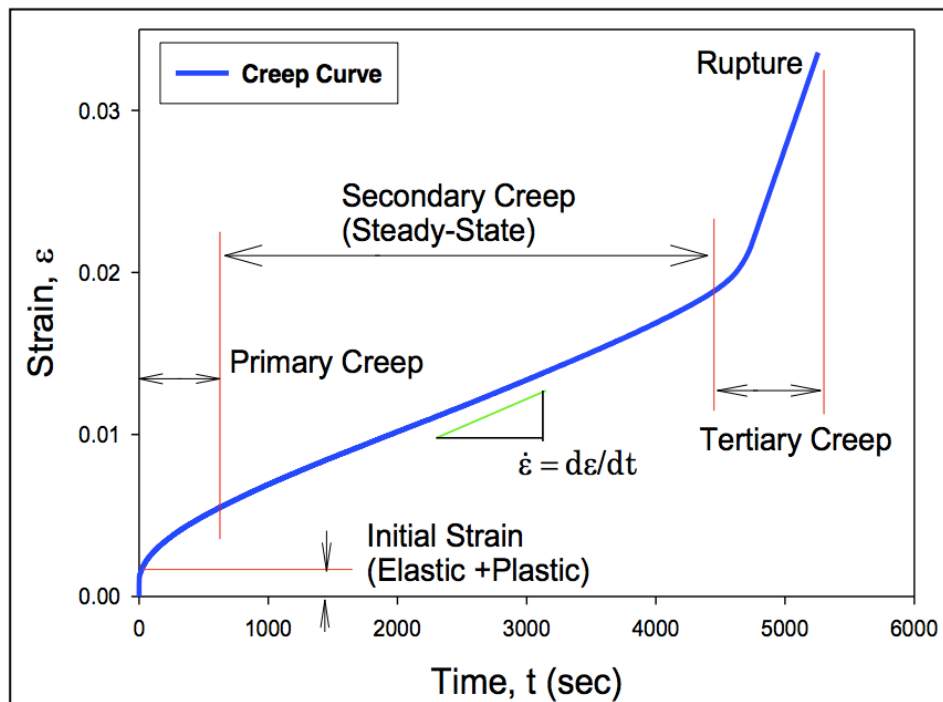


Figure 2.12 - Typical Solder Creep Curve [63]

A typical set of cyclic stress-strain curve for SAC solder is shown in Figure 2.13. A rather stable set of hysteresis loops were found to occur for several cycles. Although several different empirical models can be used to represent the observed stress-strain data for solder, we have found that a four-parameter hyperbolic tangent model is best able to represent experimental SAC solder stress-strain curves [75]. To process the cyclic stress-strain data and calculate the areas of the associated hysteresis loops, a pair of hyperbolic tangent empirical models has been used to represent the tension portion and the compression portion of the cyclic stress-strain curve in each cycle. Figure 2.13 illustrates the definitions of the two portions of the stress-strain cycle and the empirical fits $f_1(\varepsilon)$ for the compression loading region (bottom of the hysteresis loop) and $f_2(\varepsilon)$ for the tensile region (top of the hysteresis loop).

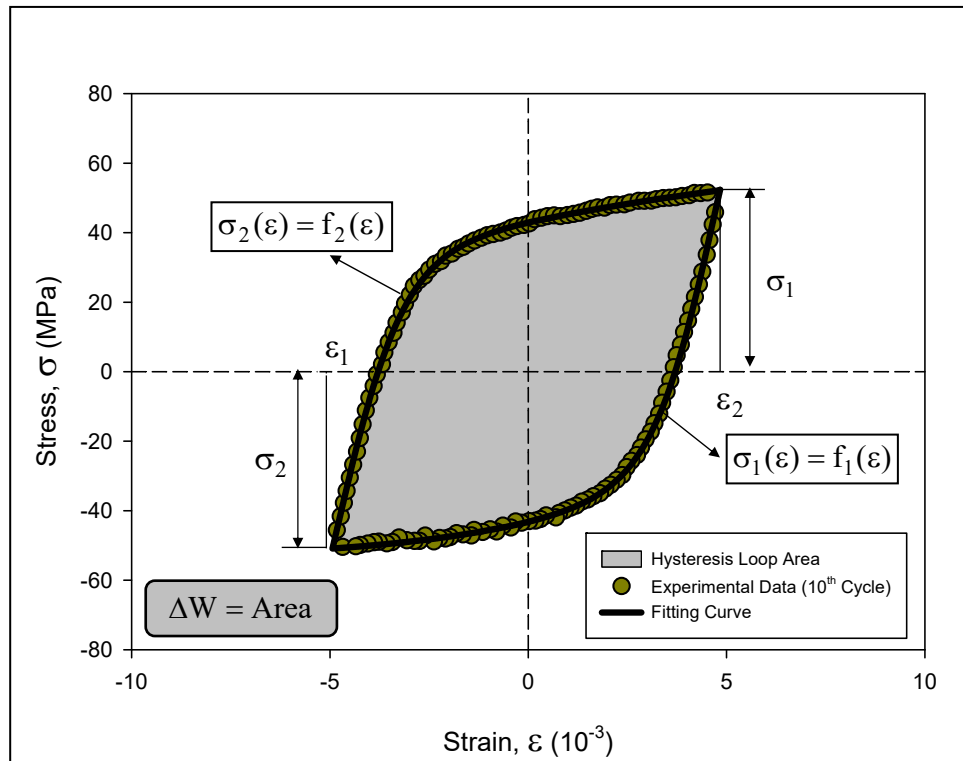


Figure 2.13 - Solder Stress-Strain Curves and Empirical Model

Using the approach presented by Mustafa, et al. [75], the upper and lower curves were represented as:

$$\begin{aligned}
 f_1(\varepsilon) &= -A_1 \tanh(A_2(-\varepsilon + \varepsilon_2)) - A_3 \tanh(A_4(-\varepsilon + \varepsilon_2)) + \sigma_1 \\
 f_2(\varepsilon) &= B_1 \tanh(B_2(\varepsilon - \varepsilon_1)) + B_3 \tanh(B_4(\varepsilon - \varepsilon_1)) + \sigma_2 \\
 \varepsilon_1 &\leq \varepsilon \leq \varepsilon_2
 \end{aligned}
 \tag{2.7}$$

From the stress-strain data for each cycle, the constants in the empirical models in Eq. (2.7) can be determined through a nonlinear regression analysis. The hysteresis loop area can then be evaluated using

$$\Delta W = \int_{\varepsilon_1}^{\varepsilon_2} [f_2(\varepsilon) - f_1(\varepsilon)] d\varepsilon
 \tag{2.8}$$

This area represents the energy density dissipated per cycle during the cyclic loading.

From the recorded cyclic stress-strain curves, the areas of the hysteresis loops are calculated using the procedure outlined above. In addition, the plastic strain ranges and peak stresses are determined as illustrated in Figure 2.14. The plastic strain range is equal to the total strain range minus the elastic strain range, which is the distance between the two strain axis intercepts on the graph. The peak stress is simply the maximum stress recorded during the cycle. The hysteresis loop area and plastic strain range are usually considered as fatigue damage driving forces, and are widely used in models to predict fatigue life of solders.

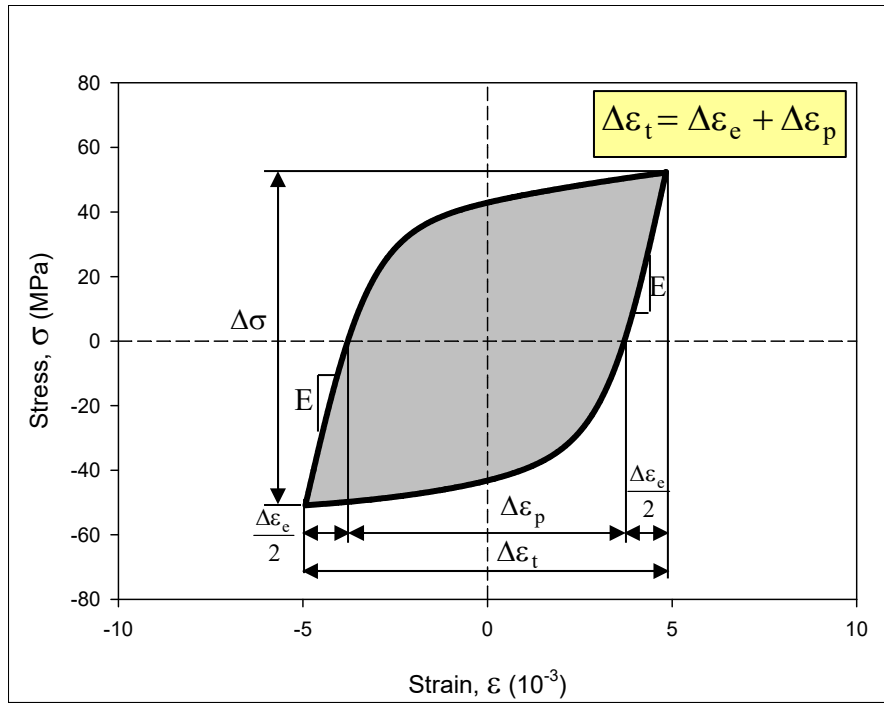


Figure 2.14 - Determination of Plastic Strain Range and Peak Stress

2.5 Microstructural Study

Scanning Electron Microscope (SEM), as shown in Figure 2.15, has been utilized to examine the microstructural changes occurring within lead free solders due to aging or mechanical cycling. By scanning the sample with a focused beam of electrons, SEM can be used to produce images with high resolving power and high depth of focus. There are various signals that result from the interactions of the electron beam with the sample atoms, including secondary electrons (SE), back-scattered electrons (BSE), photons of characteristic X-rays, etc. [138, 139]. Figure 2.16 shows the various depths of the produced signals within the sample [139]. SE and BSE have been used to form images in this study. The inelastic collision of electronic beam and the sample results in secondary electrons, and SE images provide information about morphology and surface topography. The back-scattered electrons emit backwards elastically during the collision of electron beam and the sample, and they are sensitive to atomic mass of the nuclei

they scatter from. The brightness of a heavier element is greater than that of a lighter element in BSE imaging [139].



Figure 2.15 - JEOL JSM-7000F Field Emission SEM

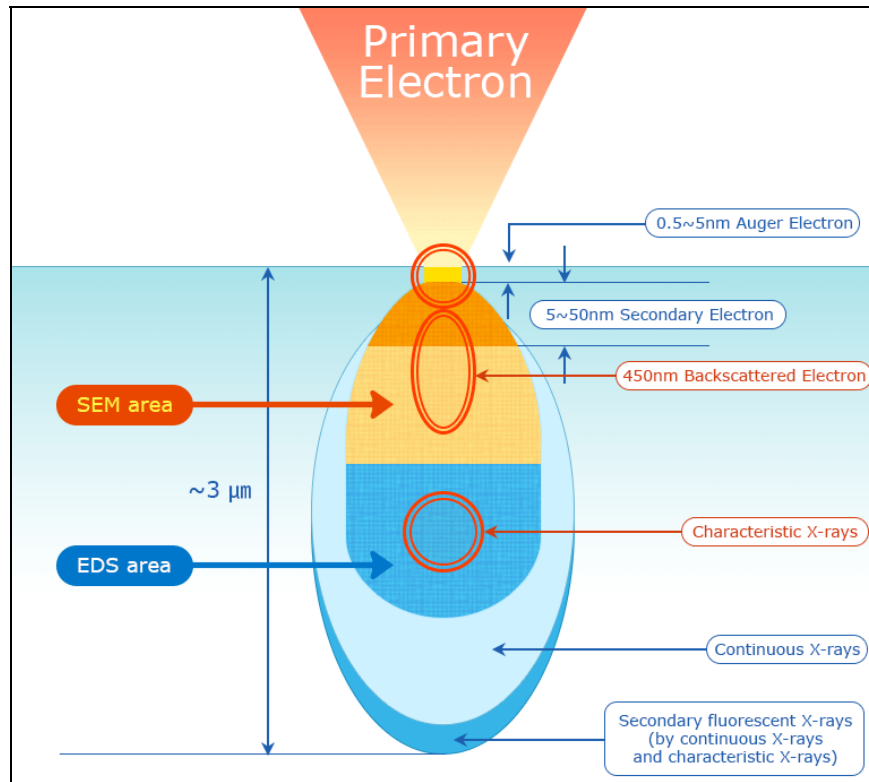


Figure 2.16 - Various Signals at Different Depths Within the Sample [139]

To study the solder microstructural changes during aging, SAC305 solder samples were formed with RF and WQ cooling profiles and resulting initial microstructures, and then microscopy cross-sections were prepared. As stated earlier, the RF solidification samples were prepared using a nine-zone reflow oven and a typical BGA solder joint temperature profile. The WQ samples were cooled rapidly by quenching, yielding a much finer (and more unstable) microstructure, as well as superior mechanical properties. The solder cross-sectional specimens were polished using industry standard procedures. After polishing, regions of interest with typical microstructures were identified on the cross-sections. To facilitate locating the identical regions of interest in subsequent microscopy observations after aging, small indentation marks were added to the cross-sections near the corners of the regions of interest using Hysitron TI 950 nanoindentation system. For example, Figure 2.17 shows a typical region of interest and the applied indentation markers. In this case, the region of interest was approximately $60 \times 40 \mu\text{m}$, and the center-to-center spacing between the indentation marks was approximately $90 \mu\text{m}$. The indentation marks were positioned close enough to enable region identification, but far enough away from the region to avoid influencing the microstructure evolution. This region was used to study aging induced microstructural changes, including coarsening of IMCs and subgrains, and breakdown of dendrite structures.

To study the effects of mechanical cycling on the solder microstructure of SAC305, uniaxial samples with various durations of prior mechanical cycling have been prepared. The cycled microstructures were then examined using SEM and polarized light microscope. Figure 2.18 shows the Zeiss Axio Imager 2 polarized light microscope that used in this work, which was used to differentiate grains with different orientations. Also, EDS was utilized to perform element mapping analysis on the cycled microstructures.

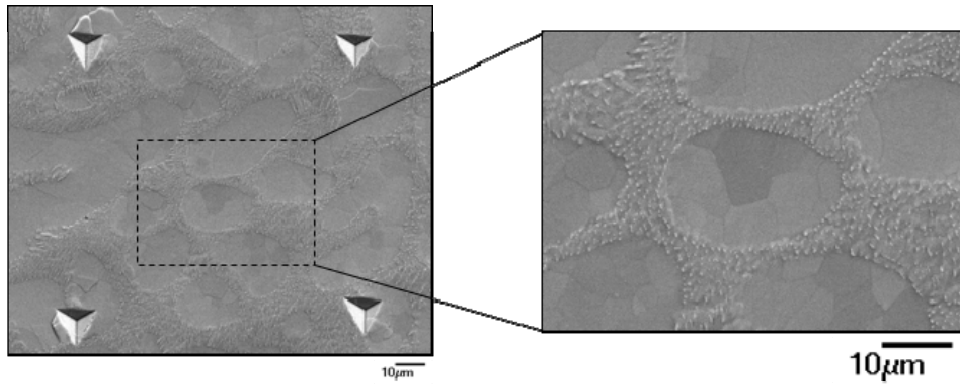


Figure 2.17 - Example Region of Interest and Nanoindentation Locating Markers

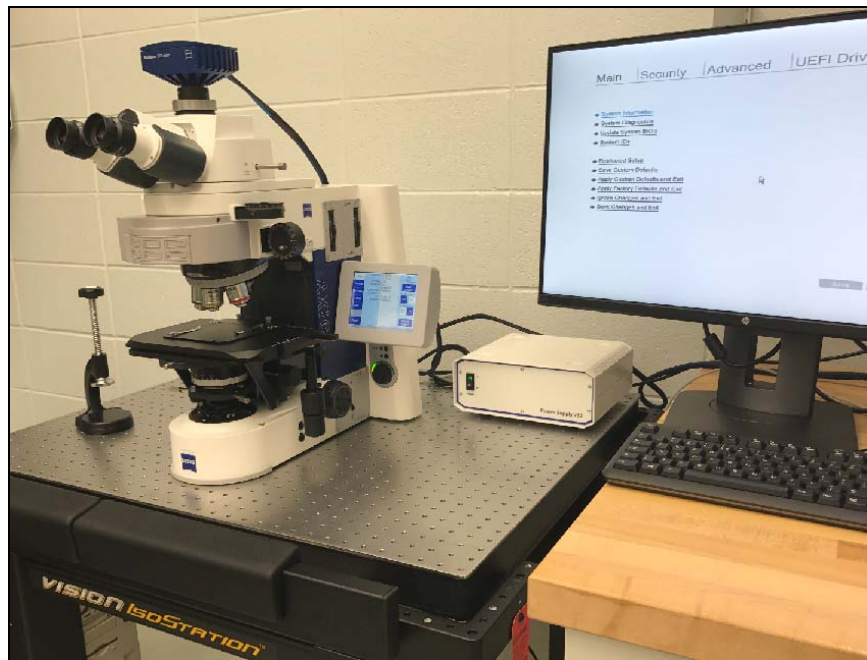


Figure 2.18 - Zeiss Axio Imager 2 Polarized Light Microscope

2.6 Summary and Discussion

In this study, newly designed micro-cylinder shaped uniaxial lead free solder test specimens have been prepared in glass tubes using a vacuum suction process. The cylindrical specimens were introduced to solve the buckling problem during compression in the cyclic or fatigue testing. The mechanical testing was performed using a tension/torsion thermo-

mechanical test system. Gripping fixtures were designed and added to the test system to grip the cylindrical specimens. After testing, empirical models were utilized to represent the stress-strain, creep, and cyclic stress-strain experimental data.

To study the solder microstructural changes during aging, SAC305 solder samples were formed with RF and WQ cooling profiles and resulting initial microstructures, and then microscopy cross-sections were prepared. After polishing, small indentation marks were added to the cross-sections to facilitate locating the identical regions of interest. Then the microstructural changes in the fixed regions during aging were examined using SEM. To study the effects of mechanical cycling on the solder microstructure, uniaxial samples with various durations of prior mechanical cycling have been prepared. The cycled microstructures were then examined using SEM and polarized light microscope.

CHAPTER 3

AGING INDUCED EVOLUTION OF THE CYCLIC STRESS-STRAIN BEHAVIOR OF LEAD FREE SOLDERS

3.1 Introduction

Fatigue of solder joints exposed to thermal cycling is a common electronic packaging failure mode. Stresses and strains often result in electronic assemblies exposed to a temperature changing environment due to mismatches in the coefficients of thermal expansion (CTE) of the soldered components and the printed circuit board (PCB). Therefore, cyclic temperature changes can lead to alternating stresses and strains within the solder joints. Such exposures can occur in products that experience power cycling or during accelerated life thermal cycling tests used for qualification. Cyclic loading typically leads to micro cracks forming within the solder material, followed by macro cracks and eventually to fatigue failure. Energy dissipation occurs during cyclic loading due to yielding and occurrence of viscoplastic deformations, and can be quantified using the area of the cyclic stress-strain curve hysteresis loops, which is equal to the strain energy density dissipated per cycle. While effects of aging have been studied in some detail on the solder constitutive behavior such as stress-strain and creep, there have been few prior studies on the effects of aging on solder cyclic stress-strain behavior of lead free solders.

In this chapter, effects of aging on the cyclic stress-strain behavior of lead free solders have been explored. Different aging durations (up to 1 year), silver contents (SAC305 and SAC405), solidification profiles (WQ and RF), and aging temperatures (125 °C and 25 °C) have

been examined. Prior to testing, cylindrical uniaxial lead free solder test specimens were prepared and aged (preconditioned) at 125 °C or 25 °C for various aging times (0, 5, 10, 20, 30, 45, 60, 80, 110, 150, 200, 260, and 360 days). The 0-day aging specimens represented non-aged samples, which were tested within a few minutes after solidification. After aging, the fabricated samples were subjected to strain controlled cyclic stress-strain loading (constant positive and negative strain limits) at room temperature (25 °C). In this chapter, all specimens were tested at a constant strain rate of $\dot{\epsilon} = 0.001 \text{ sec}^{-1}$. The nominal diameter of the uniaxial specimens in this work was 1.2 mm. The applied strain limits were ± 0.005 , and the gage length was chosen as 10 mm. In addition, at least 5 tests were conducted for each solder alloy and aging condition.

For each set of cyclic stress-strain data, the four-parameter hyperbolic tangent empirical model (Eq. (2.7)) has been used to fit the entire cyclic stress-strain curve. From the recorded cyclic stress-strain curves, the evolutions of the solder hysteresis loop area, plastic strain range, and peak load with aging have been characterized and empirically modeled. Either the loop area or the plastic strain range is often considered to be the fatigue damage driving force and widely used in fatigue life prediction models. The mechanical behavior of a solder test specimen is closely tied to its microstructure. Therefore, to better understand aging induced evolution of cyclic stress-strain behavior, the effects of aging on solder microstructure of a fixed region have been studied using SEM.

3.2 Cyclic Stress-Strain Response

Lead free solder alloys are used in industry for solder balls in lead free BGAs, CSPs, and flip chip die, as well as for solder pastes used in SMT processes. In this study, strain controlled cyclic testing has been performed on the SAC305 (WQ and RF) and SAC405 (WQ) uniaxial specimens subjected to prior aging. The two cooling profiles used in the sample preparation

(WQ and RF) yielded two distinctly different initial microstructures for the samples. WQ samples have finer microstructures and better mechanical properties because of the fast cooling rate. Cyclic stress-strain curves were developed during the cyclic testing. Figure 3.1 shows the first 10 cyclic stress-strain curves for a non-aged WQ SAC305 test specimen, and it has been found that the hysteresis loop did not change much. The determined hysteresis loop areas for each cycle were 0.6608, 0.6453, 0.6585, 0.6625, 0.6395, 0.6544, 0.6417, 0.6304, 0.6422, 0.6263 MJ/m³, respectively. Figure 3.2 illustrates and compares how the hysteresis loop area changed with cycles at beginning for 5 non-aged WQ SAC305 samples. For the study of cyclic stress-strain behavior, the hysteresis loops were studied at the 10th cycle, when the loops tend to be more stable from one loop to the next. Figure 3.3 shows the cyclic stress-strain behavior for WQ SAC305 samples at no aging condition, and the plot contains 5 results tested at the same conditions. The results showed a high level of consistency and repeatability from one sample to another.

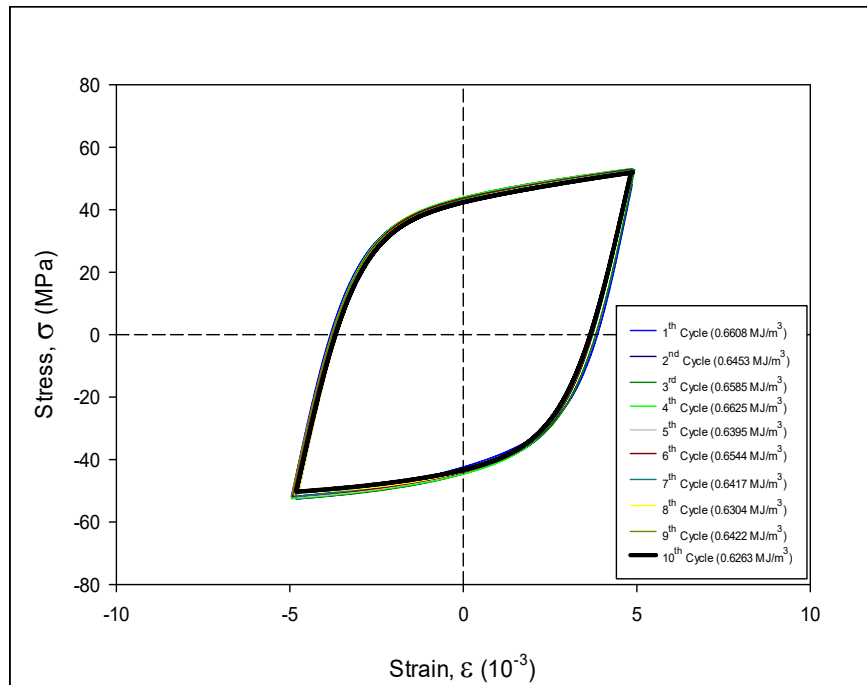


Figure 3.1 - The First 10 Hysteresis Loops for a WQ SAC305 Sample (No Aging)

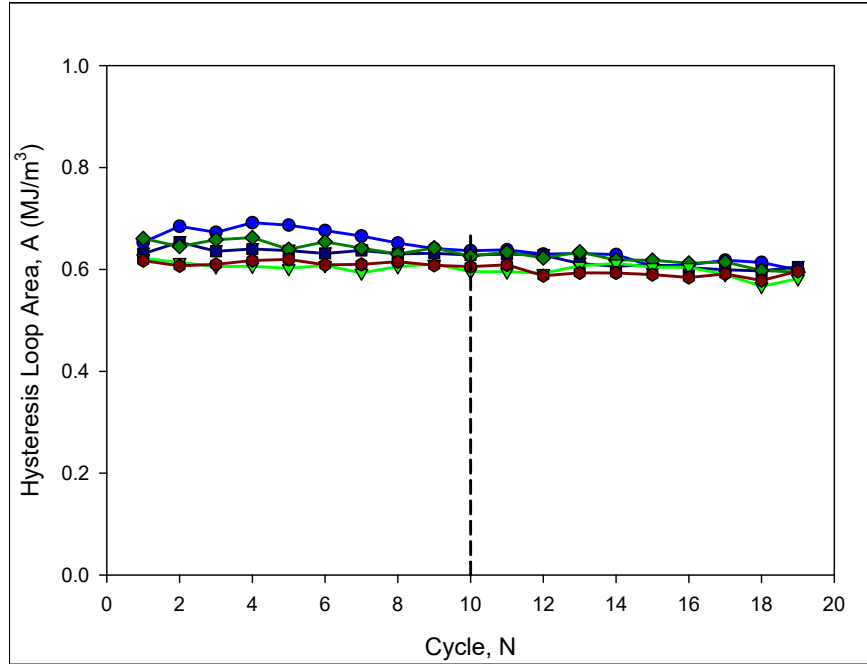


Figure 3.2 - The Changes of Loop Area with Cycles for WQ SAC305 from 5 Tests (No Aging)

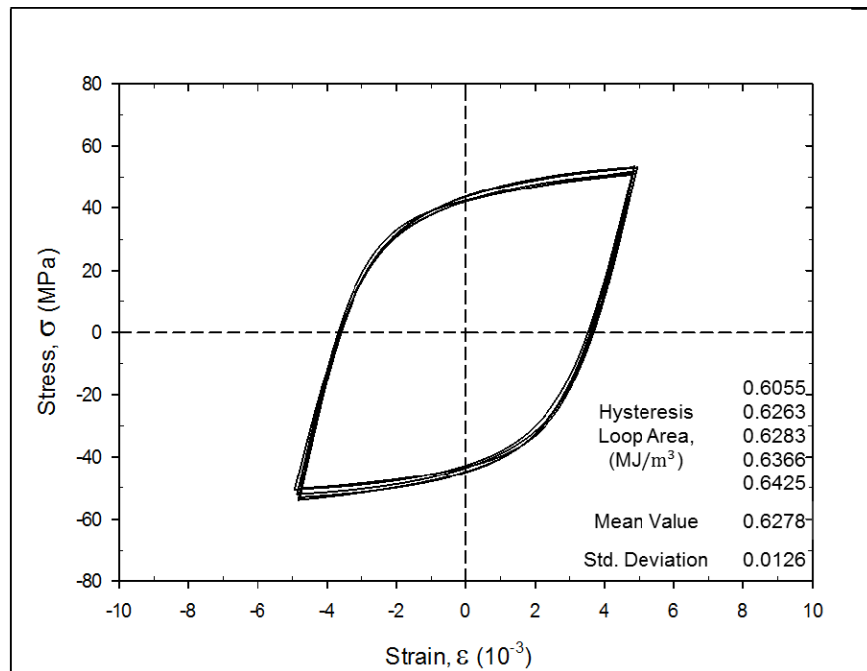


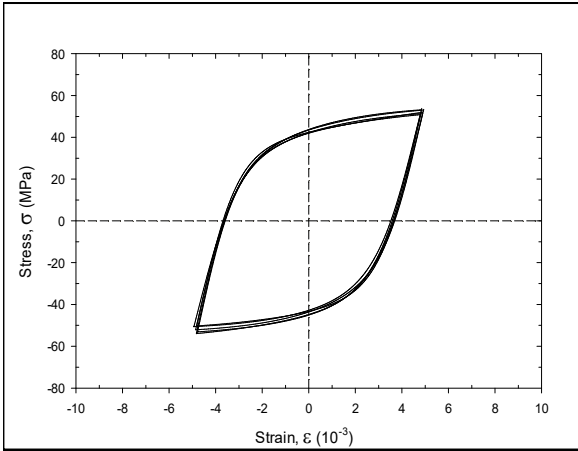
Figure 3.3 - The Cyclic Stress-Strain Behavior for WQ SAC305 from 5 Tests (No Aging)

3.3 Evolution of the Hysteresis Loop with Aging

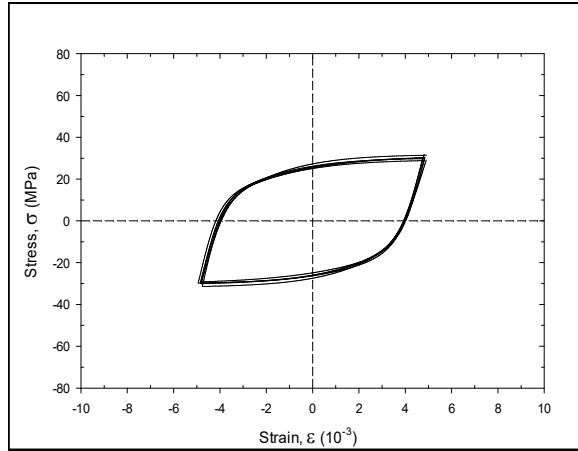
Elevated temperature aging (125 °C) induced evolution of the hysteresis loop has been characterized for three lead free solders, i. e., WQ SAC305, RF SAC305 and WQ SAC405. At the same time, the loop evolution caused by room temperature aging (25 °C) has also been studied for RF SAC305. Figure 3.4 illustrates some example plots of the cyclic stress-strain behavior for WQ SAC305 samples that were subjected to elevated temperature aging. Again, each plot contains five results tested at the same conditions for a particular aging duration, and the results were consistent and repeatable. It has been observed that the shape and size of cyclic stress-strain curves changed a lot during aging. The most noticeable changes occurred during the first 5 days of aging, with slower changes occurring for longer aging times. For aging times greater than 30 days, the hysteresis loop changes were very small. The evolution of the hysteresis loop with elevated temperature aging for WQ SAC305 solder is shown on a single plot in Figure 3.5. In this plot, a typical hysteresis loop was chosen to represent the results of five tests for each aging duration.

Similar analysis has been done for RF SAC305 (Figure 3.6 and Figure 3.7) and WQ SAC405 (Figure 3.8 and Figure 3.9) with elevated temperature aging, and for RF SAC305 (Figure 3.10 and Figure 3.11) with room temperature aging. From Figures 3.5, 3.7 and 3.9, the evolutions of hysteresis loop with aging time were similar for the three lead free solder alloys that were aged at elevated temperature. In general, hysteresis loops compressed vertically while expanded horizontally with increased aging, which indicates the decrease of peak stress and the increase of plastic strain range. For all the three alloys, the most significant changes of the hysteresis loops took place within the first 5 days of aging, and the changes became much less noticeable for long term aging. It has also been found that from no aging to 5 days of aging, RF

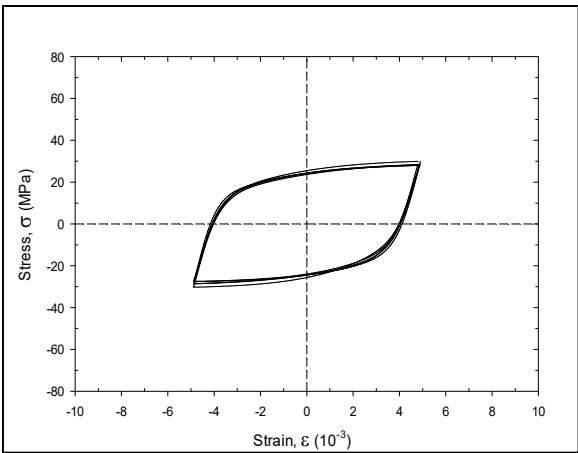
SAC305 test specimens suffered smallest changes on a percentage basis, followed by WQ SAC305 and then WQ SAC405 specimens. From Figure 3.7 and Figure 3.11, while the changes of hysteresis loop caused by aging were still obvious, the RF SAC305 test samples aged at room temperature suffered less changes than the samples aged at elevated temperature. It means the elevated temperature aging caused more degradations on the cyclic stress-strain behavior than the room temperature aging did, which was expected.



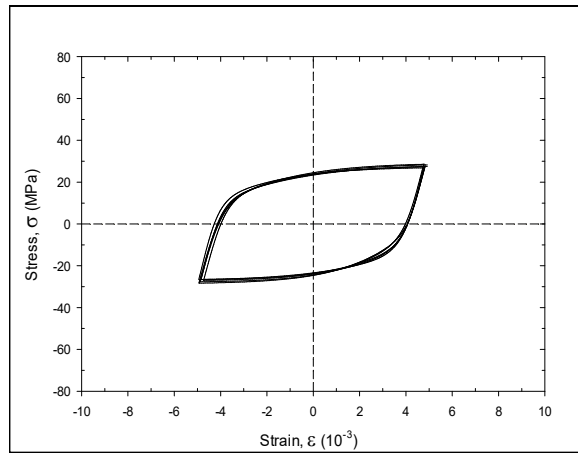
(a) No Aging



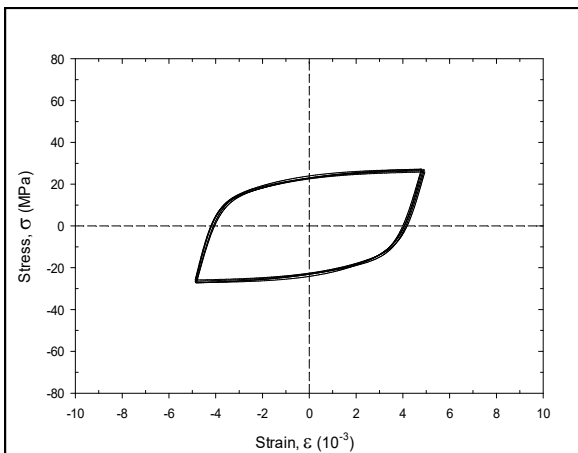
(b) 5 Days of Aging



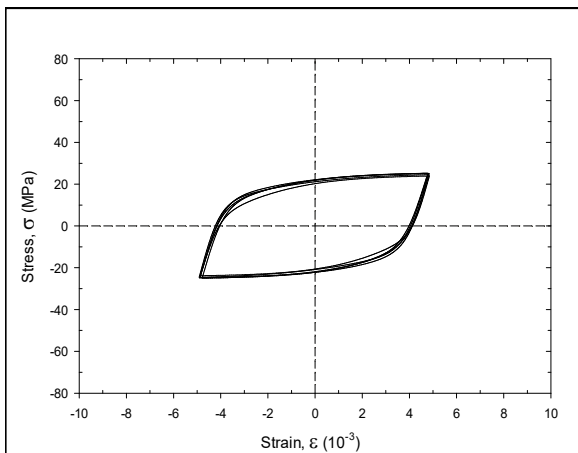
(c) 10 Days of Aging



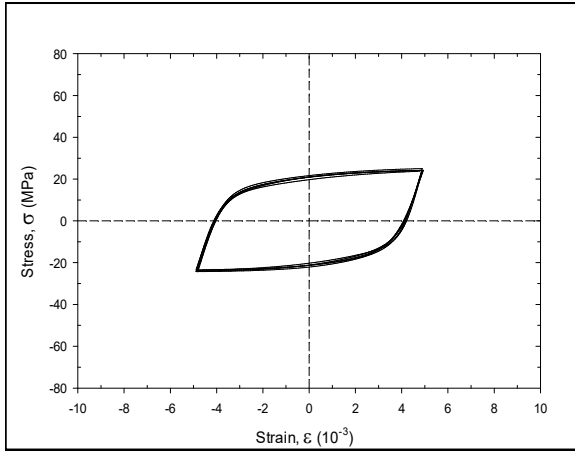
(d) 20 Days of Aging



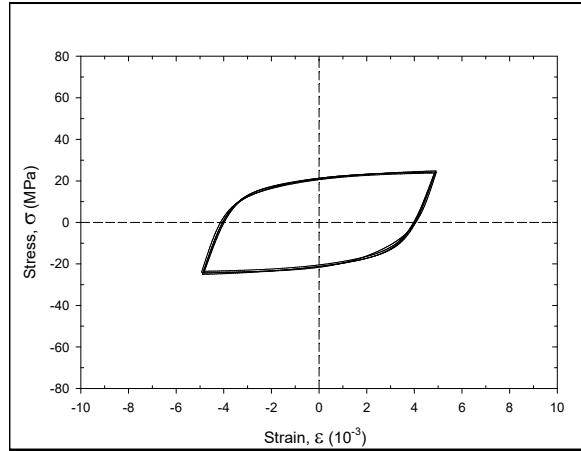
(e) 30 Days of Aging



(f) 60 Days of Aging



(g) 150 Days of Aging



(h) 360 Days of Aging

Figure 3.4 - Hysteresis Loops for Cyclic Stress-Strain Testing of WQ SAC305 (Aging at 125 °C)

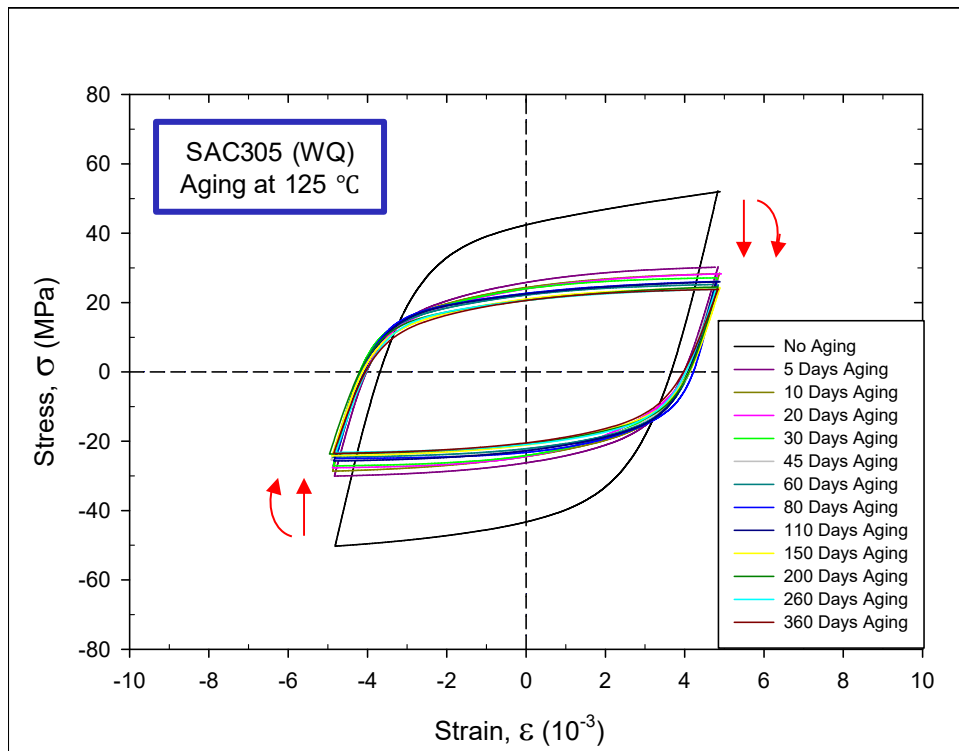
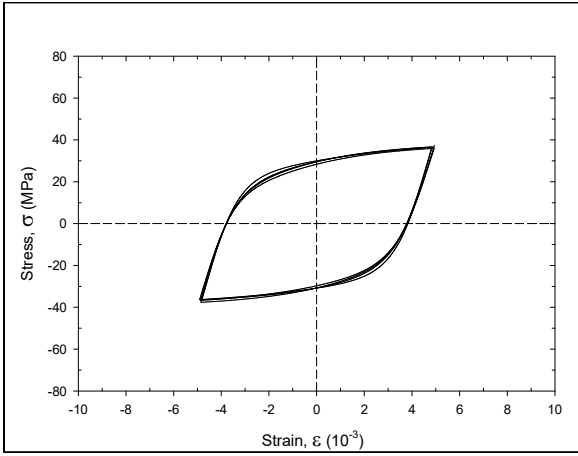
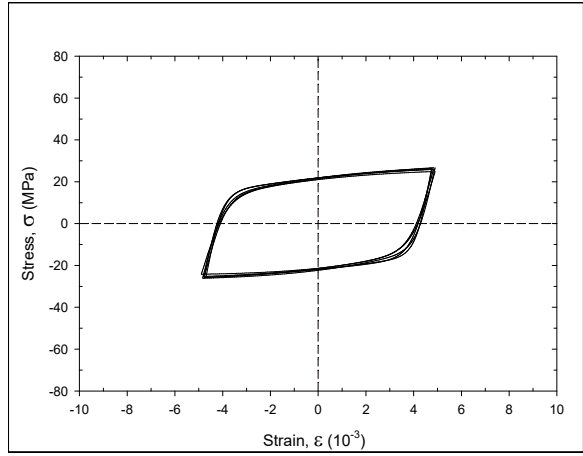


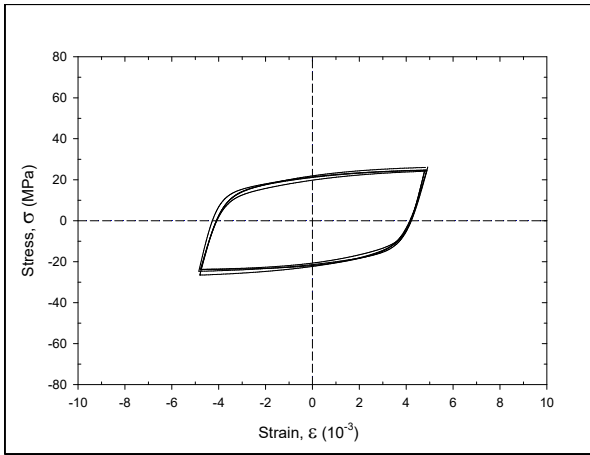
Figure 3.5 - Aging Induced Evolution of Hysteresis Loop for WQ SAC305 (Aging at 125 °C)



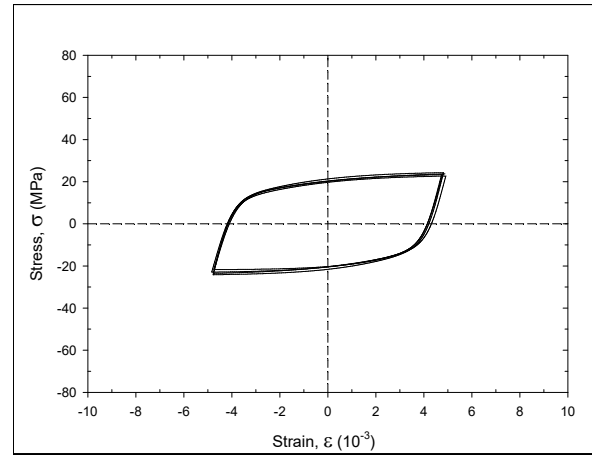
(a) No Aging



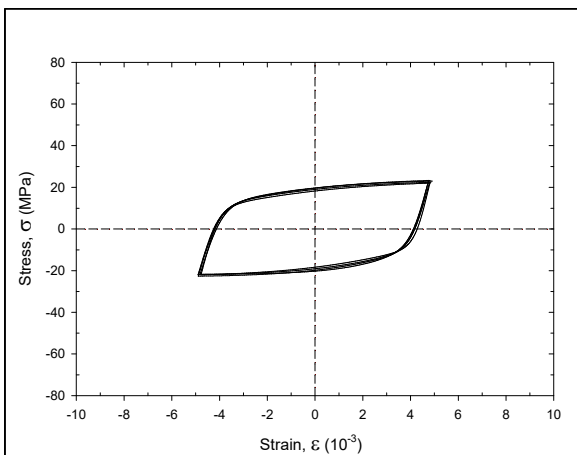
(b) 5 Days of Aging



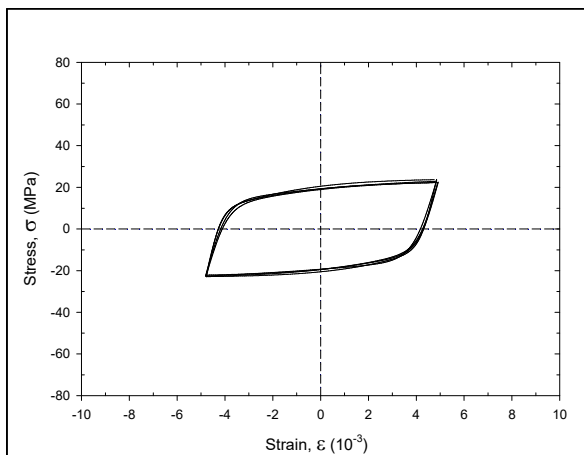
(c) 10 Days of Aging



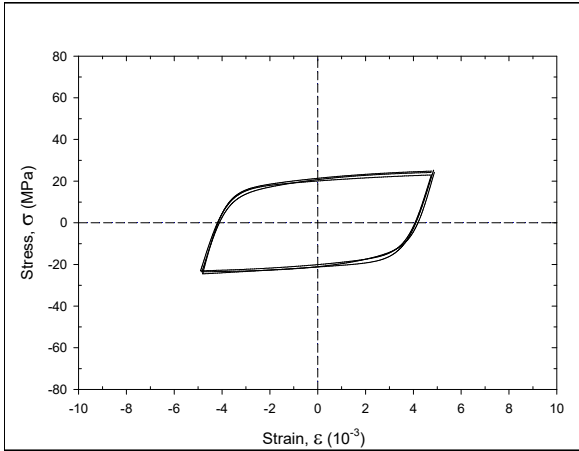
(d) 20 Days of Aging



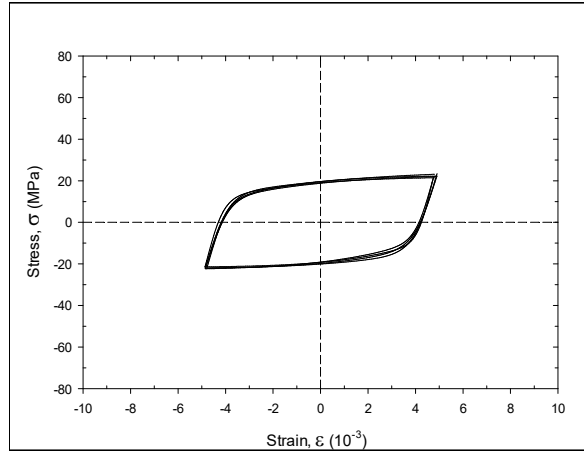
(e) 30 Days of Aging



(f) 60 Days of Aging



(g) 150 Days of Aging



(h) 360 Days of Aging

Figure 3.6 - Hysteresis Loops for Cyclic Stress-Strain Testing of RF SAC305 (Aging at 125 °C)

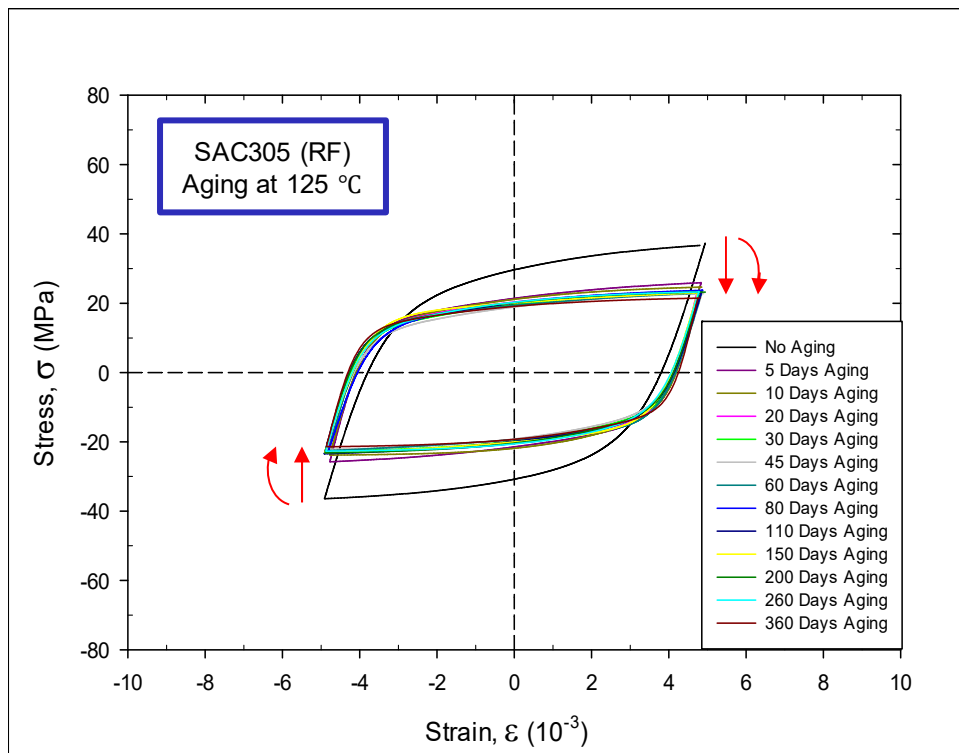
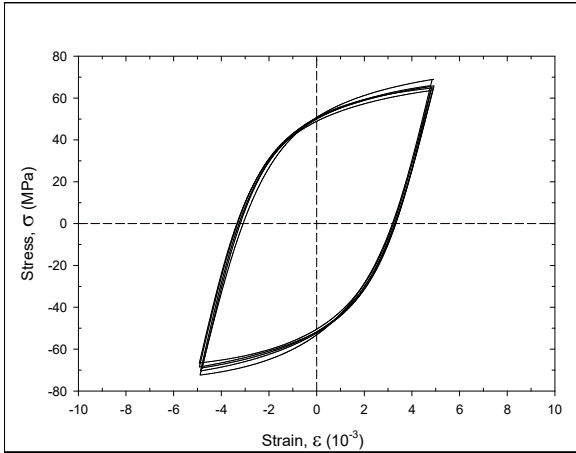
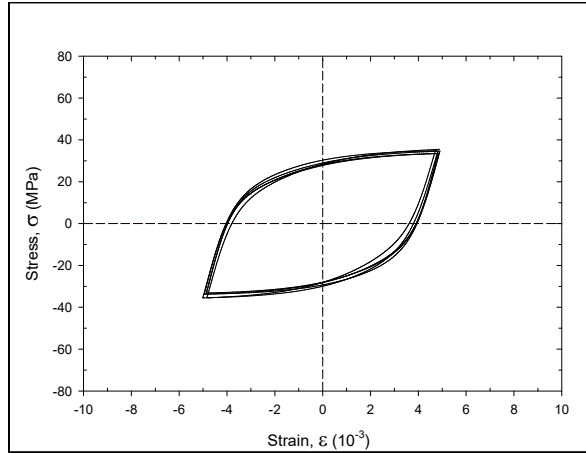


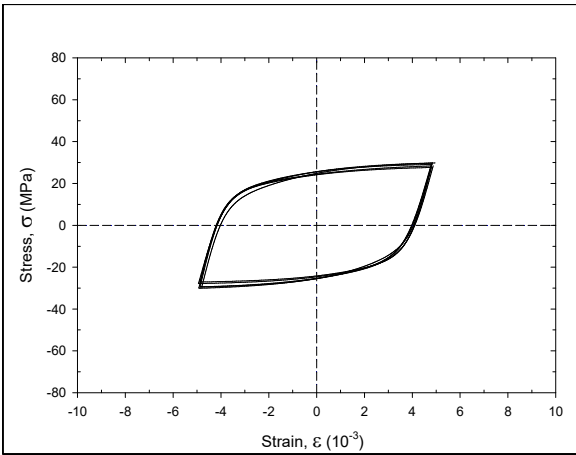
Figure 3.7 - Aging Induced Evolution of Hysteresis Loop for RF SAC305 (Aging at 125 °C)



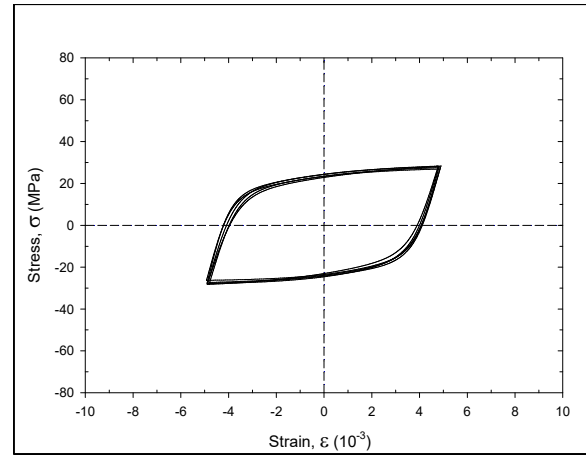
(a) No Aging



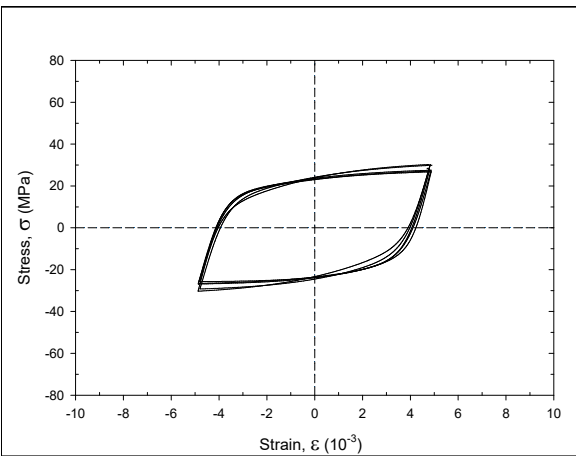
(b) 5 Days of Aging



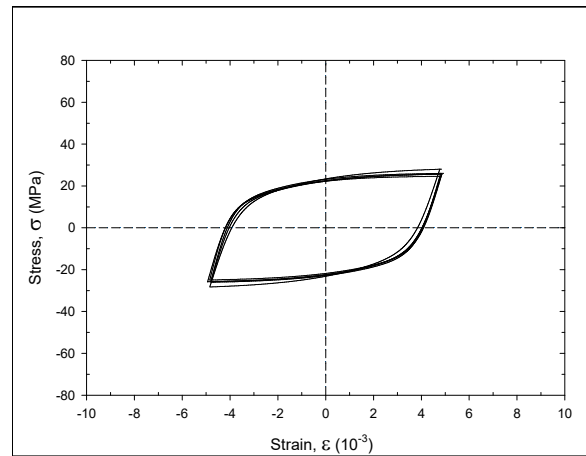
(c) 10 Days of Aging



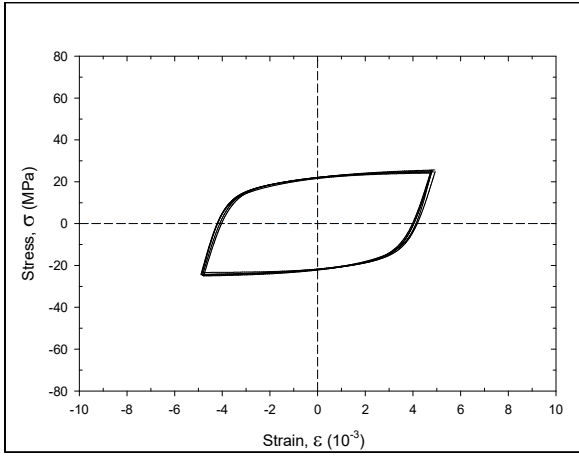
(d) 20 Days of Aging



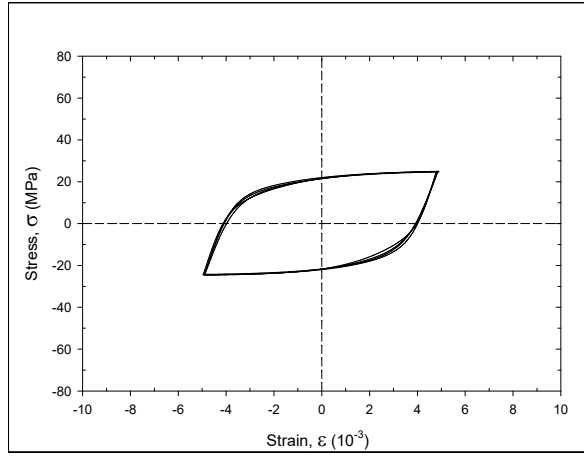
(e) 30 Days of Aging



(f) 60 Days of Aging



(g) 150 Days of Aging



(h) 360 Days of Aging

Figure 3.8 - Hysteresis Loops for Cyclic Stress-Strain Testing of WQ SAC405 (Aging at 125 °C)

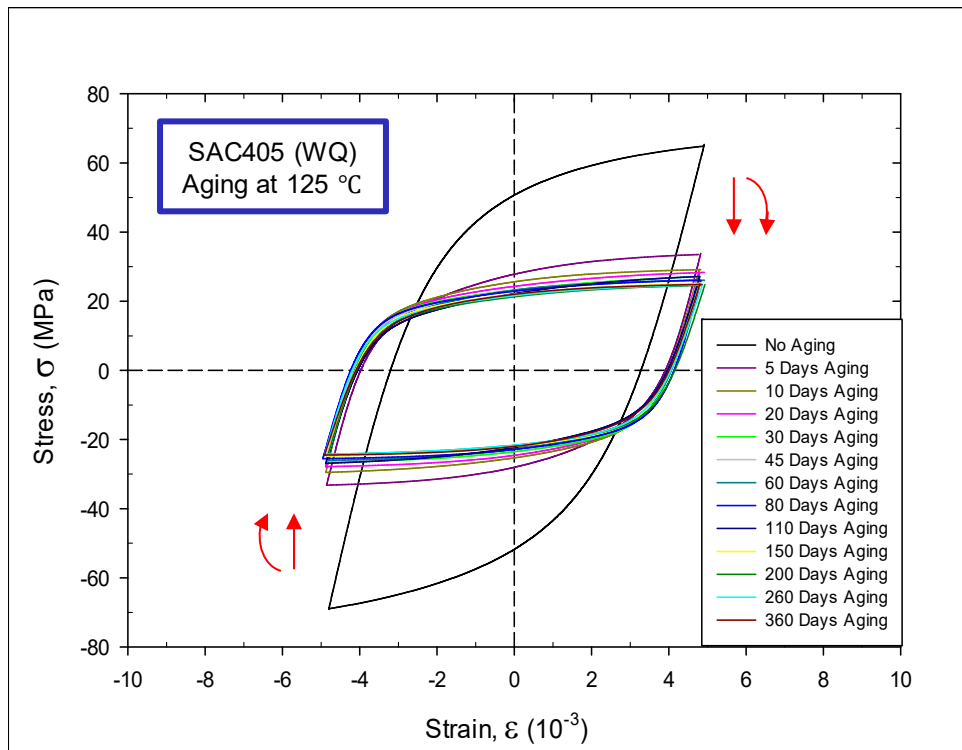
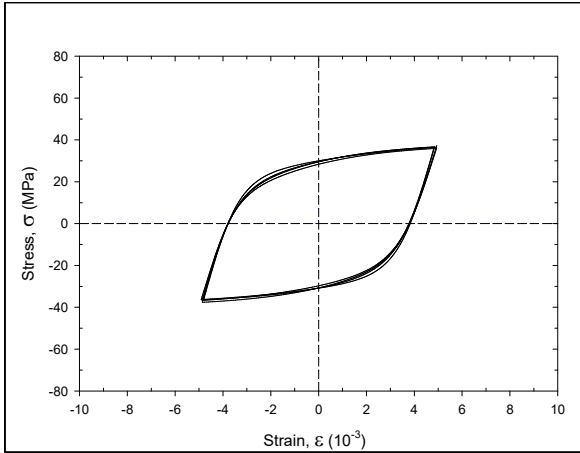
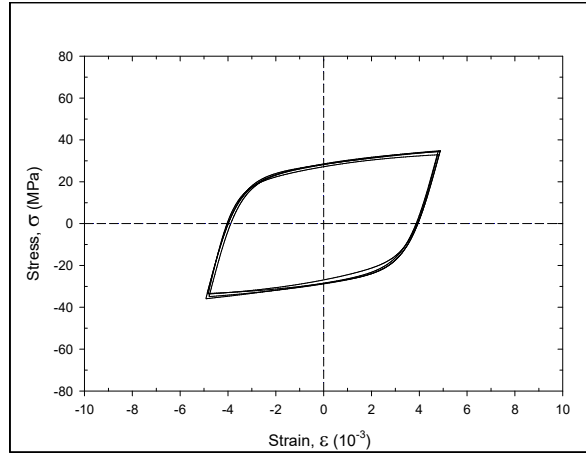


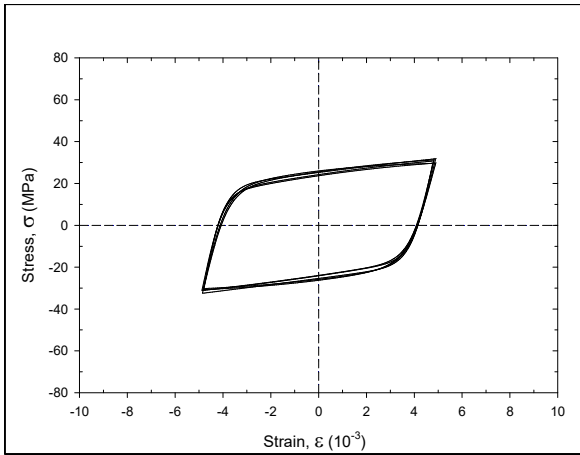
Figure 3.9 - Aging Induced Evolution of Hysteresis Loop for WQ SAC405 (Aging at 125 °C)



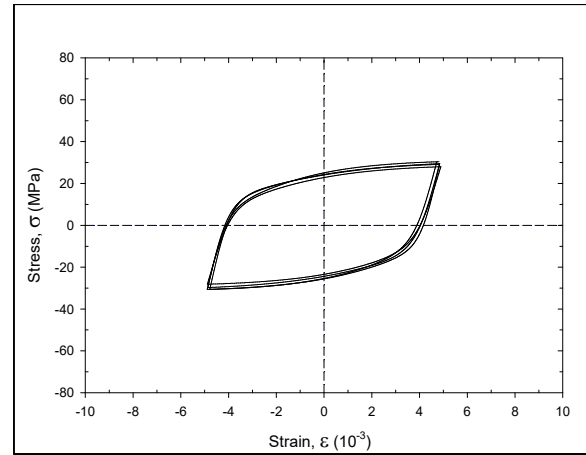
(a) No Aging



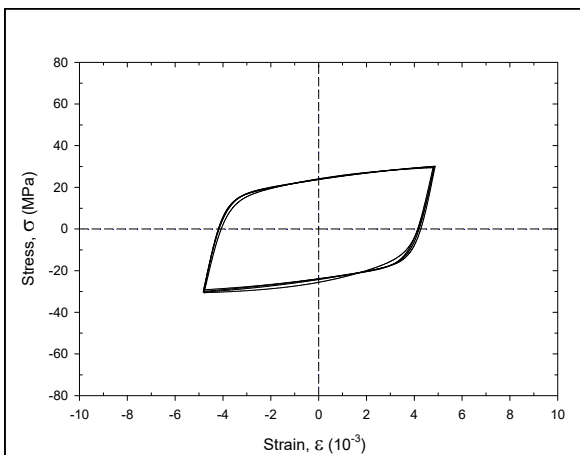
(b) 5 Days of Aging



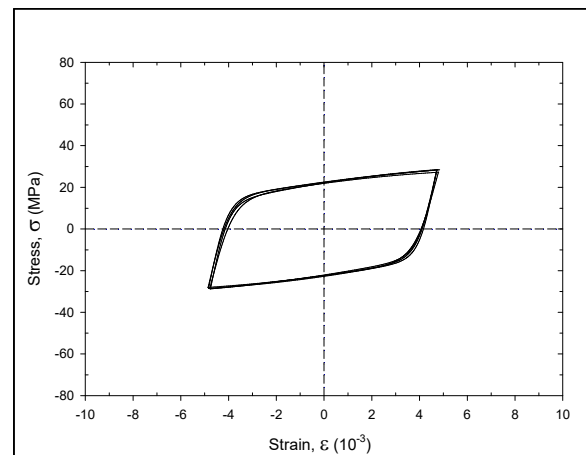
(c) 10 Days of Aging



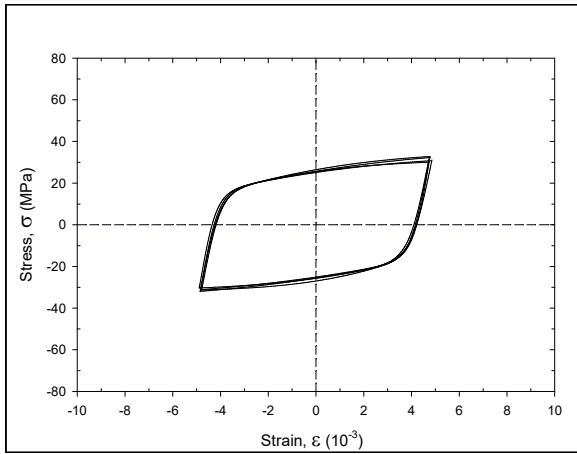
(d) 20 Days of Aging



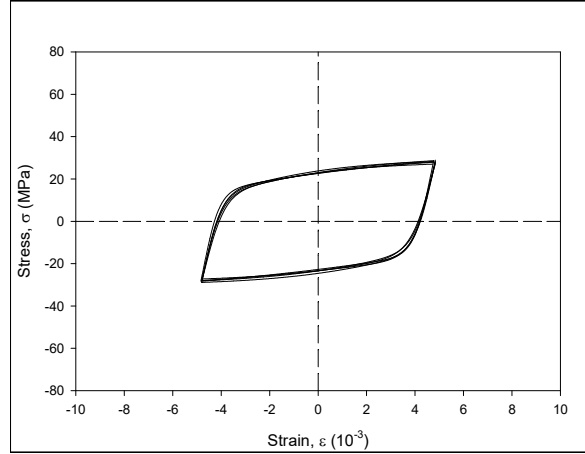
(e) 30 Days of Aging



(f) 60 Days of Aging



(g) 150 Days of Aging



(h) 360 Days of Aging

Figure 3.10 - Hysteresis Loops for Cyclic Stress-Strain Testing of RF SAC305 (Aging at 25 °C)

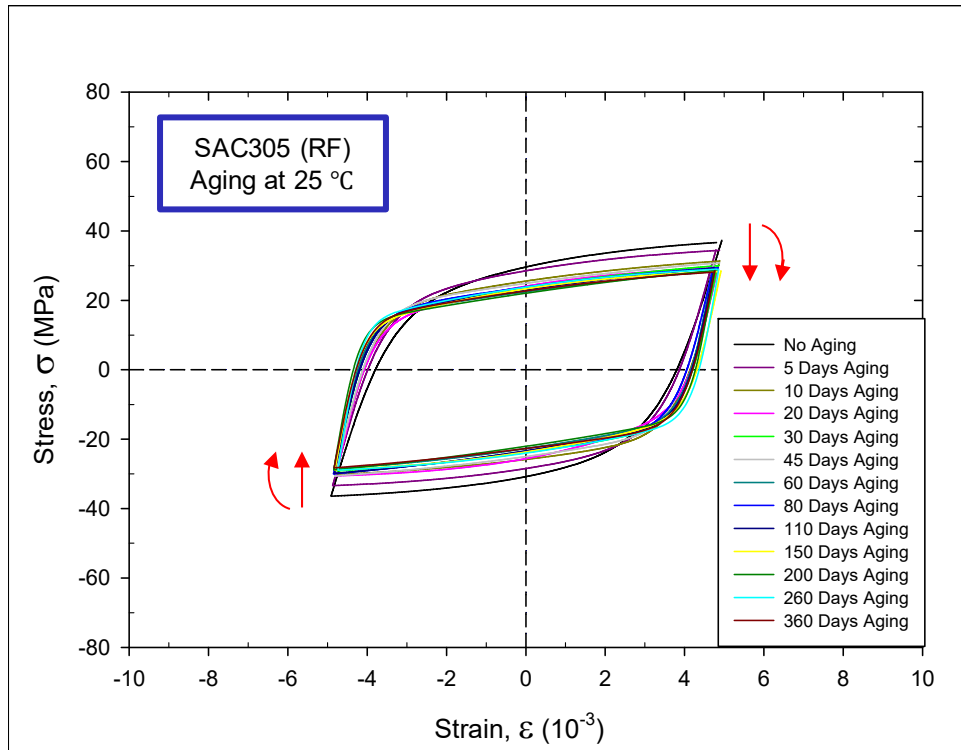


Figure 3.11 - Aging Induced Evolution of Hysteresis Loop for RF SAC305 (Aging at 25 °C)

3.4 Breakdown of the Evolution

From the recorded cyclic stress-strain curves, the areas of the hysteresis loops, plastic strain ranges and peak stresses were determined using the procedure outlined in Chapter 2.4. The loop area and plastic strain range are usually considered as fatigue damage driving forces, and are widely used in models to predict fatigue life of solders. The hysteresis loop area represents the plastic strain energy density dissipated per cycle, and is related to the damage accumulation in the specimen at that cycle. The units of the loop area are in MJ/m^3 (energy per unit volume). Fatigue models that view plastic strain energy density as the fundamental mechanism being responsible for inducing damage are typically called energy-based models. Such models include Morrow model, Syed model, and Darveaux model. Fatigue models for solder joints based on the plastic strain have been proposed by Coffin-Manson, Solomon, Engelmaier, and Miner, and these models can be categorized into plastic strain-based models [140].

Table 3.1 shows the calculated hysteresis loop area, plastic strain range, and peak stress of WQ SAC305 for each duration of prior aging at 125 °C. In this table, each data point represents the average value of 5 tests performed at the same conditions for a particular aging duration. To better understand the aging induced evolution of the cyclic stress-strain behavior, the evolution has been broken down to three parts, i. e., the evolutions of loop area, plastic strain range and peak stress. The evolutions of the hysteresis loop area, plastic strain range, and peak stress with aging time for WQ SAC305 solder are shown in Figures 3.12, 3.13, and 3.14, respectively. In general, it is observed that loop area and peak stress dropped with increased aging times, while plastic strain range increased with aging. Dramatic changes of all three parameters occurred within the first few days of aging. The applied total strain range was 0.01 in

this study. According to Figure 3.13, plastic deformation was dominant during the cyclic tests as the plastic strain range accounted for more than 70% of the total strain range.

Morrow [141] suggested that on the microscopic level, cyclic plastic strain is related to the dislocation movement while the cyclic stress is related to the ability to resist the movement. With increased aging times, the increase of plastic strain range means more dislocation movement occurred during the test. Aging also caused decrease of the peak stress, which indicates the specimen was losing ability to resist the movement of dislocations. The decrease of the hysteresis loop area with increased aging suggests that energy dissipation was mitigated with aging. However, the reduction in loop area occurred primarily because a strain controlled method was used in the testing, and thus all tests were performed using the same total strain range (0.01), or width of the hysteresis loop. Aging led to large drop of peak stress (vertical height of hysteresis loop), and a relatively smaller increase of plastic strain range. As a result, the loop area dropped as the aging duration increased, which is opposite to that using stress controlled method.

In addition, aging has similar effects on the three parameters for the other studied lead free solders. Tables 3.2, 3.3 and 3.4 list the values of the three parameters under each aging condition for RF SAC305 and WQ SAC405 (aging at 125 °C), and RF SAC305 (aging at 25 °C), respectively. Also, aging induced evolutions of loop area, plastic strain range and peak stress were quantified for RF SAC305 (Figures 3.15, 3.16 and 3.17) and WQ SAC405 (Figures 3.18, 3.19 and 3.20) with elevated temperature aging, and RF SAC305 (Figures 3.21, 3.22 and 3.23) with room temperature aging.

Table 3.1 - Determination of Loop Areas, Plastic Strain Ranges, and Peak Stresses (WQ SAC305, Aging at 125 °C)

Aging Time (Days)	Loop Area (MJ/m ³)	Plastic Strain Range, (10 ⁻³)	Peak Stress (MPa)
0	0.6278	7.24	52.36
5	0.4023	8.03	30.34
10	0.3862	8.14	28.62
20	0.3760	8.21	27.85
30	0.3666	8.27	26.70
45	0.3504	8.25	26.06
60	0.3394	8.32	24.81
80	0.3614	8.40	26.03
110	0.3571	8.34	25.81
150	0.3349	8.22	24.33
200	0.3372	8.31	24.47
260	0.3204	8.19	23.70
360	0.3288	8.18	24.35

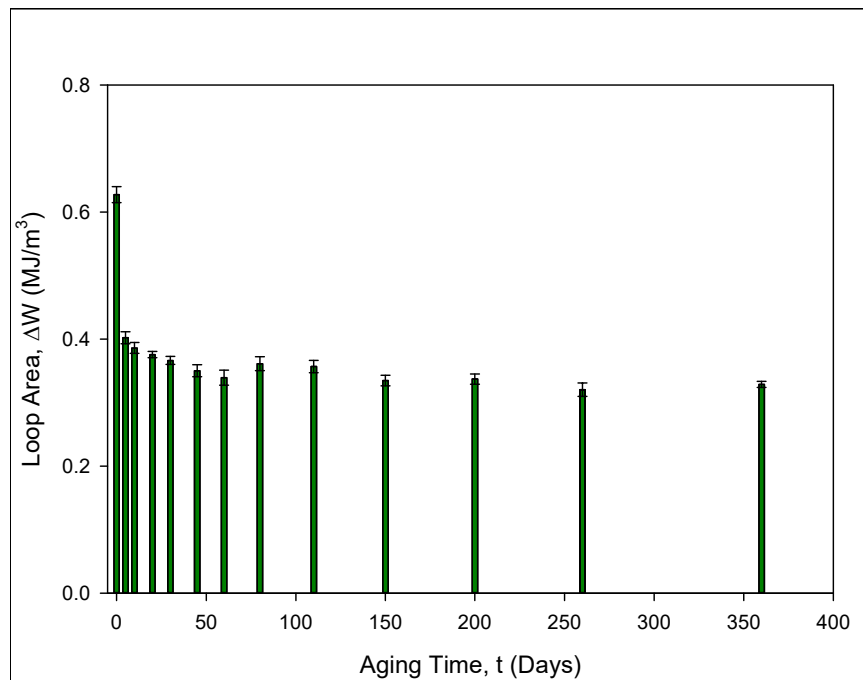


Figure 3.12 - Variation of Loop Area with Aging (WQ SAC305, Aging at 125 °C)

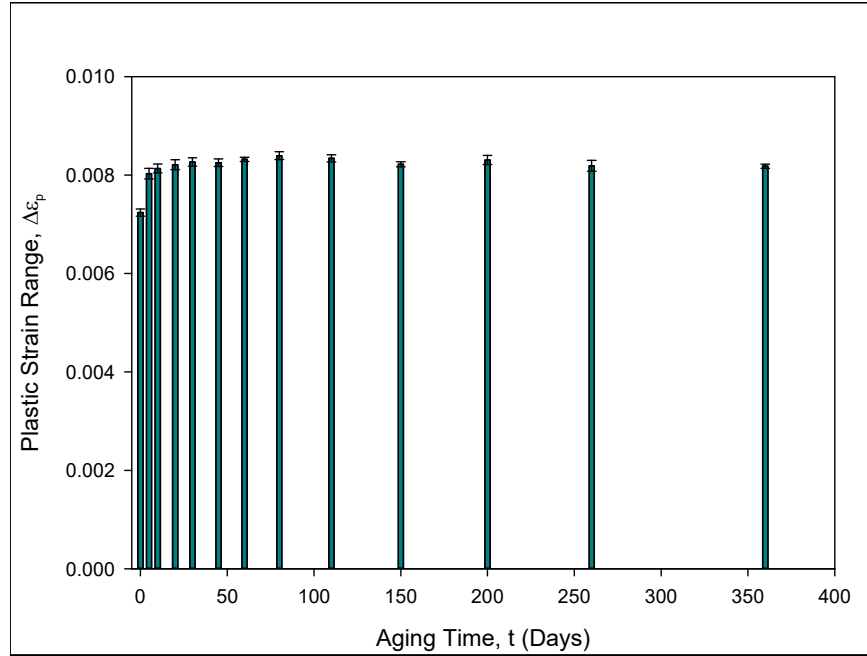


Figure 3.13 - Variation of Plastic Strain Range with Aging (WQ SAC305, Aging at 125 °C)

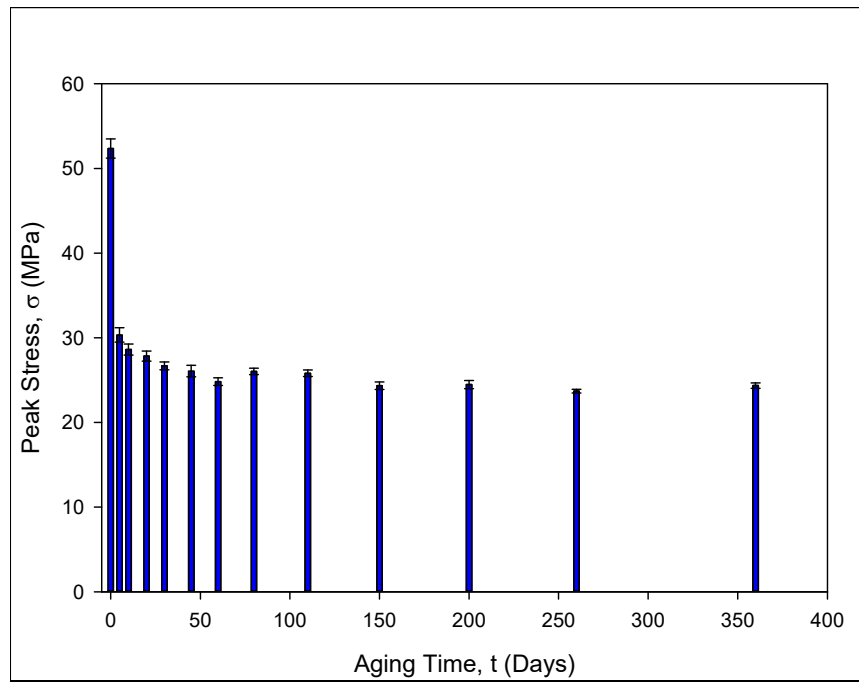


Figure 3.14 - Variation of Peak Stress with Aging (WQ SAC305, Aging at 125 °C)

Table 3.2 - Determination of Loop Areas, Plastic Strain Ranges, and Peak Stresses (RF SAC305, Aging at 125 °C)

Aging Time (Days)	Loop Area (MJ/m ³)	Plastic Strain Range, (10 ⁻³)	Peak Stress (MPa)
0	0.4579	7.58	37.20
5	0.3574	8.33	26.14
10	0.3455	8.36	24.80
20	0.3306	8.43	23.60
30	0.3258	8.47	23.53
45	0.3232	8.43	23.70
60	0.3256	8.45	23.37
80	0.3316	8.41	24.01
110	0.3281	8.39	23.51
150	0.3325	8.38	23.95
200	0.3344	8.45	23.93
260	0.3214	8.46	22.88
360	0.3207	8.51	22.39

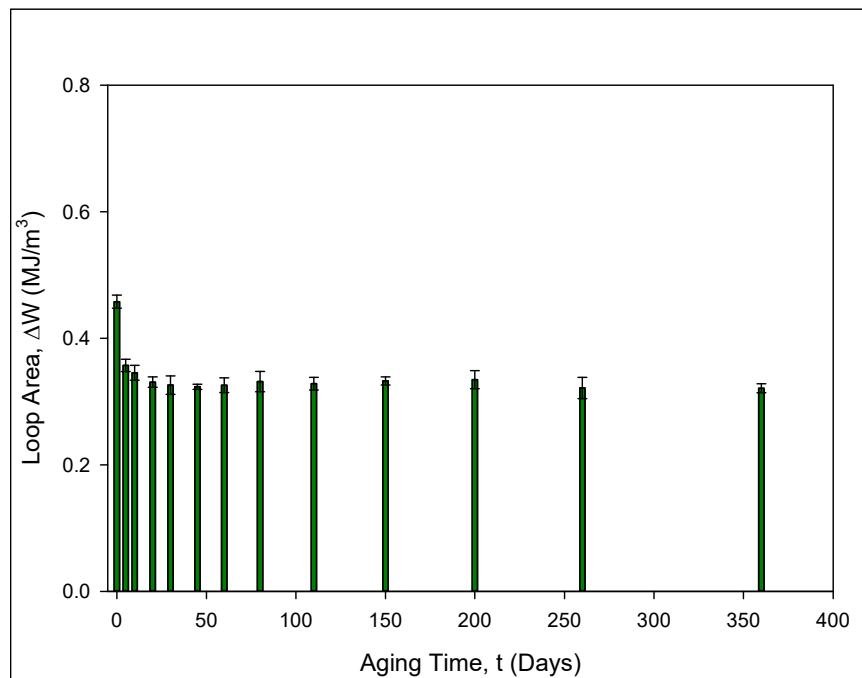


Figure 3.15 - Variation of Loop Area with Aging (RF SAC305, Aging at 125 °C)

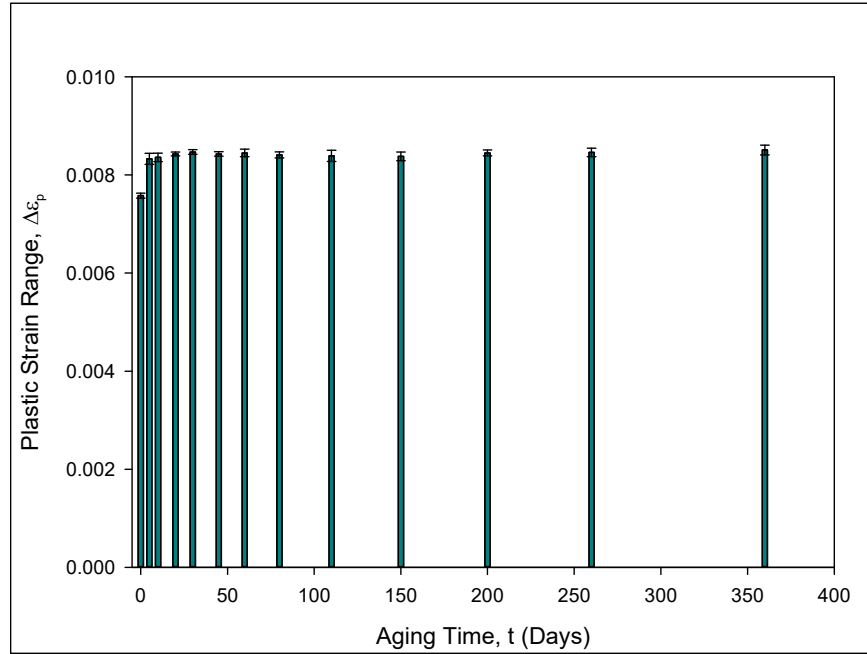


Figure 3.16 - Variation of Plastic Strain Range with Aging (RF SAC305, Aging at 125 °C)

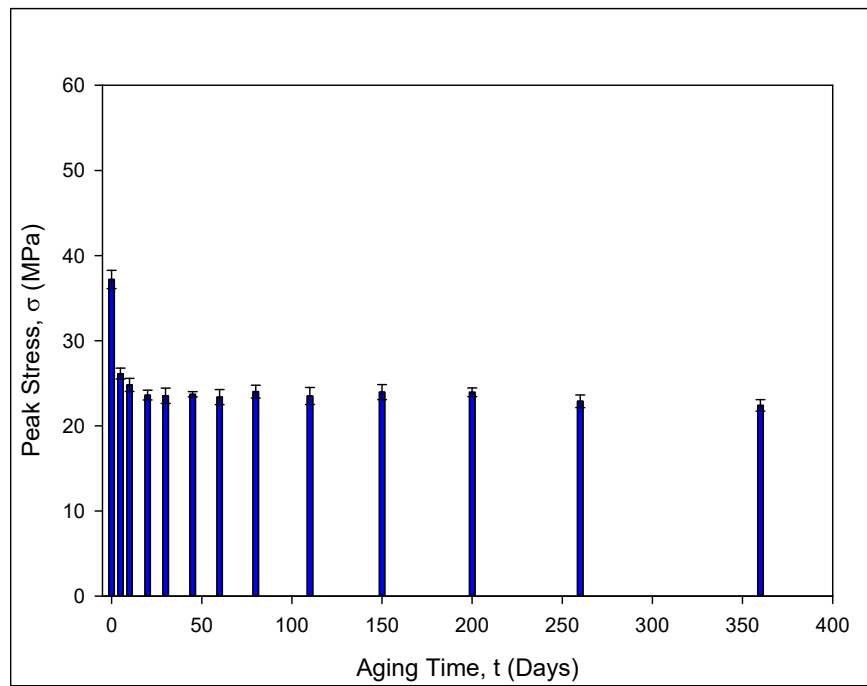


Figure 3.17 - Variation of Peak Stress with Aging (RF SAC305, Aging at 125 °C)

Table 3.3 - Determination of Loop Areas, Plastic Strain Ranges, and Peak Stresses (WQ SAC405, Aging at 125 °C)

Aging Time (Days)	Loop Area (MJ/m ³)	Plastic Strain Range, (10 ⁻³)	Peak Stress (MPa)
0	0.7035	6.60	66.03
5	0.4316	7.79	34.61
10	0.3966	8.21	29.08
20	0.3879	8.12	27.90
30	0.3759	8.16	27.92
45	0.3633	8.20	26.67
60	0.3547	8.21	26.11
80	0.3718	8.25	25.88
110	0.3569	8.08	26.82
150	0.3481	8.26	25.03
200	0.3449	8.13	25.10
260	0.3456	8.28	24.60
360	0.3338	8.13	24.90

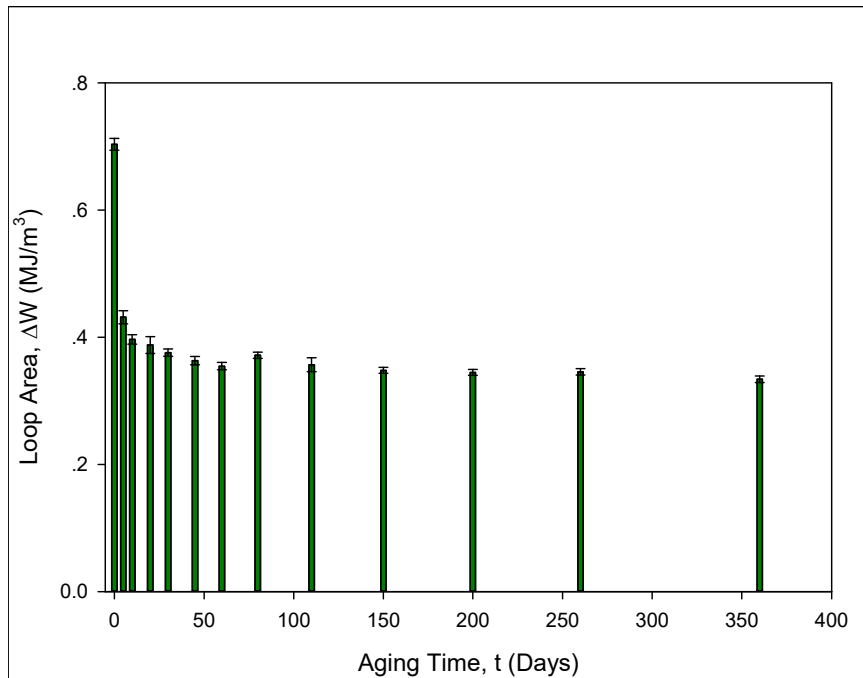


Figure 3.18 - Variation of Loop Area with Aging (WQ SAC405, Aging at 125 °C)

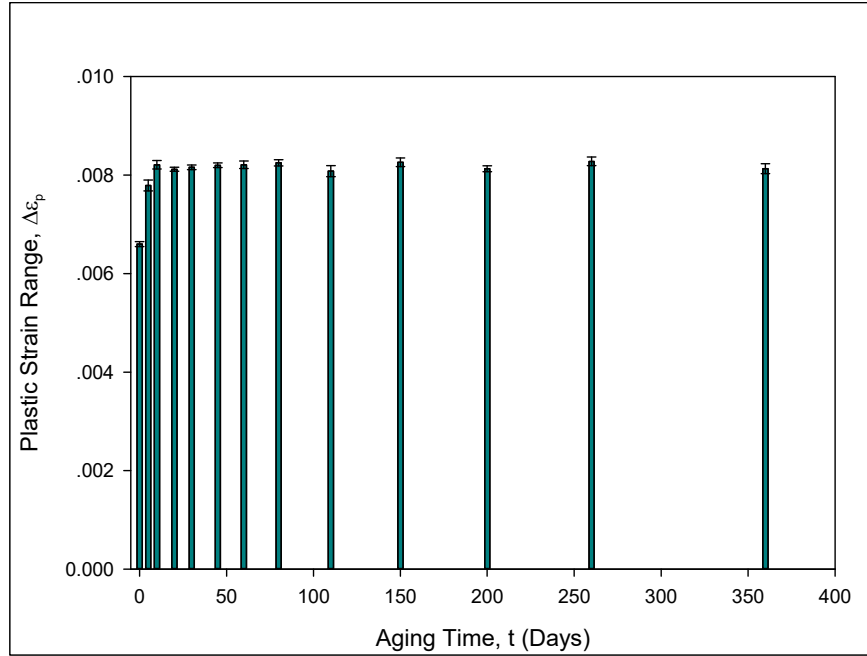


Figure 3.19 - Variation of Plastic Strain Range with Aging (WQ SAC405, Aging at 125 °C)

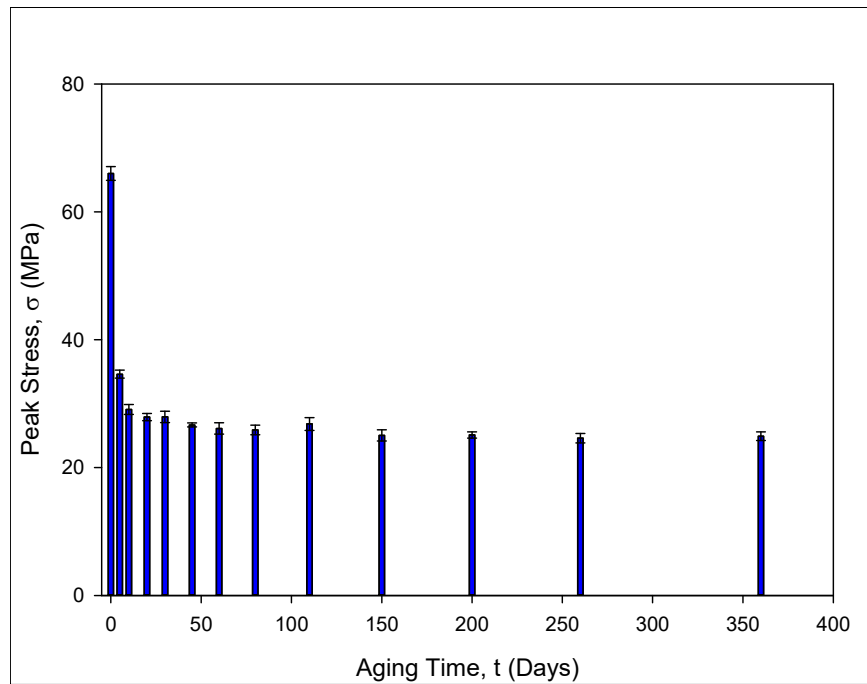


Figure 3.20 - Variation of Peak Stress with Aging (WQ SAC405, Aging at 125 °C)

Table 3.4 - Determination of Loop Areas, Plastic Strain Ranges, and Peak Stresses (RF SAC305, Aging at 25 °C)

Aging Time (Days)	Loop Area (MJ/m ³)	Plastic Strain Range, (10 ⁻³)	Peak Stress (MPa)
0	0.4579	7.58	37.20
5	0.4377	7.94	34.18
10	0.4138	8.25	31.18
20	0.3935	8.20	29.76
30	0.3994	8.37	30.09
45	0.3971	8.37	30.31
60	0.3732	8.34	28.25
80	0.3921	8.30	29.58
110	0.3876	8.35	29.31
150	0.4095	8.48	29.99
200	0.3809	8.55	28.45
260	0.4044	8.50	29.60
360	0.3836	8.50	28.23

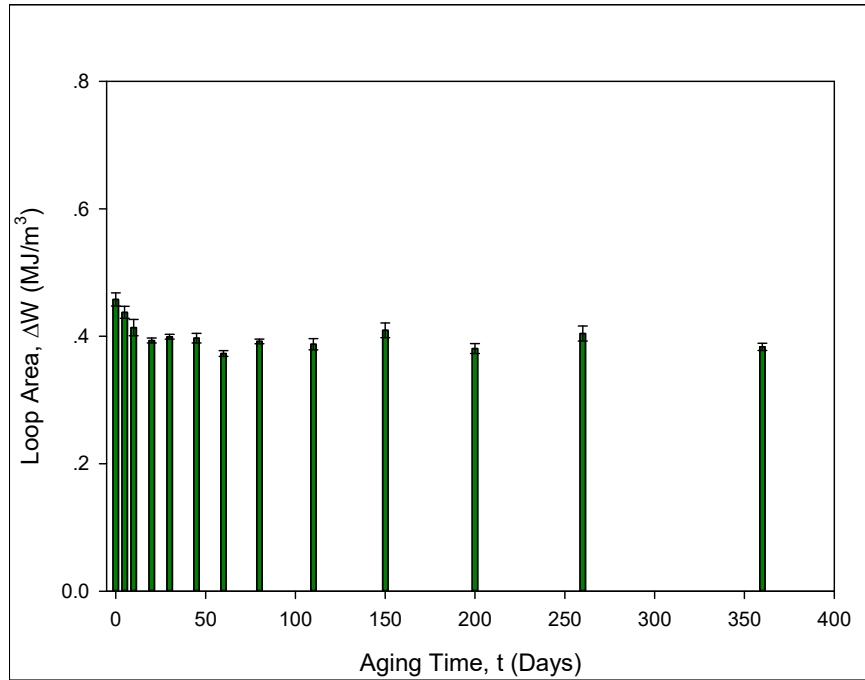


Figure 3.21 - Variation of Loop Area with Aging (RF SAC305, Aging at 25 °C)

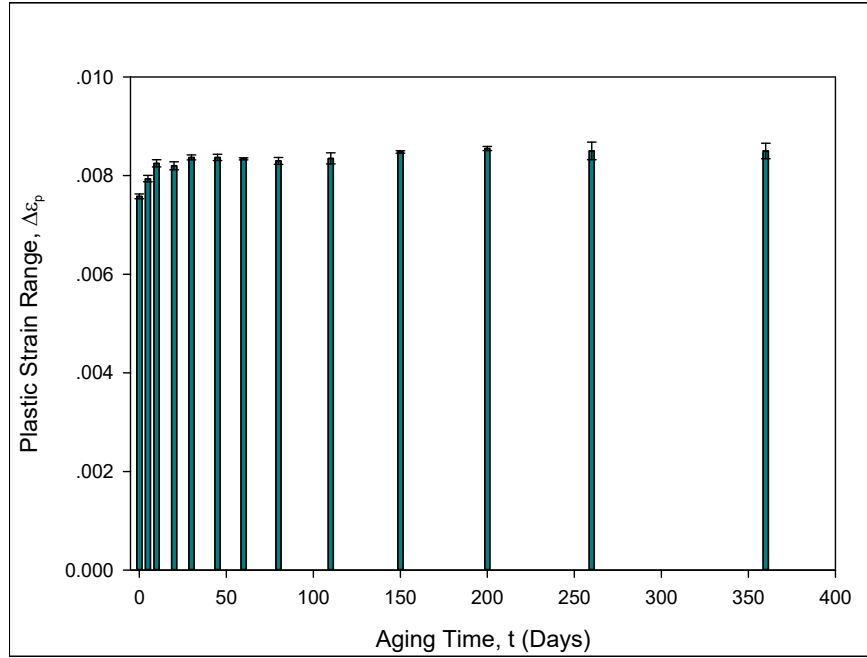


Figure 3.22 - Variation of Plastic Strain Range with Aging (RF SAC305, Aging at 25 °C)

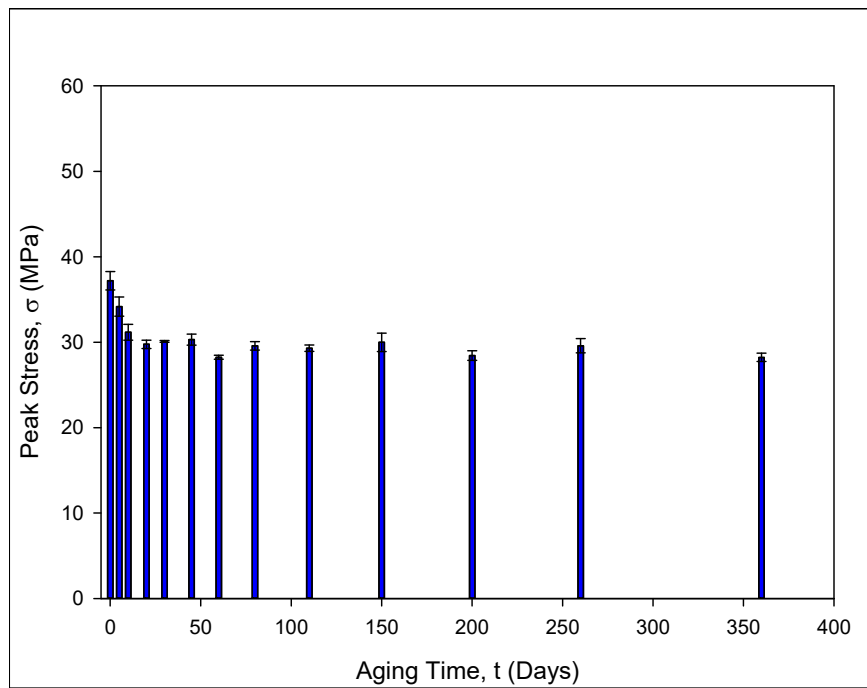


Figure 3.23 - Variation of Peak Stress with Aging (RF SAC305, Aging at 25 °C)

To make comparisons of aging effects on the studied alloys, the evolutions of hysteresis loop area with increased aging time have been modeled. The experimental data of loop area versus aging time can be fit well with a universal empirical model. This four-parameter model contains exponential and linear terms as shown in Eq. (3.1) [75],

$$A = \frac{k_1}{1 + k_2 e^{-k_3 t}} + k_4 t \quad (3.1)$$

where A is loop area, t denotes aging time in days, and k₁, k₂, k₃ and k₄ are material constants. Figure 3.24 shows the evolutions of loop area with aging for WQ SAC305, RF SAC305 and WQ SAC405 test specimens that were aged at 125 °C. Figure 3.25 shows the comparison of RF SAC305 test samples aged at 125 °C with those aged at 25 °C. The determined values of material constants are listed in Table 3.5 for all the studied alloys.

According to Figure 3.24, the evolutions caused by elevated temperature aging are similar for the three lead free solder alloys. Aging had a dramatic influence on the hysteresis loop area within the first few days, while the effects were much less for long term aging. The material constant k₄ in the model has a very small value for each alloy (see Table 3.5), which indicates the changes of loop area with aging were very small for long aging times. Without aging (0-day aging), the loop area of WQ SAC305 was much greater than that of RF SAC305 due to the much finer initial microstructure of WQ SAC305. As aging progressed, the difference became smaller and smaller, and eventually the loop areas of the two alloys became identical. This is because the water quenched and reflowed microstructures converged to similar states with increased aging. Figure 3.25 shows the comparison of elevated temperature and room temperature aging effects on the hysteresis loop area of RF SAC305. It is clear that elevated temperature aging led to more changes of the hysteresis loop, which is expected.

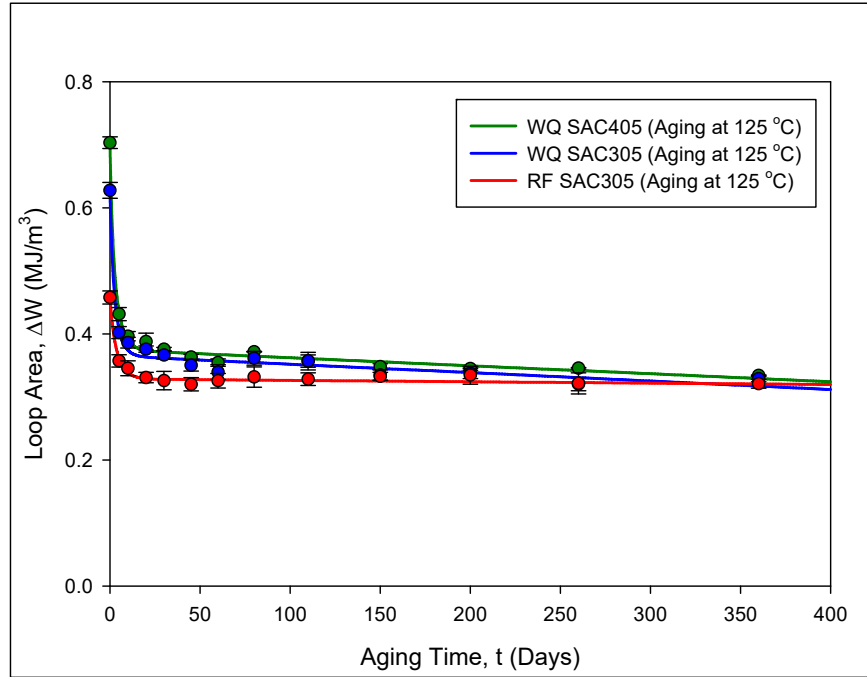


Figure 3.24 - Evolutions of Loop Area with Aging Time (WQ and RF SAC305, WQ SAC405, Aging at 125 °C)

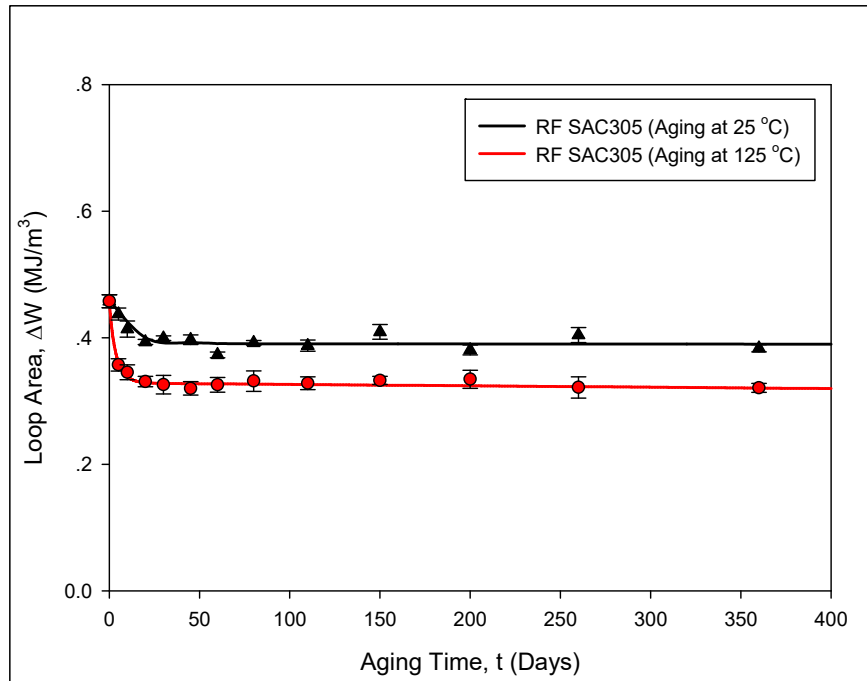


Figure 3.25 - Evolutions of Loop Area with Aging Time (RF SAC305, Aging at 125 °C and 25 °C)

Table 3.5 - Empirical Model Material Constants

Solder	k ₁	k ₂	k ₃	k ₄
WQ SAC305 (125 °C)	0.3655	-0.4175	0.2746	-1.3448×10 ⁻⁴
RF SAC305 (125 °C)	0.3284	-0.2821	0.2237	-0.2193×10 ⁻⁴
WQ SAC405 (125 °C)	0.3751	-0.4665	0.2402	-1.2775×10 ⁻⁴
RF SAC305 (25 °C)	0.3907	-0.1506	0.0913	-0.0150×10 ⁻⁴

3.5 Effects of Aging on Solder Microstructure

The mechanical behavior of a solder test specimen is closely tied to its microstructure. As discussed in Chapter 1.3, prior researchers usually observed the aging induced microstructural changes by comparing different solder joints. To remove the limitations, SEM has been used to explore microstructural changes that occurred in a fixed region due to elevated temperature aging in this study. Typically, β -Sn is surrounded by Ag_3Sn and Cu_6Sn_5 intermetallic compounds (IMCs) in SAC lead free solder microstructures. The dendrite structure can effectively pin and block the movement of dislocations. Figures 3.26 and 3.27 compare the microstructures of RF and WQ SAC305 at different magnifications, and the dendrite structure has been found in both of the two microstructures. However, the microstructure of WQ SAC305 is much finer than that of RF SAC305, because the cooling rate of WQ profile is much faster. Take Figure 3.27 for example, there is just one complete dendrite in the studied region of RF SAC305 sample, while there are approximately eight dendrites in the region of same size for WQ SAC305. Also, IMC particles are much finer in WQ microstructure. It explains why WQ specimens have better mechanical behavior than RF specimens do.

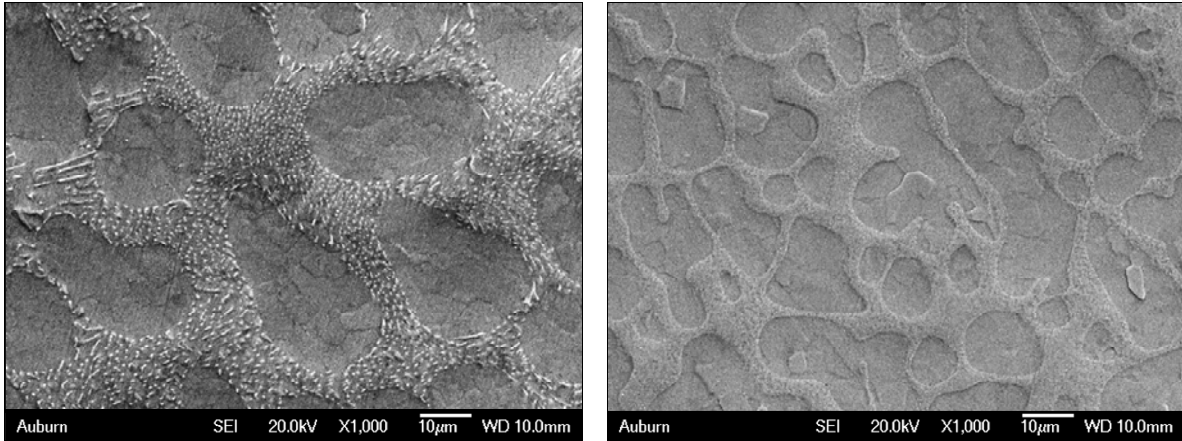


Figure 3.26 - Comparison of RF and WQ SAC305 Microstructures Without Aging (Left: RF SAC305; Right: WQ SAC305, 1000X)

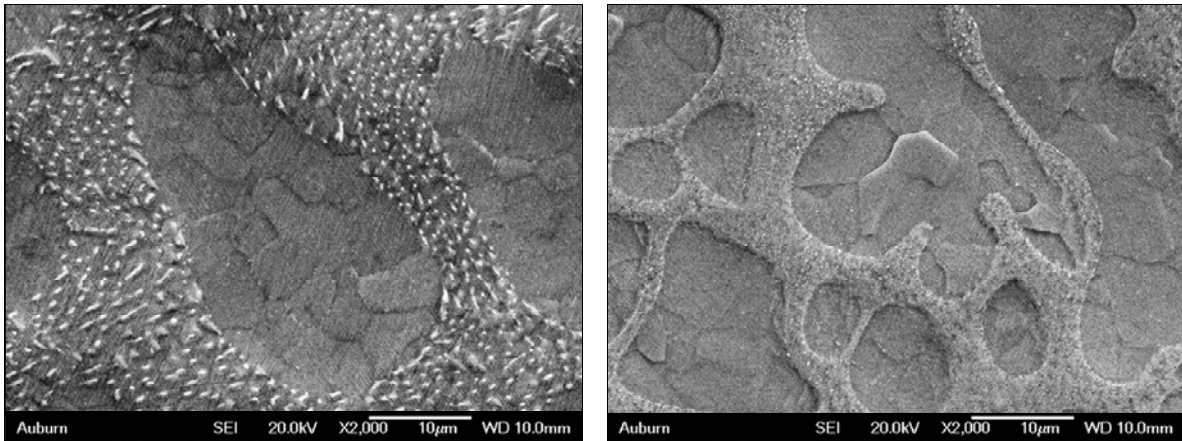


Figure 3.27 - Comparison of RF and WQ SAC305 Microstructures Without Aging (Left: RF SAC305; Right: WQ SAC305, 2000X)

Figure 3.28 shows aging induced microstructural changes of WQ SAC305 in an identical region. Similar to mechanical testing results, dramatic microstructural changes occurred within first 5 days, while the changes were much less significant after 5 days. With increased aging time, typical changes were the weakening of dendrite structure and the coarsening of IMC particles. For example, the coalescence and growth of IMC particles were obvious in locations 1, 2 and 3, while the migration of IMC particles into adjacent tin matrix was observed in location 4. Compared with WQ SAC305, effects of aging on the microstructure were less obvious for RF

SAC305 (Figure 3.29). It indicates that RF microstructure is more stable when subjected to aging, which can also be verified by the mechanical testing results (Figure 3.24). However, the coarsening of IMC particles can still be discerned, such as in locations 1 and 2.

Detailed study of microstructural changes due to aging is presented in Chapter 5. The microstructure of an identical region was continuously scanned for various aging durations using SEM. These micrographs were used to create the first experimentally recorded movies of the microstructural evolution in SAC solder joints exposed to aging. Therefore, aging phenomena such as the coarsening of IMC particles can be visualized.

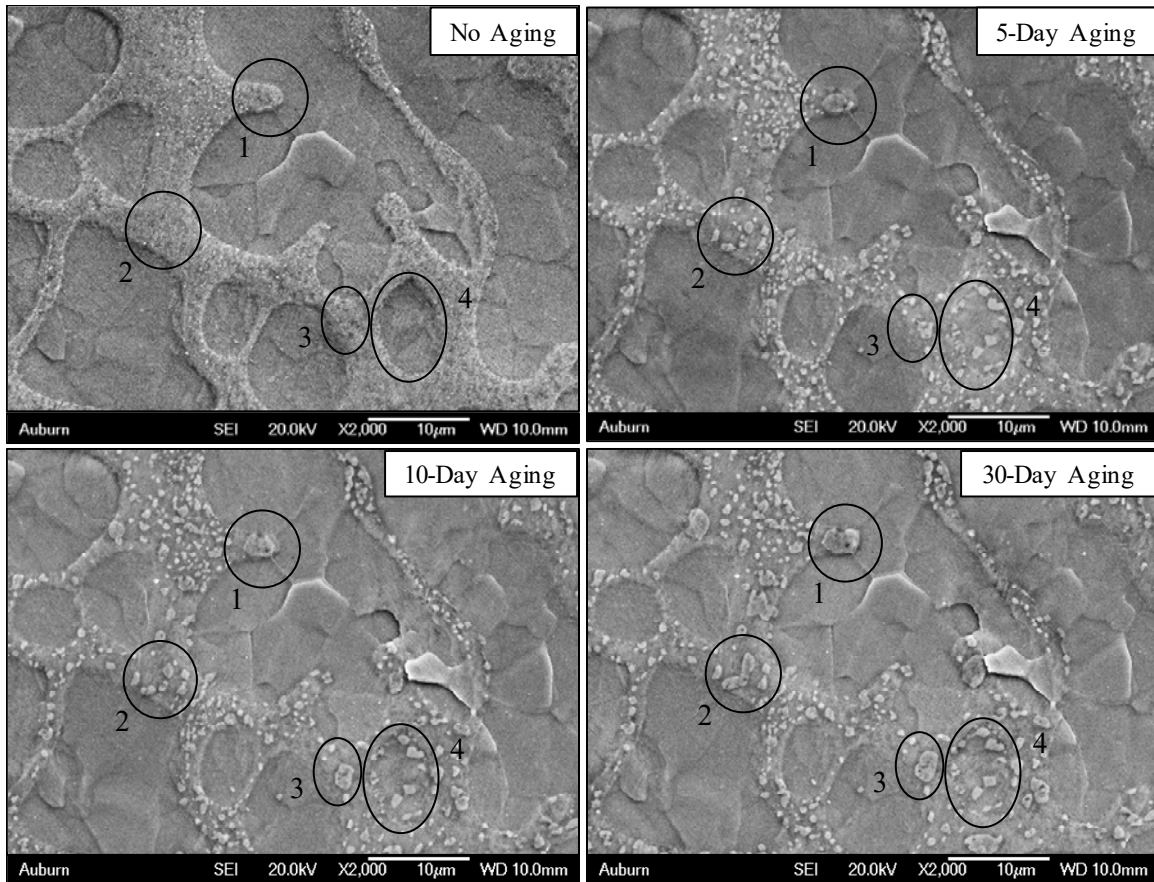


Figure 3.28 - Aging Induced Microstructural Evolution of WQ SAC305 (Aging at 125 °C)

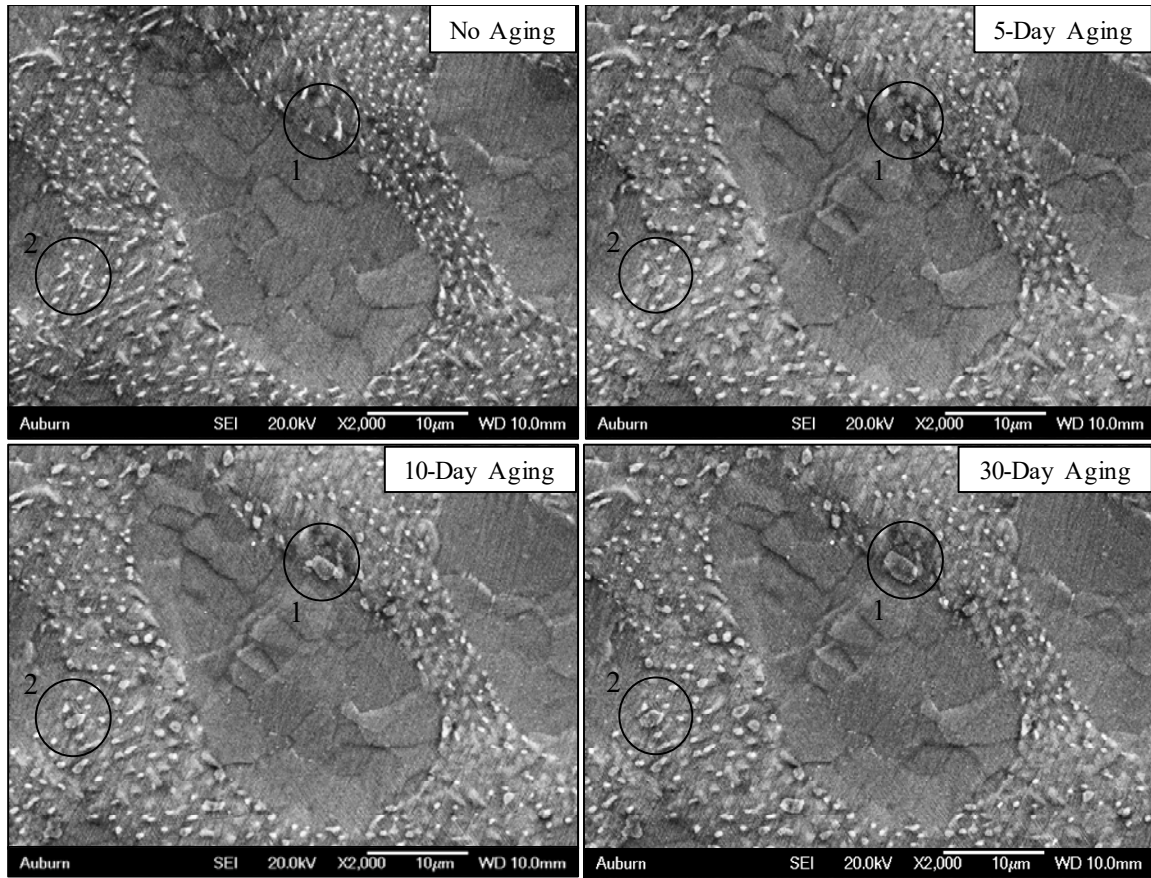


Figure 3.29 - Aging Induced Microstructural Evolution of RF SAC305 (Aging at 125 °C)

3.6 Summary and Discussion

In this chapter, effects of aging on the cyclic stress-strain behavior of lead free solders have been investigated, and several influential factors have been examined, such as aging duration, silver content, solidification profile and aging temperature. The evolution of hysteresis loop with aging has been characterized for the studied lead free solders. It has been found that the size and shape of the hysteresis loop changed dramatically during the first few days of aging, with slower changes occurring for longer aging times. Generally, hysteresis loops compressed in the vertical direction while expanded in the horizontal direction with increased aging.

In addition, aging induced evolution of the cyclic stress-strain behavior (hysteresis loop area, plastic strain range and peak stress) has been quantified. It has been observed that

increased aging led to the drop of loop area and peak stress and the increase of plastic strain range, which indicates the increased ability of dislocation movement. Also, dramatic changes of all the three parameters occurred within the first few days of aging. The evolutions of hysteresis loop area with aging have been modeled, and comparison of the studied solder microstructures has been done. It has been found that RF microstructure was more stable than WQ microstructure when exposed to aging, and elevated temperature aging led to more degradation of the cyclic stress-strain behavior than room temperature aging did.

Finally, effects of aging on solder microstructure have been studied in a fixed region of a single solder sample using SEM. The WQ microstructure is much finer than the RF microstructure at no aging condition due to the faster cooling rate. Typically, aging led to the weakening of dendrite structure and the coarsening of IMC particles, especially during the first few days of aging.

CHAPTER 4

CYCLIC STRESS-STRAIN BEHAVIOR: EFFECTS OF AGING, TEMPERATURE, STRAIN RATE, AND PLASTIC STRAIN RANGE

4.1 Introduction

Effects of aging on the cyclic stress-strain behavior of several lead free solder alloys have been characterized and quantified in previous chapter. Apart from aging, various testing parameters such as testing temperature and strain rate (frequency) also have a significant influence on the cyclic stress-strain and fatigue behaviors of solders, and several models have been developed to describe the effects of these testing parameters. In prior studies, the influence of aging (initial microstructure) of the test samples was not examined. We believe that a better understanding of the effects of aging and test conditions on the cyclic mechanical behavior of solder materials is critical to resolving the large discrepancies in solder fatigue data found in the literature.

In this investigation, we have examined the effects of prior aging conditions and several testing parameters on the cyclic stress-strain behavior of WQ SAC305 lead free solder. Prior to testing, the samples were aged for various durations (0, 5, 10 and 20 days) at 125 °C. After aging, the fabricated samples were then subjected to cyclic stress-strain loading under several different conditions. The examined range of cyclic loading test parameters included testing temperature (25 to 100 °C), testing strain rate (0.0001 to 0.001 sec⁻¹), and total strain range (0.004 to 0.013). The nominal diameter of the uniaxial specimens in this work was 1.2 mm, and

the gage length was chosen as 10 mm. In addition, at least 5 tests were conducted for each aging and test condition. Finally, the effects of aging have been quantified for the first time for different testing temperatures, strain rates, and plastic strain ranges.

4.2 Effects of Test Temperature

The effects of the test temperature on cyclic stress-strain behavior have been studied by performing a series of experiments with the same total strain range of 0.01 (strain limits of ± 0.005) and same strain rate (frequency) of 0.001 sec^{-1} . The test temperatures considered were $T = 25 \text{ }^\circ\text{C}$, $50 \text{ }^\circ\text{C}$, $75 \text{ }^\circ\text{C}$, and $100 \text{ }^\circ\text{C}$. Initially, the effects of temperature were investigated for non-aged samples. Figure 4.1 illustrates the recorded cyclic stress-strain curves under each test temperature. The cyclic stress-strain behavior has also been quantified, and the determined values of the three parameters are listed in Table 4.1. It is observed that the loop compressed in the vertical direction while expanded horizontally. To be more specific, peak stress and loop area dropped while plastic strain range increased during the cyclic loading at elevated testing temperatures.

Figures 4.2, 4.3 and 4.4 show quantitative comparisons of the loop areas, plastic strain ranges and peak stresses, respectively, for different test temperatures. Due to the increase of creep and dislocation movement at higher temperatures, the peak stress and loop area dropped while plastic strain range increased. In general, significant creep is expected with a homologous temperature (the ratio of ambient temperature to melting temperature) larger than 0.5. For Sn-Ag-Cu lead free solders, creep is not negligible even at room temperature ($T = 25 \text{ }^\circ\text{C}$), at which the homologous temperature is 0.61 [16]. At elevated temperatures, creep is more severe because thermally activated dislocations can move along preferred slip planes or cut through dislocation barriers [142, 143]. In addition, the interstitial atoms and lattice vacancies tend to

migrate along the gradient of a grain boundary in the presence of tensile or compressive pressure in reversed directions [144].

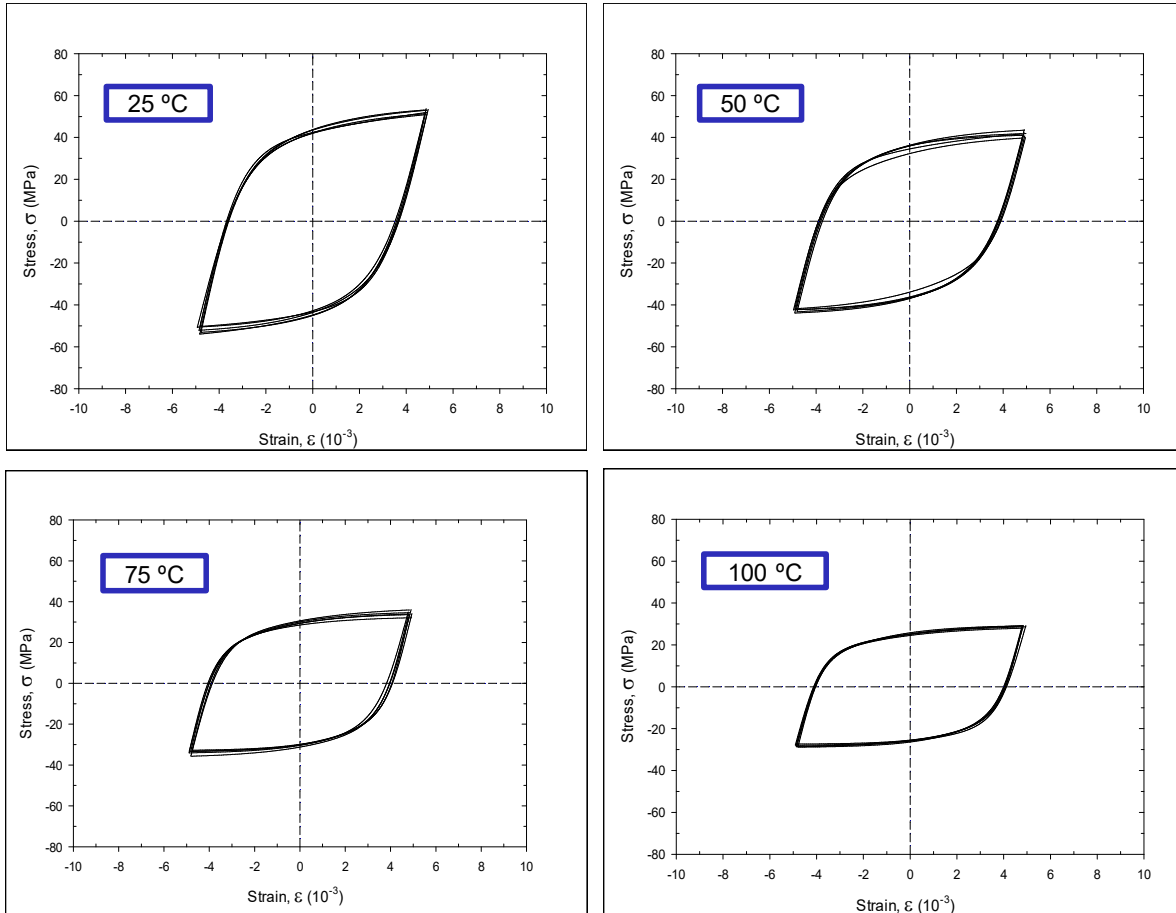


Figure 4.1 - Effects of Test Temperature on Cyclic Stress-Strain Curves (No Aging)

Table 4.1 - Effects of Test Temperature on Cyclic Stress-Strain Behavior (No Aging)

Test Temp. (°C)	Loop Area (MJ/m ³)	Plastic Strain Range, (10 ⁻³)	Peak Stress (MPa)
25	0.6278	7.24	52.36
50	0.5367	7.68	41.60
75	0.4612	7.94	34.34
100	0.3998	8.17	28.90

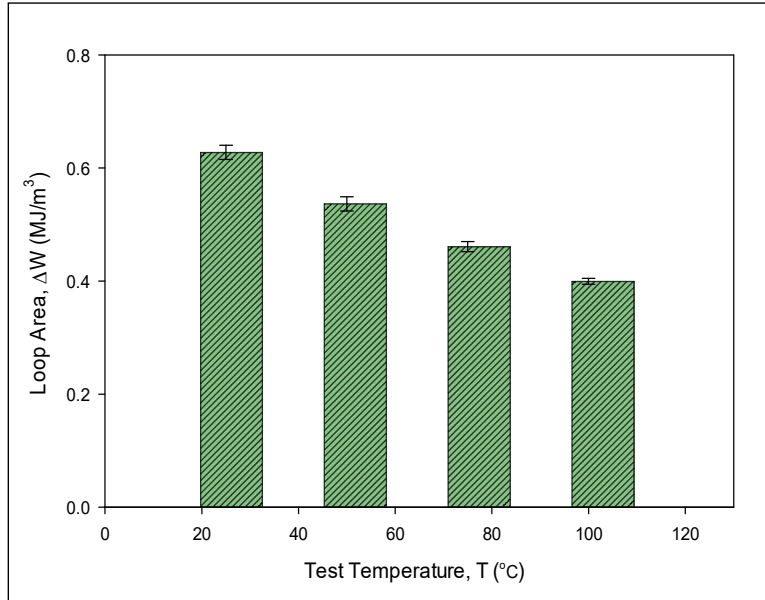


Figure 4.2 - Drop of Loop Area with Increased Test Temperature (No Aging)

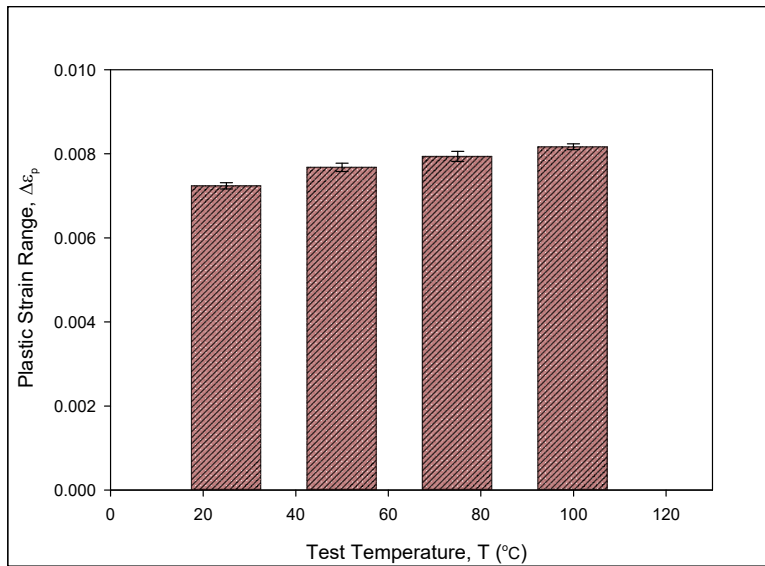


Figure 4.3 - Increase of Plastic Strain Range with Increased Test Temperature (No Aging)

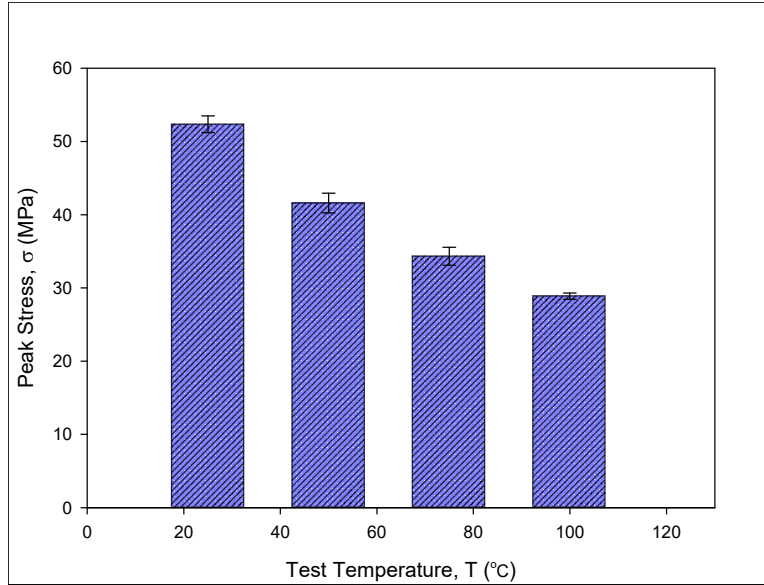


Figure 4.4 - Drop of Peak Stress with Increased Test Temperature (No Aging)

Similar trends for elevated test temperatures have been observed for samples subjected to aging before testing. In addition to the non-aged specimens, tests were also performed on samples aged for 5, 10, and 20 days at $T = 125\text{ }^{\circ}\text{C}$ prior to testing. In these experiments, the same total strain range of 0.01 (strain limits of ± 0.005) and same strain rate (frequency) of 0.001 sec^{-1} were also used. Plots of the loop area, plastic strain range and peak stress as a function of aging time for the various test temperatures are shown in Figures 4.5, 4.6 and 4.7, respectively. The experimental data points in each curve can be fit well with a universal empirical model that includes exponential and linear terms:

$$Q = \frac{k_1}{1 + k_2 e^{-k_3 t}} + k_4 t \quad (4.1)$$

where Q denotes the quantity being plotted (i.e. hysteresis loop area, peak stress, or plastic strain range), t is the aging duration in days, and k_1 , k_2 , k_3 and k_4 are temperature dependent material constants. From Figures 4.5, 4.6 and 4.7, the variations with aging are similar from one test temperature to another. It is also observed that the plastic strain range is less sensitive to aging

in the first few days of aging, relative to the loop area and peak stress. The total strain range applied in these experiments was 0.01. Thus, it is evident that plastic deformation was dominant during these tests as the plastic strain range accounts for around 80% of the total strain range for each condition (see Figure 4.6).

Table 4.2 lists the values of loop area, plastic strain range and peak stress for each aging and test temperature condition. It is clear that aging degrades the mechanical properties of SAC305 solder, and testing at elevated test temperatures exacerbates the degradations. The degradations caused by aging and test temperature can be quantified by comparing results for non-aged samples tested at 25 °C with results for aged samples (20 days of aging) tested at 100 °C. The degradations in loop area, plastic strain range, and peak stress are 58.3%, and 19.7%, 66.0%, respectively.

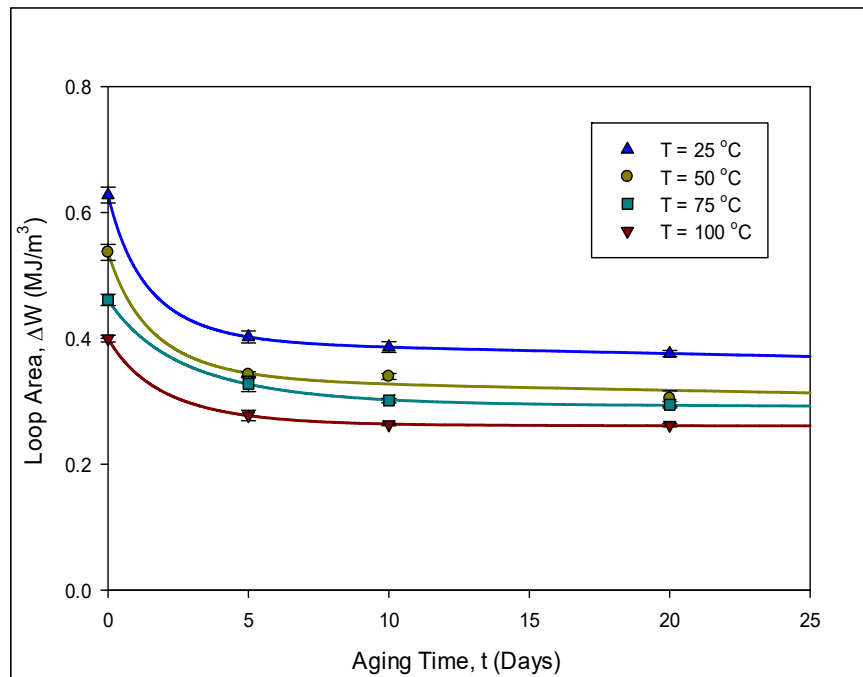


Figure 4.5 - Effects of Aging and Temperature on Loop Area

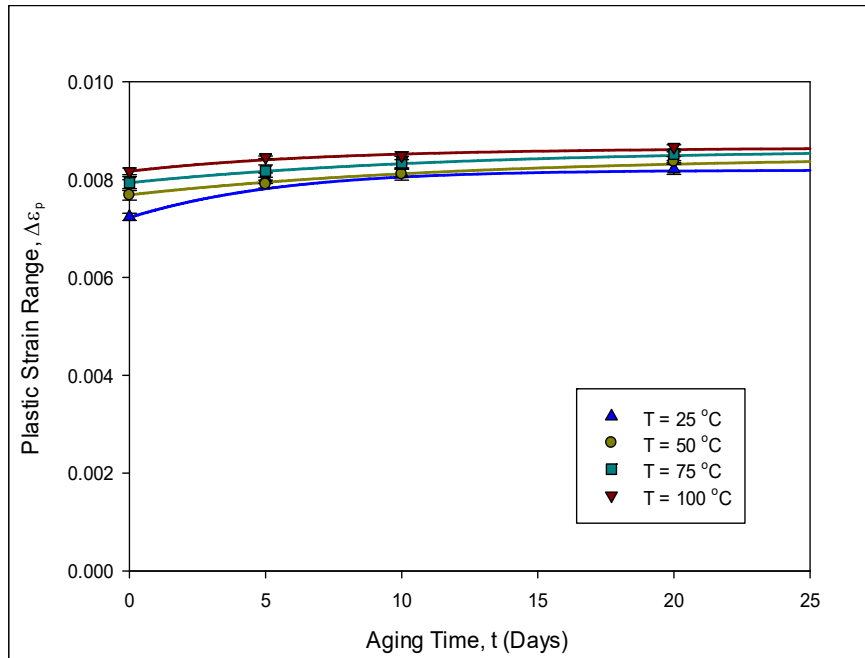


Figure 4.6 - Effects of Aging and Temperature on Plastic Strain Range

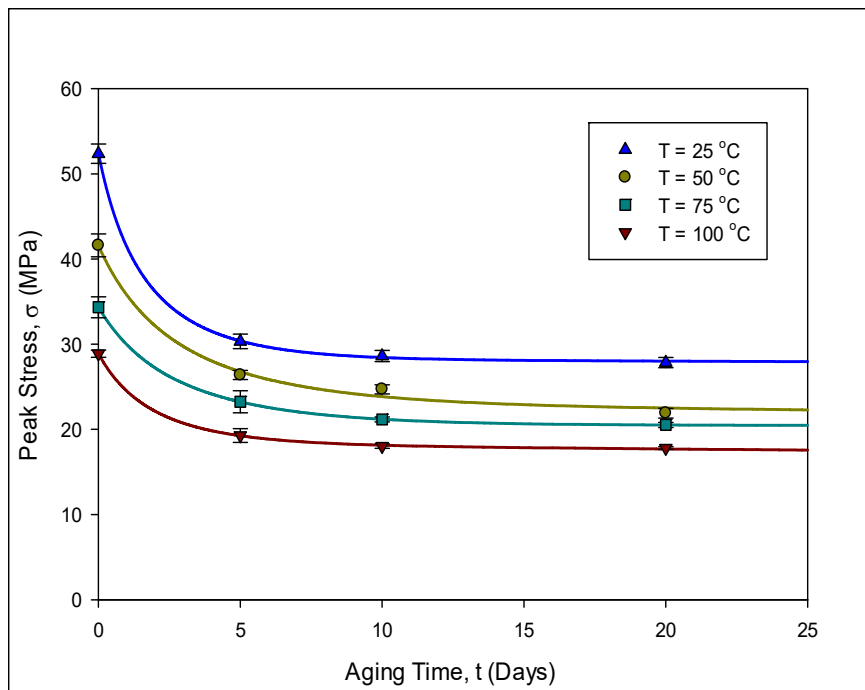


Figure 4.7 - Effects of Aging and Temperature on Peak Stress

Table 4.2 - Effects of Aging and Temperature on Cyclic Stress-Strain Behavior

Aging Time (Days)	Test Temp. (°C)	Loop Area (MJ/m ³)	Plastic Strain Range, (10 ⁻³)	Peak Stress (MPa)
0	25	0.6278	7.24	52.36
	50	0.5367	7.68	41.60
	75	0.4612	7.94	34.34
	100	0.3998	8.17	28.90
5	25	0.4023	8.03	30.34
	50	0.3422	7.91	26.40
	75	0.3276	8.18	23.23
	100	0.2774	8.46	19.28
10	25	0.3862	8.14	28.62
	50	0.3394	8.12	24.70
	75	0.3010	8.35	21.16
	100	0.2629	8.49	18.03
20	25	0.3760	8.21	27.85
	50	0.3043	8.37	21.89
	75	0.2944	8.52	20.53
	100	0.2620	8.67	17.80

4.3 Effects of Strain Rate

The effects of the strain rate (frequency) on the cyclic stress-strain behavior have been studied by performing a series of experiments on non-aged and aged samples with the same total strain range of 0.01 (strain limits of ± 0.005) and temperature $T = 25$ °C. The strain rates considered were 0.0001, 0.0002, 0.0005 and 0.0010 sec⁻¹. Figure 4.8 shows the hysteresis loops of non-aged specimens tested at each strain rate. At no aging condition, the effects of strain rate on cyclic stress-strain behavior have also been quantified (see Figures 4.9, 4.10 and 4.11). In addition, the effects of aging on loop area, plastic strain range and peak stress have been quantified for different strain rates, as shown in Figure 4.12, Figure 4.13 and Figure 4.14, respectively. From these figures, the effects of strain rate on the loop area, peak stress, and plastic strain range are opposite to the effects of test temperature. Specifically, the loop area and

peak stress increased at higher strain rates for all aging times. Similarly, the plastic strain range dropped at higher strain rates for all aging times. In other words, the hysteresis loops stretched vertically and shrunk horizontally with increasing strain rate (frequency). This is because creep and dislocation movement are curtailed when testing samples at a higher strain rates. Table 4.3 lists the values of the three parameters for each aging and strain rate condition. Comparison has been made on the cyclic stress-strain behavior of non-aged specimens tested at 0.001 sec^{-1} and that of aged specimens (20-day aging) tested at 0.0001 sec^{-1} . The degradations in loop area, plastic strain range, and peak stress are 54.6%, and 18.8%, 58.2%, respectively. Therefore, aging leads to the degradations of the cyclic stress-strain behavior, and testing at lower strain rate exacerbates the degradations.

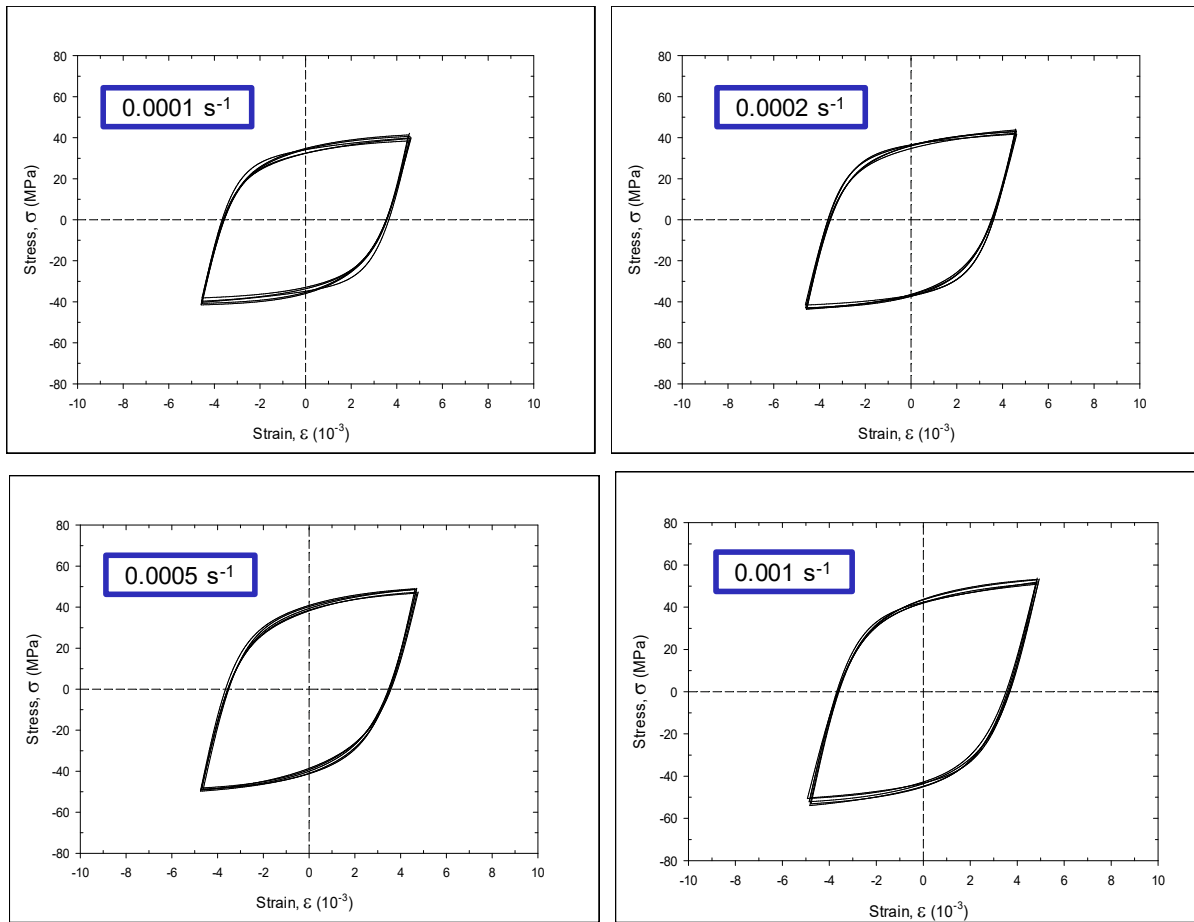


Figure 4.8 - Effects of Strain Rate on Cyclic Stress-Strain Curves (No Aging)

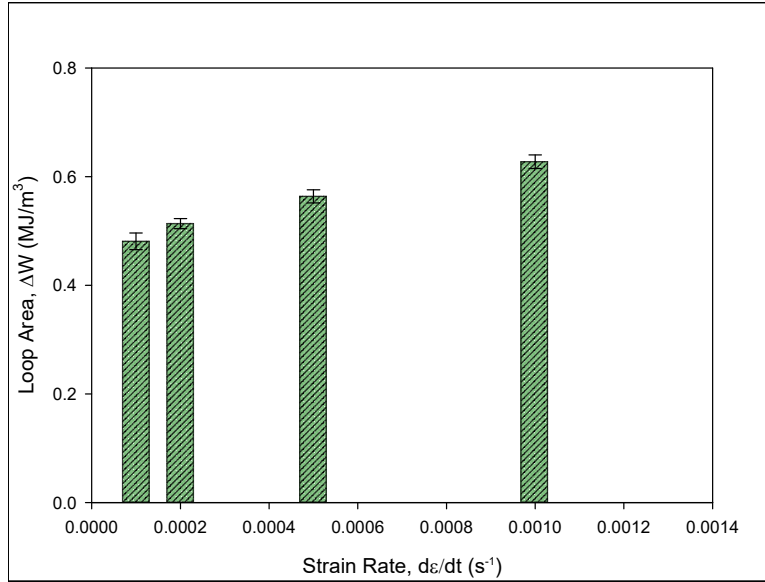


Figure 4.9 - Increase of Loop Area with Increased Strain Rate (No Aging)

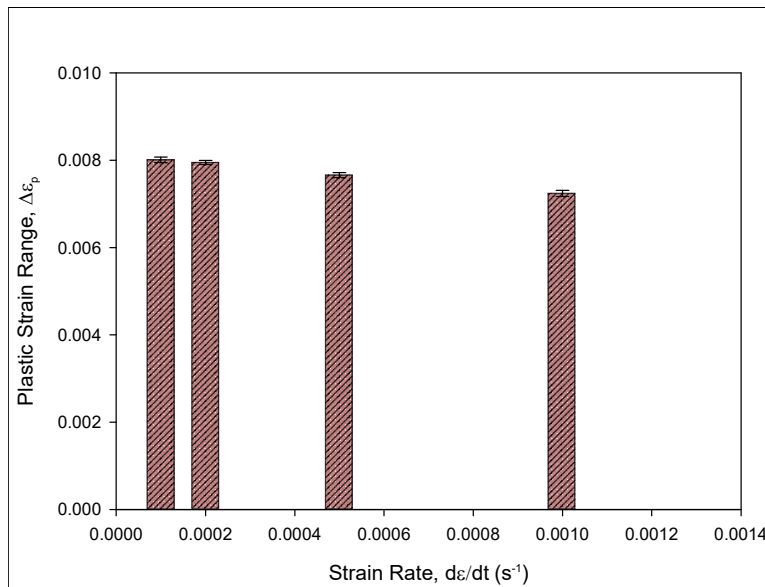


Figure 4.10 - Drop of Plastic Strain Range with Increased Strain Rate (No Aging)

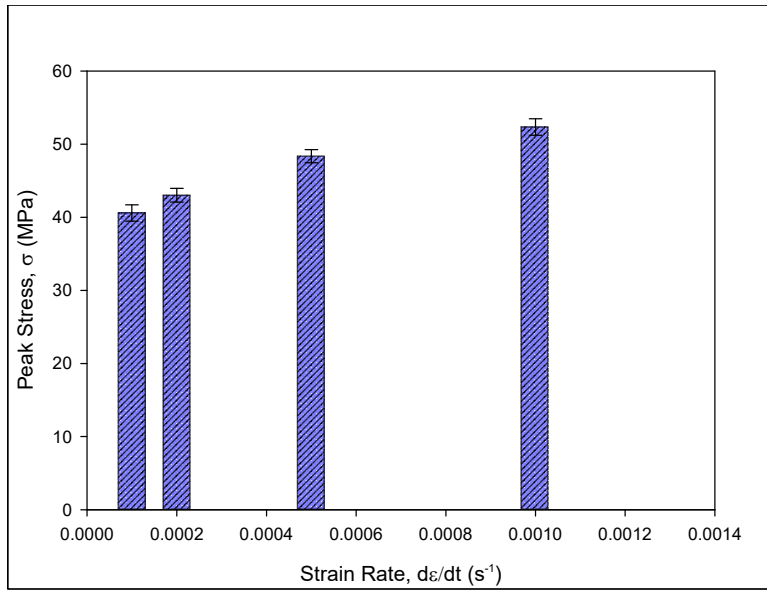


Figure 4.11 - Increase of Peak Stress with Increased Strain Rate (No Aging)

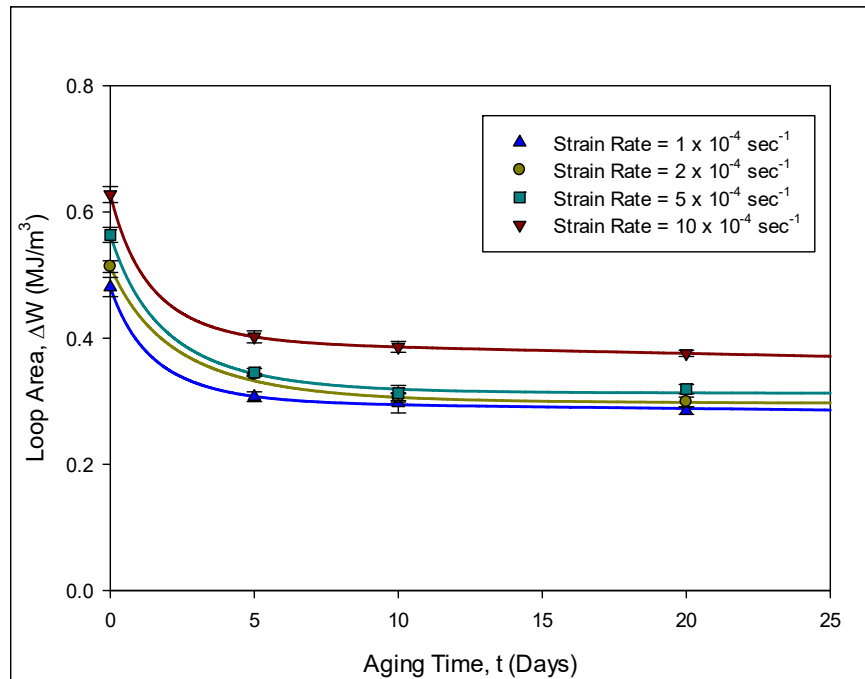


Figure 4.12 - Effects of Aging and Strain Rate on Loop Area

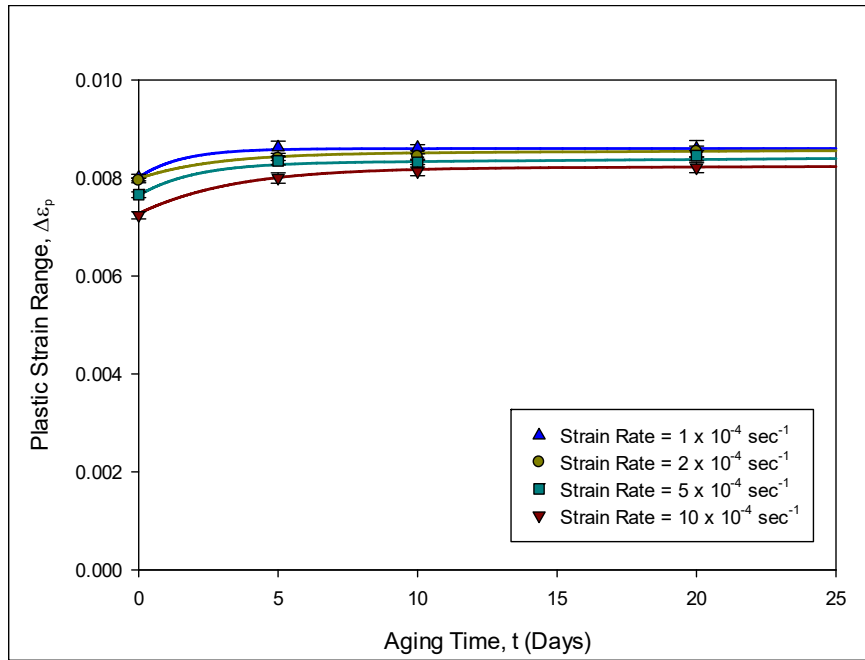


Figure 4.13 - Effects of Aging and Strain Rate on Plastic Strain Range

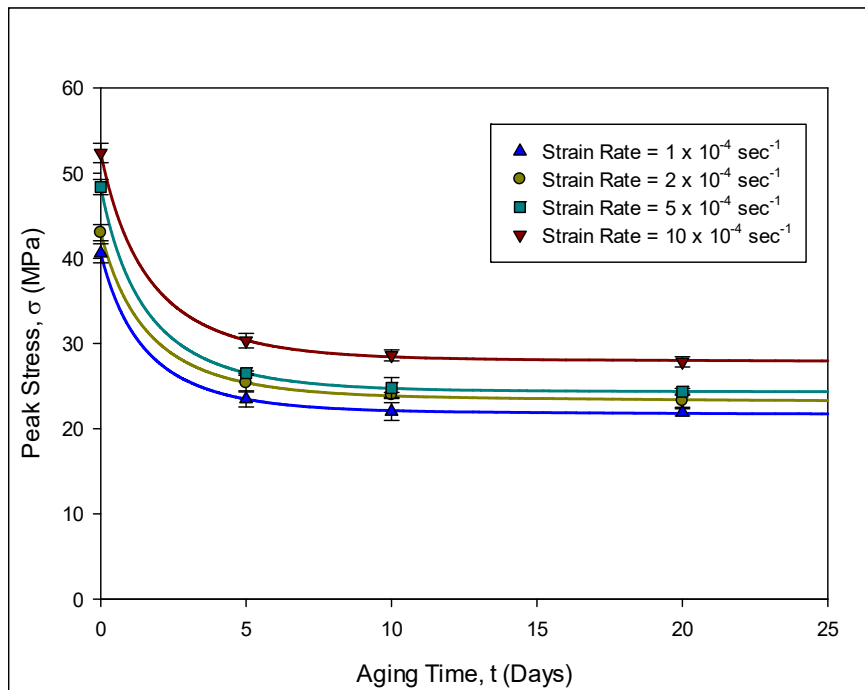


Figure 4.14 - Effects of Aging and Strain Rate on Peak Stress

Table 4.3 - Effects of Aging and Strain Rate on Cyclic Stress-Strain Behavior

Aging Time (Days)	Strain Rate (sec ⁻¹)	Loop Area (MJ/m ³)	Plastic Strain Range, (10 ⁻³)	Peak Stress (MPa)
0	0.0001	0.4811	8.01	40.60
	0.0002	0.5137	7.95	43.02
	0.0005	0.5638	7.66	48.37
	0.0010	0.6278	7.24	52.36
5	0.0001	0.3071	8.63	23.48
	0.0002	0.3425	8.40	25.37
	0.0005	0.3457	8.35	26.53
	0.0010	0.4023	8.03	30.34
10	0.0001	0.2974	8.62	22.01
	0.0002	0.3053	8.44	23.96
	0.0005	0.3129	8.32	24.77
	0.0010	0.3862	8.14	28.62
20	0.0001	0.2851	8.60	21.91
	0.0002	0.2988	8.54	23.28
	0.0005	0.3191	8.46	24.33
	0.0010	0.3760	8.21	27.85

4.4 Effects of Plastic Strain Range

Experiments have also been done to investigate the effects of plastic strain range including aging on the cyclic stress-strain behavior of WQ SAC305. A series of tests were performed on non-aged and aged samples with the same strain rate of 0.001 sec⁻¹ and temperature T = 25 °C. Four different total strain ranges were applied including 0.004, 0.007, 0.010 and 0.013 (the total strain range was specified instead of the plastic strain range during the cyclic loadings because of the difficulty of maintaining a fixed plastic strain range for different tests). Figure 4.15 illustrates the cyclic stress-strain response of non-aged samples for each strain range condition. Figures 4.16, 4.17 and 4.18 show the effects of total strain range on loop area, plastic strain range and peak stress, respectively (no aging).

The results for the loop area, plastic strain range, and peak stress as a function of aging time and total strain range are shown in Figures 4.19-4.21. In general, an increase in the total strain range led to a larger plastic strain range, which represents more plastic deformation occurring per cycle (Figure 4.20). Additionally, a greater applied total (or plastic) strain range tended to increase the loop area and peak stress (Figures 4.19, 4.21), as expected.

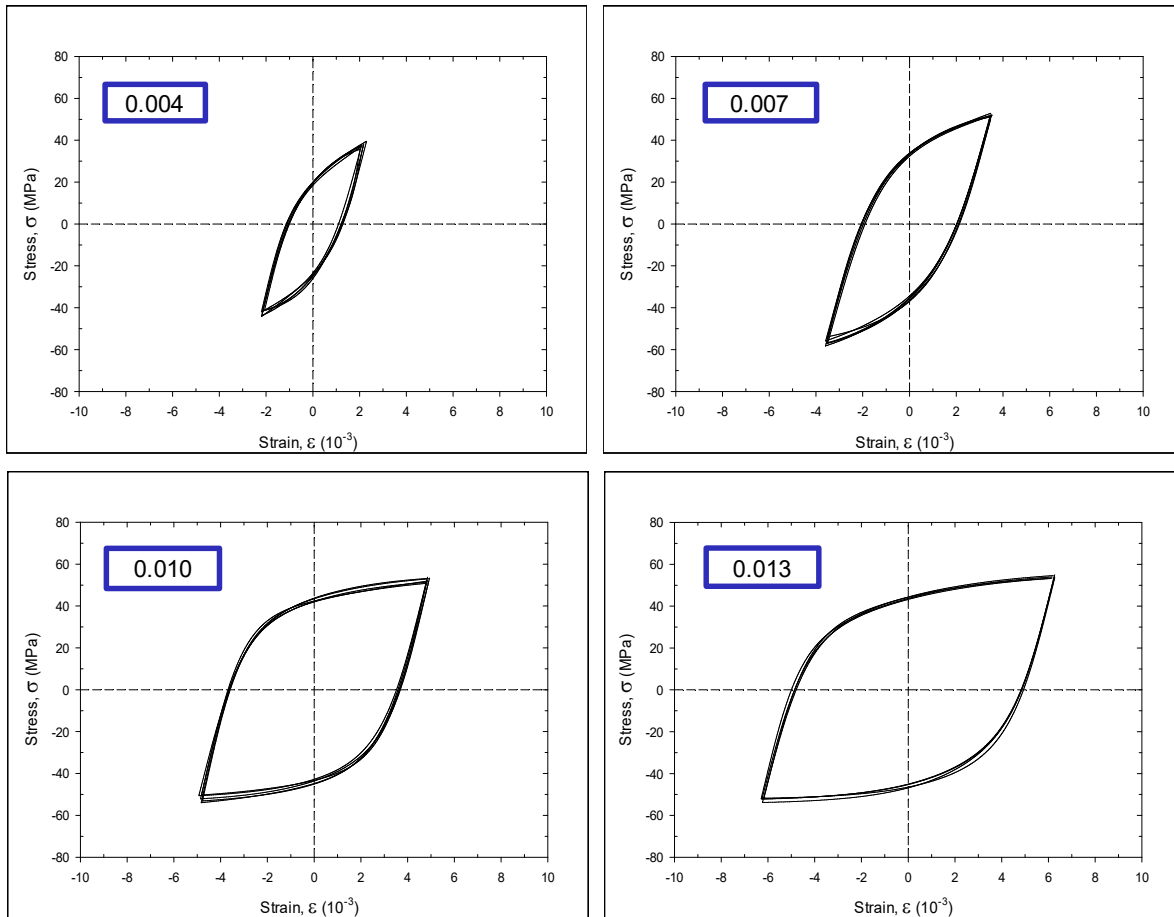


Figure 4.15 - Effects of Strain Range on Cyclic Stress-Strain Curves (No Aging)

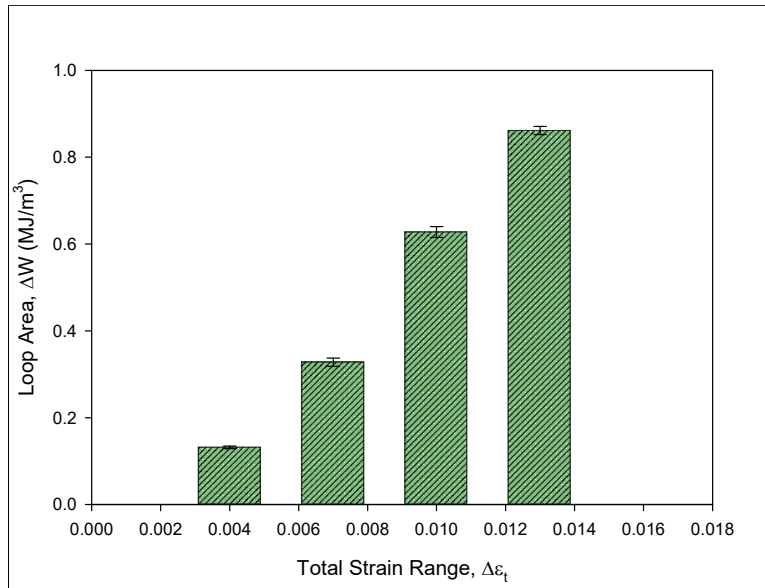


Figure 4.16 - Increase of Loop Area with Increased Strain Range (No Aging)

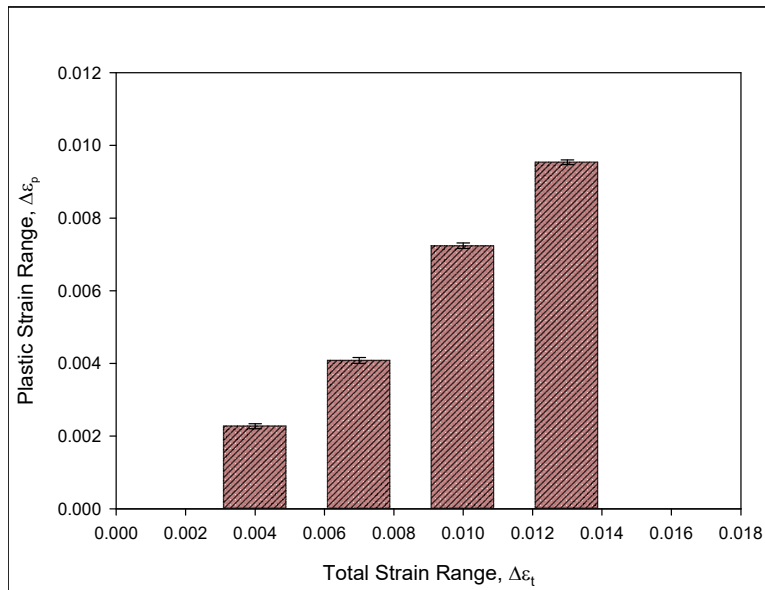


Figure 4.17 - Increase of Plastic Strain Range with Increased Strain Range (No Aging)

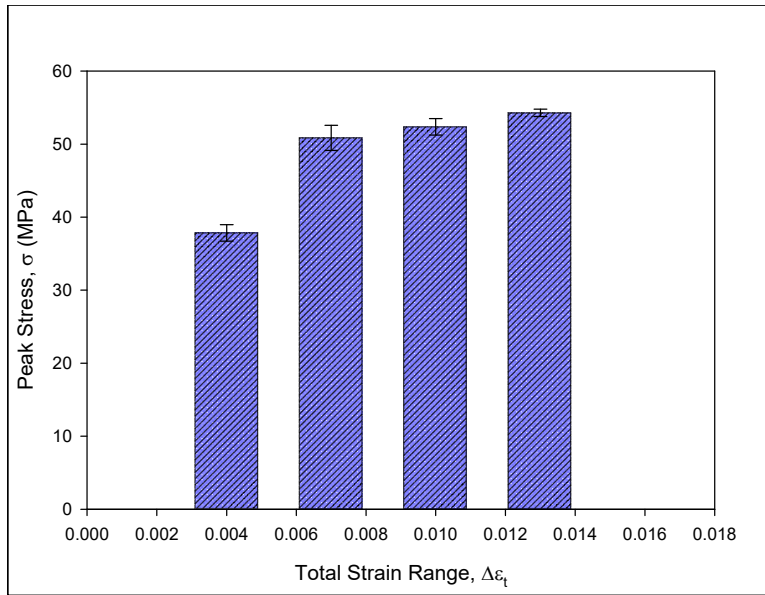


Figure 4.18 - Increase of Peak Stress with Increased Strain Range (No Aging)

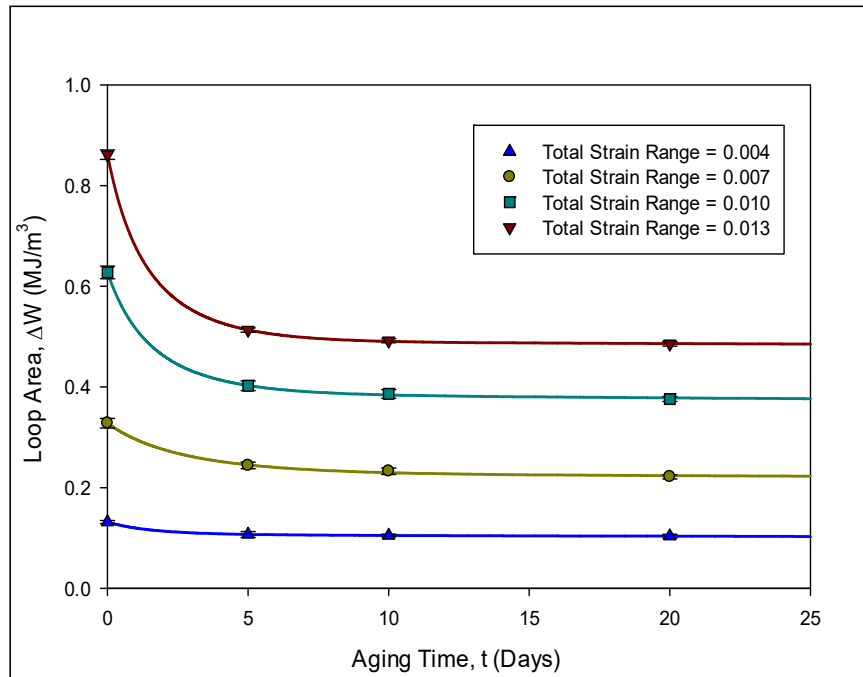


Figure 4.19 - Effects of Aging and Strain Range on Loop Area

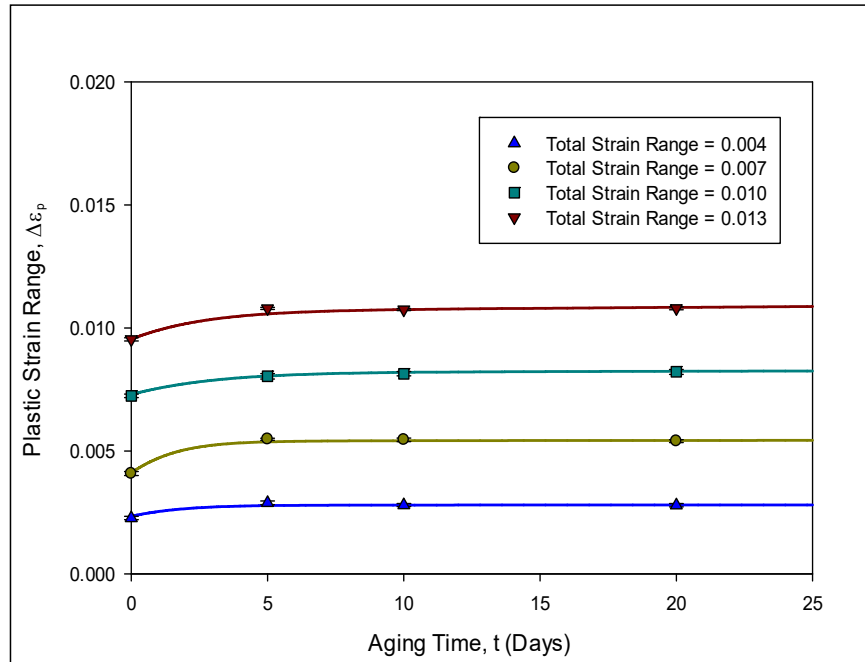


Figure 4.20 - Effects of Aging and Strain Range on Plastic Strain Range

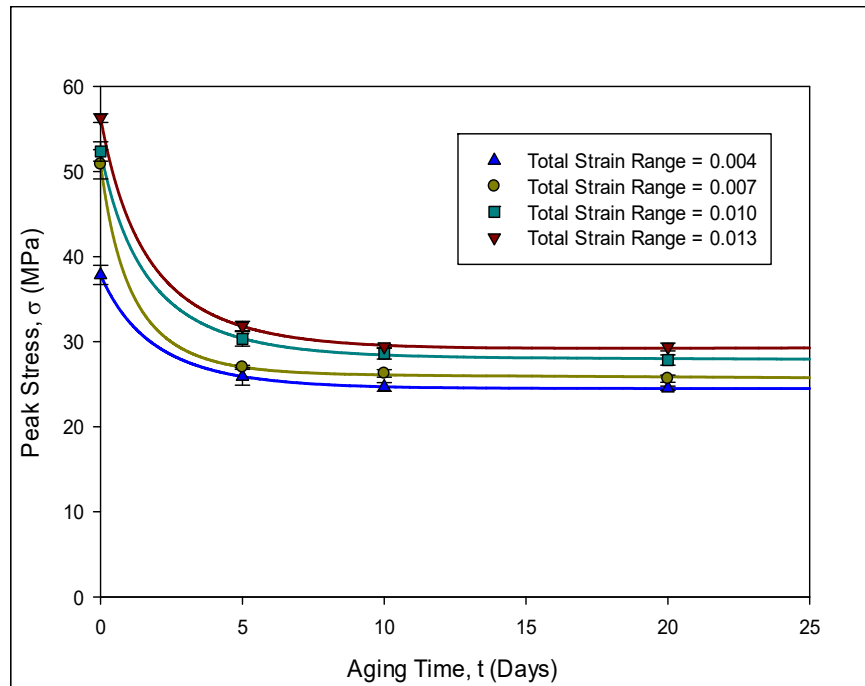


Figure 4.21 - Effects of Aging and Strain Range on Peak Stress

Table 4.4 - Effects of Aging and Strain Range on Cyclic Stress-Strain Behavior

Aging Time (Days)	Total Strain Range, (10^{-3})	Loop Area (MJ/m^3)	Plastic Strain Range, (10^{-3})	Peak Stress (MPa)
0	4	0.1315	2.27	37.85
	7	0.3278	4.08	50.86
	10	0.6278	7.24	52.36
	13	0.8617	9.54	56.28
5	4	0.1069	2.89	25.92
	7	0.2439	5.48	27.00
	10	0.4023	8.03	30.34
	13	0.5133	10.8	31.86
10	4	0.1049	2.80	24.68
	7	0.2324	5.45	26.28
	10	0.3862	8.14	28.62
	13	0.4918	10.8	29.44
20	4	0.1034	2.79	24.52
	7	0.2215	5.40	25.65
	10	0.3760	8.21	27.85
	13	0.4858	10.8	29.38

4.5 Summary and Discussion

In this investigation, we have examined the effects of prior aging conditions and several testing parameters on the cyclic stress-strain behavior of WQ SAC305 lead free solder. Prior to testing, specimens aged at 125 °C for various durations (0, 5, 10, and 20 days) have been prepared for this purpose. The examined range of cyclic loading test parameters included testing temperature (25 to 100 °C), testing strain rate (0.0001 to 0.001 sec^{-1}), and total strain range (0.004 to 0.013). The effects of test temperature, strain rate, and strain range were investigated by subjecting non-aged and aged samples to cyclic loadings under different conditions. At elevated test temperatures or lower test strain rates, an increase in the plastic strain range and a drop of the peak stress and loop area were found for all aging times, which indicates more creep and dislocation movement occurred during the cycling. Moreover, the plastic strain range, loop

area, and peak load increased as expected with greater applied total strain range. Finally, the effects of aging have been quantified for the first time for different testing temperatures, strain rates, and plastic strain ranges.

CHAPTER 5

INVESTIGATION OF AGING INDUCED EVOLUTION OF THE MICROSTRUCTURE OF SAC305 LEAD FREE SOLDER

5.1 Introduction

Due to their low melting temperatures, lead free solders are exposed to high homologous temperatures in most product applications. Thus, there is a continuous state of active diffusion processes in the solder alloys, and their microstructures are inherently unstable and will continually evolve during normal operating temperature conditions of electronic packaging assemblies. Typical microstructure evolution in lead free solders includes coarsening of intermetallic phases and subgrains, breakdown of dendrite structures, as well as potential recrystallization of Sn grains. Such changes in solder microstructure are accompanied by dramatic changes in mechanical response and failure behavior, and these multifaceted evolutions occurring in the material are typically referred to as solder aging phenomena.

In this chapter, Scanning Electron Microscopy (SEM) has been utilized to examine the aging induced microstructural changes occurring within lead free solders. Unlike many prior studies, fixed regions in the solder joint cross-sections were monitored throughout the aging process, rather than examining different samples and/or different regions after the various aging exposures. SAC305 lead free solder joint samples were formed with reflowed (RF) and water quenched (WQ) cooling profiles and resulting initial microstructures, and then polished microscopy cross-sections were prepared. Nanoindentation marks were added to the cross-

sections at certain locations to facilitate locating the fixed regions of interest in subsequent microscopy observations. The joints were then aged at $T = 125\text{ }^{\circ}\text{C}$, and the microstructures were observed and recorded in the selected regions after various aging exposures using SEM. With this approach, time-lapse imagery of the microstructure evolution in a particular region of a solder joint has been recorded as a function of the aging time.

The coalescence and migration of Ag_3Sn IMCs and the coarsening of $\beta\text{-Sn}$ dendrites have been observed as a function of aging time, and quantitative analysis of the variations in IMC particle size during aging has been performed. Three aging increments (1 hour, 1 day and 10 days) and two solidification profiles (RF and WQ) have been examined. Several SAC305 lead free solder samples were prepared and well-polished for this purpose. To date, the work up to 11 hours, 4 days, and 50 days of aging has been done, respectively. After each aging duration, the microstructures of the regions of interest in the samples were captured using SEM microscopy. Multiple regions were observed in several different RF and WQ solder joint samples. At last, the coarsening of IMC particles in fixed regions during aging has been recorded as a function of the aging time. Particularly, the aging induced evolutions of number of IMCs, total area of all IMCs, average particle area, and average particle diameter have been quantified.

5.2 Disadvantages of the Conventional Procedure

The conventional procedure to study the effects of aging on solder microstructure is comparing two different solder joint samples subjected to different aging conditions. However, this method is not accurate and sometimes can be misleading as two different samples cannot be directly compared even they have the same composition. Figure 5.1 shows the solder microstructures of RF SAC305 in three different regions at the same magnification. In all the three regions, there are many subgrains within the dendrite and the subgrain boundaries can be

discerned. However, the size and shape of the subgrains, IMCs or dendrites vary from region to region. Therefore, the results of microstructural changes may not be reliable by comparing two different samples or regions, especially when it comes to the quantitative analysis such as determination of the growth of IMC particles or subgrains with aging. This kind of comparison can lead us to either right conclusion or wrong one. For example, Figures 5.2-5.7 illustrate the comparisons of non-aged microstructures (left-hand side) with aged microstructures (right-hand side) of RF SAC305 in different regions. Figure 5.2 shows the coarsening of IMC particles with aging, which is the known/expected trend. However, by choosing two other regions, the result can be opposite, that is, aging led to finer IMC particles (Figure 5.3). Similarly, Figure 5.4 shows the increase of subgrain size during aging, while Figure 5.5 shows the decrease of subgrain size with aging. Additionally, opposite conclusions of aging effects on dendrite structure can also be reached by comparing different regions (see Figure 5.6 and Figure 5.7). In this chapter, the microstructure of an identical region has been examined before and after aging for various durations at 125 °C.

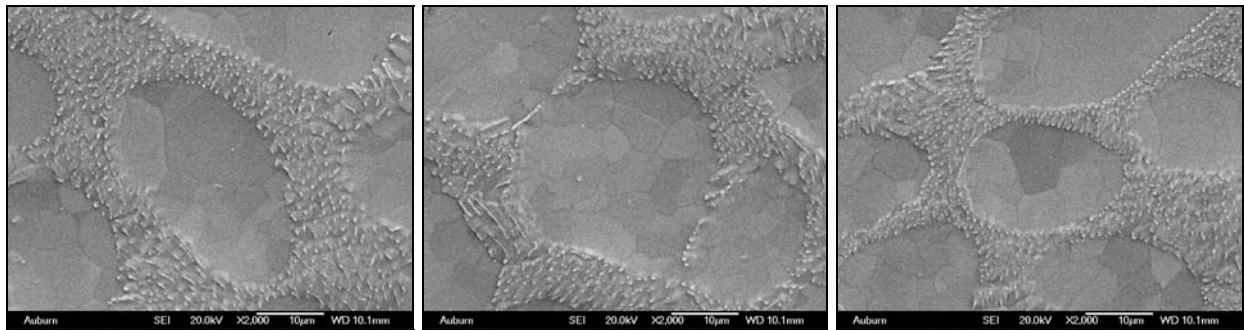


Figure 5.1 - Comparison of RF SAC305 Microstructures in Three Different Regions

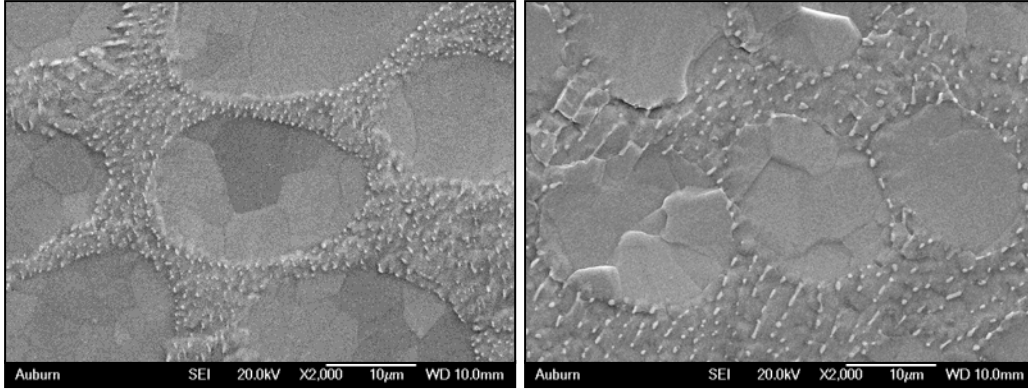


Figure 5.2 - Aging Led to Coarser IMC Particles (Left: No Aging; Right: 6-Hour Aging)

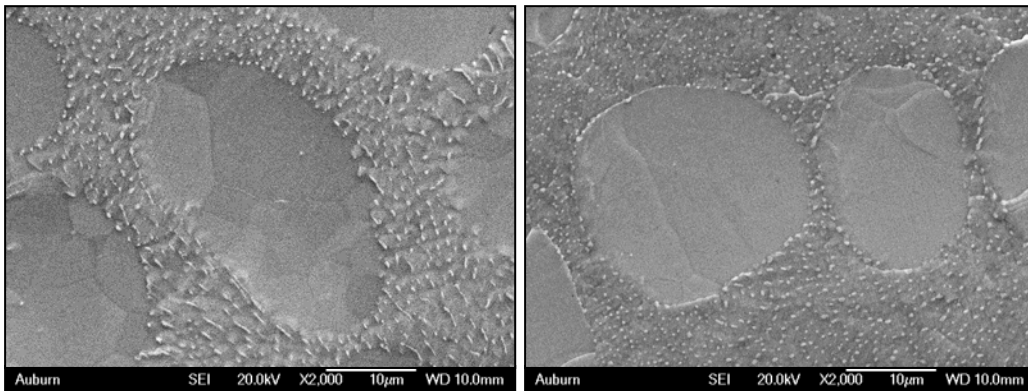


Figure 5.3 - Aging Led to Finer IMC Particles (Left: No Aging; Right: 7-Hour Aging)

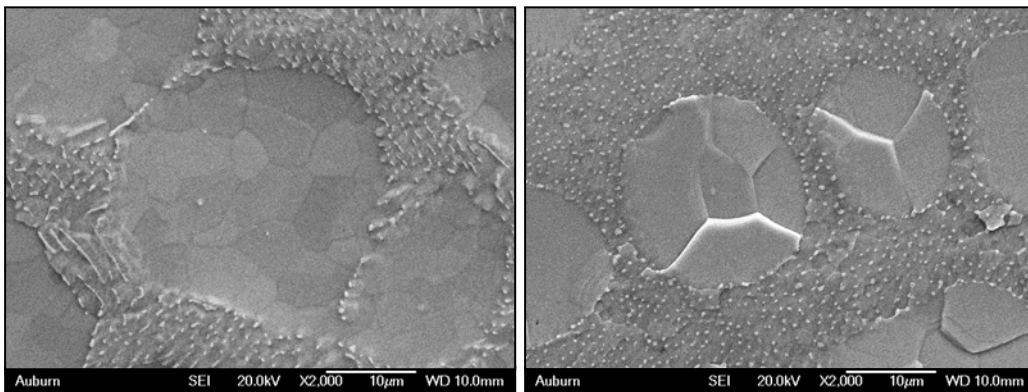


Figure 5.4 - Aging Increased the Subgrain Size (Left: No Aging; Right: 6-Hour Aging)

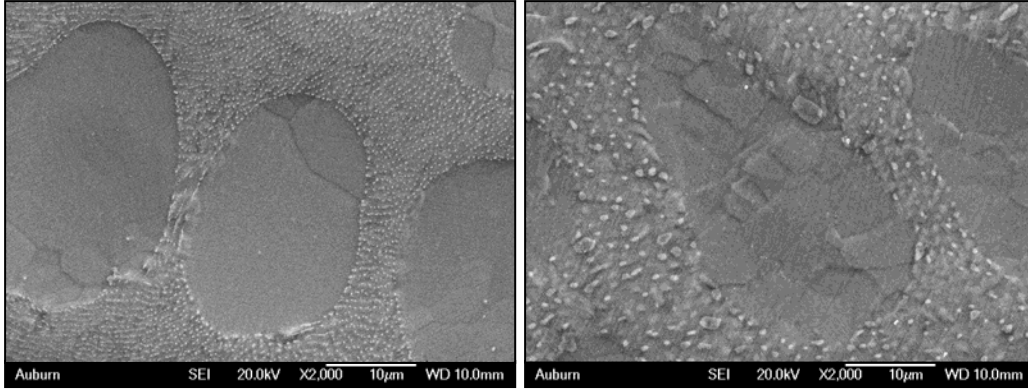


Figure 5.5 - Aging Decreased the Subgrain Size (Left: No Aging; Right: 1-Month Aging)

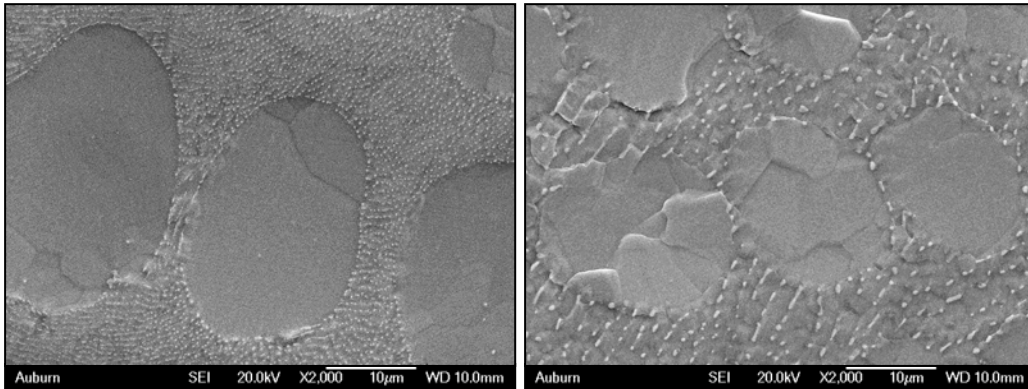


Figure 5.6 - Aging Weakened the Dendrite Structure (Left: No Aging; Right: 6-Hour Aging)

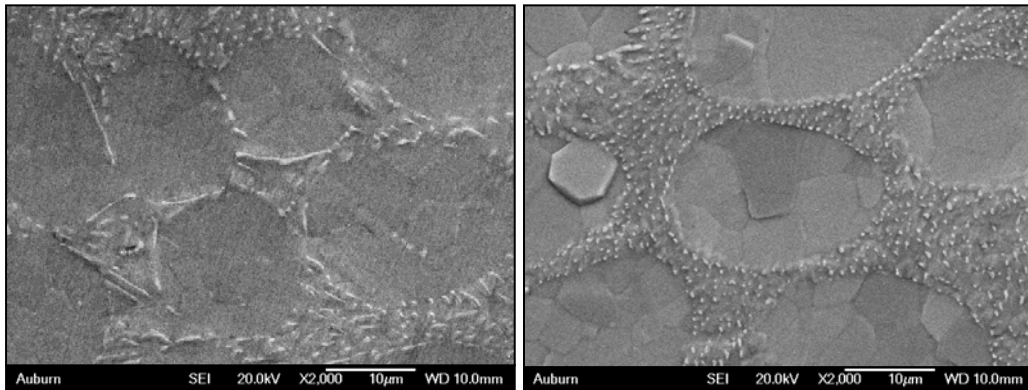
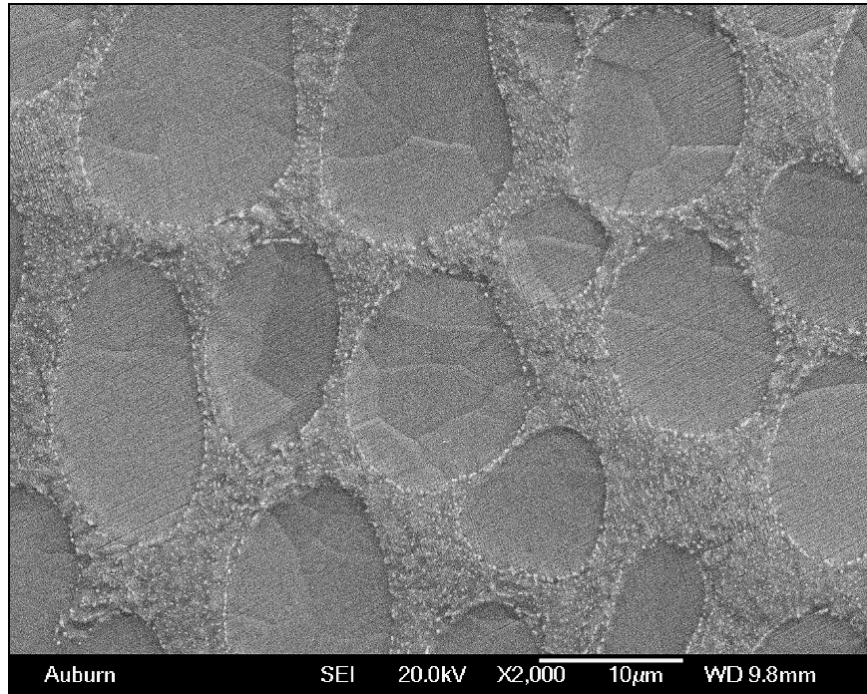


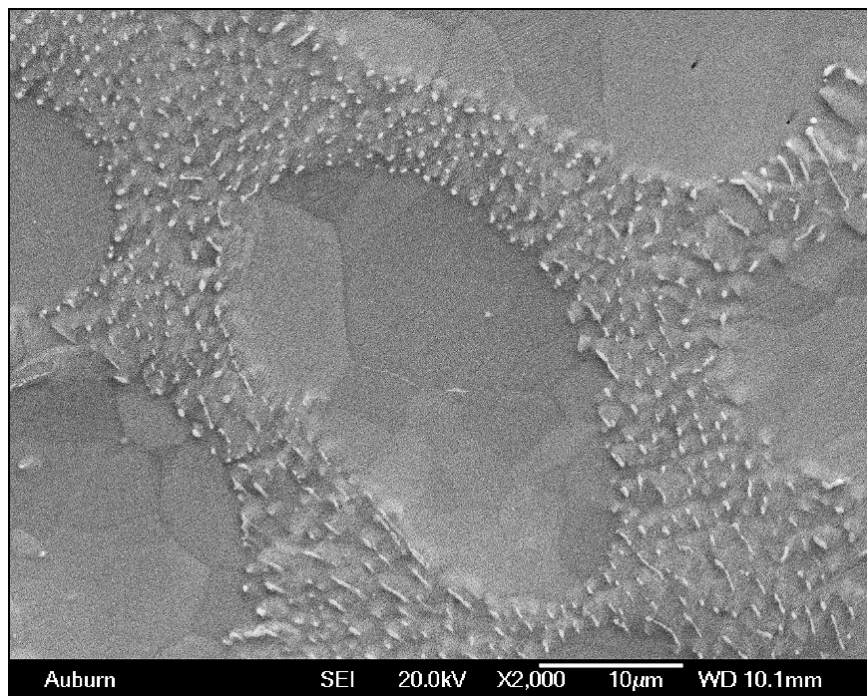
Figure 5.7 - Aging Strengthened the Dendrite Structure (Left: No Aging; Right: 3-Hour Aging)

5.3 Aging Induced Solder Microstructural Evolution

Sn-Ag-Cu (SAC) lead free solder microstructures typically consist of β -Sn dendrites surrounded by interdendritic eutectic regions incorporating a fine dispersion of Ag_3Sn and Cu_6Sn_5 intermetallic particles in β -Sn. For example, Figure 5.8 shows typical WQ and RF microstructures for the non-aged solder joint samples in this work. Since the same length scale has been used in each image, it is clear that the microstructure of WQ SAC305 is much finer than that of RF SAC305. This was expected due to the much faster cooling rate of WQ temperature profile. Relative to the RF solder sample, the WQ sample features smaller IMC particles and dendrites, as well as smaller β -Sn subgrains within the dendrites and interdendritic eutectic regions. For instance, there is just one complete dendrite in the field of view of the RF SAC305 sample (Figure 5.8(b)), while there are approximately twelve dendrites in the region of same size for WQ SAC305 sample (Figure 5.8(a)). In addition, the IMC particles are clearly much finer in the WQ microstructure relative to the RF microstructure, which has been verified quantitatively by image analysis as discussed later in this chapter. The IMC particles and dendrite structures can pin and block the movement of dislocations. Thus, the WQ specimens have superior mechanical properties and reduced creep relative to the RF specimens. However, the WQ microstructure is inherently more unstable and suffers larger changes when exposed to isothermal aging. The coarsening of Ag_3Sn particles has greater influence on solder mechanical properties than the coarsening of Cu_6Sn_5 does, as the volume fraction of Ag_3Sn is much higher in SAC alloys [99, 145].



(a) Water Quenched (WQ)



(b) Reflowed (RF)

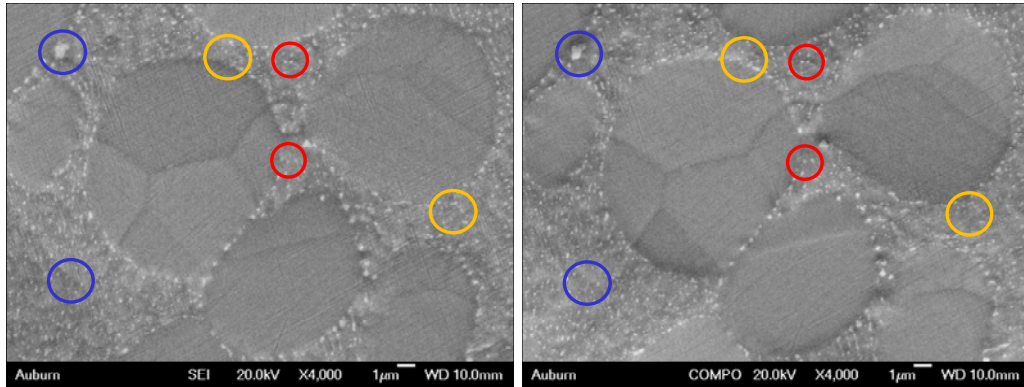
Figure 5.8 - Non-Aged SAC305 Microstructures

Figure 5.9 shows the observed microstructural evolution in the selected region of the WQ SAC305 sample with isothermal aging at 125 °C for up to 11 hours. Both secondary electron (SE) images and backscattered electron (BSE) images have been presented to illustrate the microstructural evolution. Even though the sample was only aged for few hours, the WQ microstructure changed significantly. As expected, the most obvious changes were the coarsening of IMC particles. In particular, the number of IMC particles decreased, while the average size of the particles and average particle separation distance increased significantly with aging. For example, blue circles in Figure 5.9 show typical positions where particles were growing, while red circles illustrate positions where the particles disappeared and the number of particles decreased. In addition, the coalescence of several particles is obvious in the areas indicated by orange circles. After this short 11-hour aging exposure, no significant changes of the size and shape of dendrites were observed.

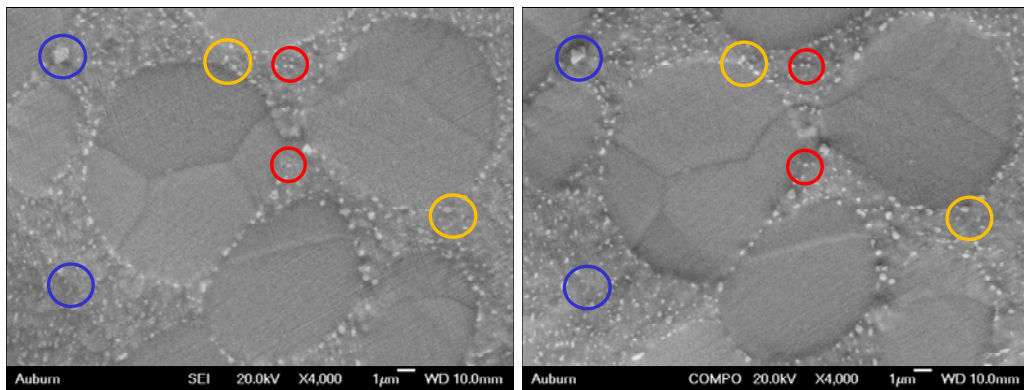
As shown in Figure 5.10, the microstructure of RF SAC305 also evolved with aging, but to a lesser degree than the WQ microstructure. Aging still led to the obvious coarsening of IMC particles in the RF microstructure. In Figure 5.10, the blue circles show typical regions featuring the coalescence of several particles into a single larger IMC particle, while the red circles show typical regions where disappearance of a particle occurred. Additionally, it was observed that needle-shaped IMCs broke into several small rounded sphere-like particles with aging, as shown in the regions within the black circles. Note that the scale of WQ microstructure images in Figure 5.9 is twice as big as the scale of RF microstructure images in Figure 5.10.

In addition, several other regions of RF and WQ SAC305 have also been studied, and the results (both SE and BSE images) are shown in Appendix B. It is noticeable that some Sn grains experienced the issue of “pop-up” during aging, and this is mainly due to the free surface created

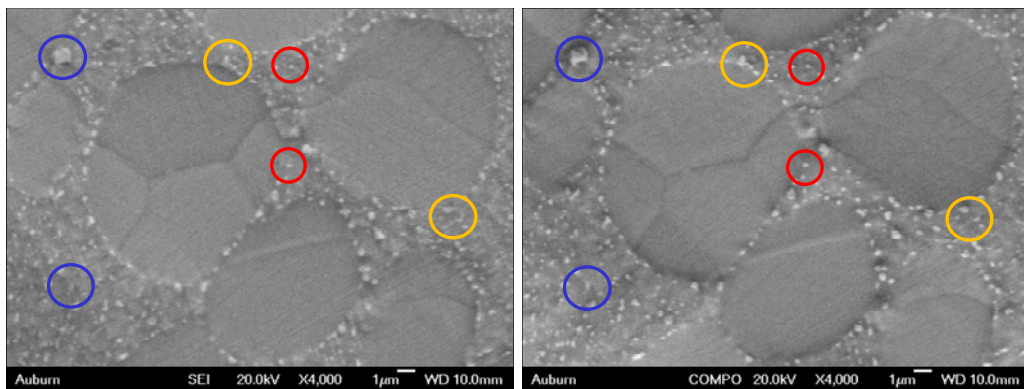
by cross-sectioning. During aging, the thermal anisotropy of Sn results in the force to elevate some subgrains, and there are no constraints in the Z direction (perpendicular to the field of view) as it is free surface. As a result, the “pop-up” of those subgrains is more and more obvious as the aging progresses, which can be observed in the microstructural evolution of several regions of interest.



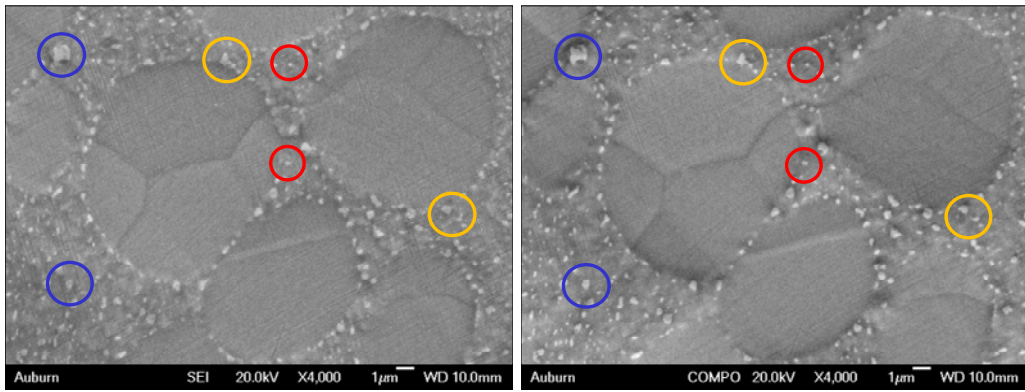
(a) No Aging (Left: SE; Right: BSE)



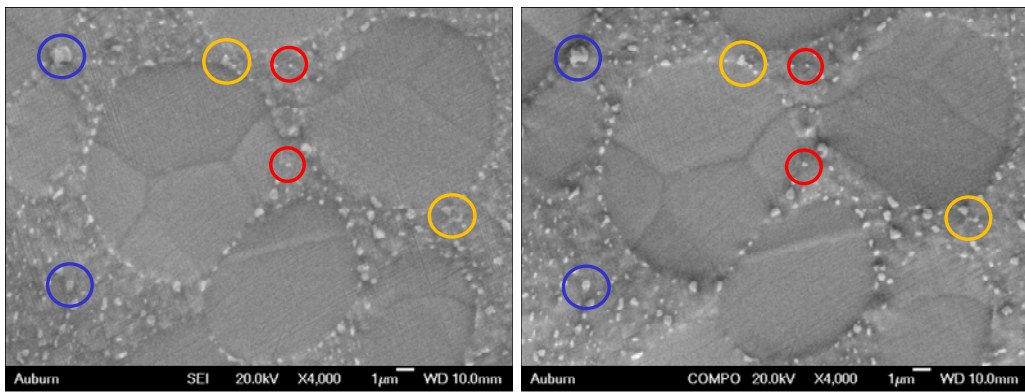
(b) 1 Hour of Aging (Left: SE; Right: BSE)



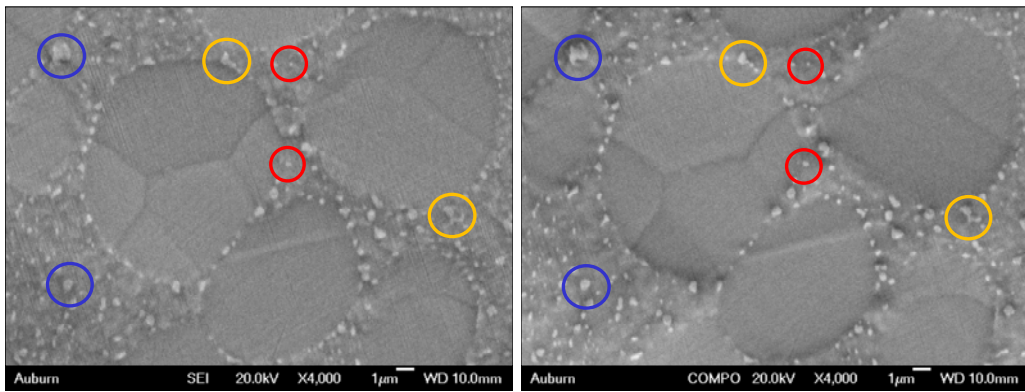
(c) 2 Hours of Aging (Left: SE; Right: BSE)



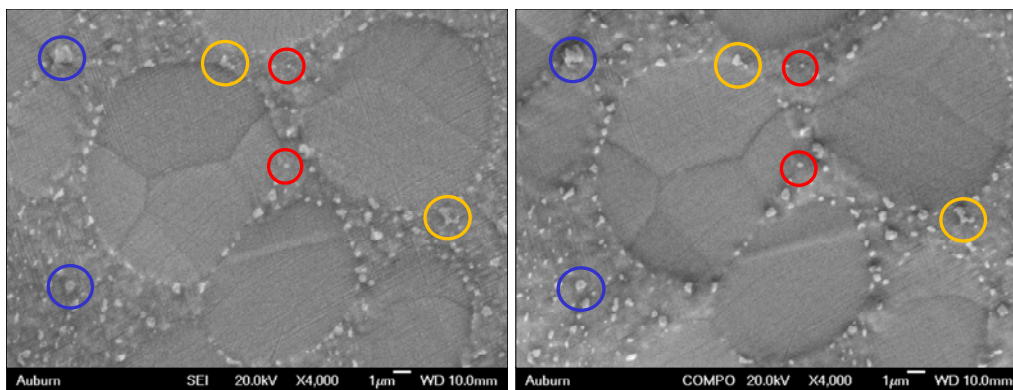
(d) 3 Hours of Aging (Left: SE; Right: BSE)



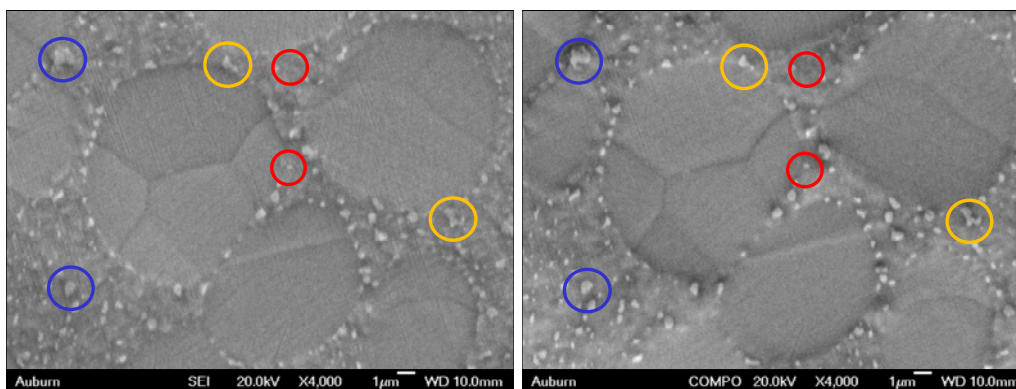
(e) 4 Hours of Aging (Left: SE; Right: BSE)



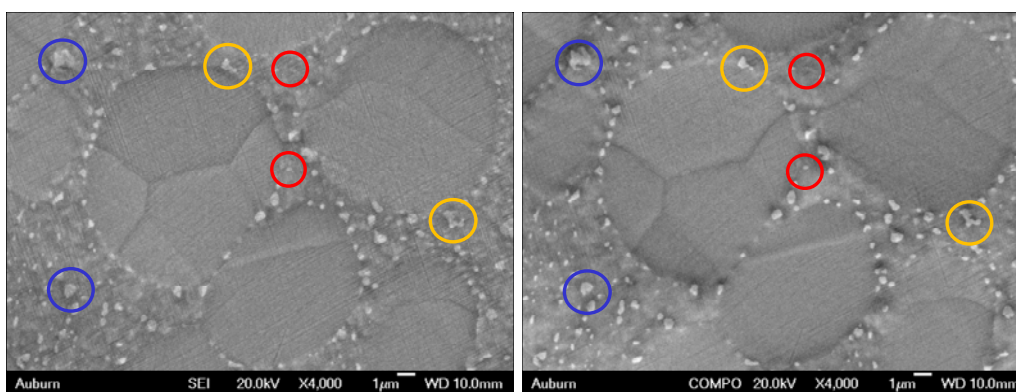
(f) 5 Hours of Aging (Left: SE; Right: BSE)



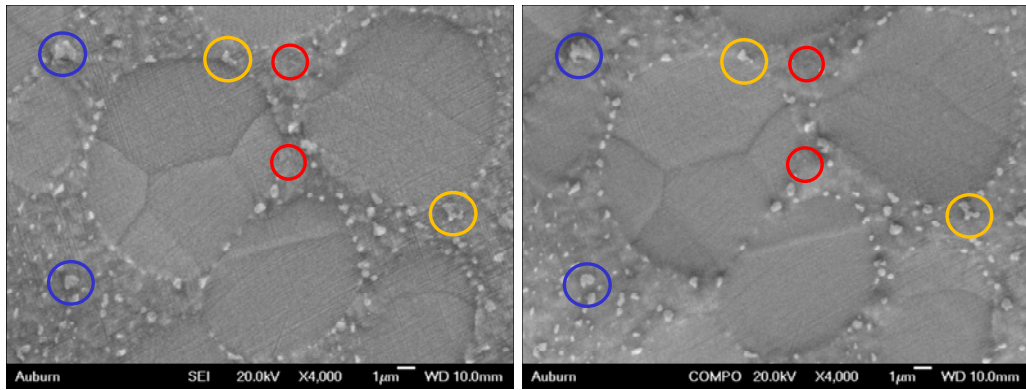
(g) 6 Hours of Aging (Left: SE; Right: BSE)



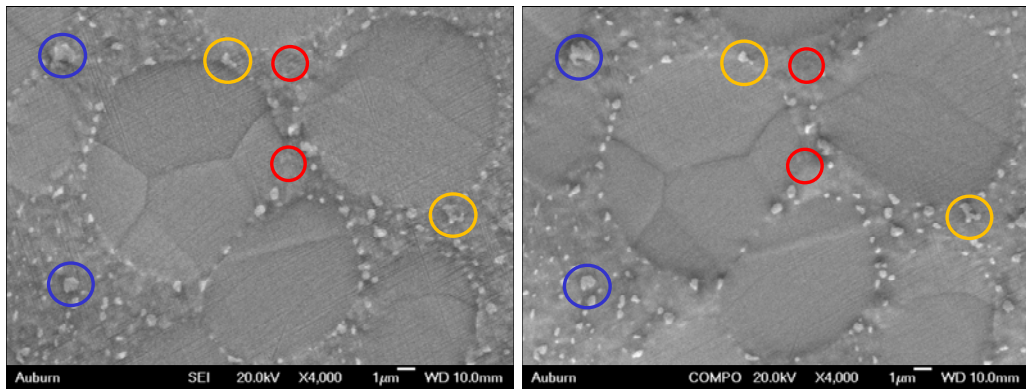
(h) 7 Hours of Aging (Left: SE; Right: BSE)



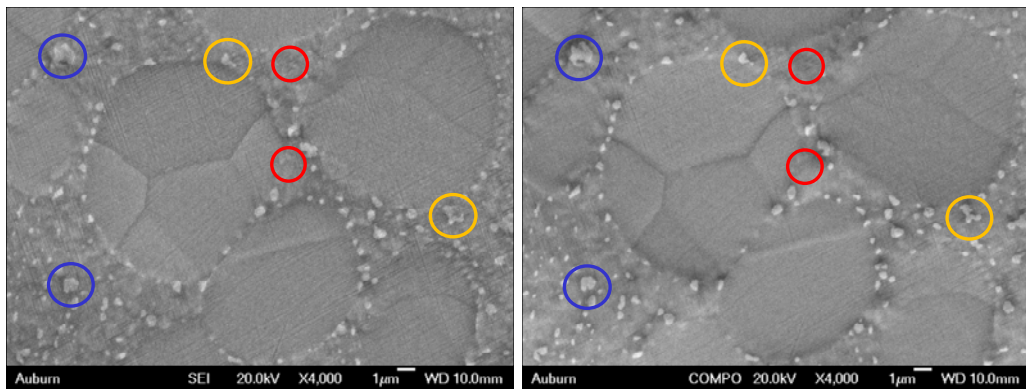
(i) 8 Hours of Aging (Left: SE; Right: BSE)



(j) 9 Hours of Aging (Left: SE; Right: BSE)



(k) 10 Hours of Aging (Left: SE; Right: BSE)



(l) 11 Hours of Aging (Left: SE; Right: BSE)

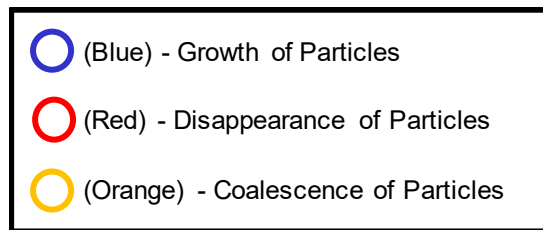
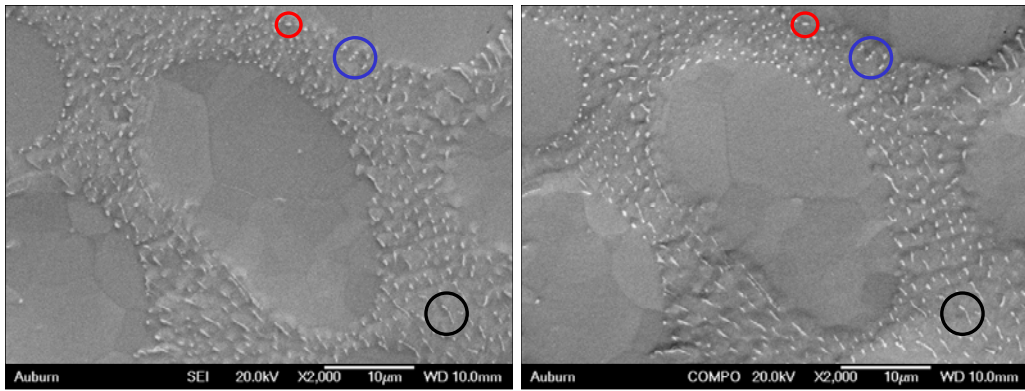
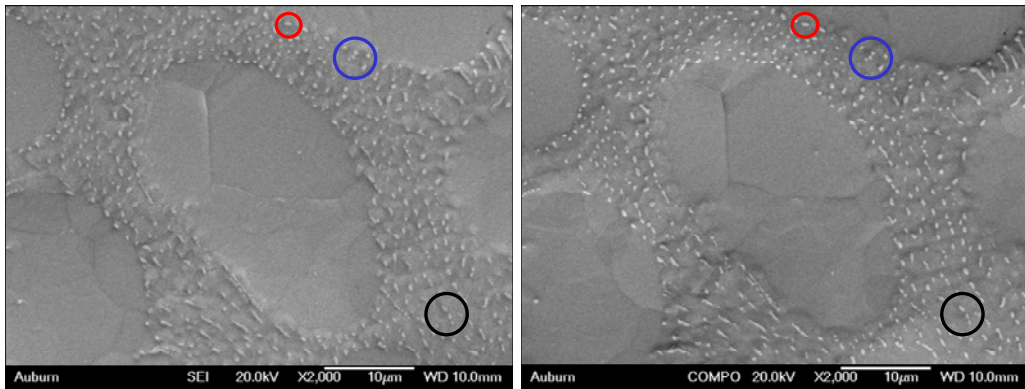


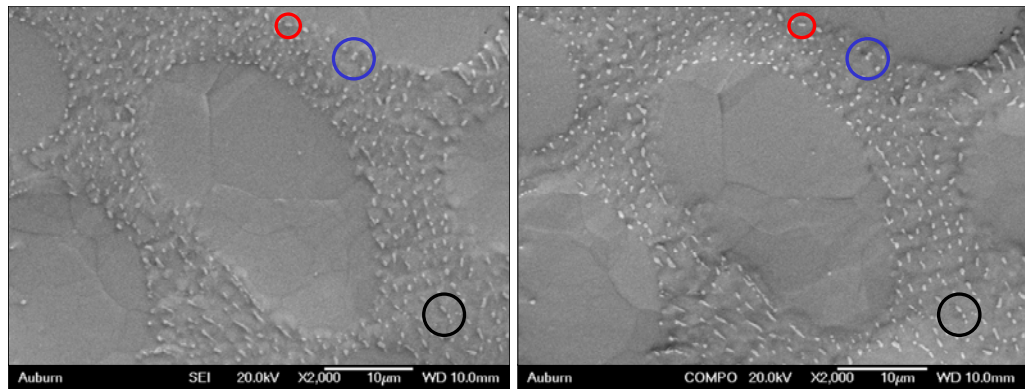
Figure 5.9 - Aging Induced Microstructural Evolution of WQ SAC305 by SEM Microscopy (Aging at T = 125 °C, up to 11 Hours)



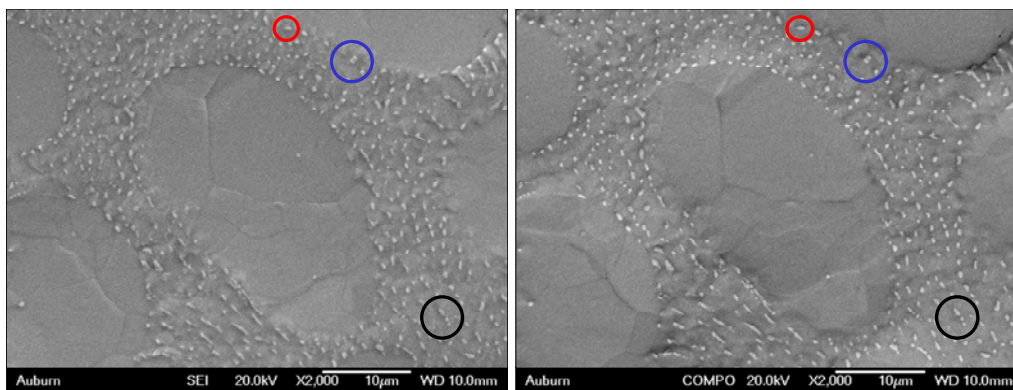
(a) No Aging (Left: SE; Right: BSE)



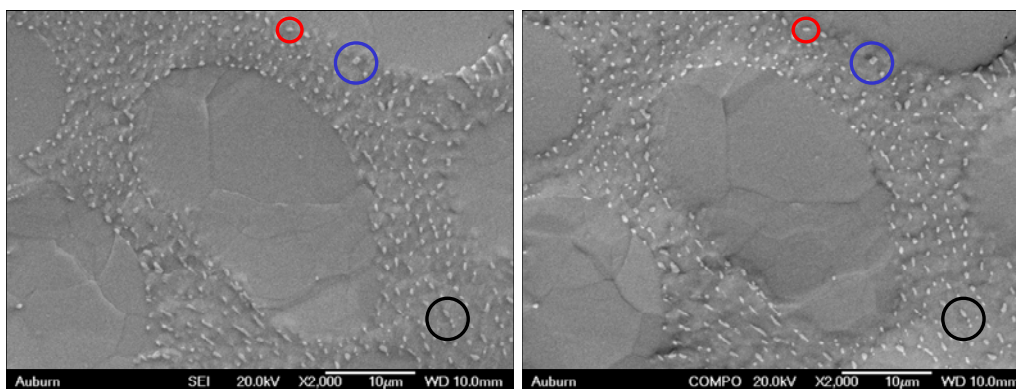
(b) 1 Hour of Aging (Left: SE; Right: BSE)



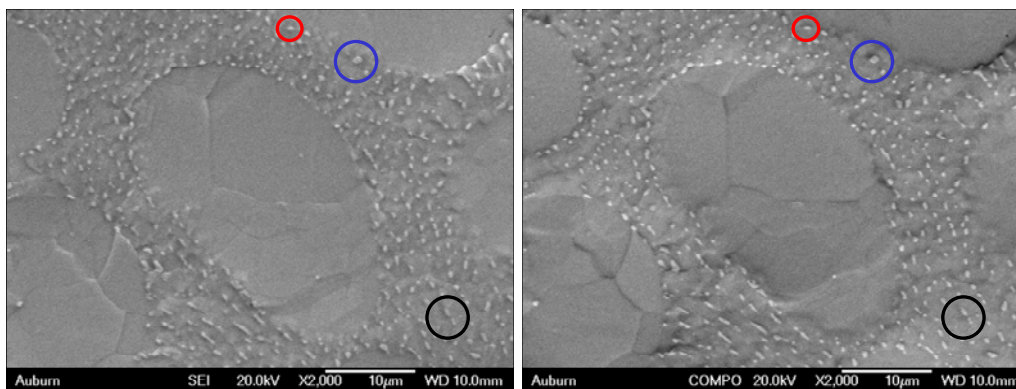
(c) 2 Hours of Aging (Left: SE; Right: BSE)



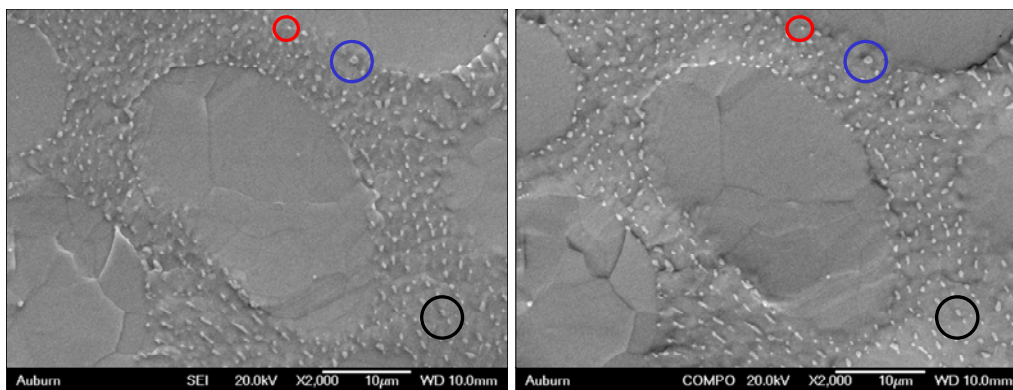
(d) 3 Hours of Aging (Left: SE; Right: BSE)



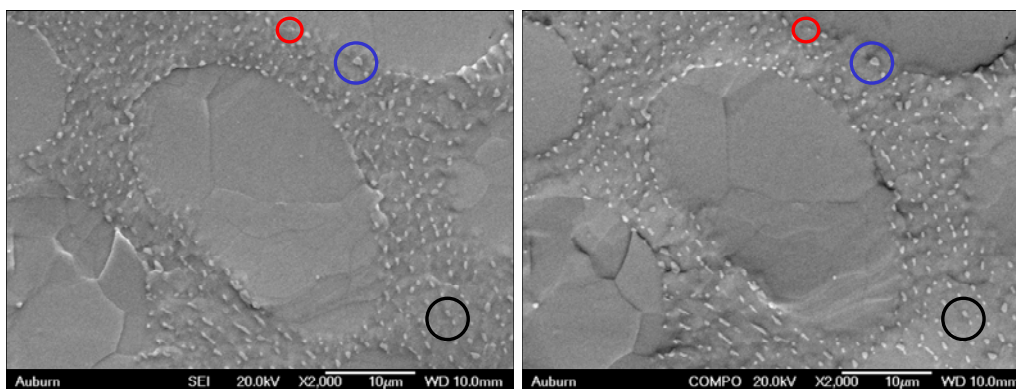
(e) 4 Hours of Aging (Left: SE; Right: BSE)



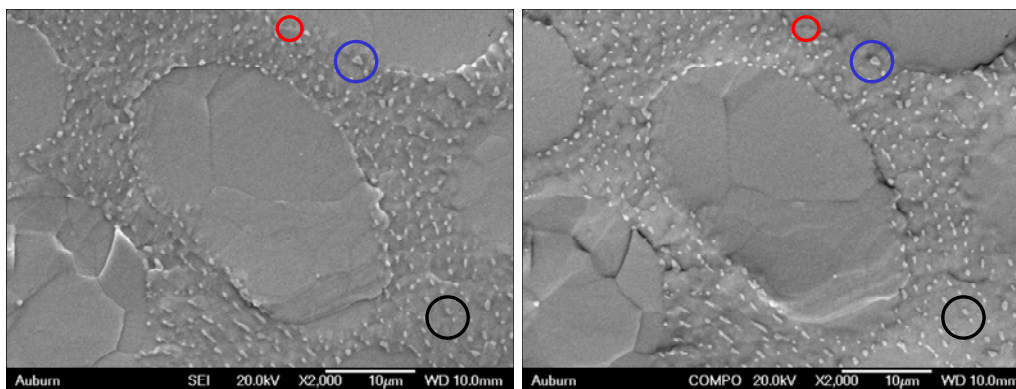
(f) 5 Hours of Aging (Left: SE; Right: BSE)



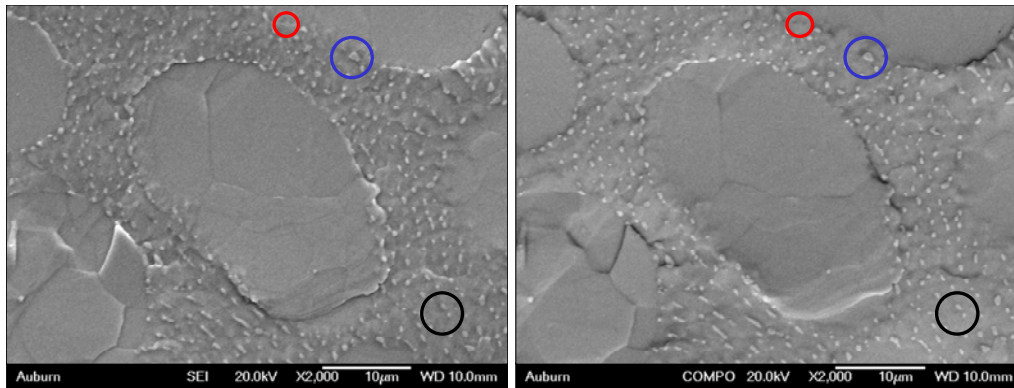
(g) 6 Hours of Aging (Left: SE; Right: BSE)



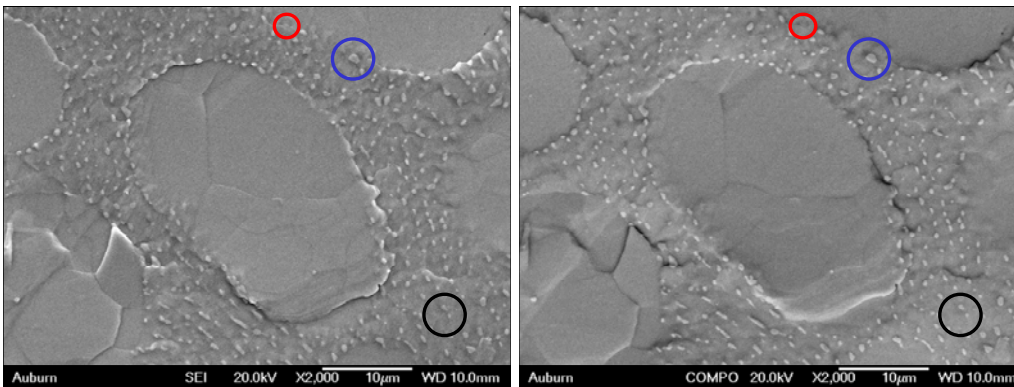
(h) 7 Hours of Aging (Left: SE; Right: BSE)



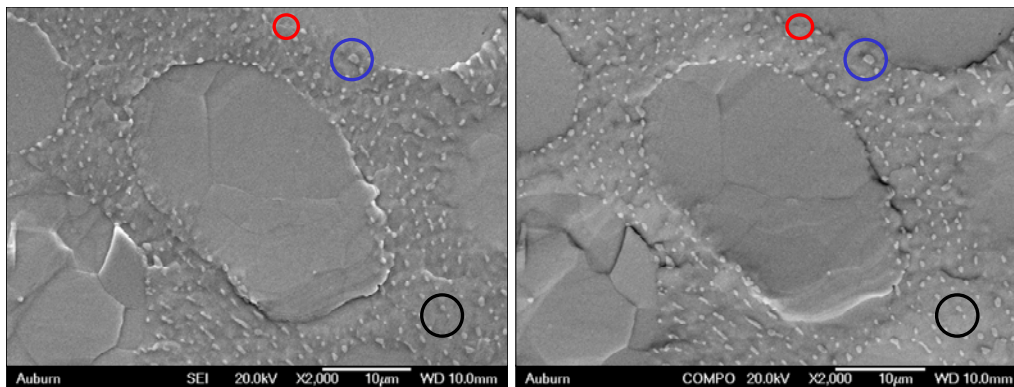
(i) 8 Hours of Aging (Left: SE; Right: BSE)



(j) 9 Hours of Aging (Left: SE; Right: BSE)



(k) 10 Hours of Aging (Left: SE; Right: BSE)



(l) 11 Hours of Aging (Left: SE; Right: BSE)

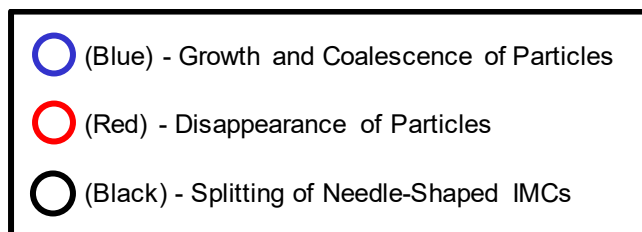


Figure 5.10 - Aging Induced Microstructural Evolution of RF SAC305 by SEM Microscopy (Aging at T = 125 °C, up to 11 Hours)

Similar microstructural changes have been found on the samples that were aged at 125 °C for a longer time. Figure 5.11 and Figure 5.12 show the microstructural changes of RF and WQ SAC305 caused by 1 day and 10 days of aging, respectively. Compared with RF SAC305, WQ SAC305 had much finer initial IMC particles but they coarsened to a greater degree during isothermal aging. The coarsening of IMCs was more obvious for longer durations of aging, which was expected.

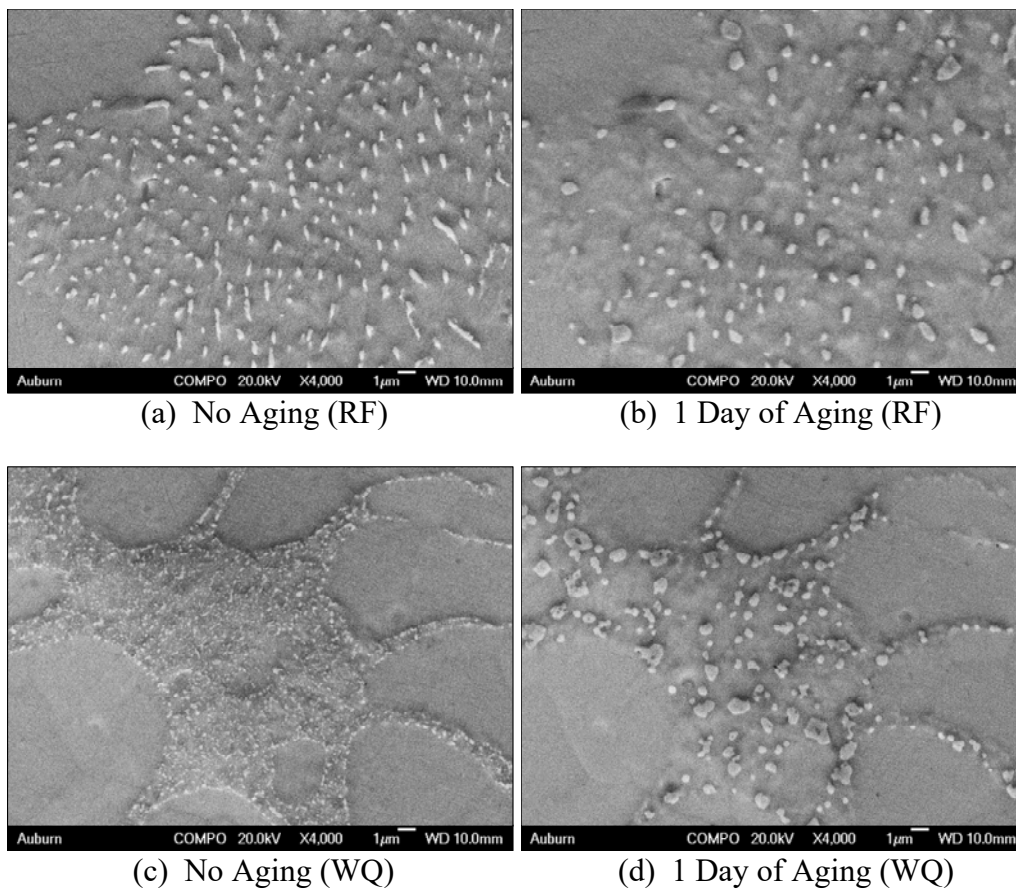


Figure 5.11 - Aging Induced Coarsening of IMCs (Aging at 125 °C; Aging Increment: 1 Day)

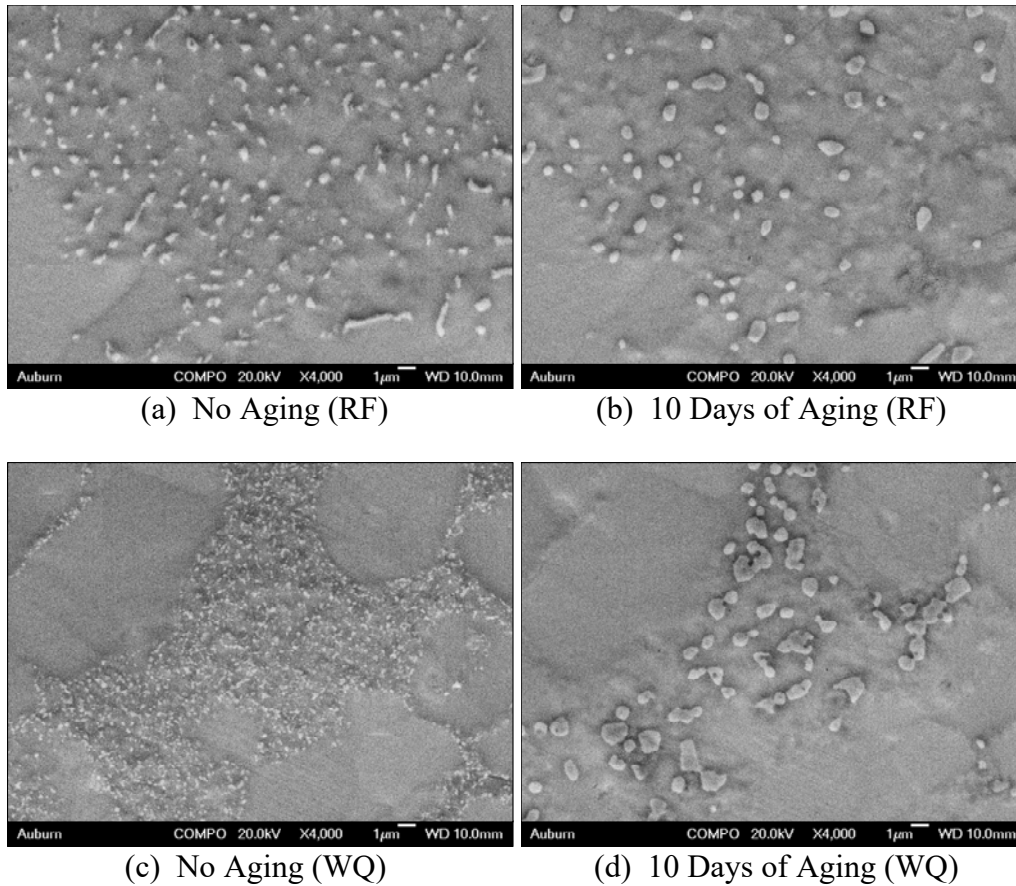


Figure 5.12 - Aging Induced Coarsening of IMCs (Aging at 125 °C; Aging Increment: 10 Days)

5.4 Discussions on the Coarsening of IMCs with Aging

Typically, IMC particles tend to become more round (spherical) with aging. Atoms on the surface of a particle have higher energy than the atoms inside a particle due to unsatisfied bonds in the surface atoms. A cylindrical or elongated particle has a higher fraction of surface atoms (or higher surface to volume ratio) compared to a spherical (round) particle with the same volume. As a result, the free energy per atom of an elongated particle is higher than that of a round particle. This free energy difference is the driving force that causes the transition of IMC particles from needle-shaped to a more rounded shape.

Another common observation is that larger particles are produced at the expense of smaller particles. This IMC coarsening phenomenon is also known as Ostwald Ripening. According to the Gibbs-Thompson effect [146-148], an increase in particle size is accompanied by a decrease of the solute concentration in the matrix surrounding the particle. This leads to a concentration gradient, and solute atoms near smaller particles will diffuse towards the larger particles where the reduction in solute concentration has occurred. In addition, atoms from the smaller particles will go back into solution. The overall effects are shrinkage of smaller particles, and growth of larger particles. Since Ostwald Ripening is a diffusion-based process, use of higher aging temperatures will increase the rate of coarsening significantly.

The coarsening and coalescing of IMC particles during aging is known to play a critical role in the degradations of solder mechanical properties. IMC particles will pin and block the movement of dislocations. However, aging leads to both a smaller number of larger IMC particles and increased spacing between the IMC particles. Orowan proposed a mechanism that when a dislocation crosses incoherent precipitate particles (like the IMC particles in present case), it will bow and leave a loop of stress field around the particle [149]. The yield stress and strength of a material depends on the shear stress (also known as the Orowan stress) that is required for a dislocation to pass through the particles. This shear stress will decrease as the inter-particle spacing increases during aging. Therefore, the yield stress and strength of a material will decrease with the coarsening and coalescing of IMC particles.

5.5 Quantitative Analysis of Aging Induced Evolution of IMCs

To quantitatively analyze the coarsening of IMC particles during aging, several sub-regions have been selected and Figure 5.13 shows an example interdendritic eutectic sub-region present in the SEM micrograph of RF SAC305 sample. Image analysis methods were used to

perform the quantitative analysis. The gray-scale images were first converted to binary images, and then the areas of IMC particles (white objects) were calculated using image analysis toolbox in MATLAB. The microstructure of this sub-region was studied every one hour of aging, and Figure 5.14 shows both gray-scale and binary images that illustrate aging induced evolution of IMC particles up to 11 hours in this sub-region. From these images, it is easy to see that aging causes: (1) the number of IMC particles to decrease, (2) the average size of the intermetallic particles to increase, and (3) the average spacing between intermetallic particles to increase. Figure 5.15 shows the evolution of IMCs with aging up to 11 hours for WQ SAC305, and similar microstructural changes have been observed. Similar changes have also been found in other studied sub-regions of RF and WQ SAC305 samples that were subjected to longer durations of aging (see Figures 5.16-5.19). It is clear that WQ microstructures suffered more changes during aging relative to RF microstructures. For the samples that were aged at an increment of 1 day or 10 days, relative larger sub-regions were chosen to perform the analysis as they experienced more significant microstructural changes. The length scales are the same in Figures 5.14, 5.16, 5.17, 5.18, and 5.19, and they are half the scale in Figure 5.15.

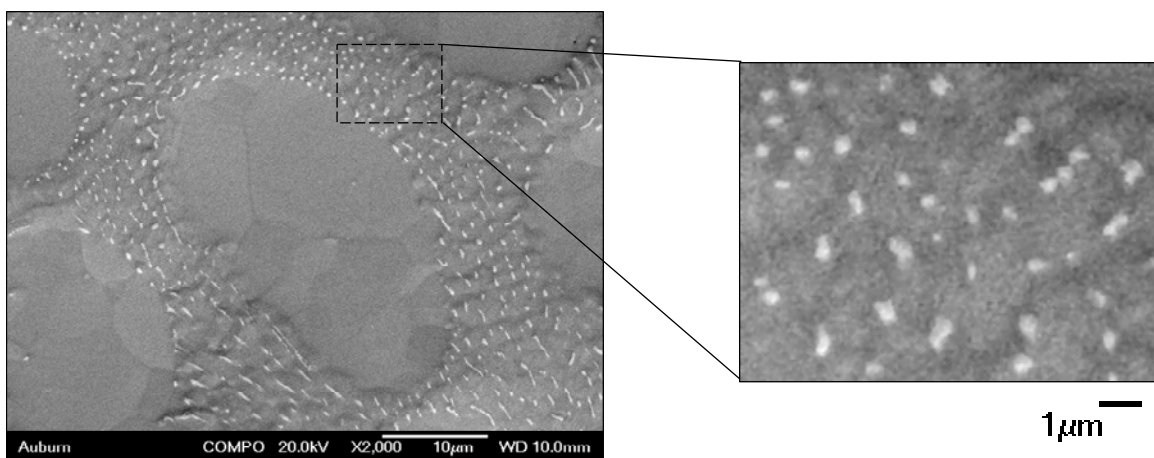


Figure 5.13 - Sub-Region for Quantitative Analysis of Aging Effects on IMCs

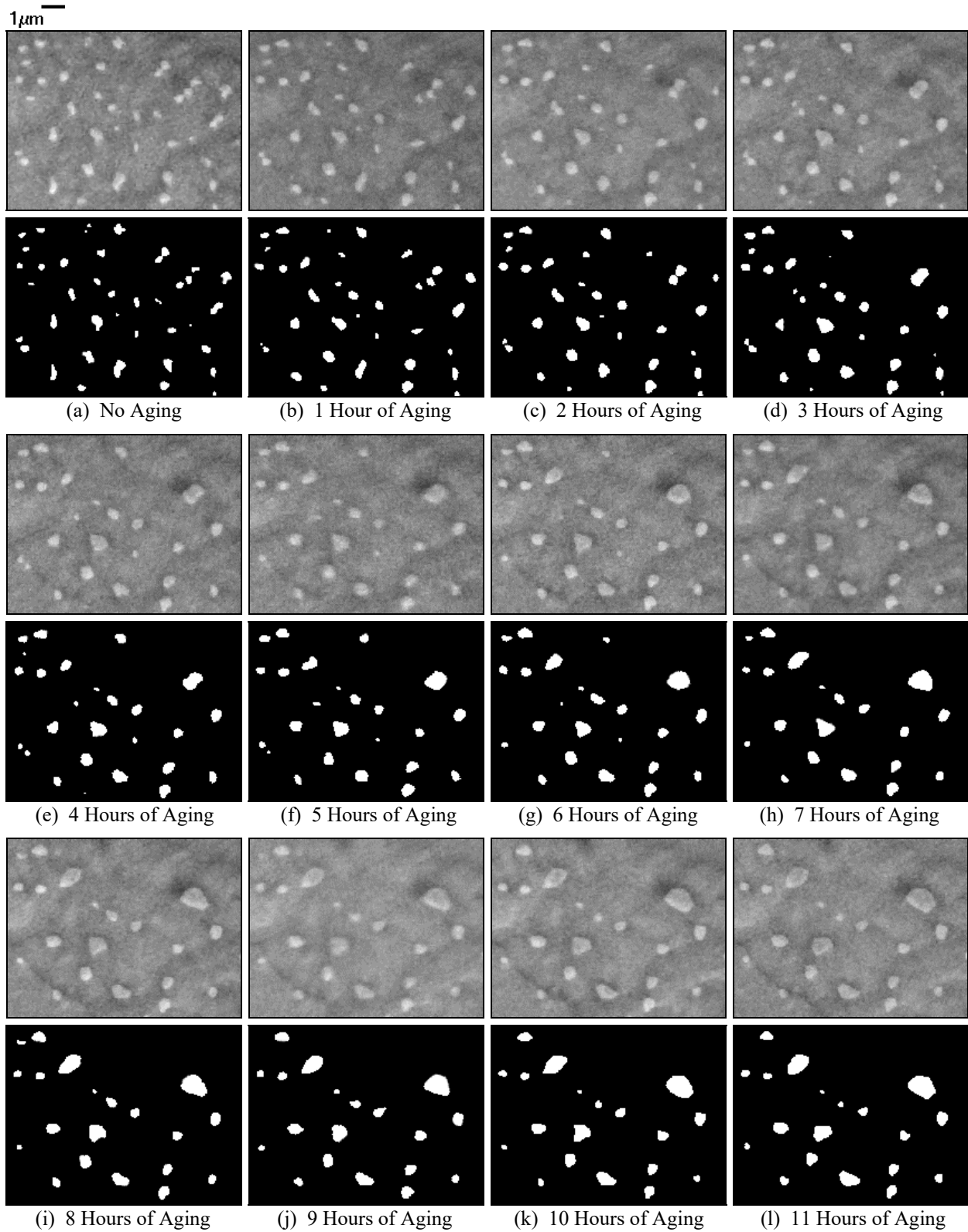


Figure 5.14 - Aging Induced Evolution of IMCs at 125 °C (Aging Increment: 1 Hour; RF SAC305; Top: Gray-Scale Image, Bottom: Binary Image)

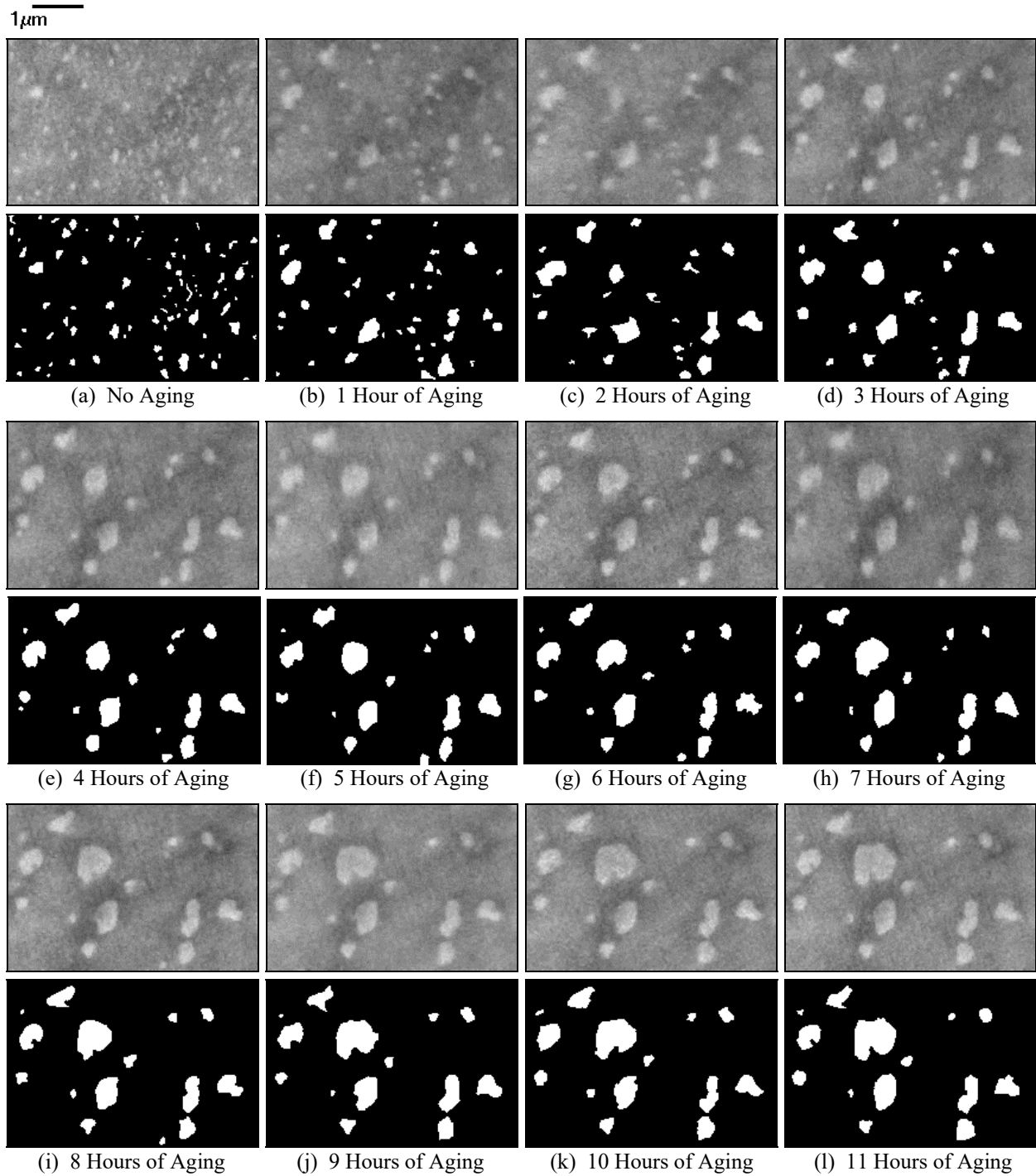
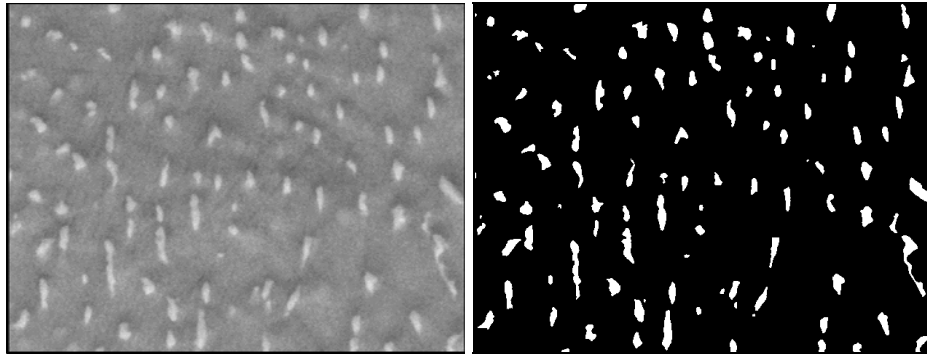
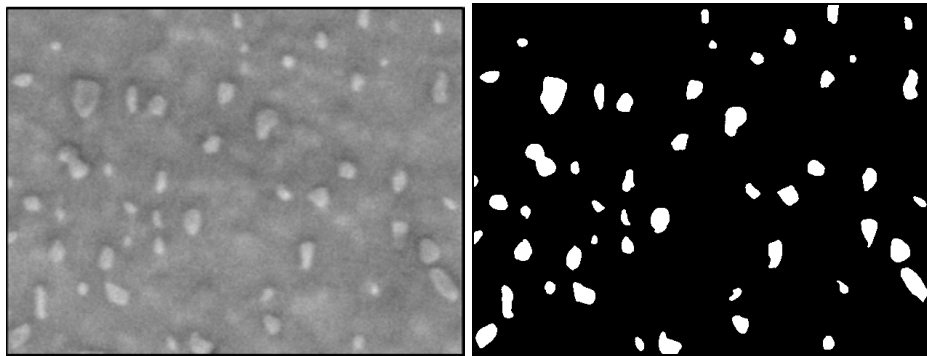


Figure 5.15 - Aging Induced Evolution of IMCs at 125 °C (Aging Increment: 1 Hour; WQ SAC305; Top: Gray-Scale Image, Bottom: Binary Image)

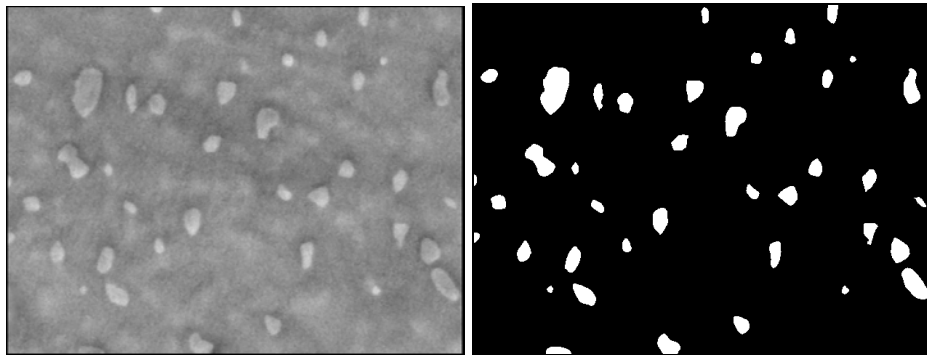
1 μ m



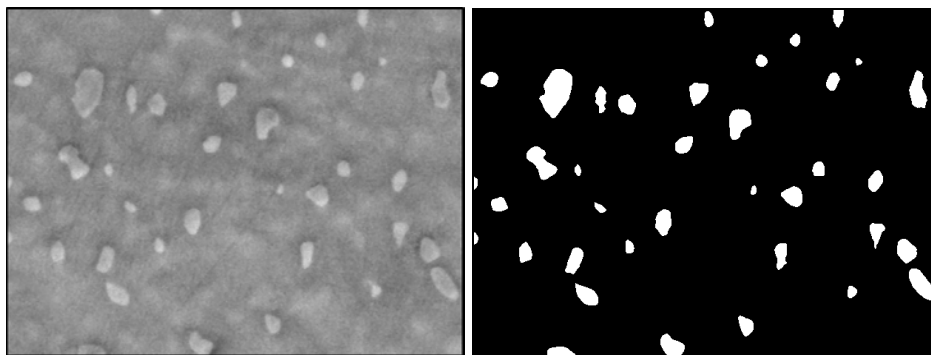
(a) No Aging (Left: Gray-Scale; Right: Binary)



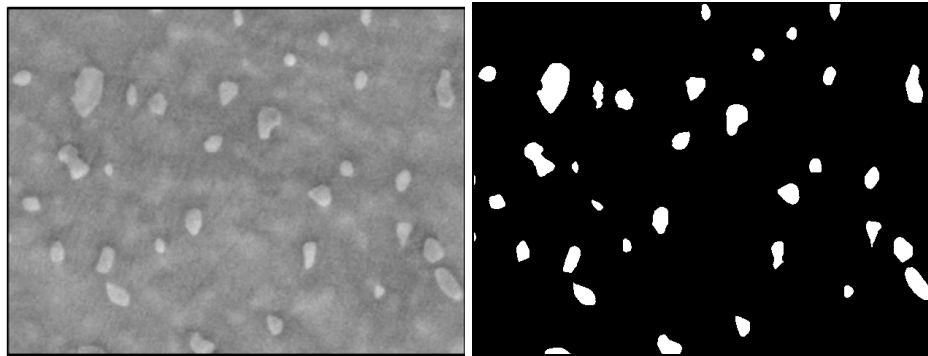
(b) 1 Day of Aging (Left: Gray-Scale; Right: Binary)



(c) 2 Days of Aging (Left: Gray-Scale; Right: Binary)



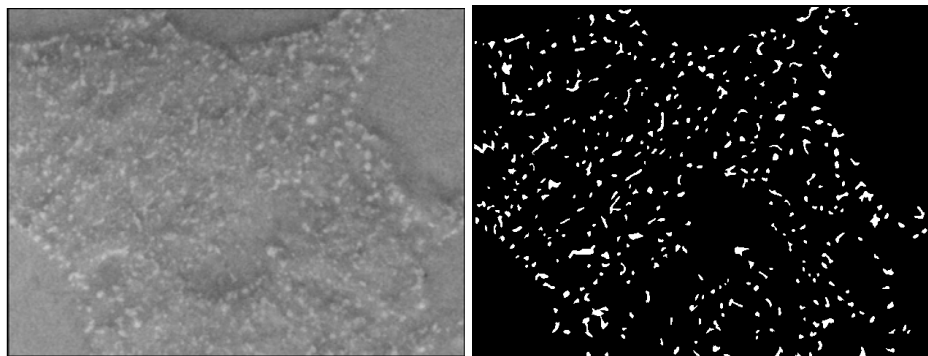
(d) 3 Days of Aging (Left: Gray-Scale; Right: Binary)



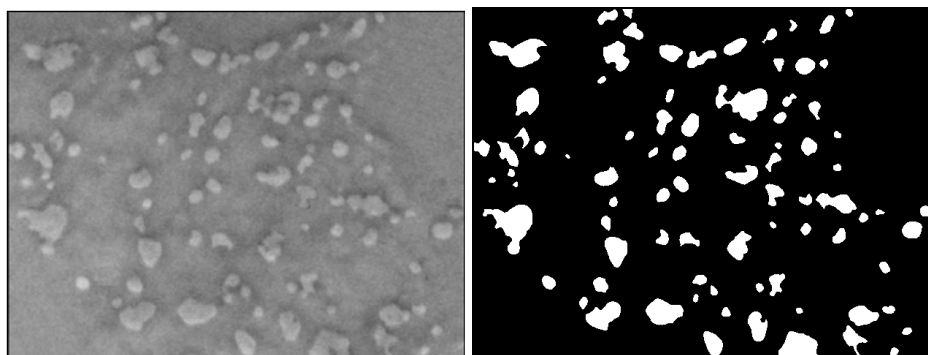
(e) 4 Days of Aging (Left: Gray-Scale; Right: Binary)

Figure 5.16 - Aging Induced Evolution of IMCs at 125 °C
(Aging Increment: 1 Day; RF SAC305)

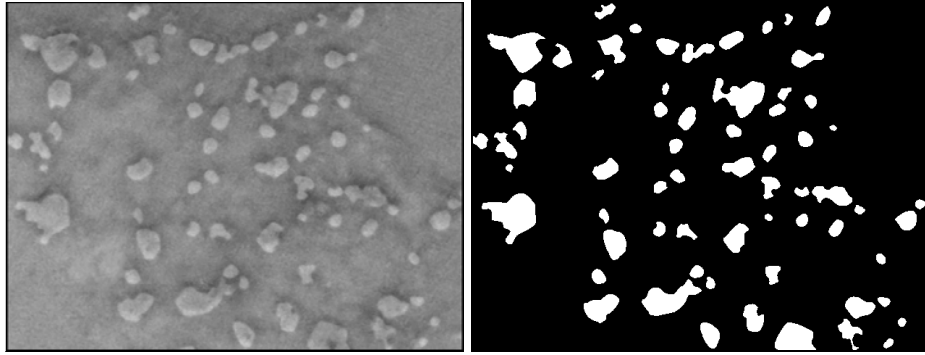
1 μ m



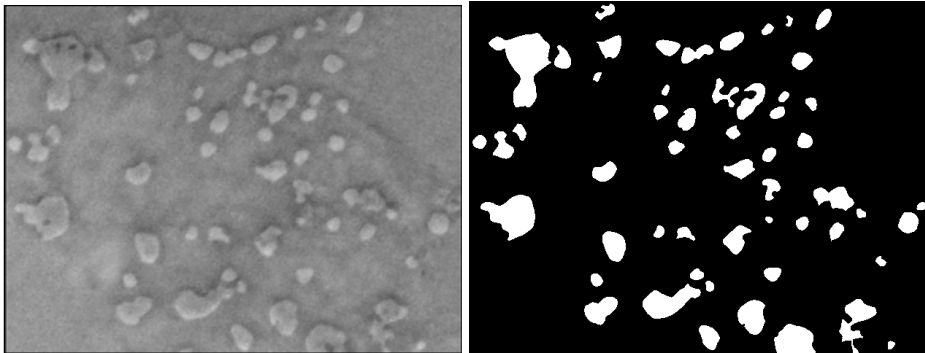
(a) No Aging (Left: Gray-Scale; Right: Binary)



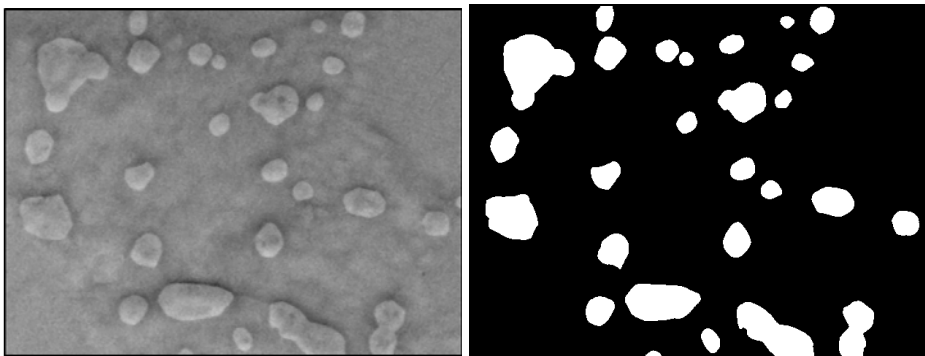
(b) 1 Day of Aging (Left: Gray-Scale; Right: Binary)



(c) 2 Days of Aging (Left: Gray-Scale; Right: Binary)



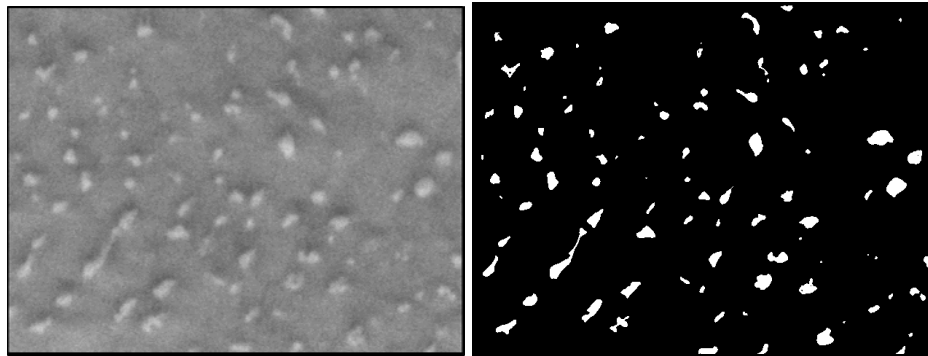
(d) 3 Days of Aging (Left: Gray-Scale; Right: Binary)



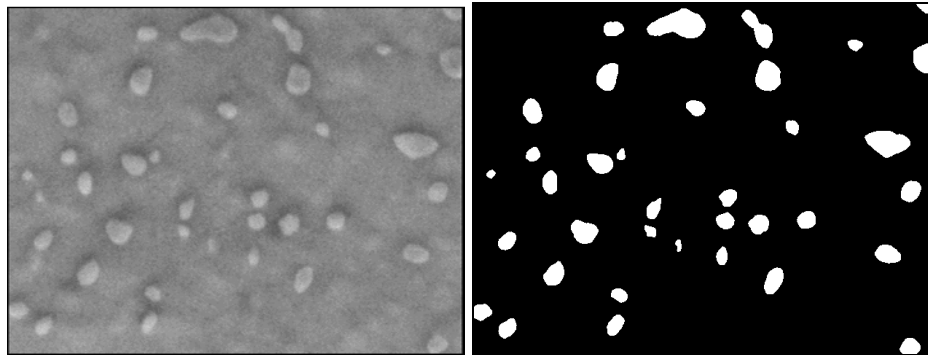
(e) 4 Days of Aging (Left: Gray-Scale; Right: Binary)

Figure 5.17 - Aging Induced Evolution of IMCs at 125 °C
(Aging Increment: 1 Day; WQ SAC305)

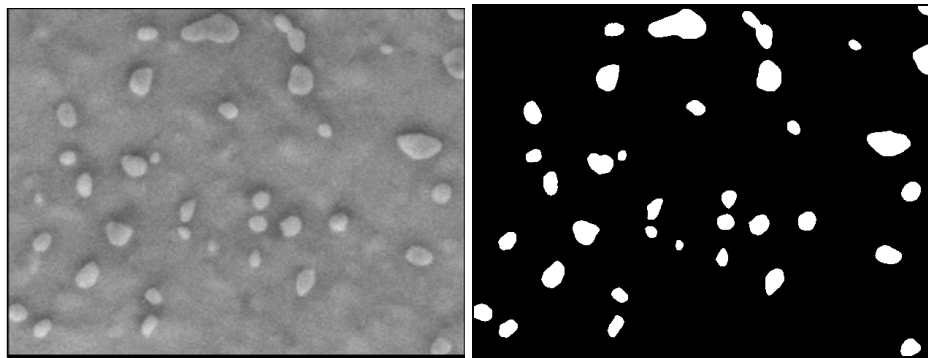
1 μ m



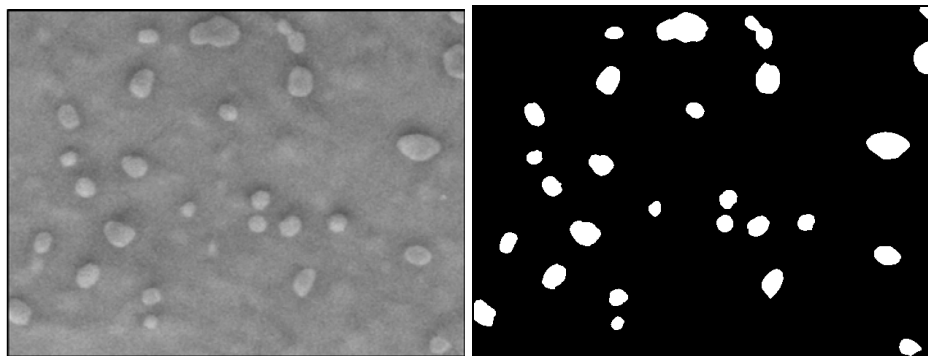
(a) No Aging (Left: Gray-Scale; Right: Binary)



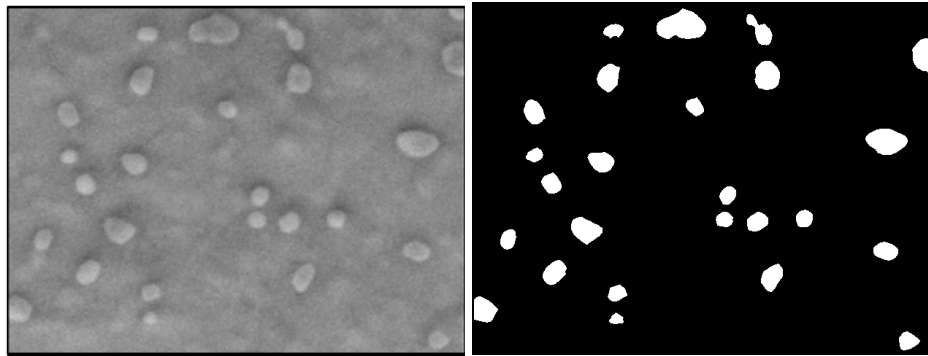
(b) 10 Days of Aging (Left: Gray-Scale; Right: Binary)



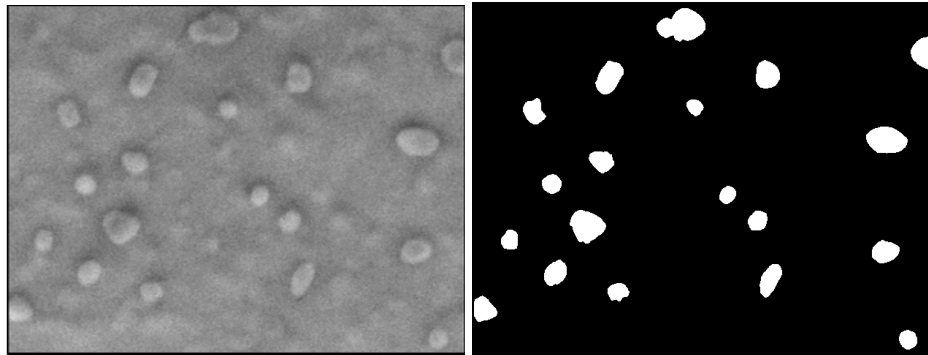
(c) 20 Days of Aging (Left: Gray-Scale; Right: Binary)



(d) 30 Days of Aging (Left: Gray-Scale; Right: Binary)



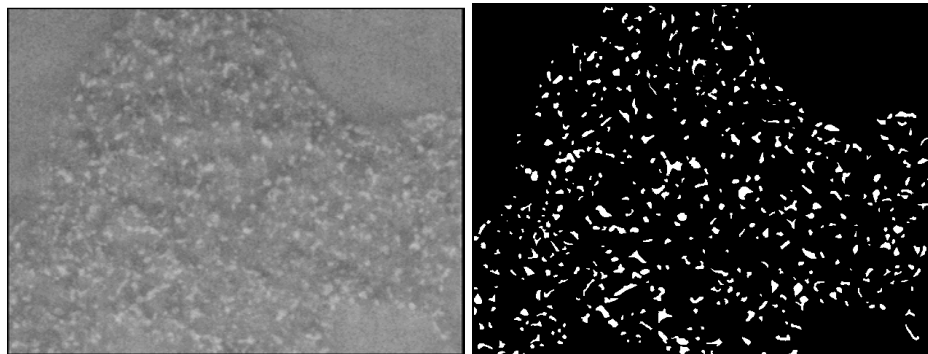
(e) 40 Days of Aging (Left: Gray-Scale; Right: Binary)



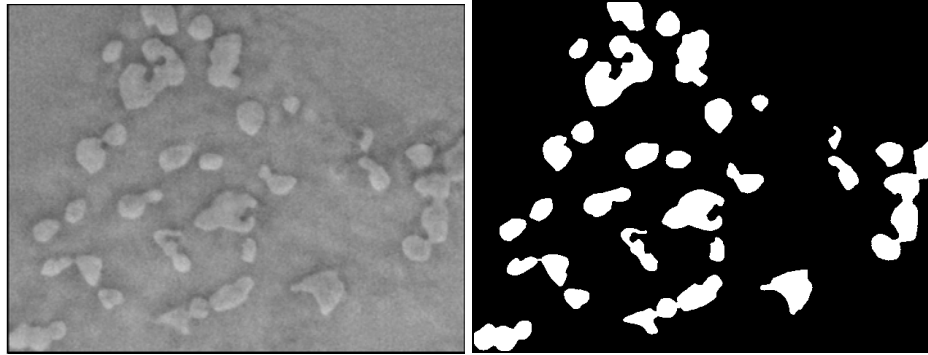
(f) 50 Days of Aging (Left: Gray-Scale; Right: Binary)

Figure 5.18 - Aging Induced Evolution of IMCs at 125 °C
(Aging Increment: 10 Days; RF SAC305)

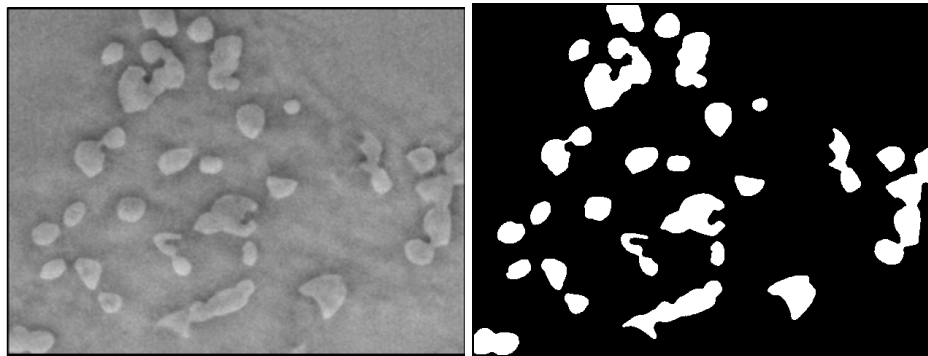
1 μ m



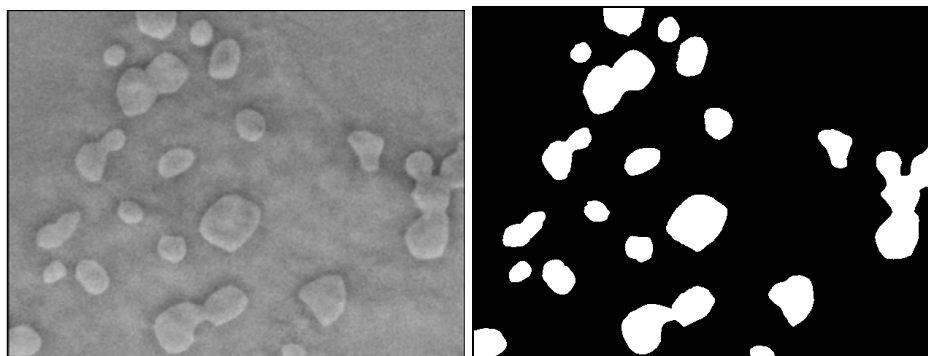
(a) No Aging (Left: Gray-Scale; Right: Binary)



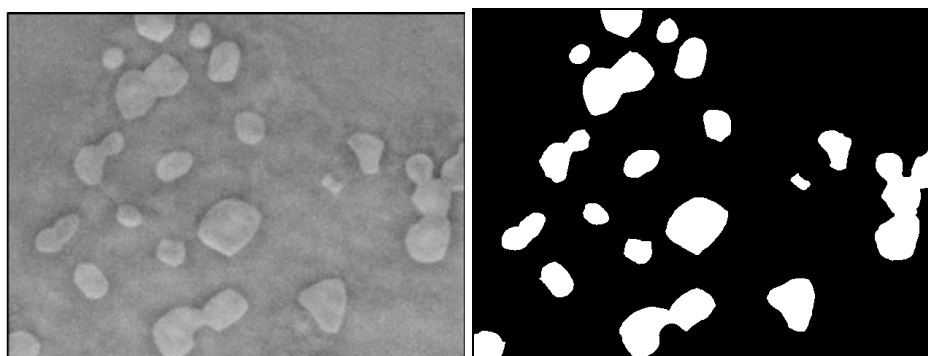
(b) 10 Days of Aging (Left: Gray-Scale; Right: Binary)



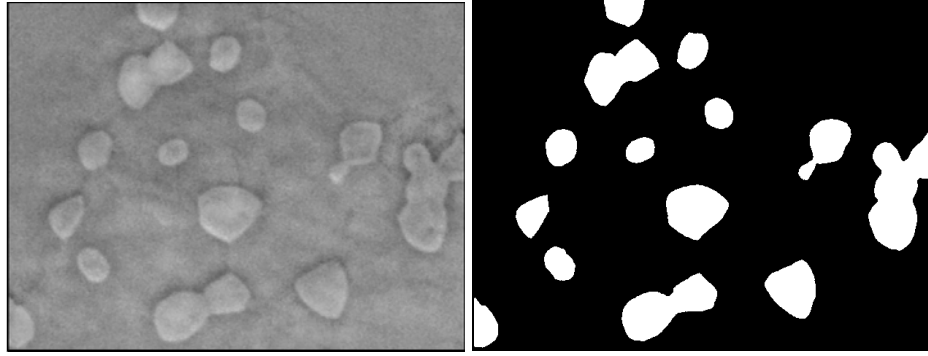
(c) 20 Days of Aging (Left: Gray-Scale; Right: Binary)



(d) 30 Days of Aging (Left: Gray-Scale; Right: Binary)



(e) 40 Days of Aging (Left: Gray-Scale; Right: Binary)



(f) 50 Days of Aging (Left: Gray-Scale; Right: Binary)

Figure 5.19 - Aging Induced Evolution of IMCs at 125 °C
(Aging Increment: 10 Days; WQ SAC305)

The analyzed area in Figure 5.13 had a digital image with a size of 33,600 pixels. Using the provided scale bar, this was equivalent to $76.2 \mu\text{m}^2$. Therefore, each pixel in the digital image was equivalent to 2268 nm^2 . Table 5.1 lists the determined values of number of IMCs, total area of all IMCs, average IMC particle area, average IMC particle diameter, and average IMC particle normalized diameter for RF SAC305 at each aging condition. The evolutions of the number of IMC particles and average IMC particle diameter with aging are shown graphically in Figure 5.20. Similar analysis was performed for WQ SAC305 and those parameters were quantified for each aging duration, as shown in Table 5.2 and Figure 5.21.

It has been found that the IMCs of WQ SAC305 are much finer than those of RF SAC305 at no aging condition, as their initial average particle diameters are 121 and 327 nm, respectively. However, the WQ microstructure suffered more changes due to aging. As shown in Figure 5.20, the number of IMC particles in the analyzed region decreased by over 50% from 40 to 19 during the 11 hours of aging for RF SAC305, while it decreased by over 80% from 81 to 14 for WQ SAC305 (Figure 5.21). The most dramatic changes of particle number occurred during the first few hours of aging for both microstructures, and then the changes became smaller. From Figure 5.20 and Figure 5.21, it has also been found that the average IMC particle

diameter increased by approximately 62% (327 to 530 nm) for RF SAC305 and about 227% (121 to 395 nm) for WQ SAC305 during the 11 hours of aging. For each microstructure, there was an increase in the total area of all IMC particles with aging, suggesting that IMC atoms from other regions had diffused into the region under consideration.

Similar quantitative analyses have also been performed for RF and WQ SAC305 that were aged at an increment of 1 day or 10 days, and the results are listed in Tables 5.3-5.6. Again, aging led to significant drop of number of IMCs and increase of average particle diameter, as graphically illustrated in Figures 5.22-5.25. For example, after aging for 50 days at 125 °C, the number of IMC particles dropped about 80% (93 to 19) and 97% (495 to 15) for RF SAC305 and WQ SAC305, respectively. Moreover, the average diameter of IMC particles increased by around 157% (307 to 789 nm) for RF SAC305 and 781% (167 to 1472 nm) for WQ SAC305 during the 50 days of aging.

Table 5.1 - Effects of Aging on IMC Particles at 125 °C
(Aging Increment: 1 Hour; RF SAC305)

Aging Time (Hours)	Number of IMCs	Total Area of All IMCs (um²)	Average Area of a Particle (nm²)	Average Particle Diameter (nm)	Normalized Diameter
0	40	3.35	83859	327	1.00
1	35	3.61	103097	362	1.11
2	33	3.67	111132	376	1.15
3	30	3.78	126025	401	1.22
4	26	3.71	142622	426	1.30
5	24	3.78	157343	448	1.37
6	23	3.95	171776	468	1.43
7	20	3.92	196182	500	1.53
8	20	4.11	205481	511	1.56
9	19	4.04	212476	520	1.59
10	19	4.07	214147	522	1.60
11	19	4.20	220832	530	1.62

Table 5.2 - Effects of Aging on IMC Particles at 125 °C
(Aging Increment: 1 Hour; WQ SAC305)

Aging Time (Hours)	Number of IMCs	Total Area of All IMCs (um²)	Average Area of a Particle (nm²)	Average Particle Diameter (nm)	Normalized Diameter
0	81	0.93	11461	121	1.00
1	40	1.04	26103	182	1.51
2	24	1.19	49411	251	2.08
3	22	1.29	58551	273	2.26
4	18	1.34	74297	308	2.55
5	16	1.35	84430	328	2.71
6	16	1.40	87405	334	2.76
7	16	1.43	89299	337	2.79
8	15	1.57	104593	365	3.02
9	14	1.65	117590	387	3.20
10	14	1.66	118788	389	3.22
11	14	1.72	122768	395	3.27

Table 5.3 - Effects of Aging on IMC Particles at 125 °C
(Aging Increment: 1 Day; RF SAC305)

Aging Time (Days)	Number of IMCs	Total Area of All IMCs (um²)	Average Area of a Particle (nm²)	Average Particle Diameter (nm)	Normalized Diameter
0	110	10.51	95590	349	1.00
1	50	11.04	220815	530	1.52
2	39	8.91	228357	539	1.55
3	37	9.25	249927	564	1.62
4	34	9.13	268463	585	1.68

Table 5.4 - Effects of Aging on IMC Particles at 125 °C
(Aging Increment: 1 Day; WQ SAC305)

Aging Time (Days)	Number of IMCs	Total Area of All IMCs (um²)	Average Area of a Particle (nm²)	Average Particle Diameter (nm)	Normalized Diameter
0	393	8.10	20608	162	1.00
1	84	18.15	216046	524	3.24
2	64	18.93	295800	614	3.79
3	54	18.11	335380	653	4.03
4	28	22.46	802264	1011	6.24

Table 5.5 - Effects of Aging on IMC Particles at 125 °C
(Aging Increment: 10 Days; RF SAC305)

Aging Time (Days)	Number of IMCs	Total Area of All IMCs (um ²)	Average Area of a Particle (nm ²)	Average Particle Diameter (nm)	Normalized Diameter
0	93	6.90	74187	307	1.00
10	36	11.60	322135	640	2.09
20	35	11.42	326161	644	2.10
30	27	10.53	390001	705	2.30
40	25	9.94	397678	712	2.32
50	19	9.30	489520	789	2.57

Table 5.6 - Effects of Aging on IMC Particles at 125 °C
(Aging Increment: 10 Days; WQ SAC305)

Aging Time (Days)	Number of IMCs	Total Area of All IMCs (um ²)	Average Area of a Particle (nm ²)	Average Particle Diameter (nm)	Normalized Diameter
0	495	10.89	21993	167	1.00
10	27	23.13	856824	1044	6.24
20	26	22.69	872612	1054	6.30
30	20	24.51	1225690	1249	7.47
40	19	24.34	1281173	1277	7.63
50	14	23.84	1702604	1472	8.80

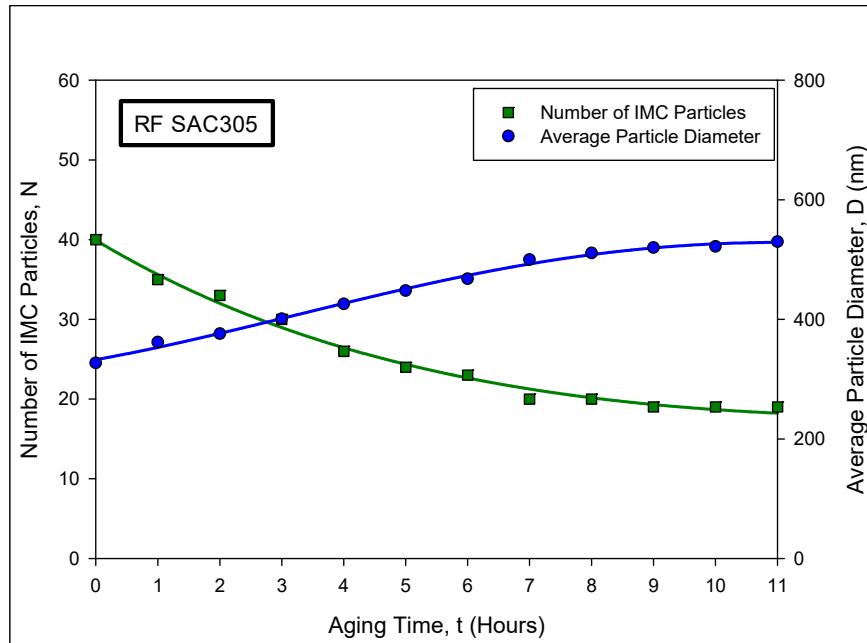


Figure 5.20 - Variation of Number and Average Diameter of IMC Particles with Aging Time at 125 °C (Aging Increment: 1 Hour, RF SAC305)

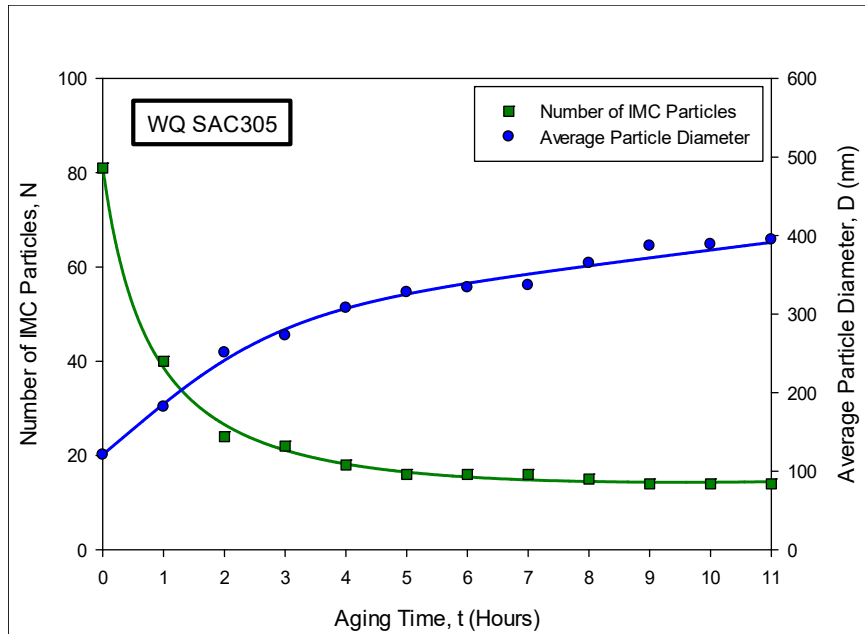


Figure 5.21 - Variation of Number and Average Diameter of IMC Particles with Aging Time at 125 °C (Aging Increment: 1 Hour, WQ SAC305)

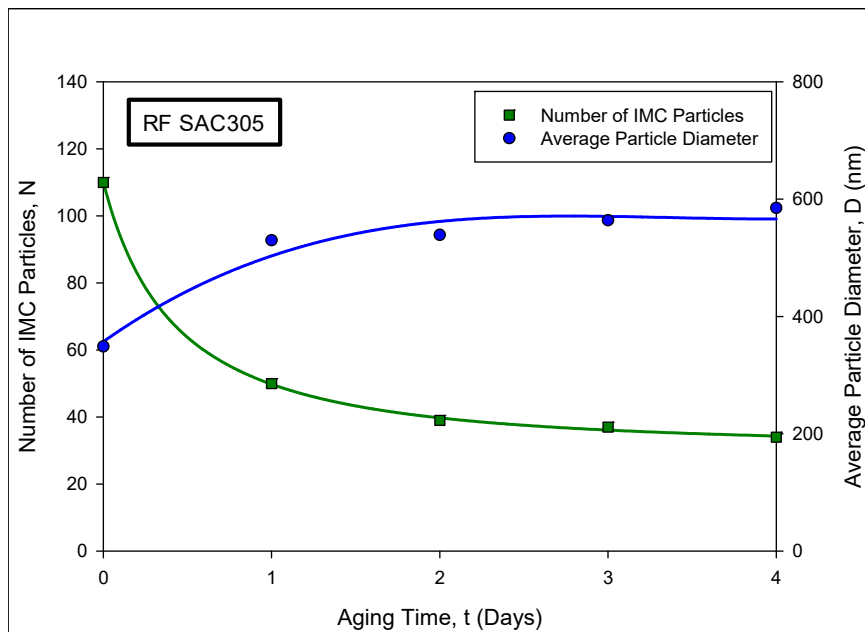


Figure 5.22 - Variation of Number and Average Diameter of IMC Particles with Aging Time at 125 °C (Aging Increment: 1 Day, RF SAC305)

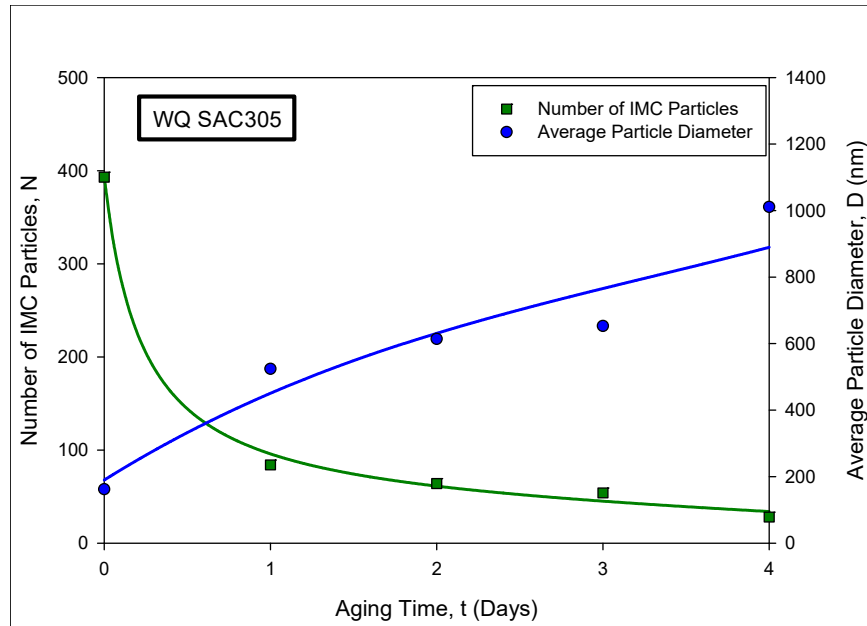


Figure 5.23 - Variation of Number and Average Diameter of IMC Particles with Aging Time at 125 °C (Aging Increment: 1 Day, WQ SAC305)

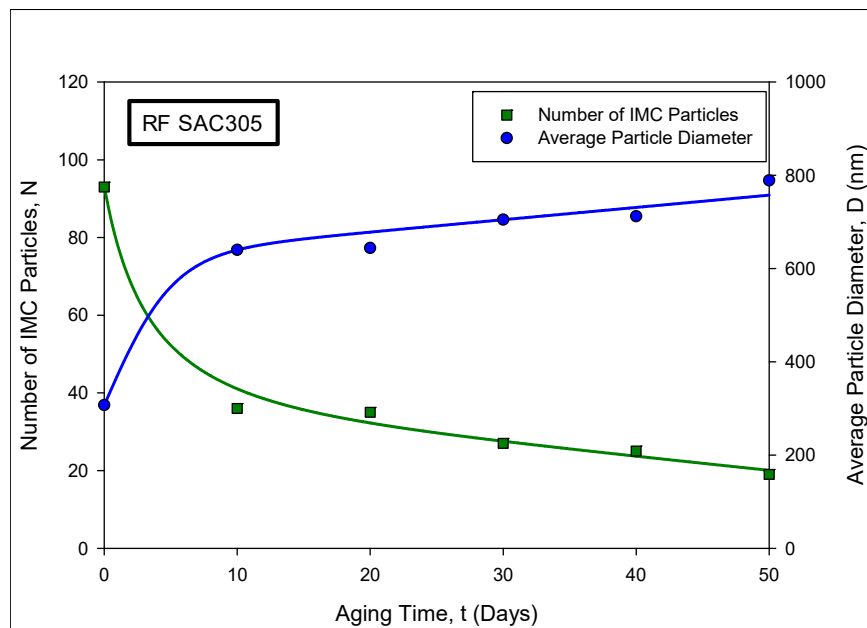


Figure 5.24 - Variation of Number and Average Diameter of IMC Particles with Aging Time at 125 °C (Aging Increment: 10 Days, RF SAC305)

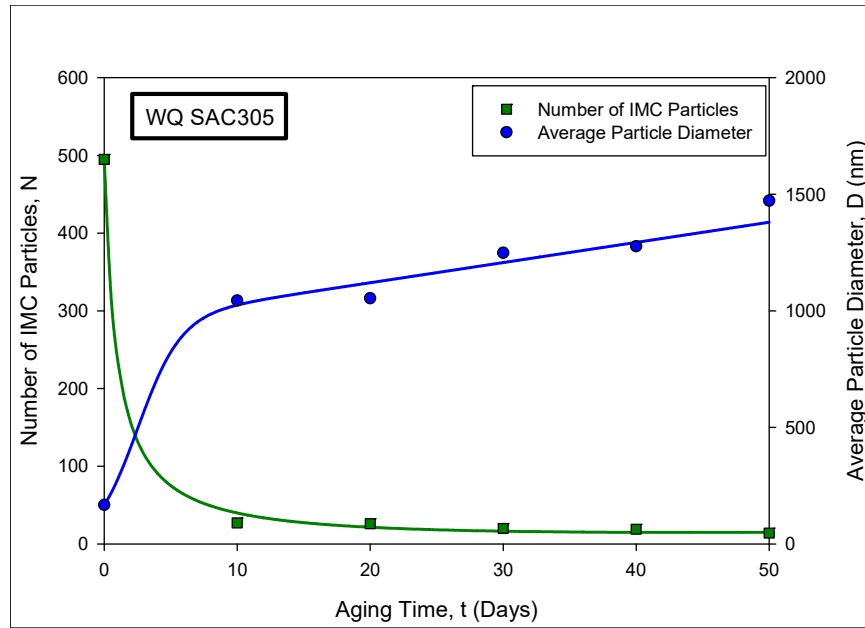


Figure 5.25 - Variation of Number and Average Diameter of IMC Particles with Aging Time at 125 °C (Aging Increment: 10 Days, WQ SAC305)

5.6 Summary and Discussion

In this investigation, Scanning Electron Microscopy (SEM) has been utilized to examine aging induced microstructural changes occurring within lead free solders. Unlike many prior studies, fixed regions in the solder joint cross-sections were monitored throughout the aging process, rather than examining different samples and/or different regions after the various aging exposures. Nanoindentation marks were added to the cross-sections at certain locations to facilitate locating the fixed regions of interest. Three aging increments (1 hour, 1 day and 10 days) and two solidification profiles (RF and WQ) have been examined. After preparation of suitable cross-sectional samples, the samples were then aged at $T = 125\text{ }^{\circ}\text{C}$, and the microstructures were observed and recorded in the selected regions after various aging exposures using SEM. With this approach, time-lapse imagery of the microstructure evolution in a particular region of a solder joint has been recorded as a function of the aging time.

Using the recorded images, migration, coalescence, and coarsening of intermetallic compounds were visualized. It has been found that the number of IMC particles decreased, while the average size of the particles and average particle separation distance increased significantly with aging. The early aging period features the most rapid and dramatic changes in microstructure. Compared with RF SAC305, WQ SAC305 had much finer initial IMC particles but they coarsened to a greater degree during isothermal aging. For small aging times up to 11 hours at $T = 125\text{ }^{\circ}\text{C}$, experimentally recorded movies of microstructural evolution during aging have been made to visualize those aging phenomena.

Additionally, the coarsening of IMC particles in fixed regions during aging has been quantitatively analyzed. Particularly, the aging induced evolutions of number of IMCs, total area of all IMCs, average particle area, and average particle diameter have been quantified. For instance, during the first 11 hours of aging at $125\text{ }^{\circ}\text{C}$, the average IMC particle diameter increased by approximately 62% for RF SAC305 and 227% for WQ SAC305. After 50 days of aging, the average diameter increased by around 157% and 781% for RF SAC305 and WQ SAC305, respectively.

CHAPTER 6

EVOLUTION OF SOLDER MECHANICAL BEHAVIOR AND MICROSTRUCTURE DURING FATIGUE TESTING

6.1 Introduction

While it has been known that the reversal of inelastic strain can change the stress-strain behavior of materials (Bauschinger effect), there have been very few prior studies on how the cycling changes the microstructure and degrades the mechanical properties of lead free solders during fatigue testing. In this chapter, we have explored the effects of mechanical cycling on the microstructure and constitutive behavior (stress-strain and creep) of RF SAC305 lead free solder in fatigue testing. At the same time, the evolution of the cyclic stress-strain behavior (hysteresis loop area, plastic strain range, and peak stress) during the cycling tests has been studied. Cylindrical uniaxial SAC305 lead free solder test specimens have been prepared. The uniaxial specimens had a nominal diameter of 1.2 mm, and the gage length was 5 mm in this work. All the tests were conducted at room temperature (25 °C) at a strain rate of $\dot{\epsilon} = 0.002 \text{ sec}^{-1}$. Strain-controlled method has been used in the cyclic testing, and the cyclic strain limits were ± 0.01 .

To study the evolution of the cyclic stress-strain behavior, the specimens have been subjected to cyclic stress/strain loading at room temperature (25 °C) until fatigue failure. The cyclic stress-strain curves at after various durations of cycling have been examined. From the recorded cyclic stress-strain curves, the evolution of the solder hysteresis loops with number of

cycles has been characterized. Also, the duration of cycling on the hysteresis loop area (plastic strain energy density), plastic strain range, and peak load have been studied.

To study the effects of cycling on the constitutive behavior and microstructure of RF SAC305, uniaxial samples with various durations of prior mechanical cycling have been prepared. The cycled samples were then subjected to stress-strain or creep testing, or cross-sectioned and studied using SEM and polarized light microscope. After fitting the experimental data from mechanical testing, we have been able to characterize the cycling induced evolution of several mechanical properties of RF SAC305 lead free solder. These have been correlated with the observed changes in microstructure that occurred during the cycling. The goal of the study is to explore damage accumulation that occurs during fatigue testing.

6.2 Evolution of Cyclic Stress-Strain Behavior During Fatigue Testing

To study the evolution of the cyclic stress-strain behavior with cycling, the specimens have been subjected to cyclic strain loading (± 0.01) at room temperature until fatigue failure occurred. The cyclic stress-strain curves at after various durations of cycling have been examined. Prior to the study of cycling induced evolution, fatigue testing has been done on the SAC305 test specimens under the same test conditions. As shown in Figure 6.1, the descending peak stress curve with cycles can be divided into three stages: transient stage, steady state stage and tertiary stage. The tertiary stage shows an accelerated decline in peak stress leading to the failure. Fatigue life (cycles to failure) was defined to be the point in the cyclic test where a 50% load drop occurred. Five specimens were tested and the average fatigue life was determined as 1228 (± 76) cycles. Accordingly, the cyclic stress-strain behavior (hysteresis loop area, plastic strain range, and peak stress) was studied at after cycling for 1, 10, 50, 100, 200, 300, 400, 500, 600, 700, 800, 900, 1000, 1100, 1200 cycles, respectively.

The four-parameter hyperbolic tangent empirical model (Eq. (2.7)) has been used to fit the entire cyclic stress-strain curve at each chosen increment of cycling. From the recorded cyclic stress-strain curves, the evolution of the solder hysteresis loops with number of cycles has been characterized during a typical fatigue test, see Figure 6.2. From Figure 6.2, most significant changes of the loop occurred within the first 100 cycles, and then the loop went to a steady state. In addition, hysteresis loop area, plastic strain range, and peak load have been determined at after each cycling duration. The first two parameters are usually considered as the fatigue damage driving force that causes fatigue damage, and they are widely used in the models to predict fatigue life of solders. Table 6.1 shows the determined values of the three parameters at after each cycling duration. The cycling induced evolutions of loop area, plastic strain range and peak stress before fatigue failure are shown in Figures 6.3, 6.4, and 6.5, respectively. It is clear that loop area and peak stress were decreasing as the strain controlled cycling progressed, while plastic strain range remained stable with cycling.

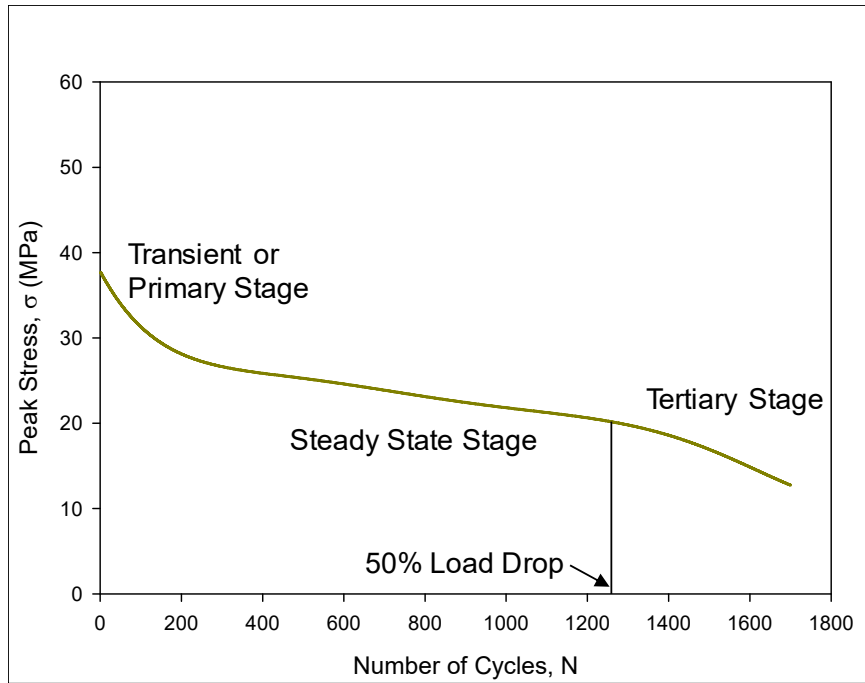


Figure 6.1 - Typical Uniaxial Fatigue Test

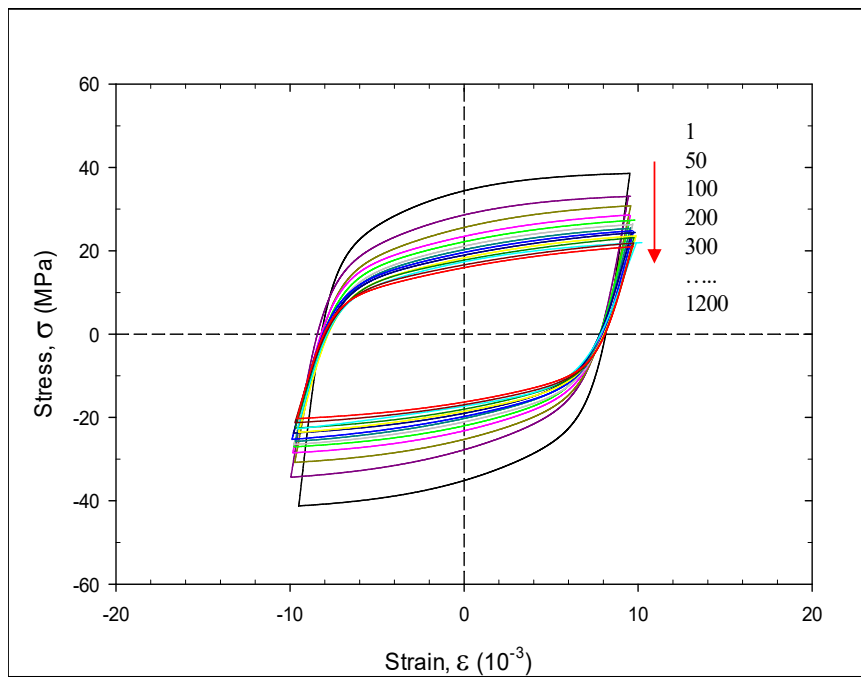


Figure 6.2 - Cycling Induced Evolution of Hysteresis Loop

Table 6.1 - Cycling Induced Changes of Loop Area, Plastic Strain Range, and Peak Stress

Cycling Duration (Cycles)	Loop Area (MJ/m ³)	Plastic Strain Range	Peak Stress (MPa)
1	1.1605	1.65%	38.65
10	1.0456	1.60%	38.08
50	0.8832	1.63%	33.18
100	0.8041	1.61%	30.62
200	0.7432	1.62%	28.52
300	0.7087	1.59%	27.28
400	0.6651	1.59%	26.55
500	0.6345	1.58%	25.55
600	0.6166	1.59%	24.71
700	0.5955	1.60%	24.14
800	0.5835	1.60%	23.71
900	0.5700	1.61%	23.10
1000	0.5565	1.60%	21.97
1100	0.5413	1.60%	21.55
1200	0.5141	1.61%	20.18

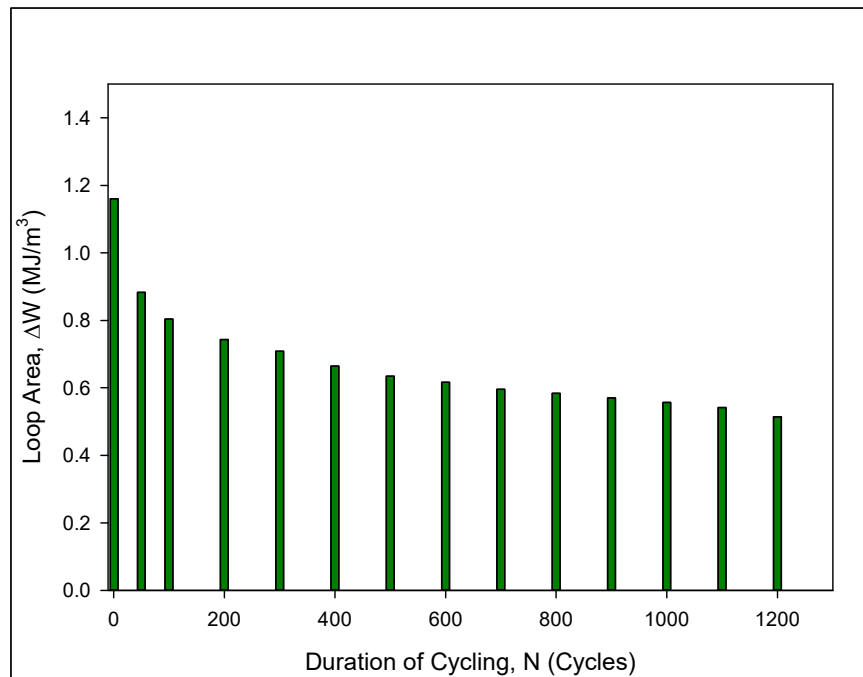


Figure 6.3 - Variation of Loop Area with Cycling

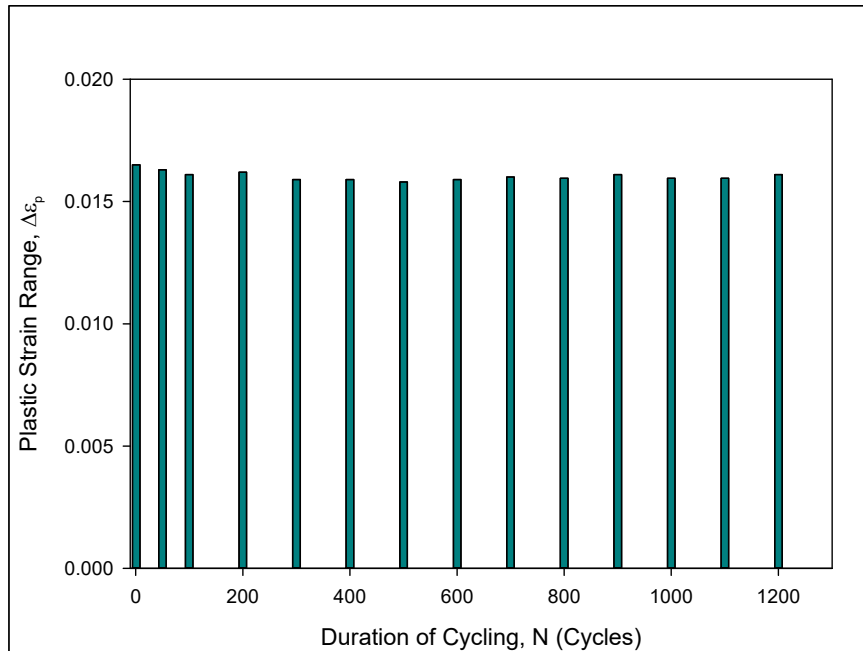


Figure 6.4 - Variation of Plastic Strain Range with Cycling

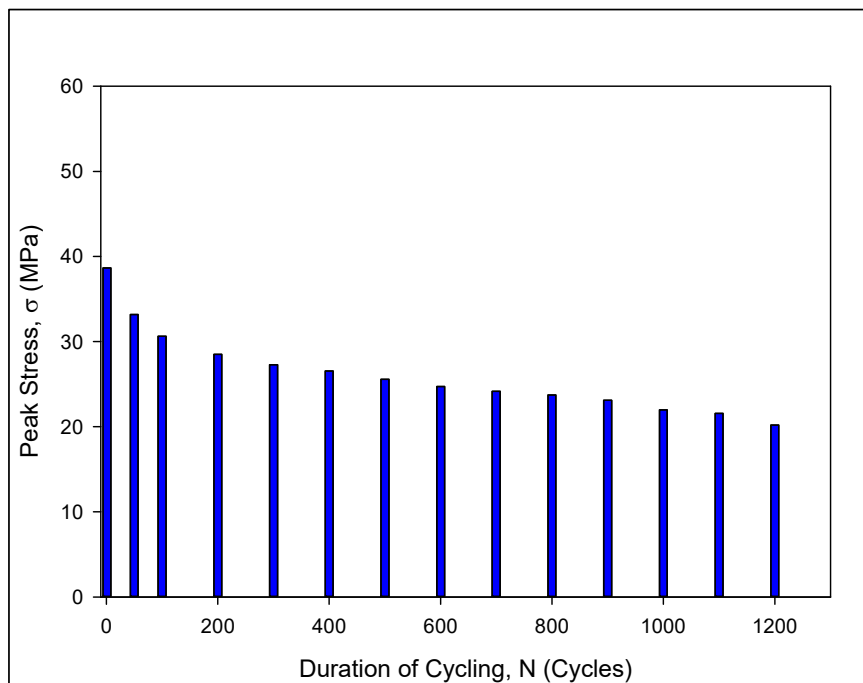


Figure 6.5 - Variation of Peak Stress with Cycling

6.3 Evolution of Constitutive Behavior During Fatigue Testing

The effects of mechanical cycling on the constitutive behavior (stress-strain and creep) of RF SAC305 have also been studied. Uniaxial test specimens with various durations of prior mechanical cycling have been prepared. The examined durations of mechanical cycling were 0 (no cycling), 50, 100, 300, 600, 900 and 1200 cycles, which correspond to 0%, 4%, 8%, 24%, 49%, 73% and 98% of the fatigue life of SAC305 test specimens. The cycled samples were then subjected to stress-strain or creep testing under the same test conditions. In the solder creep experiments, the applied stress was 15 MPa for all the tests. After fitting the experimental data, we have been able to characterize the cycling induced evolutions of several mechanical properties, such as elastic modulus, yield strength, ultimate strength, and creep strain rate.

Figure 6.6 illustrates the plots of stress-strain curve at each chosen increment of cycling. With increased cycling, both the initial slope and height of the stress-strain curve were decreasing, which indicates fatigue damage was accumulating with cycling. Particularly, the stress-strain behavior of SAC305 solder changed dramatically after 1200 cycles of cycling when the fatigue failure occurred. For each cycling duration, solder mechanical properties extracted from the stress-strain curve are listed in Table 6.2. It has been found that increased cycling led to a continuous drop in elastic modulus, ultimate tensile strength and yield stress. Compared with non-cycled test specimens, the degradations on elastic modulus, ultimate strength and yield stress are 61.61%, 38.87% and 43.91%, respectively, for the specimens pre-cycled for 1200 cycles. In other words, mechanical properties of the lead free solder samples degraded a lot from no cycling to fatigue failure during the cyclic testing. Similar effects of mechanical cycling have been found on the solder creep behavior. Figure 6.7 illustrates the cycling induced evolution of creep curve and Table 6.3 shows the secondary strain rate at after each duration of cycling. It is

clear that fatigue cycling changed solder creep behavior significantly. The secondary strain rate of solder samples increased as the cycling progressed, especially after cycling the specimens for 600 cycles or more. The creep rate increased by a factor of 46 when the fatigue failure occurred. Each curve in Figure 6.6 and Figure 6.7 is the typical curve that represents the results from three tests, and the mechanical properties listed in Table 6.2 and Table 6.3 were extracted from the typical curves. In addition, longer cycling duration results in larger scatter of results, as the variation between specimens becomes greater with increased cycling. For example, the standard deviation of elastic modulus is 2.14 GPa for the non-cycled samples, while it is 4.17 GPa for the samples with 1200 cycles of pre-cycling.

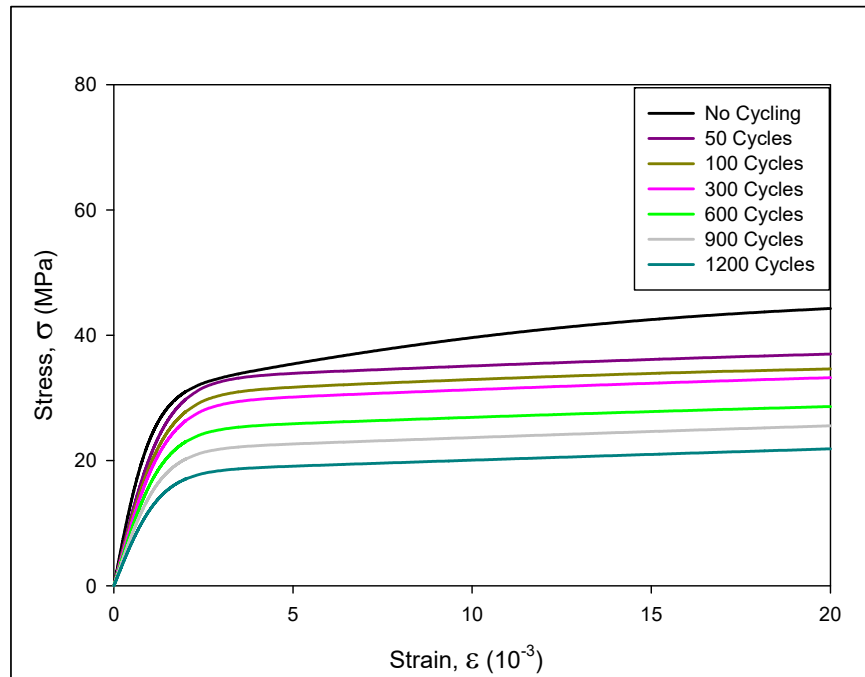


Figure 6.6 - Cycling Induced Evolution of Stress-Strain Curve

Table 6.2 - Cycling Induced Changes of Mechanical Properties

Cycling Duration (Cycles)	Elastic Modulus (GPa)	Ultimate Tensile Strength (MPa)	Yield Stress (MPa)
0	37.72	48.19	33.09
50	30.35	40.23	32.95
100	23.89	38.22	31.77
300	21.89	37.15	29.23
600	19.06	32.12	25.18
900	18.88	31.03	22.04
1200	14.48	29.46	18.56

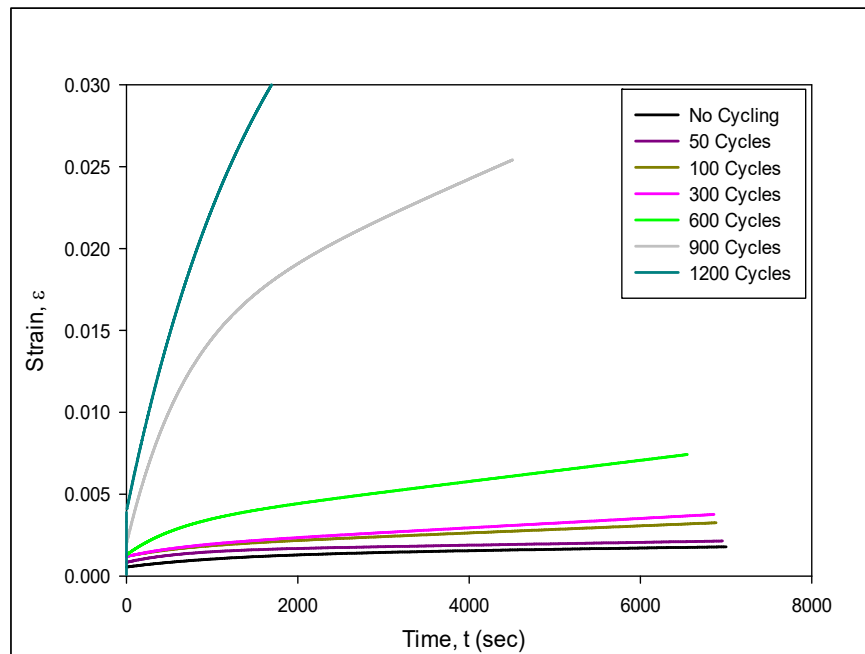


Figure 6.7 - Cycling Induced Evolution of Creep Curve

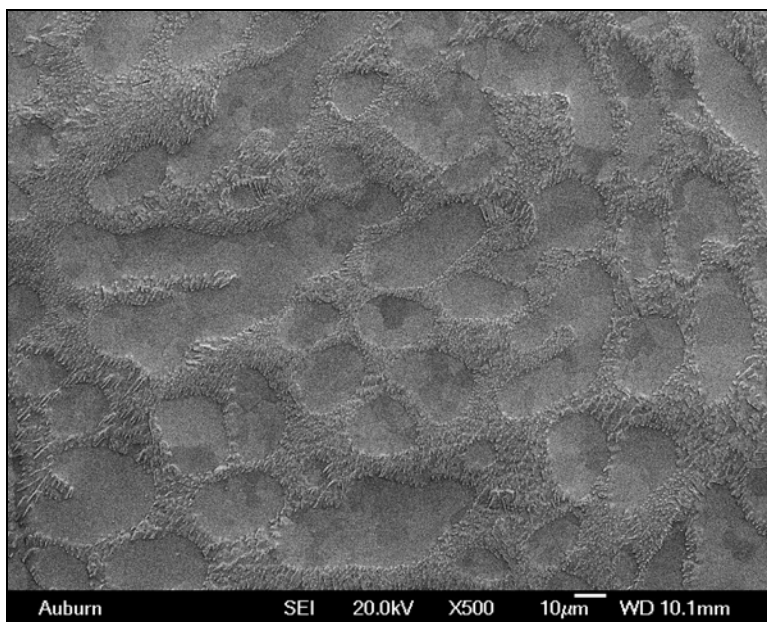
Table 6.3 - Cycling Induced Changes of Creep Strain Rate

Cycling Duration (Cycles)	Secondary Strain Rate ($\times 10^{-8} \text{ sec}^{-1}$)
0	7.14
50	8.61
100	21.6
300	28.5
600	64.5
900	227
1200	335

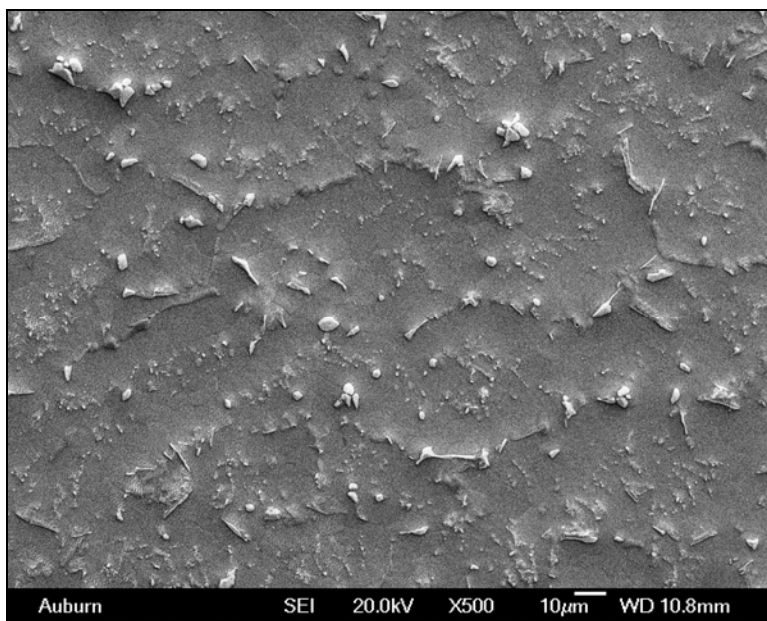
6.4 Effects of Fatigue Cycling on Solder Microstructure

6.4.1 Cycling on IMCs and Dendrite Structure

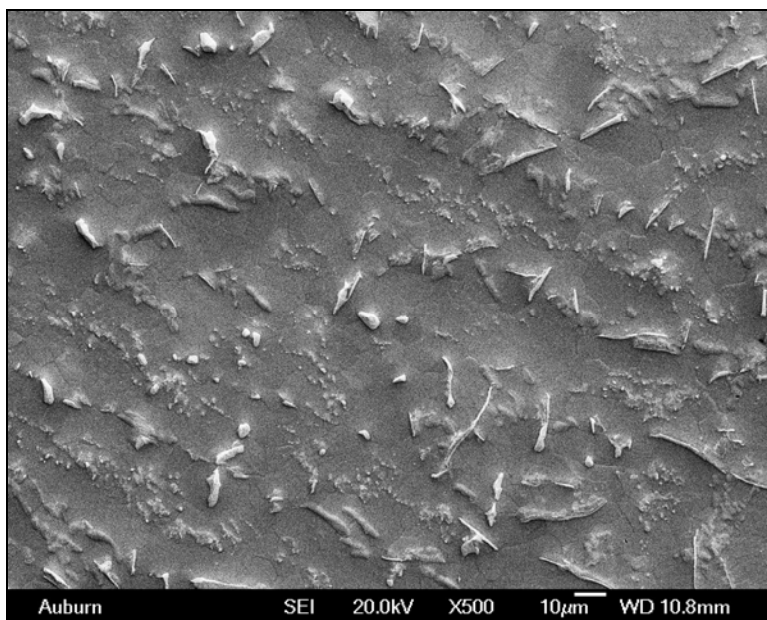
SEM has been used to study the changes of microstructural features like IMCs and dendrite structure during fatigue testing. Typically, β -Sn is surrounded by Ag_3Sn and Cu_6Sn_5 IMC particles in the pristine (non-cycled) microstructure. This kind of dendrite structure contributes to pinning and blocking movement of dislocations. Figure 6.8 illustrates the microstructural evolution of SAC305 during fatigue testing. To observe the overall structure clearly, a relatively lower magnification was chosen. Each SEM micrograph represents the typical microstructure at after particular duration of cycling. It is clear that the microstructure changed significantly with fatigue cycling, and the most dramatic changes occurred within the first 50 cycles of cycling. In particular, cycling led to the weakening and disappearance of dendrite structure, and the coarsening of IMC particles (especially the formation and growth of large needle-shaped IMCs). Initially, the major changes were the weakening of dendrite structure and the transition of IMCs from fine particles to large sticks. With increased fatigue cycling, the dendrite structure gradually disappeared and the large needle-shaped IMCs continued to grow. In addition, elemental mapping analysis has been done to analyze the large needle-shaped IMCs. In Figure 6.9, each element has its own color, for example, tin is green, silver is blue and copper is yellow. It is clear that the large needle-shaped IMCs consist of tin and silver, and it is a result of the coalescence of initial fine Ag_3Sn IMC particles.



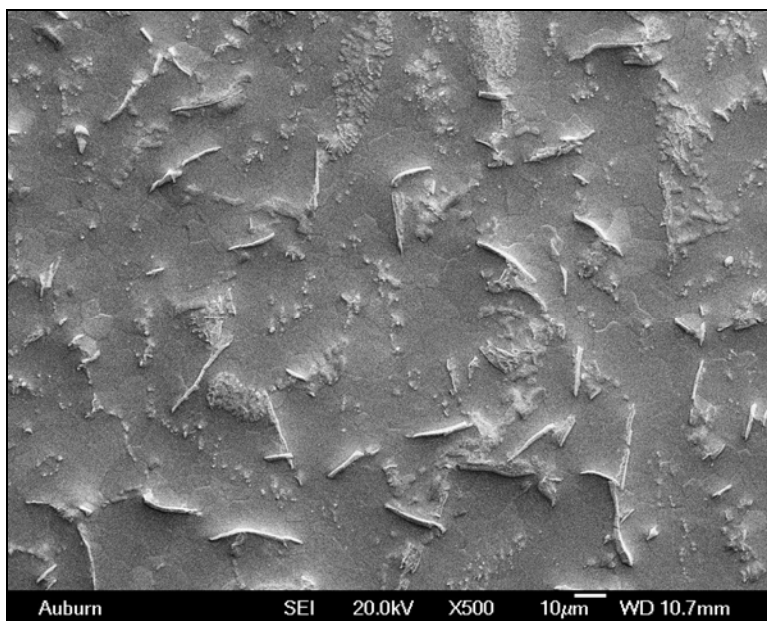
(a) No Cycling



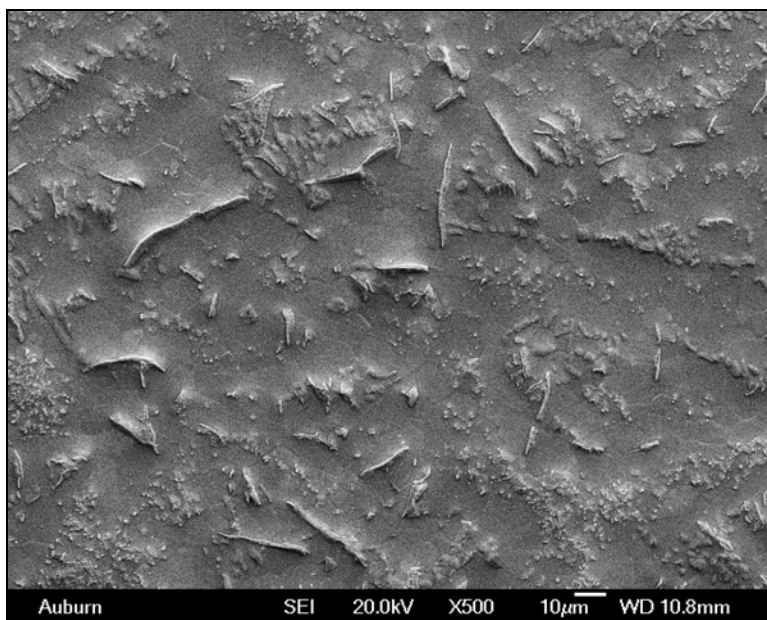
(b) Cycled for 50 Cycles



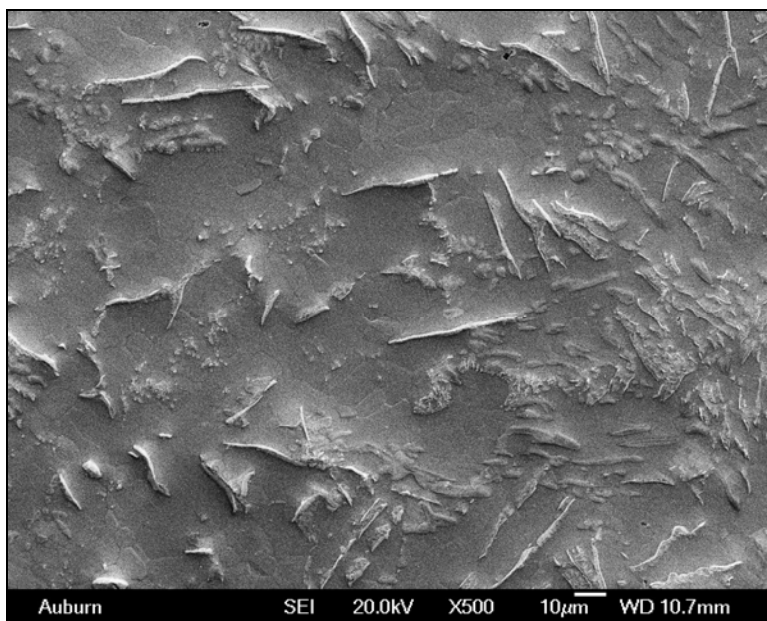
(c) Cycled for 100 Cycles



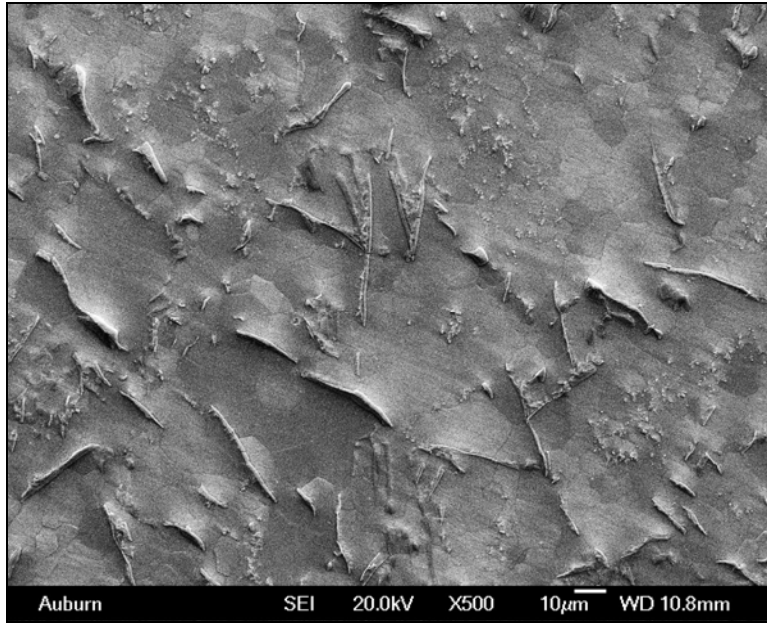
(d) Cycled for 300 Cycles



(e) Cycled for 600 Cycles



(f) Cycled for 900 Cycles



(g) Cycled for 1200 Cycles

Figure 6.8 - Microstructural Evolution of RF SAC305 During Fatigue Testing (500X)

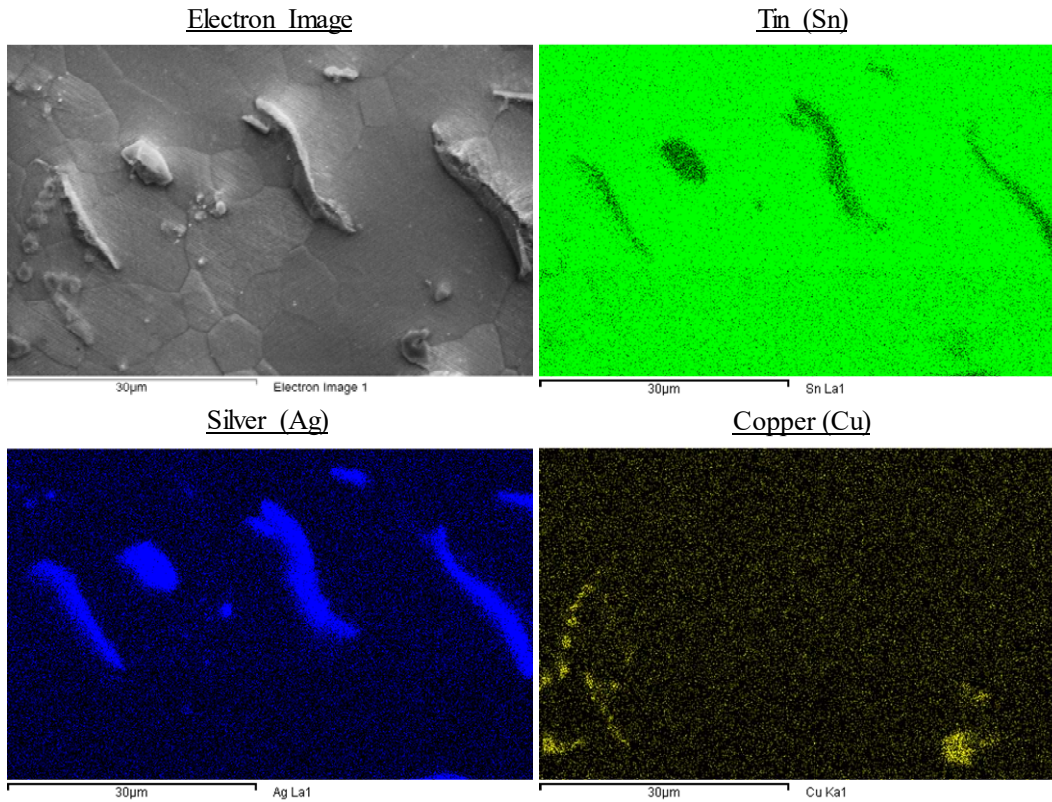
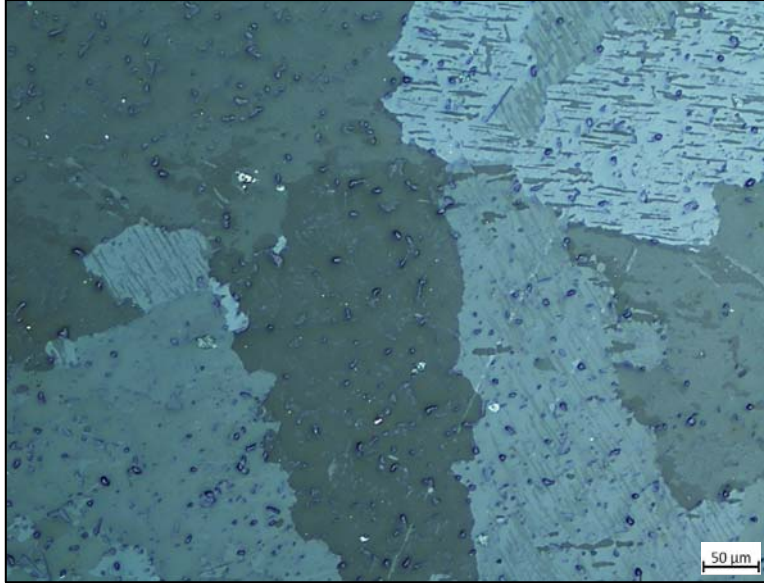


Figure 6.9 - Elemental Mapping of Cycled Microstructure

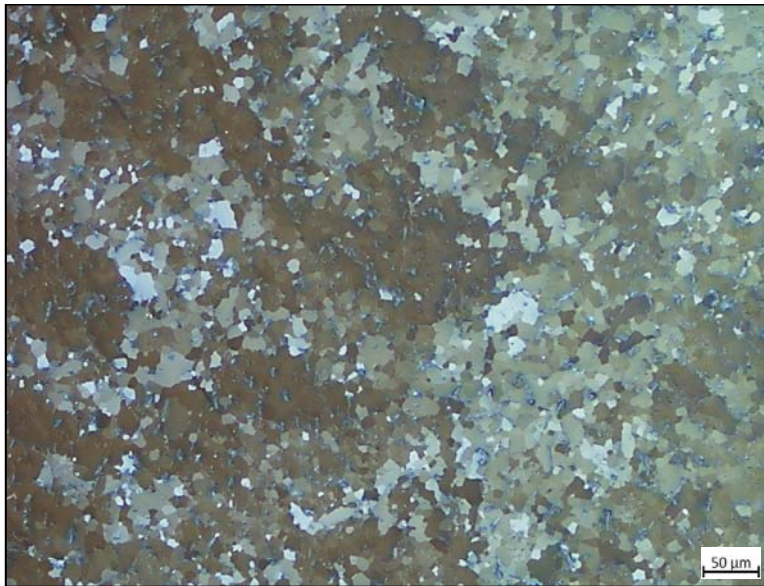
6.4.2 Recrystallization of Sn Grains

Recrystallization is the formation of a new grain structure by the formation and migration of grain boundaries with misorientation angle greater than $10-15^\circ$, which is driven by the stored deformation energy [126]. Polarized light microscope was utilized to explore the recrystallization of Sn grains that occurred during fatigue testing in this work. Figure 6.10 shows the polarized light images of the microstructures at after being cycled for 0, 50, 100, 300, 600, 900, and 1200 cycles. Again, a typical image of the microstructure was chosen for each cycling condition in Figure 6.10.

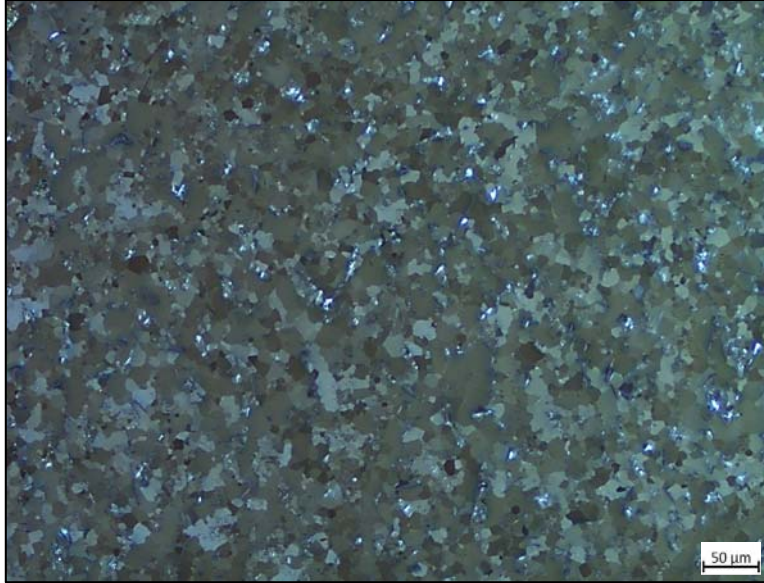
Figure 6.10(a) shows a typical polarized light image of non-cycled RF SAC305 microstructure, which consists of several grains with clear grain boundaries. It has been observed that fatigue cycling led to grain recrystallization, and the large grains were replaced by lots of newly formed small grains in the recrystallized regions. Similar to the SEM results, the most significant changes occurred during the first 50 cycles of cycling (Figure 6.10(b)). After 50 cycles, the grain boundaries weakened a lot, and many small grains formed in this region. With increased cycling, the initial boundaries of large grains disappeared and the small grains became more uniform in the recrystallized region (Figure 6.10(c)-(g)). Also, the small recrystallized grains appeared to grow up after a long time of cycling, which has also been found in [125, 131, 132]. According to [132], the growth of recrystallized grains is a result of the coalescence of neighboring grains to lower the stored energy.



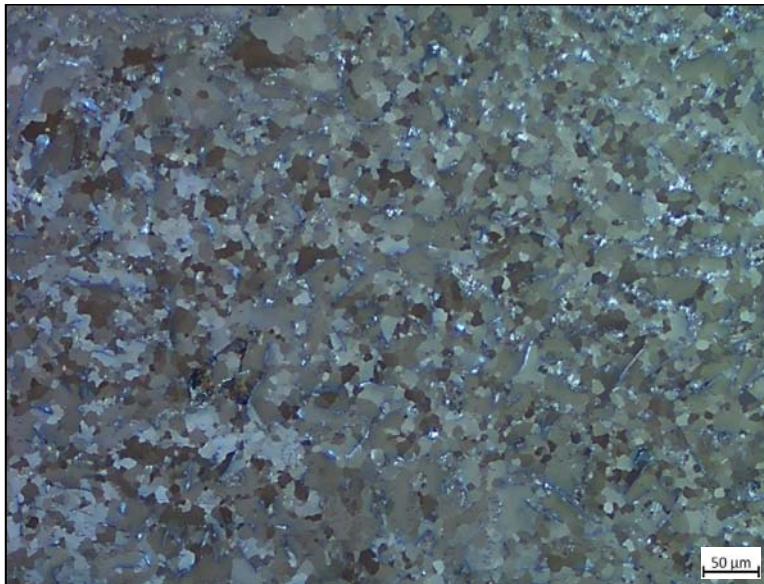
(a) No Cycling



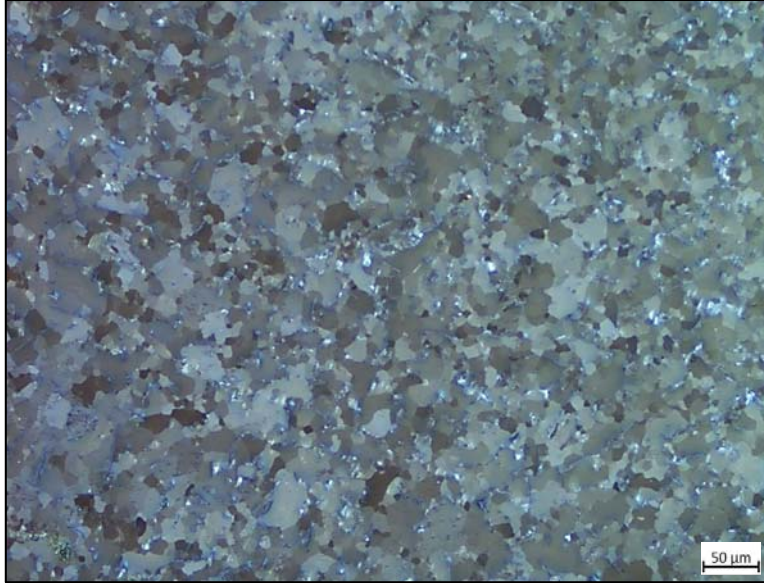
(b) Cycled for 50 Cycles



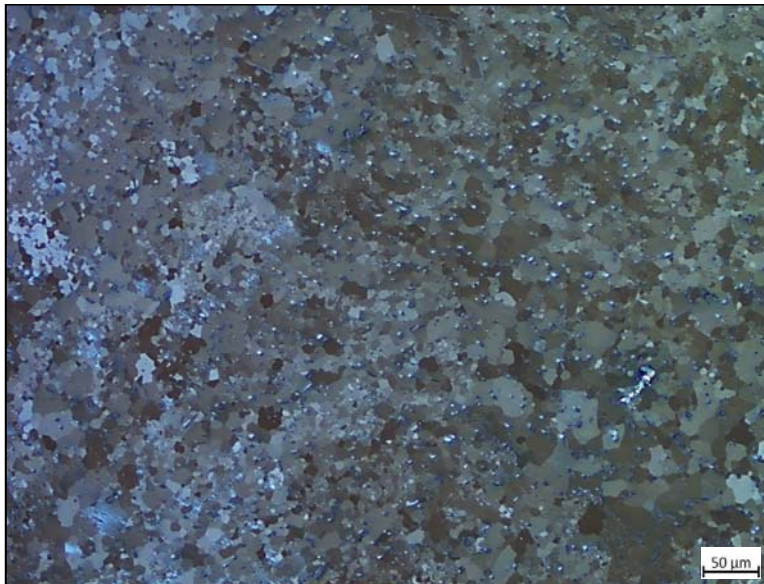
(c) Cycled for 100 Cycles



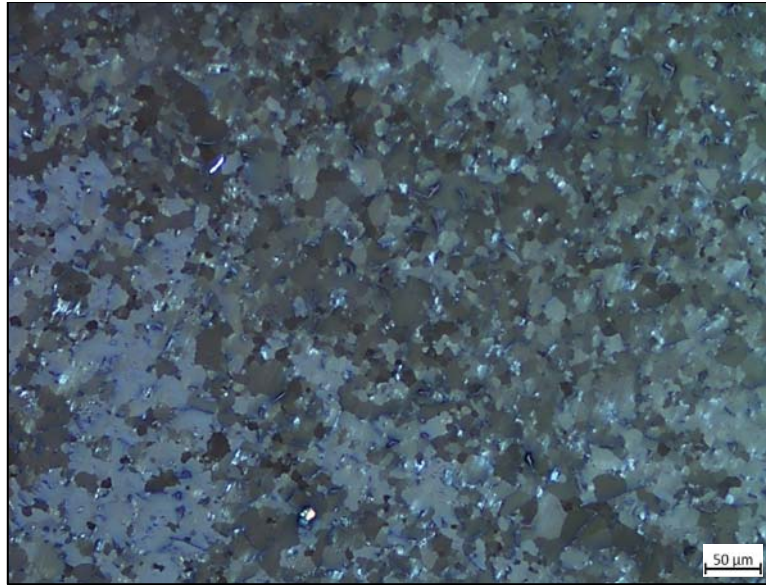
(d) Cycled for 300 Cycles



(e) Cycled for 600 Cycles



(f) Cycled for 900 Cycles



(g) Cycled for 1200 Cycles

Figure 6.10 - Evolution of Sn Grains During Fatigue Testing Using Polarized Light Microscope

6.4.3 Fatigue Cracks

Polarized light microscope has also been used to investigate the initiation and propagation of cracks during fatigue testing. It has been found that cracks can be observed in recrystallized regions after 600 fatigue cycles, and then the number and size of cracks continued to increase with cycling. Figure 6.11 shows both the polarized light and optical images of the cycled microstructure at the same region where fatigue cracks were found. This sample was pre-cycled for 1200 cycles, when the fatigue failure occurred. This recrystallized region contains four visible cracks in different size. Crack 1 is the smallest one, followed by cracks 2, 3 and 4, as shown in the optical image in Figure 6.11. All the four cracks were found to be along grain boundaries. In addition, this observation also applies to most of examined cracks in other regions. Therefore, it is reasonable to conclude that fatigue cracks initiated at the boundaries of newly formed grains in recrystallized regions, and then propagated along those boundaries.

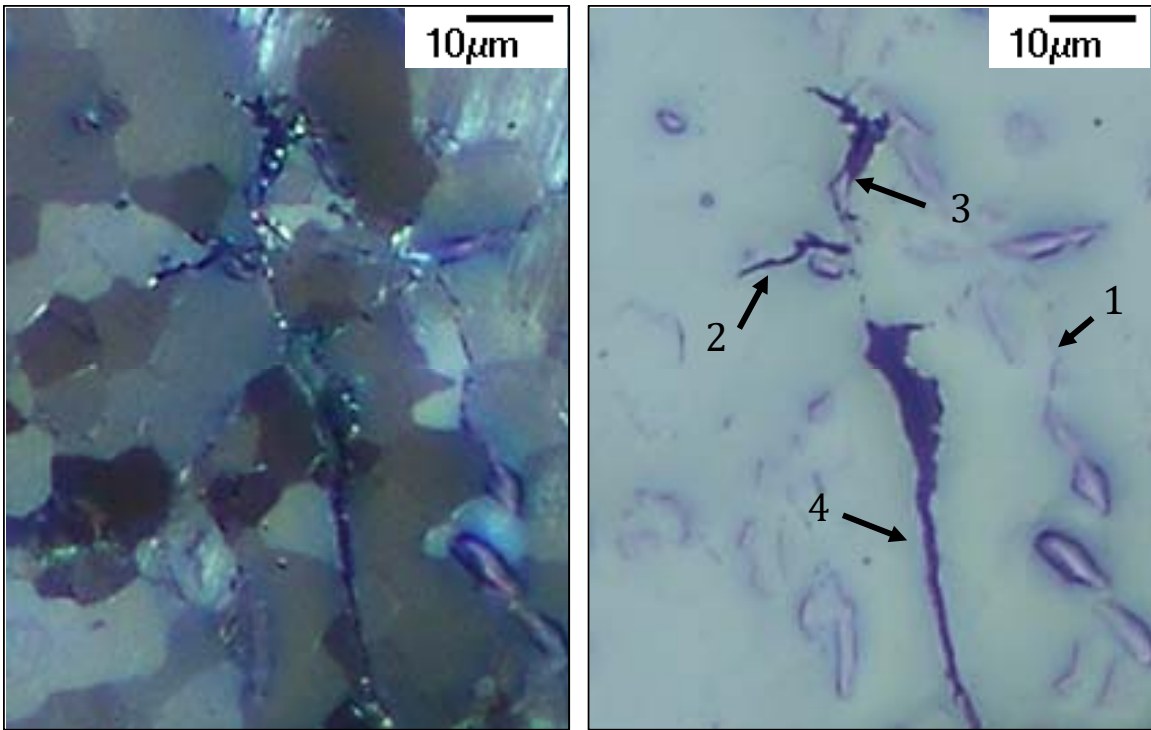


Figure 6.11 - Fatigue Cracks in the Microstructure that Cycled for 1200 Cycles (Right: Polarized Light Image; Left: Optical Image)

6.5 Summary and Discussion

To better understand the damage accumulation during fatigue testing, we have studied cycling induced evolution of mechanical behavior of RF SAC305 lead free solder. Particularly, the evolutions of cyclic stress-strain curve, stress-strain curve and creep curve have been characterized and quantified. With increased mechanical cycling, damage accumulated in the specimen and its various mechanical properties degraded. These have been correlated with the observed microstructural changes caused by fatigue cycling. SEM and polarized light microscope have been utilized to examine the changes that occurred for each cycling condition. It has been found that the initial damage caused by fatigue cycling was the weakening of dendrite structure, coarsening of IMCs (formation of large needle-shaped IMCs), and recrystallization of Sn grains. With increased cycling, the major changes were the disappearance of dendrite

structure, the growth of those large needle-shaped IMCs, and the growth of newly formed small grains. Also, fatigue cracks tended to form at the boundaries of newly formed grains in recrystallized regions, and then propagate along those boundaries.

CHAPTER 7

ESTABLISH BETTER CAPABILITY FOR FATIGUE TESTING IN OUR LABORATORY

7.1 Introduction

The MT-210 tension/torsion thermo-mechanical test system has been used to perform the cyclic stress-strain testing in this work. This test system has also been utilized to perform tensile and creep testing by other fellow graduate students. However, this machine has been in use for nearly twenty years and often in high demand, and it will reach the end of its lifetime eventually. In addition, load capacity of the machine in the uniaxial testing direction is 50 lb. (222 N) that makes it not suitable to test “large specimens”, such as the cylindrical specimens in diameter of 2 mm. Therefore, it is necessary to improve the capability for fatigue testing or other testing in our laboratory.

There are two practical ways to establish better testing capability in the lab. One is to take advantage of the Instron 5948 universal tester that placed in our lab, but gripping fixtures need to be designed and manufactured in order to test the specimens in our application. Another way is to design and build a new tester based on the current MT-210 microtester, which involves selection of several parts, design of fixtures, programming, etc. We have been working on both of them the same time to reach the goal.

7.2 Current MT-210 Microtester

As briefly described in Chapter 2.3, the MT-210 tension/torsion thermo-mechanical test system (Figure 2.6) from Wisdom Technology, Inc., has been used to perform the tests in this study. The system provides an axial displacement resolution of 0.1 micron and a rotation resolution of 0.001°. Testing can be performed in tension, shear, torsion, bending, and in combinations of these loadings, on small specimens such as thin films, solder joints, gold wire, fibers, etc. The minimum test speed is 0.1 $\mu\text{m/s}$, while the maximum travel distance is 103 mm. Cyclic (fatigue) testing can also be performed at frequencies up to 5 Hz. In addition, a universal 6-axis load cell was utilized to simultaneously monitor three forces and three moments/torques during sample mounting and testing. Environmental chambers added to the system allow samples to be tested over a temperature range of -185 to +300 °C. In addition, to grip and test the cylindrical specimens in this work, fixtures with V-shaped groove were designed and added to the test system, as shown in Figure 2.7 and Figure 2.8.

Table 7.1 lists the major parts of the current MT-210 tester, and several of them have been obsolete for many years. An introduction to the load cell and linear motor has been given below.

Table 7.1 - Major Parts of the MT-210 Tester

Parts	Brand	Part #	Obsolete	Close Part #
Load Cell Sensor	JR3	67M25A-I40 25L65	No	–
Load Cell Receiver	JR3	P/N 15003	No	–
Linear Motor	Anorad	LCK-S-2-P	Yes	LC-075-200
Encoder System	Anorad	MERS 50 (800319 E00Z10);	Yes	–
Servo Controller	Anorad	D-SERV-DLM1	Yes	–
Rotation Stage	Newport	URM80CCHL	Yes	URS100; URS75

(1) Load Cell Sensor and Receiver [150]

The JR3 multi-axis load cell (Figure 7.1) was from JR3, Inc., and it is a cylindrically shaped device that can measure the forces along three orthogonal axes (x, y and z) and the moments about those axes. The load cell receiver is a one channel PCI receiver card that required for data acquisition. Technical specifications for the current sensor model 67M25A3 (25L65) are listed in Table 7.2. The x and y axes are at the horizontal midplane of the load cell, and the z axis is along the central axis. The geometric center of the load cell is the reference point for all loading data. In our application (uniaxial fatigue testing, tensile and creep testing), the uniaxially applied forces are along z axis and the capacity of the load cell in z direction is 222 N.

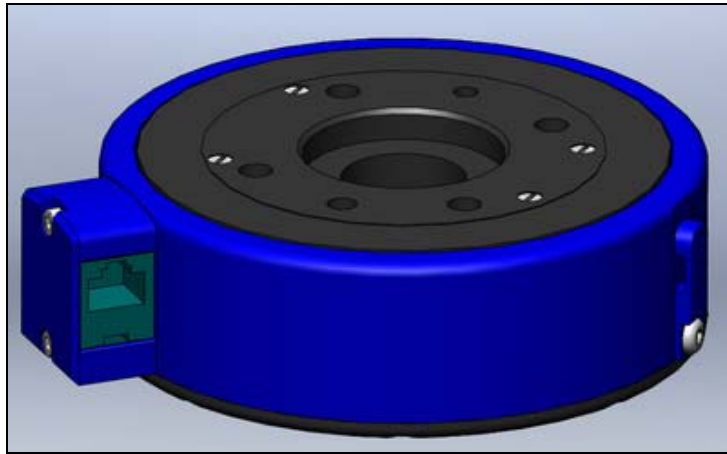


Figure 7.1 - JR3 Multi-Axis Load Cell

Table 7.2 - Technical Specifications for Load Cell 67M25A3 (25L65)

Diameter (mm)	67
Thickness (mm)	25
Material	AL 2024
Weight (g)	175
Nominal Accuracy, All Axes (%)	±1.0
Operating Temp. Range (°C)	-40 to +65

Standard Measurement Range (N)	$F_x, F_y (\pm 111); F_z (\pm 222)$
Digital Resolution (N)	$F_x, F_y (0.028); F_z (0.058)$
Stiffness (N/m)	$F_x, F_y (5.08e6); F_z (50.8e6)$
Standard Measurement Range (Nm)	$M_x, M_y, M_z (\pm 7.34)$
Digital Resolution (Nm)	$M_x, M_y, M_z (0.0018)$
Stiffness (Nm/rad)	$M_x, M_y (21467); M_z (5310)$

(2) Linear Motor

The Anorad LCK-S-2-P motor that incorporated in the MT-210 tester is a linear motor. In industry, the term “linear motor” typically refers to the primary and secondary electromagnetic parts (a coil assembly and a magnet assembly). When other related system components such as bearings, feedback, and structure are included, it is often called a positioning stage or actuator [151]. In many linear motion applications, linear motors have many advantages over the rotary motors that coupled with rotary-to-linear mechanisms, which introduce the inertia, friction, compliance, backlash, etc. [151]. Table 7.3 lists the main specifications for the LCK-S-2-P linear motor.

Table 7.3 - Technical Specifications for LCK-S-2-P Linear Motor

Continuous Force (N)	368 (Coil at 25 °C); 312 (Coil at 125 °C)
Continuous Current (A rms)	6.6 (Coil at 25 °C); 5.6 (Coil at 125 °C)
Peak Force (N)	791 (0.25 sec); 691 (1 sec)
Peak Current (A rms)	20 (0.25 sec); 16.2 (1 sec)
Back EMF (V rms/m/sec)	18.5
Magnetic Attraction (N)	2327

7.3 Instron 5948 Tester

The Instron 5948 universal microtester (Figure 7.2) has the ability to perform tension, compression, and fatigue tests with load capacity up to 2 kN. Its major components include load

frame, 5900 controller module, power module, load cell, grips and Instron Bluehill Software. The load frame comprises a base beam, two columns, and an actuator mounted on a fixed crosshead. The system communicates primarily through the 5900 controller module. It transfers data between the transducers and the computer, and communicates with the load frame via a frame interface board (FIB). The FIB is located inside the power module and it links all the frame electrical components. In addition, the Bluehill software is used to set test parameters, operate the system, and collect experimental data. A control panel can also be used to perform certain functions at the frame instead of using the software. The displacement resolution of the system is 20 nm, and use of the pictured chamber allows the specimens being thermally cycled between -70 °C and +250 °C. Table 7.4 lists the performance specifications of this test system.



Figure 7.2 - Instron 5948 Universal Microtester

Table 7.4 - Performance Specifications for the Instron 5948 Tester

Load Capacity (Static) (kN)	± 2.0
Maximum Speed (mm/min)	1500
Minimum Speed (mm/min)	0.000024
Maximum Cyclic Frequency (Hz)	2.0
Actuator Speed Accuracy	$\pm 0.1\%$
Position Repeatability (mm)	± 0.0005
Position Resolution (nm)	20

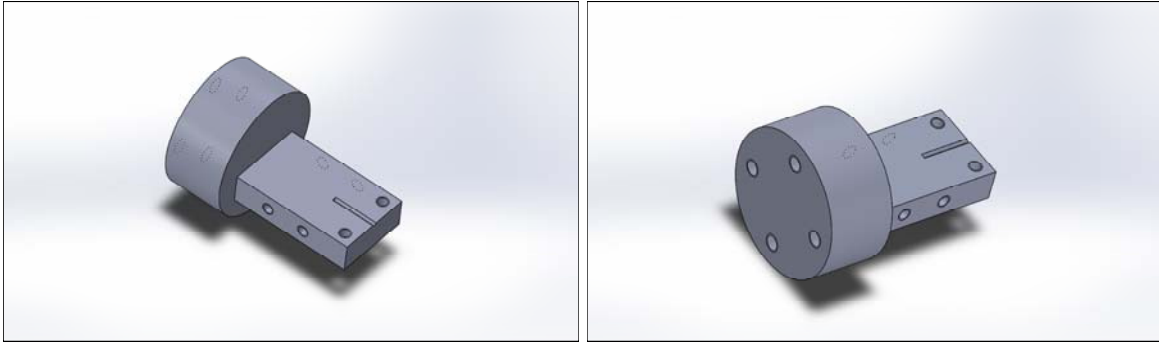
This universal tester does not include the special fixtures for the fatigue testing of micro-cylindrical specimens. Thus, a set of fixtures has been designed and manufactured based on the crossheads and fixtures of current MT-210 microtester. Figure 7.3 shows the 3-D models of the designed fixtures for the Instron 5948 tester, which also feature the V-shaped groove. Figure 7.4 shows the assembly of the fixtures with the cylindrical specimen. One end of the fixtures will be connected to the actuator on the top, while the other end will be connected to the load cell mounted on the bottom plate. The fixtures will be connected to the tester via four M5 threads. The connection types of the load cell and actuator are clevis pin connection, and Instron adapters are required to convert it to thread connection. Figure 7.5 illustrates the schematic of the gripping of cylindrical specimen using the designed fixtures. To determine the dimensions of the groove, there are several factors to be considered:

- (1) Contact points of the specimen and the fixtures should be inside the groove;
- (2) There should be a gap between the grips after mounting the specimen;
- (3) The solder specimen will deform in the gripping area during mounting and testing due to its viscoplasticity.

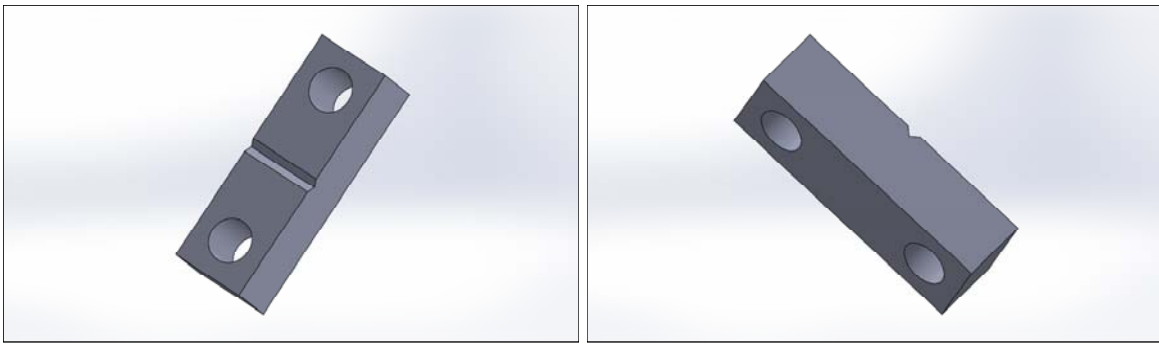
In our application, there are three different sizes of the cylindrical test specimens, and their nominal diameters are 1.2, 1.5, and 2.0 mm. The height ranges of the 90° V-shaped groove for the three types of specimens are 0.43-0.85 mm, 0.53-1.06 mm, and 0.71-1.42 mm, respectively. Therefore, the height of the groove has been chosen as 0.75 mm. Therefore, the fixtures can be used to test specimens range from 1.06 mm to 2.12 mm in diameter, including the three mentioned specimen sizes. The dimensional drawings of the fixtures are attached in Appendix A.2. Figure 7.6 shows the picture of the manufactured fixtures attached to the Instron 5948 microtester, which has been used to perform uniaxial fatigue testing on non-aged WQ SAC305 at room temperature. The tests were strain controlled with a fixed strain rate at 0.002 sec⁻¹. The nominal diameter of the cylindrical specimens was 2 mm and the gage length was set as 5 mm. Figure 7.7 shows the uniaxial fatigue data of WQ SAC305 and the fitting curve using Coffin-Manson model. The Coffin-Manson model is expressed as [152, 153]

$$N^n \Delta \epsilon_p = C \quad (7.1)$$

where $\Delta \epsilon_p$ is the plastic strain range, N is the fatigue life (50% load drop criterion), n is the fatigue exponent, and C is the fatigue ductility. The coefficients C and n were determined using least-squares regression analysis, and the values are 0.621 and 0.563, respectively.



(a) Part 1 (Different Views)



(b) Part 2 (Different Views)

Figure 7.3 - 3-D Models of the Designed Fixtures for Instron 5948 Tester

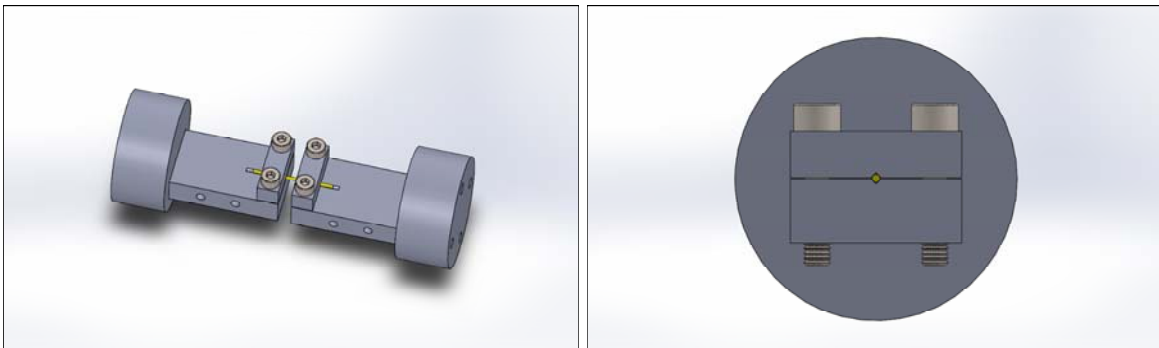


Figure 7.4 - Assembly of the Fixtures

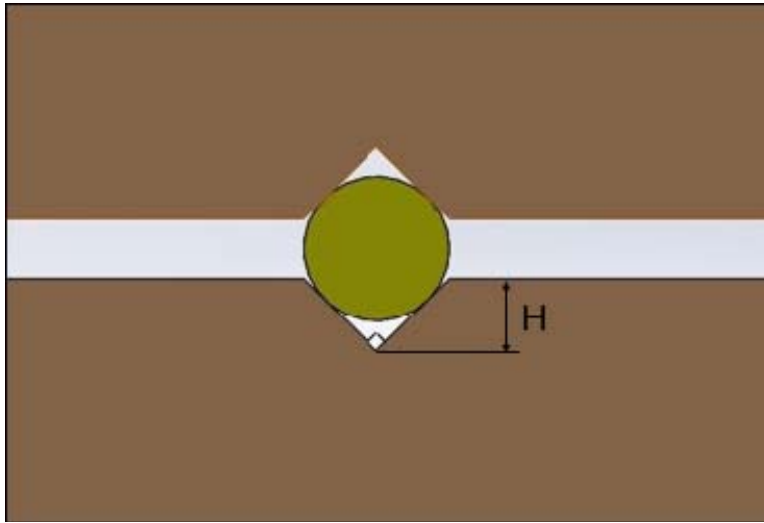


Figure 7.5 - Schematic of the Gripping and Dimensions of the Groove



Figure 7.6 - Instron 5948 Microtester with the Fixtures

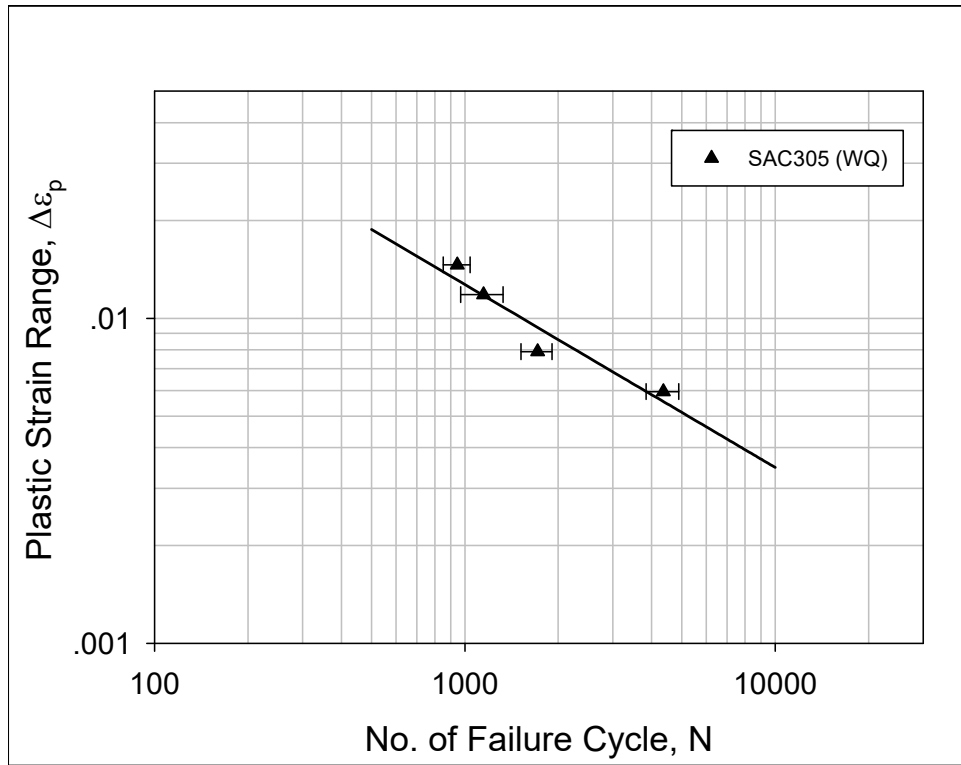


Figure 7.7 - Uniaxial Fatigue Life of WQ SAC305
(Using Instron 5948 with Designed Fixtures)

In addition, this set of Instron fixtures is compatible with previously designed fixtures for the current MT-210 microtester (Figure 2.7). They can be used together to test cylindrical specimens (Figure 7.8) or flat specimens (Figure 7.9), and the specimens are along the centerline of load cell and actuator in either set-up. Furthermore, the Instron fixtures can also be used to work with shear fatigue fixtures, designed by Mustafa [79], for the Iosipescu shear specimens (see Figure 7.10).

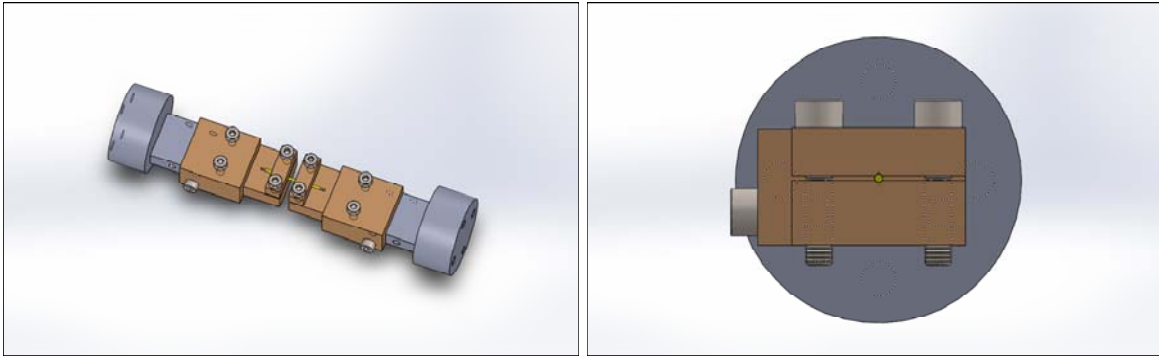


Figure 7.8 - Compatible with MT-210 Microtester Fixtures (Set-up for Cylindrical Specimens)

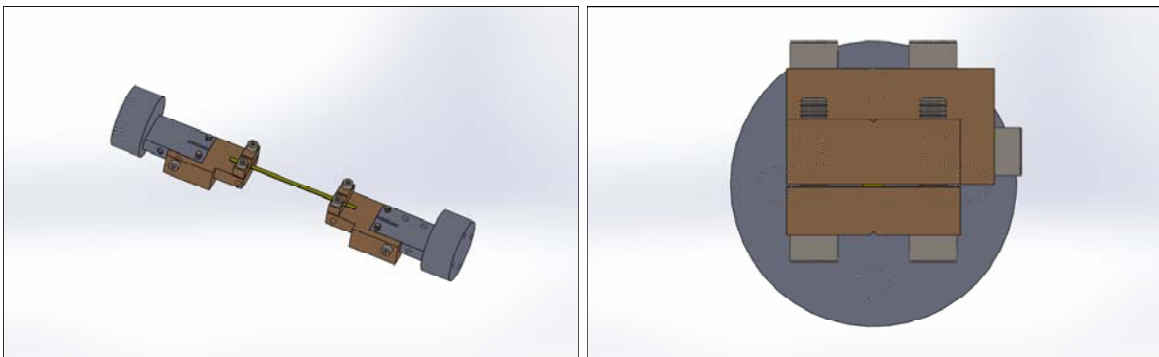


Figure 7.9 - Compatible with MT-210 Microtester Fixtures (Set-up for Flat Specimens)

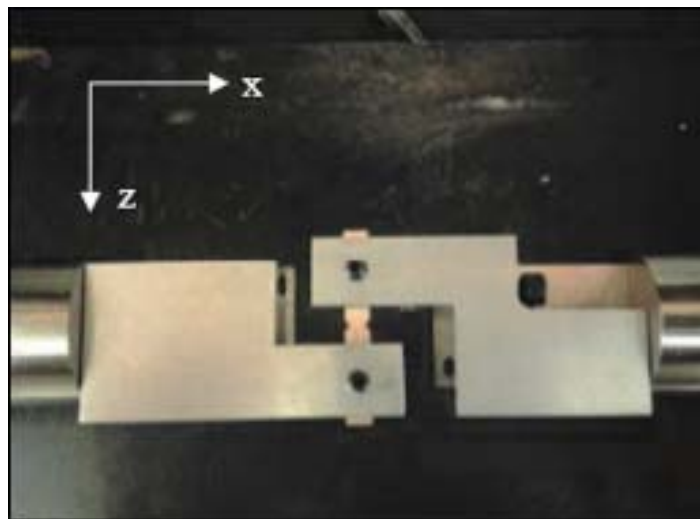


Figure 7.10 - Compatible with MT-210 MicrotesFter Shear Fatigue Fixtures [79]

7.4 Own Designed Microtester

Based on the current MT-210 microtester, a new microtester is to be designed and built, which involves selection of several parts, design of fixtures, programming, etc. As illustrated in Table 7.1, linear motor, encoder and servo controller from Anorad have been obsolete and need to be replaced by similar parts available on the market. The rotation stage is excluded from this designed tester as our applications seldom involve torsion testing. Although the load cell sensor and receiver are still available on the market, it is necessary to search for their replacements to lower the costs. The current multi-axis load cell can measure the forces along three orthogonal axes and the moments about those axes. But in our applications, the majority of the tests are uniaxial and only require the force measurement along the testing direction. A simple tension/compression load cell can meet the needs and it is much less expensive. The new tester is designed to have better performance than the current MT-210 microtester does. Table 7.5 lists the criteria for the design of the new tester. Ideally, the linear stage would be compatible with LabVIEW, a system-design platform and development environment from National Instruments (NI). This is because LabVIEW is the commonly used programming software in the lab and its training sessions from NI are often available on campus for engineering students. Also, our lab owns many NI hardware devices that can be used for data acquisition with LabVIEW.

Table 7.5 - Design Criteria for the New Tester

	Resolution (um)	Max. Driving Force (N)	Min. Velocity (um/s)	Travel Length (mm)	Feedback	Programming
Current Tester	0.1	222	0.1	103	Linear Encoder	—
Design Criteria	≤ 0.1	≥ 250	≤ 0.1	≥ 103	Linear Encoder	Compatible with LabVIEW

Instead of buying linear motor, linear bearing, encoder, cable management, shock absorber, etc. individually, a linear stage that incorporates these parts is to be selected and purchased. There are many companies that sale the linear stage, but Anorad linear stage from Rockwell Automation was our top choice as it is the same brand with the current linear motor system. The MT-210 linear motor LCK-S-2-P is obsolete, and the close model (Anorad) available on the market is LC-075-200. Anorad offers CHPS-250 linear stage which incorporates LC-075-200 linear motor can meet our design requirements. However, the Anorad CHPS linear stages are not compatible with NI LabVIEW. The other potential products include LS-270 (DC or stepper motor) from Physik Instrumente (PI), and PRO-225, ATS-2010, and ACT-165 from Aerotech. However, there is only one linear stage can well satisfy all the design requirements, i. e., the LS-270 linear stage with upgraded stepper motor (PK-268). Therefore, LS-270 linear stage together with SMC Hydra TT controller (PI) have been chosen and purchased. Figure 7.11 shows a picture of the LS-270 linear stage, and Table 7.6 illustrates the performance specifications of this linear stage (or the new microtester).

LCMHD-50 tension/compression load cell from OMEGA (Figure 7.12) has been chosen to replace the JR3 multi-axis load cell. The chosen load cell can measure tension or compression force within 50 kg (490 N), which can fulfill the requirements at a low price. Table 7.7 lists the specifications of the LCMHD-50 load cell. There are several DAQ devices from National Instruments in the lab can be used to acquire data from the load cell, such as NI 9237. In addition, the new microtester will be equipped with the same fixtures as the Instron fixtures (see Appendix A.2). The production of the new microtester is still ongoing, and more work such as assembly of the parts and programming using LabVIEW will be done in the future.



Figure 7.11 - PI LS-270 Linear Stage

Table 7.6 - Performance Specifications of the New Tester (with LS-270 Linear Stage)

	Resolution (um)	Max. Driving Force (N)	Min. Velocity (um/s)	Travel Length (mm)	Feedback	Programming
Current Tester	0.1	222	0.1	103	Linear Encoder	—
Design Criteria	≤ 0.1	≥ 250	≤ 0.1	≥ 103	Linear Encoder	Compatible with LabVIEW
New Tester (LS-270)	0.05	400	0.02	155	Linear Encoder	Compatible with LabVIEW



Figure 7.12 - OMEGA LCMHD-50 Tension/Compression Load Cell

Table 7.7 - Technical Specifications for OMEGA LCMHD-50 Load Cell

Diameter (mm)	76
Thickness (mm)	25
Material	17-4 PH Stainless Steel
Excitation (V)	10 (15 Max)
Output (FSO, mV/V)	3 ± 0.25%
Operating Temp. Range (°C)	-54 to 121
Compensated Temp. Range (°C)	16 to 71
5-Point Calibration (in Tension)	0%, 50%, 100%, 50%, 0%
Linearity (FSO)	± 0.10%
Hysteresis (FSO)	± 0.10%
Repeatability (FSO)	± 0.03%
Safe Overload	150% of Capacity
Ultimate Overload	300% of Capacity
Input and Output Resistance (Ω)	350 ± 10

7.5 Summary and Discussion

To establish better testing capability in our lab, gripping fixtures have been designed and added to the Instron 5948 universal tester for the testing of micro-cylinder shaped specimens. The fixtures feature a 90° V-shaped groove with height of 0.75 mm, which can be used to test specimens range from 1.06 to 2.12 mm in nominal diameter. The fixtures can also be used together with previously designed fixtures to test flat specimens or Iosipescu shear specimens. At the same time, the production of a new microtester based on the current MT-210 microtester is underway. Many parts of the MT-210 microtester are obsolete, so similar products on the market have been searched to replace them. The new microtester is designed to have better testing performance than the current one. The major parts have been determined and purchased, and more work such as assembly of the parts and programming using LabVIEW will be done in the future.

CHAPTER 8

SUMMARY AND CONCLUSIONS

8.1 Literature Review

Literature review has been done on Sn-Ag-Cu lead free solders, effects of aging on solder mechanical properties and microstructure, various influential factors on solder mechanical behavior, and effects of thermo-mechanical cycling on solder microstructure.

Among the candidates for replacing the conventional eutectic lead solder, Sn-Ag-Cu (SAC) lead free solder series are the most widely used lead free solders in the industry at present [9]. Recent studies tend to agree that the eutectic point of SAC solder is close to Sn-3.5Ag-0.9Cu, and its melting point is around 217.2 °C [13-15]. The typical microstructure of SAC lead free solders consists of β -Sn dendrites surrounded by interdendritic eutectic regions incorporating a fine dispersion of Ag_3Sn and Cu_6Sn_5 intermetallic particles in β -Sn. In addition, Sn has a Body-Center Tetragonal (BCT) crystal structure, and it is highly anisotropic in mechanical and thermal properties [22, 23].

Aging has a strong effect on mechanical properties of lead free solders, as they have high homologous temperatures in most product applications. It has been found that aging is universally detrimental to solder constitutive and failure behaviors. The changes in solder mechanical behavior are a result of the evolution of the solder microstructure that occurs during aging. The most well-known and widely observed microstructural changes are coarsening of the Ag_3Sn and Cu_6Sn_5 IMCs present in the eutectic regions between β -Sn dendrites. In many studies

on the effects of aging on solder microstructure, observations were made on two different solder joints (one non-aged and one aged). There are limited investigations that have involved the monitoring of evolving microstructure in a fixed region in a single solder sample.

Apart from aging, there are many other parameters such as cooling rate, strain rate (frequency) and testing temperature that can influence the mechanical behavior of solder materials. Typically, fast cooling rates lead to a finer initial lead free solder microstructure and better mechanical properties. When tested at lower temperatures or higher strain rates, solder test specimens exhibit better mechanical properties.

Finally, the effects of thermo-mechanical cycling (TMC) on the microstructure of lead free solders have been reviewed, and several conclusions were reached:

- (1) Several useful experimental techniques have been used to explore solder microstructural changes during TMC, such as Scanning Electron Microscopy (SEM), Orientation Imaging Microscopy (OIM), and polarized light microscopy;
- (2) Thermo-mechanical cycling tends to result in recrystallization of β -Sn in the region where stresses or strains are high, and the recrystallized region expands as the cycling progresses;
- (3) Thermo-mechanical cycling also leads to the coarsening of IMC particles, and the coarsening is severer in the recrystallized region;
- (4) Generally, the fatigue crack initiates at the Sn grain boundaries in the recrystallized region, and then propagates along the boundaries between recrystallized grains;
- (5) Thermo-mechanical cycling leads to the degradation of various mechanical properties of lead free solders.

8.2 Experimental Procedure

Newly designed micro-cylinder shaped uniaxial lead free solder test specimens have been prepared in glass tubes using a vacuum suction process. The cylindrical specimens were introduced to solve the buckling problem during compression in the cyclic or fatigue testing. The mechanical testing was performed using a tension/torsion thermo-mechanical test system. Gripping fixtures were designed and added to the test system to grip the cylindrical specimens. After introducing the cylindrical specimens and gripping fixtures, we have solved many problems such as buckling during compression, specimen breaks in the grip, and slippage during testing. After testing, empirical models were utilized to represent the stress-strain, creep, and cyclic stress-strain experimental data. To process the cyclic stress-strain data and calculate the areas of the associated hysteresis loops, a pair of hyperbolic tangent empirical models has been used to represent the tension portion and the compression portion of the stress-strain behavior in each cycle. Then, hysteresis loop area (plastic strain energy density), plastic strain range and peak stress can be determined for each cycle.

To study the solder microstructural changes during aging, SAC305 solder samples were formed with RF and WQ cooling profiles and resulting initial microstructures, and then microscopy cross-sections were prepared. After polishing, small indentation marks were added to the cross-sections to facilitate locating the identical regions of interest. Then the microstructural changes in the fixed regions during aging were examined using SEM. To study the effects of mechanical cycling on the solder microstructure, uniaxial samples with various durations of prior mechanical cycling have been prepared. The cycled microstructures were then examined using SEM and polarized light microscope.

8.3 Aging Induced Evolution of the Cyclic Stress-Strain Behavior of Lead Free Solders

In this study, effects of aging on the cyclic stress-strain behavior of lead free solders have been investigated, and several influential factors have been examined, such as aging duration (up to 1 year), silver content (SAC305 and SAC405), solidification profile (WQ and RF), and aging temperature (125 °C and 25 °C). The evolution of hysteresis loop with aging has been characterized for the studied lead free solders. Prior to testing, cylindrical uniaxial lead free solder test specimens were prepared and aged (preconditioned) at 125 °C or 25 °C for various aging times (0, 5, 10, 20, 30, 45, 60, 80, 110, 150, 200, 260, and 360 days). After aging, the fabricated samples were subjected to strain controlled cyclic stress-strain loading (constant positive and negative strain limits) at room temperature (25 °C). For each set of cyclic stress-strain data, the four-parameter hyperbolic tangent empirical model (Eq. (2.7)) has been used to fit the entire cyclic stress-strain curve.

It has been found that the size and shape of the hysteresis loop changed dramatically during the first few days of aging, with slower changes occurring for longer aging times. Generally, hysteresis loops compressed in the vertical direction while expanded in the horizontal direction with increased aging. In addition, aging induced evolution of the cyclic stress-strain behavior (hysteresis loop area, plastic strain range and peak stress) has been quantified. It has been observed that increased aging led to the drop of loop area and peak stress and the increase of plastic strain range, which indicates the increased ability of dislocation movement. Also, dramatic changes of all the three parameters occurred within the first few days of aging. The evolutions of hysteresis loop area with aging have been modeled, and comparison of the studied solder microstructures has been done. It has been found that RF microstructure was more stable

than WQ microstructure when exposed to aging, and elevated temperature aging led to more degradation of the cyclic stress-strain behavior than room temperature aging did.

Finally, effects of aging on solder microstructure have been studied in a fixed region of a single solder sample using SEM. The WQ microstructure is much finer than the RF microstructure at no aging condition due to the faster cooling rate. Typically, aging led to the weakening of dendrite structure and the coarsening of IMC particles, especially during the first few days of aging.

8.4 Cyclic Stress-Strain Behavior: Effects of Aging, Temperature, Strain Rate, and Plastic Strain Range

Apart from aging, various testing parameters such as testing temperature and strain rate (frequency) also have a significant influence on the cyclic stress-strain and fatigue behaviors of lead free solders. In this investigation, we have examined the effects of prior aging conditions and several testing parameters on the cyclic stress-strain behavior of WQ SAC305 lead free solder. Prior to testing, specimens aged at 125 °C for various durations (0, 5, 10, and 20 days) have been prepared for this purpose. The examined range of cyclic loading test parameters included testing temperature (25 to 100 °C), testing strain rate (0.0001 to 0.001 sec⁻¹), and total strain range (0.004 to 0.013).

The Effects of test temperature, strain rate, and strain range were investigated by subjecting non-aged and aged samples to cyclic loadings under different conditions. At elevated test temperatures or lower test strain rates, an increase in the plastic strain range and a drop of the peak stress and loop area were found for all aging times, which indicates more creep and dislocation movement occurred during the cycling. Moreover, the plastic strain range, loop area, and peak load increased as expected with greater applied total strain range. Finally, the effects of

aging have been quantified for the first time for different testing temperatures, strain rates, and plastic strain ranges.

8.5 Investigation of Aging Induced Evolution of the Microstructure of SAC305 Lead Free Solder

In this investigation, Scanning Electron Microscopy (SEM) has been utilized to examine aging induced microstructural changes occurring within lead free solders. Unlike many prior studies, fixed regions in the solder joint cross-sections were monitored throughout the aging process, rather than examining different samples and/or different regions after the various aging exposures. Nanoindentation marks were added to the cross-sections at certain locations to facilitate locating the fixed regions of interest. Three aging increments (1 hour, 1 day and 10 days) and two solidification profiles (RF and WQ) have been examined. After preparation of suitable cross-sectional samples, the samples were then aged at $T = 125\text{ }^{\circ}\text{C}$, and the microstructures were observed and recorded in the selected regions after various aging exposures using SEM. With this approach, time-lapse imagery of the microstructure evolution in a particular region of a solder joint has been recorded as a function of the aging time.

Using the recorded images, migration, coalescence, and coarsening of intermetallic compounds were visualized. It has been found that the number of IMC particles decreased, while the average size of the particles and average particle separation distance increased significantly with aging. The early aging period features the most rapid and dramatic changes in microstructure. Compared with RF SAC305, WQ SAC305 had much finer initial IMC particles but they coarsened to a greater degree during isothermal aging. For small aging times up to 11 hours at $T = 125\text{ }^{\circ}\text{C}$, experimentally recorded movies of microstructural evolution during aging have been made to visualize those aging phenomena.

Additionally, the coarsening of IMC particles in fixed regions during aging has been quantitatively analyzed. Particularly, the aging induced evolutions of number of IMCs, total area of all IMCs, average particle area, and average particle diameter have been quantified. For instance, during the first 11 hours of aging at 125 °C, the average IMC particle diameter increased by approximately 62% for RF SAC305 and 227% for WQ SAC305. After 50 days of aging, the average diameter increased by around 157% and 781% for RF SAC305 and WQ SAC305, respectively.

8.6 Evolution of Solder Mechanical Behavior and Microstructure During Fatigue Testing

To better understand the damage accumulation during fatigue testing, we have studied cycling induced evolution of mechanical behavior of RF SAC305 lead free solder. Particularly, the evolutions of cyclic stress-strain curve, stress-strain curve and creep curve have been characterized and quantified. To study the evolution of the cyclic stress-strain behavior, the specimens have been subjected to cyclic stress/strain loading at room temperature (25 °C) until fatigue failure. The cyclic stress-strain curves at after various durations of cycling have been examined. To study the effects of cycling on solder constitutive behavior, uniaxial samples with various durations of prior mechanical cycling have been prepared. The cycled samples were then subjected to stress-strain or creep testing. With increased mechanical cycling, damage accumulated in the specimen and its various mechanical properties degraded. For example, compared with non-cycled test specimens, the degradations on elastic modulus, ultimate strength and yield stress are 61.61%, 38.87% and 43.91%, respectively, for the specimens pre-cycled for 1200 cycles.

These have been correlated with the observed microstructural changes caused by fatigue cycling. SEM and polarized light microscope have been utilized to examine the changes that

occurred for each cycling condition. It has been found that the initial damage caused by fatigue cycling was the weakening of dendrite structure, coarsening of IMCs (formation of large needle-shaped IMCs), and recrystallization of Sn grains. With increased cycling, the major changes were the disappearance of dendrite structure, the growth of those large needle-shaped IMCs, and the growth of newly formed small grains. Also, fatigue cracks tended to form at the boundaries of newly formed grains in recrystallized regions, and then propagate along those boundaries.

8.7 Establish Better Capability for Fatigue Testing in Our Laboratory

To establish better testing capability in our lab, gripping fixtures have been designed and added to the Instron 5948 universal tester for the testing of micro-cylinder shaped specimens. The fixtures feature a 90° V-shaped groove with height of 0.75 mm, which can be used to test specimens range from 1.06 to 2.12 mm in nominal diameter. The fixtures can also be used together with previously designed fixtures to test flat specimens or Iosipescu shear specimens. At the same time, the production of a new microtester based on the current MT-210 microtester is underway. Many parts of the MT-210 microtester are obsolete, so similar products on the market have been searched to replace them. The new microtester is designed to have better testing performance than the current one. The major parts have been determined and purchased, and more work such as assembly of the parts and programming using LabVIEW will be done in the future.

8.8 Recommendations for Future Work

- (1) Continue the study of aging induced microstructural changes in a fixed region for SAC305 to include more aging times, and then explore the changes of dendrite structure and subgrains due to aging;

- (2) To more accurately quantify the coarsening of IMC particles during aging, analyze more fixed regions and then average the results; Compare the results with those from other researchers and verify the existing models that predict the increase of particle size due to aging; Propose a model based on the results in fixed regions;
- (3) Characterize and quantify the effects of aging on grain size and grain orientation of lead free solders in the same region using SEM, polarized light microscope and EBSD;
- (4) Use the same procedures and methods to study the effects of aging on the microstructure of other lead free solders, such as doped SAC alloys;
- (5) Study mechanical cycling induced microstructural changes of lead free solders in a fixed region; A well-polished uniaxial test specimen will be cycled for various durations, and the microstructure of the same region will be examined at after each duration using SEM, polarized light microscope, etc.;
- (6) Explore the effects of mechanical cycling on mechanical properties of lead free solders using nanoindentation; The sample will be cycled for various cycles, and then use the nanoindentation system to determine the mechanical properties of the cycled sample (such as elastic modulus, hardness and creep rate) for each cycling condition;
- (7) Investigate the effects of aging on the fatigue life of lead free solders using the Instron 5948 with designed gripping fixtures;
- (8) Build the designed new microtester for fatigue testing, and the future work includes the assembly of parts and the programming using LabVIEW.

REFERENCES

1. Ma, H., Suhling, C. J., "A Review of Mechanical Properties of Lead-Free Solders for Electronic Packaging," *J Mater Sci*, Vol. 44, pp. 1141-1158, 2009.
2. Abtey, M., Selvaduray, G., "Lead-Free Solders in Microelectronics," *Materials Science and Engineering*, Vol. 27, pp. 95-141, 2000.
3. Lee, N. C., "Getting Ready for Lead-Free Solders," *Soldering & Surface Mount Technology*, Vol. 9(2), pp. 65-69, 1997.
4. Turbini, L. J., Munie, G. C., Bernier, D., Gamalski, J., Bergman, D. W., "Examining the Environmental Impact of Lead-free Soldering Alternatives," *IEEE Transactions on Electronics Packaging Manufacturing*, Vol. 24, pp. 4-9, 2001.
5. *IPC Roadmap: A Guide for Assembly of Lead-Free Electronics*, IPC, Northbrook, IL 2000.
6. Wood, E. P., Nimmo, K. L. "In Search of New Lead-free Electronic Solders," *Journal of Electronic Materials*, Vol. 23(8), pp. 709-713, 1994.
7. Hwang, J. S., *Implementing Lead-Free Electronics*, McGraw-Hill, 2004.
8. Allenby, B. R., Ciccarelli, J. P., "An Assessment of the Use of Lead in Electronic Assembly," *Proceedings of Surface Mount International Conference*, IEEE, pp. 1-28, San Jose, CA, 1992.
9. http://www.ameslab.gov/files/LeadFreeSolder_Foundation.pdf
10. Nimmo, K., "Alloy Selection," Chapter 3 of *Lead-free Soldering in Electronics: Science, Technology and Environmental Impact*, edited by K. Sukanuma, New York, Marcel Dekker, pp. 61-62, 2004.
11. Gebhardt, E., Petzow, G., "The Constitution of the Ag-Cu-Sn System," *Z. Metallkd*, Vol. 50, pp. 597-605, 1959.
12. Miller, C. M., Anderson, I. E., Smith, J. F., "A Viable Sn-Pb Solder Substitute: Sn-Ag-Cu," *Journal of Electronic Materials*, Vol. 23(7), pp.595-601, 1994.
13. Loomans, M. E., Fine, M. E., "Tin-Silver-Copper Eutectic Temperature and Composition," *Metallurgical and Materials Transactions A*, Vol. 31(4), pp. 1155-1162, 2000.

14. Moon, K. W., Boettinger, W. J., Kattner, U. R., Biancaniello, F. S., Handwerker, C. A., "Experimental and Thermodynamic Assessment of Sn-Ag-Cu Solder Alloys," *Journal of Electronic Materials*, Vol. 29, pp. 1122-1136, 2000.
15. Snugovsky, L., Perovic, D. D., Rutter, J. W., "Solidification of Ternary Eutectic and Near-Eutectic Alloys in the Ag-Cu-Sn System," *TMS Meeting*, San Diego, CA, March 2003.
16. Cai, Z., "Reduction of Lead Free Solder Aging Effects Using Doped SAC Alloys," Ph. D. Dissertation, Auburn University, 2012.
17. <http://www.metallurgy.nist.gov/phase/solder/agcusn-ll.jpg>
18. Tsai, I., Tai, L.J., Yen, S.F., Chuang, T.H., Wu, E., Lo, R. and Ku, T., Wu, E., "Identification of Mechanical Properties of Intermetallic Compounds on Lead Free Solder," *Proceedings of the 55th Electronic Components and Technology Conference*, IEEE; Vol. 55(1), pp. 687-691, 2005.
19. Fields, R. J., Low, S. R., Lucey, G. K., "Physical and Mechanical Properties of Intermetallic Compounds Commonly Found in Solder Joints," *The Metal Science of Joining*, pp.165-174, 1991.
20. Zhu, Q. S., Zhang, L., Wang, Z. G., Wu, S. D., Shang, J. K., "Effect of Intermetallics Ag₃Sn on the Tensile Property of Sn_{3.8}Ag_{0.7}Cu Solder Alloy," *Acta Metallurgica Sinica*, Vol. 43(1), pp. 41-46, 2007.
21. Ganesan, S., Pecht, M., *Lead-free Electronics*, Wiley-Interscience Publication, pp. 51-52, 2006.
22. Lee, B. Z., Lee, D. N., "Spontaneous Growth Mechanism of Tin Whiskers," *Acta Materialia*, Vol. 46(10), 1998.
23. Pearson, W. B., *A Handbook of Lattice Spacings and Structure of Metals and Alloys*, Vol. 2, Pergamon Press, London, 1958.
24. Medvedev, A. S., "Aging of Tin-Lead Solders and Joints Soldered by Them," *Metallovedenie i Obrabotka Metallov*, No.7, pp. 16-23, 1956.
25. Lampe, B. T., "Room Temperature Aging Properties of Some Solder Alloys," *Welding Journal*, Vol. 55(10), pp. 330s-340s, 1976.
26. Miyazawa, Y., Ariga, T., "Microstructural Change and Hardness of Lead Free Solder Alloys," *Proceedings of the First International Symposium on Environmentally Conscious Design and Inverse Manufacturing*, pp. 616-619, 1999.
27. Miyazawa, Y., Ariga T., "Influences of Aging Treatment on Microstructure and Hardness of Sn-(Ag, Bi, Zn) Eutectic Solder Alloys," *Materials Transactions of the Japan Institute of Metals*, Vol. 42(5), pp. 776-782, 2001.

28. Ding, Y., Wang, C. Q., Tian, Y. H., Li, M. Y., "Influence of Ageing Treatment on Deformation Behavior of 96.5Sn3.5Ag Lead Free Solder Alloy During In-Situ Tensile Tests," *Journal of Alloys and Compounds*, Vol. 428, pp. 274–285, 2007.
29. Xiao, Q., Bailey, H. J., Armstrong, W. D., "Aging Effects on Microstructure and Tensile Property of Sn3.9Ag0.6Cu Solder Alloy," *Journal of Electronic Packaging*, Vol. 126(2), pp. 208-212, 2004.
30. Hasegawa, K., Noudou, T., Takahashi, A., Nakaso, A., "Thermal Aging Reliability of Solder Ball Joint for Semiconductor Package Substrate," *Proceedings of the 2001 SMTA International*, pp. 1-8, 2001.
31. Wang, Q., Johnson, R. W., Ma, H., Gale, W. F., "Properties of Lead-Free Solder Alloys as a Function of Composition Variation," *10th Electronic Circuit and World Convention Conference (ECWC 10)*, 2005.
32. Vianco, P. T., "Fatigue and Creep of Lead-free Solder Alloys: Fundamental Properties," Chapter 3 *Lead-free Solder Interconnect Reliability*, Edited by D. Shangguan, ASM International, pp. 67-106, 2006.
33. Vianco, P. T., Rejent, J. A., Martin, J. J., "The Compression Stress-Strain Behavior of Sn-Ag-Cu Solder," *JOM*, Vol. 55 (6), pp. 50-55, 2003.
34. Vianco, P. T., Rejent, J. A., "Compression Deformation Response of 95.5Sn-3.9Ag- 0.6Cu Solder," *UCLA Workshop on Pb-free Electronics*, 2002. Available at: <http://www.seas.ucla.edu/eThinFilm/PbfreeWorkshop/pdf/vianco.pdf>
35. Vianco, P. T., Rejent, J. A., Kilgo, A. C., "Time-independent Mechanical and Physical Properties of the Ternary 95.5Sn-3.9Ag-0.6Cu Solder," *Journal of Electronic Materials*, Vol. 32 (3), pp. 142-151, 2003.
36. Xiao, Q., Nguyen, L., Armstrong, W. D., "Aging and Creep Behavior of Sn3.9Ag0.6Cu Solder Alloy," *Proceedings of the 54th Electronic Components and Technology Conference*, pp. 1325-1332, 2004.
37. Mysore, K., Chan, D., Bhate, D., Subbarayan, G., Dutta, I., Gupta, V., Zhao, J. H., Edwards, D. R., "Aging-Informed Behavior of Sn3.8Ag0.7Cu Solder Alloys," *Thermal and Thermomechanical Phenomena in Electronic Systems, ITherm*, pp.870-875, 2008.
38. Chavali, S., Singh, Y., Kumar, P., Subbarayan, G., Dutta, I., Edwards, D. R., "Aging Aware Constitutive Models for SnAgCu Solder Alloys," *Proceedings of the 61st Electronic Components and Technology Conference*, pp.701-705, 2011.
39. Solomon, H. D., "Creep Strain Rate Sensitivity and Low Cyclic Fatigue of 60/40 Solder," *Brazing and Soldering*, Vol. 11, pp. 68-75. 1986.

40. Guo, Q., Cutiongco, E. C., Keer, L. M., Fine, M. E., "Thermomechanical Fatigue Life Prediction of 63Sn/37Pb Solder," *Journal of Electronic Packaging*, Vol. 114, pp.145-151, 1992.
41. Busso, E. P., Kitano, M., Kumazawa, T., "A Visco-plastic Constitutive Model for 60/40 Tin-lead Solder used in IC Package Joints," *Journal of Engineering Materials Technology*, Vol. 114, pp. 333-337, 1992.
42. Frear, D. R., Burchett, S. N., Neilsen, M. K., and Stephens, J. J., "Microstructurally based Finite Element Simulation of Solder Joint Behavior," *Soldering and Surface Mount Technology*, Vol. 2, pp. 39-42, 1997.
43. McDowell, D. L., Miller, M. P., and Brooks, D. C., "A Unified Creep-plasticity Theory for Solder Alloys," *Fatigue of Electronic Materials*, ASTM STP, Vol. 1153, pp. 42-59, 1994.
44. Lau, J. H. (Ed.), *Solder Joint Reliability, Theory and Applications*, Van Nostrand Reinhold, New York, 1991.
45. Shi, X. Q., Zhou, W., Pang, H. L. J., and Wang, Z. P., "Effect of Temperature and Strain Rate on Mechanical Properties of 63Sn/37Pb Solder Alloy." *Journal of Electronic Packaging*, Vol. 121, pp. 179-185, 1999.
46. Yang, X. J., Chow, C. L., and Lau, K. J., "Time Dependent Cyclic Deformation and Failure of 63Sn/37Pb Solder Alloy," *International Journal of Fatigue*, Vol. 25, pp. 533-546, 2003.
47. Hall, P. M., "Forces, Moments, and Displacements During Thermal Chamber Cycling of Leadless Ceramic Chip Carriers Soldered to Printed Boards," *IEEE Transactions on Components, Hybrids, and Manufacturing Technology*, Vol. 7(4), pp. 314-327. 1984.
48. Hall, P. M., "Creep and Stress Relaxation in Solder Joints of Surface Mounted Chip Carriers," *IEEE Transactions on Components, Hybrids and Manufacturing Technology*, Vol. 12(4), pp. 556-565, 1987.
49. Pao, Y.-H., Badgley, S., Govila, R. and Jih, E., "An Experimental and Modeling Study of Thermal Cyclic Behavior of Sn-Cu and Sn-Pb Solder Joints," *Electronic Packaging Materials Science VII*, (Materials Research Society Symposium, Number 323), pp. 153-158, 1994.
50. Pao, Y.-H., Chen, K. L. and Kuo, A. Y., "A Nonlinear and Time Dependent Finite Element Analysis of Solder Joints in Surface Mounted Components under Thermal Cycling," *in Proceedings of the Materials Research Society Symposium*, Vol. 226, pp. 23-28, 1991.
51. Pao, Y.-H., Govila, R., Badgley, S. and Jih, E., "An Experimental and Finite Element Study of Thermal Fatigue Fracture of Pb-Sn Solder Joints," *Journal of Electronic Packaging*, Vol. 115, pp. 1-8, 1993.

52. Haacke, P. Sprecher, A. F. and Conrad, H., "Computer Simulation of Thermomechanical Fatigue of Solder Joints Including Microstructural Coarsening," *Journal of Electronic Packaging*, Vol. 115, pp. 153-158, 1993.
53. Raeder, C. H., Felton, L. E., Messler, R. W., and Coffin, L. F., "Thermomechanical Stress-Strain Hysteresis of Sn-Bi Eutectic Solder Alloy," *Proceedings of the IEEE International Electronics Manufacturing Technology Symposium*, pp. 263-268, 1995.
54. Dusek, M., and Hunt, C., "Low Cycle Isothermal Fatigue Properties of Lead-free Solders," *Soldering and Surface Mount Technology*, pp. 25-32, 2007.
55. Kanchanomai, C., Mutoh, Y., "Low-Cycle fatigue prediction model for Pb-free solder 96.5Sn-3.5Ag," *Journal of Electronic Materials*, Vol. 33, No. 4, 2004.
56. Pang, J. H. L., Xiong, B. S. and Low, T. H., "Creep and Fatigue Characterization of Lead Free 95.5Sn-3.8Ag0.7Cu Solder," *Proceedings of the 54th Electronic Components and Technology Conference*, pp. 1333-1337, 2004.
57. Andersson, C., Lai, Z., Liu, J., Jiang, H., Yu, Y., "Comparison of Isothermal Mechanical Fatigue Properties of Lead-Free Solder Joints and Bulk Solders," *Materials Science and Engineering*, Vol. 394, pp. 20-27, 2005.
58. Chilton, A. C., Whitmore, M. A., Hampshire, W. B., "Fatigue Failure in a Model SMD Joint," *Soldering and Surface Mount Technology*, Vol. 3, pp. 21-24, 1989.
59. Bansal, A., Lee, T. K., Liu, K. C., Xue, J., "Effects of Isothermal Aging and In-Situ Current Stress on The Reliability of Lead-Free Solder Joints," *Proceedings of the 60th Electronic Components and Technology Conference*, pp.1529-1535, 2010.
60. Venkatadri, V., Liang, Y., Yan, X., Cotts, E., Srihari, K., Borgesen, P., "Accelerating the Effects of Aging on the Reliability of Lead Free Solder Joints in A Quantitative Fashion," *Proceedings of the 59th Electronic Components and Technology Conference*, pp.398-405, 2009.
61. Ma, H., Suhling, J. C., Lall P., Bozack, M. J., "Reliability of the Aging Lead-Free Solder Joint," *Proceeding of the 56th Electronic Components and Technology Conference*, San Diego, California, pp. 849-864, 2006
62. Ma, H., Suhling, J. C., Zhang, Y., Lall, P., and Bozack, M. J., "The Influence of Elevated Temperature Aging on Reliability of Lead Free Solder Joints," *Proceedings of the 57th IEEE Electronic Components and Technology Conference*, pp. 653-668, Reno, NV, May 29-June 1, 2007.
63. Zhang, Y., Cai, Z., Suhling, J. C., Lall, P., and Bozack, M. J., "The Effects of Aging Temperature on SAC Solder Joint Material Behavior and Reliability," *Proceedings of the 58th IEEE Electronic Components and Technology Conference*, pp. 99-112, Orlando, FL, May 27-30, 2008.

64. Zhang, Y., Cai, Z., Suhling, J. C., Lall, P., and Bozack, M. J., "The Effects of SAC Alloy Composition on Aging Resistance and Reliability," *Proceedings of the 59th IEEE Electronic Components and Technology Conference*, pp. 370-389, San Diego, CA, May 27-29, 2009.
65. Cai, Z., Zhang, Y., Suhling, J. C., Lall, P., Johnson, R. W., Bozack, M. J., "Reduction of Lead Free Solder Aging Effects Using Doped SAC Alloys," *Proceedings of the 60th Electronic Components and Technology Conference*, pp. 1493-1511, 2010.
66. Zhang, J., Hai, Z., Thirugnanasambandam, S., Evans, J. L., Bozack, M. J., Sesek, R., Zhang, Y., Suhling, J. C., "Correlation of Aging Effects on Creep Rate and Reliability in Lead Free Solder Joints," *SMTA Journal*, Volume 25(3), pp. 19-28, 2012.
67. Zhang, J., Hai, Z., Thirugnanasambandam, S., Evans, J. L., Bozack, M. J., Zhang, Y., Suhling, J. C., "Thermal Aging Effects on Thermal Cycling Reliability of Lead-Free Fine Pitch Packages," *IEEE Transactions on Components and Packaging Technologies*, Vol. 3(8), pp. 1348-1357, 2013.
68. Hai, Z., Zhang, J., Shen, C., Evans, J. L., Bozack, M. J., Basit, M. M., and Suhling, J. C., "Reliability Comparison of Aged SAC Fine-Pitch Ball Grid Array Packages Versus Surface Finishes," *IEEE Transaction on Components, Packaging, and Manufacturing Technology*, Vol. 5(6), pp. 828-837, 2015.
69. Motalab, M., Cai, Z., Suhling, J. C., Zhang, J., Evans, J. L., Bozack, M. J., Lall, P., "Improved Predictions of Lead Free Solder Joint Reliability That Include Aging Effects," *Proceedings of the 62nd IEEE Electronic Components and Technology Conference*, pp. 513-531, San Diego, CA, May 30 - June 1, 2012.
70. Motalab, M., Cai, Z., Suhling, J. C., Zhang, J., Evans, J. L., Bozack, M. J., Lall, P., "Correlation of Reliability Models Including Aging Effects with Thermal Cycling Reliability Data," *Proceedings of the 63rd IEEE Electronic Components and Technology Conference*, pp. 986-1004, Las Vegas, NV, May 28-31, 2013.
71. Hasnine, M., Mustafa, M., Suhling, J. C., Prorok, B. C., Bozack, M. J., Lall, P., "Characterization of Aging Effects in Lead Free Solder Joints Using Nanoindentation," *Proceedings of the 63rd IEEE Electronic Components and Technology Conference*, pp. 166-178, Las Vegas, NV, May 28-31, 2013.
72. Hasnine, M., Suhling, J. C., Prorok, B. C., Bozack, M. J., and Lall, P., "Exploration of Aging Induced Evolution of Solder Joints Using Nanoindentation and Microdiffraction," *Proceedings of the 64th IEEE Electronic Components and Technology Conference*, pp. 379-394, Orlando, FL, May 28-30, 2014.
73. Hasnine, M., Suhling, J. C., Prorok, B. C., Bozack, M. J., and Lall, P., "Nanomechanical Characterization of SAC Solder Joints - Reduction of Aging Effects Using Microalloy Additions," *Proceedings of the 65th IEEE Electronic Components and Technology Conference*, pp. 1574-1585, San Diego, CA, May 27-29, 2015.

74. Lall, P., Shantaram, S., Suhling, J., Locker, D., "Effect of Aging on the High Strain Rate Mechanical Properties of SAC105 and SAC305 Leadfree Alloys," *Proceedings of the 63rd IEEE Electronic Components and Technology Conference*, pp. 1277-1293, Las Vegas, NV, May 28-31, 2013.
75. Mustafa M., Cai Z., Suhling J. C., Lall P., "The Effects of Aging on the Cyclic Stress-Strain Behavior and Hysteresis Loop Evolution of Lead Free Solders," *Proceedings of the 61st Electronic Components and Technology Conference*, pp. 927-939, 2011.
76. Mustafa, M., Roberts, J. C, Suhling, J. C, and Lall, P., "The Effects of Aging on The Fatigue Life of Lead Free Solders," *Proceedings of the 64th IEEE Electronic Components and Technology Conference*, pp. 666-683, Orlando, FL, May 28-30, 2014.
77. Mustafa, M., Cai, Z., Roberts, J. R., Suhling, J. C., Lall, P., "Evolution of the Tension/Compression and Shear Cyclic Stress-Strain Behavior of Lead-Free Solder Subjected to Isothermal Aging," *Proceedings of ITherm 2012*, pp. 765-780, San Diego, CA, May 30 - June 1, 2012.
78. Mustafa M., Suhling J. C., Lall P., "Experimental Determination of Fatigue Behavior of Lead Free Solder Joints in Microelectronic Packaging Subjected to Isothermal Aging," *Microelectronics Reliability*, Vol. 56, pp. 136-147, 2016.
79. Mustafa M., "Effects of Aging on the Cyclic Stress-Strain and Fatigue Behaviors of Lead-Free Solders," Ph. D. Dissertation, Auburn University, 2014.
80. Pang, J. H. L., *Lead Free Solder: Mechanics and Reliability*, Springer, 2011.
81. Shang, J. K., Zeng, Q. L., Zhang, L., Zhu, Q. S., "Mechanical Fatigue of Sn-Rich Pb-Free Solder Alloys," *J Mater Sci: Mater Electron*, Vol. 18, pp. 211-227, 2007.
82. Kanchanomai, C., Miyashita, Y., Mutoh, Y., "Low Cycle Fatigue Behavior and Mechanisms of a Eutectic Sn-Pb Solder 63Sn/37Pb," *International Journal of Fatigue*, Vol. 24, pp. 671-683, 2002.
83. Kariya, Y., Niimi, T., Suga, T., Otsuka, M., "Isothermal Fatigue Properties of Sn-Ag-Cu Alloy Evaluated by Micro Size Specimen," *Materials Transactions*, Vol. 46(11), pp. 2309-2315, 2005.
84. Oriyama, H., Kawakami, T., Kinoshita, T., "A Basic Study on Creep-Fatigue Damages Interaction for Sn-3.0Ag-0.5Cu as Lead Free Solder Material," *Proceedings of the ASME 2015 InterPACK & ICNMM*, San Francisco, CA, July 6-9, 2015.
85. Choi, W. K., Lee, H. M., "Effect of Soldering and Aging Time on Interfacial Microstructure and Growth of Intermetallic Compounds between Sn-3.5Ag Solder Alloy and Cu Substrate," *Journal of Electronic Materials*, Vol. 29(10), pp. 1207-1213, 2000.

86. Ahat, S., Sheng, M., Luo, L., "Microstructure and Shear Strength Evolution of SnAg/Cu Surface Mount Solder Joint During Aging," *Journal of Electronic Materials*, Vol. 30(10), pp. 1317-1322, 2001.
87. Guo, F., Choi, S., Lucas, J. P., Subramanian, K. N., "Microstructural Characterization of Reflowed and Isothermally-Aged Cu and Ag Particulate Reinforced Sn-3.5Ag Composite Solders," *Soldering and Surface Mount Technology*, Vol. 13(1), pp. 7-18, 2001.
88. Miao, H., Duh, J., "Microstructure Evolution in Sn-Bi and Sn-Bi-Cu Solder Joints under Thermal Aging," *Materials Chemistry and Physics*, Vol. 71, pp. 255-271, 2001.
89. Dutta, I., "A Constitutive Model for Creep of Lead-Free Solders Undergoing Strain-Enhanced Microstructural Coarsening: A First Report," *Journal of Electronic Materials*, Vol. 32, pp. 201-207, 2003.
90. Ubachs, R. L. J. M., Schreurs, P. J. G., Geers, M. G. D., "Microstructure Evolution of Tin-Lead Solder," *IEEE Transactions on Components and Packaging Technologies*, Vol. 27(4), pp. 635-642, 2004.
91. Duan, L. L., Yu, D. Q., Han, S. Q., Ma, H. T., Wang, L., "Microstructural Evolution of Sn-9Zn-3Bi Solder/Cu Joint during Long-Term Aging at 170 °C," *Journal of Alloys and Compounds*, Vol. 381, pp. 202-207, 2004.
92. Allen, S. L., Notis, M. R., Chromik, R. R., Vinci, R. P., "Microstructural Evolution in Lead-Free Solder Alloys: Part I. Cast Sn-Ag-Cu Eutectic," *Journal of Materials Research*, Vol. 19(5), pp. 1417-1424, 2004.
93. Telang, A. U., Bieler, T. R., Lucas, J. P., Subramanian, K. N., Lehman, L. P., Xing, Y., Cotts, E. J., "Grain-Boundary Character and Grain Growth in Bulk Tin and Bulk Lead-Free Solder Alloys," *Journal of Electronic Materials*, Vol. 33(12), pp. 1412-1423, 2004.
94. Dutta, I., Pan, D., Marks, R. A., Jadhav, S. G., "Effect of Thermo-Mechanically Induced Microstructural Coarsening on the Evolution of Creep Response of SnAg-Based Microelectronic Solders," *Materials Science and Engineering A*, Vol. 410-411, pp. 48-52, 2005.
95. Xu, L., Pang, J. H. L., Prakash, K. H., Low, T. H., "Isothermal and Thermal Cycling Aging on IMC Growth Rate in Lead-Free and Lead- Based Solder Interface," *IEEE Transactions on Components and Packaging Technologies*, Vol. 28(3), pp. 408-414, 2005.
96. Hao, H., Shi, Y., Xia, Z., Lei, Y., Guo, F., "Microstructure Evolution of SnAgCuEr Lead-Free Solders under High Temperature Aging," *Journal of Electronic Materials*, Vol. 37(1), pp. 2-8, 2008.
97. Fix, A. R., Nuchter, W., Wilde, J., "Microstructural Changes of Lead- Free Solder Joints During Long-Term Ageing, Thermal Cycling and Vibration Fatigue," *Soldering and Surface Mount Technology*, Vol. 20(1), pp. 13-21, 2008.

98. Seo, S., Kang, S. K., Shih, D., Lee, H. M., "The Evolution of Microstructure and Microhardness of Sn-Ag and Sn-Cu Solders During High Temperature Aging," *Microelectronics Reliability*, Vol. 49, pp. 288-295, 2009.
99. Dutta, I., Kumar, P., Subbarayan, G., "Microstructural Coarsening in Sn-Ag-Based Solders and its Effects on Mechanical Properties," *Journal of Metals (JOM)*, Vol. 61, pp. 29-38, 2009.
100. Kumar, P., Talenbanpour, B., Sahaym, U., Wen, C. H., Dutta, I., "Microstructural Evolution and Some Unusual Effects During Thermo-Mechanical Cycling of Sn-Ag-Cu Alloys," *Proceedings of the ITherm 2012*, pp. 880-887, San Diego, CA, May 30 - June 1, 2012.
101. Kumar, P., Huang, Z., Chavali, S., Chan, D., Dutta, I., Subbarayan, G., Gupta, V., "A Microstructurally Adaptive Model for Primary and Secondary Creep of Sn-Ag-based Solders," *IEEE Transactions on Components, Packaging and Manufacturing Technology*, Vol. 2(2), pp. 256-265, 2012.
102. Sahaym, U., Talebanpour, B., Seekins, S., Dutta, I., Kumar, P., Borgesen, P., "Recrystallization and Ag₃Sn Particle Redistribution during Thermomechanical Treatment of Bulk Sn-Ag-Cu Solder Alloys," *IEEE Transactions on Components, Packaging and Manufacturing Technology*, Vol. 3(11), pp. 1868-1875, 2013.
103. Borgesen, P., "Microstructurally Adaptive Constitutive Relations and Reliability Assessment Protocols for Lead Free Solder," SERDP Project WP-1752 Final Report, 2015.
104. Dariavach, N., Callahan, P., Liang, J., Fournelle, R., "Intermetallic Growth Kinetics for Sn-Ag, Sn-Cu, and Sn-Ag-Cu Lead-Free Solders on Cu, Ni, and Fe-42Ni Substrates," *Journal of Electronic Materials*, Vol. 35(7), pp. 1581-1592, 2006.
105. Kim, K. S., Huh, S. H., Sukanuma, K., "Effects of Cooling Speed on Microstructure and Tensile Properties of Sn-Ag-Cu Alloys," *Materials Science and Engineering A*, Vol. 333, pp. 106-114, 2002.
106. Hu, Q., Lee, Z. S., Zhao, Z. I., Lee, D. L., "Study of Cooling Rate on Lead-Free Soldering Microstructure of Sn-3.0Ag-0.5Cu Solder," *Proceedings of International Conference on Asian Green Electronics*, pp. 156-160, 2005.
107. Jeong, S. W., Kim, J. H., Lee, H. M., "Effect of Cooling Rate on Growth of the Intermetallic Compound and Fracture Mode of Near-Eutectic Sn-Ag-Cu/Cu Pad: Before and After Aging," *Journal of Electronic Materials*, Vol. 33(12), pp. 1530- 1544, 2004.
108. Liang, J., Dariavach, N., Shangguan, D., "Solidification Condition Effects on Microstructures and Creep Resistance of Sn-3.8Ag-0.7Cu Lead-Free Solder," *Metallurgical and Materials Transactions A*, Vol. 38(7), pp. 1530-1538, 2007.

109. Basit, M. M., Motalab, M., Suhling, J. C., Lall, P., "The Effects of Aging on the Anand Viscoplastic Constitutive Model for SAC305 Solder," *Proceedings of 2014 IEEE ITherm*, pp. 112-126, Orlando, FL, May 27 - 30, 2014.
110. Basit, M. M., Motalab, M., Roberts, J. C., Suhling, J. C., & Lall, P., "The Effects of Silver Content and Solidification Profile on the Anand Constitutive Model for SAC Lead Free Solders," *Proceedings of 2014 IEEE ITherm*, pp. 112-126, Orlando, FL, May 27 - 30, 2014.
111. Anand, L., "Constitutive Equations for the Rate-Dependent Deformation of Metals at Elevated Temperatures," *Journal of Engineering Materials and Technology*, Vol. 104, pp. 12-17, 1982.
112. Solomon, H. D., "Fatigue of 60/40 solder," *IEEE Transactions on Components, Hybrids, and Manufacturing Technology*, Vol. CHMT-9 (4), pp. 423-432, 1986.
113. Shi, X. Q., Pang, H. L. J., Zhou, W., Wang, Z. P., "Low cycle fatigue analysis of temperature and frequency effects in eutectic solder alloy," *International Journal of Fatigue*, Vol. 22, pp. 217-228, 2000.
114. Kanchanomai, C., Miyashita, Y., Mutoh, Y., Mannan, S. L., "Low Cycle Fatigue and Fatigue Crack Growth Behavior of Sn-Ag Eutectic Solder," *Soldering & Surface Mount Technology*, Vol. 14(3), pp. 30-36, 2002.
115. Pang, J. H. L., Xiong, B. S., Low, T. H., "Low Cycle Fatigue Study of Lead Free 99.3Sn-0.7Cu Solder Alloy," *International Journal of Fatigue*, Vol. 26, pp. 865-872, 2004.
116. Shohji, I., Yoshida, T., Takahashi, T., Hioki, S., "Tensile Properties of Sn-Ag Based Lead-Free Solders and Strain Rate Sensitivity," *Materials Science and Engineering A*, Vol. 366, pp. 50-55, 2004.
117. Shi, X. Q., Pang, H. L. J., Zhou, W., Wang, Z. P., "A Modified Energy-Based Low Cycle Fatigue Model for Eutectic Solder Alloy," *Scripta Materialia*, Vol. 41(3), pp. 289-296, 1999.
118. Nie, X., Bhate, D., Chan, D., Chen, W., Subbarayan, G., Dutta, I., "Rate-Dependent Behavior of Sn_{3.8}Ag_{0.7}Cu Solder over Strain Rates of 10^{-6} to 10^2 s⁻¹," *Thermal and Thermomechanical Phenomena in Electronic Systems*, pp. 676-682, 2008.
119. Pang, J. H. L., Xiong, B. S., Che, F. X., "Modeling Stress Strain Curves for Lead-Free 95.5Sn-3.8Ag-0.7Cu Solder," *Proceedings of the 5th EuroSimE Conference*, pp. 449-453, 2004.
120. Pan, T., "Thermal Cycling Induced Plastic Deformation in Solder Joints – Part I: Accumulated Deformation in Surface Mount Joints," *Journal of Electronic Packaging*, Vol. 113(1), pp. 8-15, 1991.

121. Hacke, P. L., Sprecher, A. F., Conrad, H., "Microstructure Coarsening During Thermo-Mechanical Fatigue of Pb-Sn Solder Joints," *Journal of Electronic Materials*, Vol. 26(7), pp. 774-782, 1997.
122. Hacke, P. L., Fahmy, Y., Conrad, H., "Phase Coarsening and Crack Growth Rate During Thermo-Mechanical Cycling of 63Sn37Pb Solder Joints," *Journal of Electronic Materials*, Vol. 27(8), pp. 941-947, 1998.
123. Ye, L., Lai, Z., Liu, J., Tholen, A., "Microstructural Coarsening of Lead Free Solder Joints During Thermal Cycling," *Electronic Components and Technology Conference*, pp. 134-137, 2000.
124. Vianco, P. T., Burchett, S. N., Neilsen, M. K., Rejent, J. A., "Coarsening of the Sn-Pb Solder Microstructure in Constitutive Model-Based Predictions of Solder Joint Thermal Mechanical Fatigue," *Journal of Electronic Materials*, Vol. 28(11), pp. 1290-1298, 1999.
125. Chen, H., Wang, L., Han, J., Li, M., Liu, H., "Microstructure, Orientation and Damage Evolution in SnPb, SnAgCu, and Mixed Solder Interconnects Under Thermomechanical Stress," *Microelectronic Engineering*, Vol. 96, pp. 82-91, 2012.
126. Doherty, R. D., Hughes, D. A., Humphreys, F. J., Jonas, J. J., Jensen, D. J., Kassner, M. E., King, W. E., McNelley, T. R., McQueen, H. J., Rollett, A. D., "Current Issues in Recrystallization: A Review," *Materials Science and Engineering A*, Vol. 238, pp. 219-274, 1997.
127. Berthou, M., Retailleau, P., Fremont, H., Guedon-Gracia, A., Jephos-Davennel, C., "Microstructure Evolution Observation for SAC Solder Joint: Comparison Between Thermal Cycling and Thermal Storage," *Microelectronics Reliability*, Vol. 49, pp. 1267-1272, 2009.
128. Frear, D. R., Ramanathan, L. N., Jang, J. W., Owens, N. L., "Emerging Reliability Challenges in Electronic Packaging," *Annual International Reliability Physics Symposium*, pp. 450-454, 2008.
129. Mattila, T., "Reliability of High-Density Lead-Free Solder Interconnections under Thermal Cycling and Mechanical Shock Loading," PhD Dissertation, Helsinki University of Technology, 2005.
130. Laurila, T., Mattila, T., Vuorinen, V., Karppinen, J., Li, J., Sippola, M., Kivilahti, J. K., "Evolution of Microstructure and Failure Mechanism of Lead-Free Solder Interconnections in Power Cycling and Thermal Shock Tests," *Microelectronics Reliability*, Vol. 47, pp. 1135-1144, 2007.
131. Yin, L., Wentlent, L., Yang, L., Arfaei, B., Oasaimh, A., Borgesen, P., "Recrystallization and Precipitate Coarsening in Pb-Free Solder Joints During Thermomechanical Fatigue," *Journal of Electronic Materials*, Vol. 41, pp. 241-252, 2012.

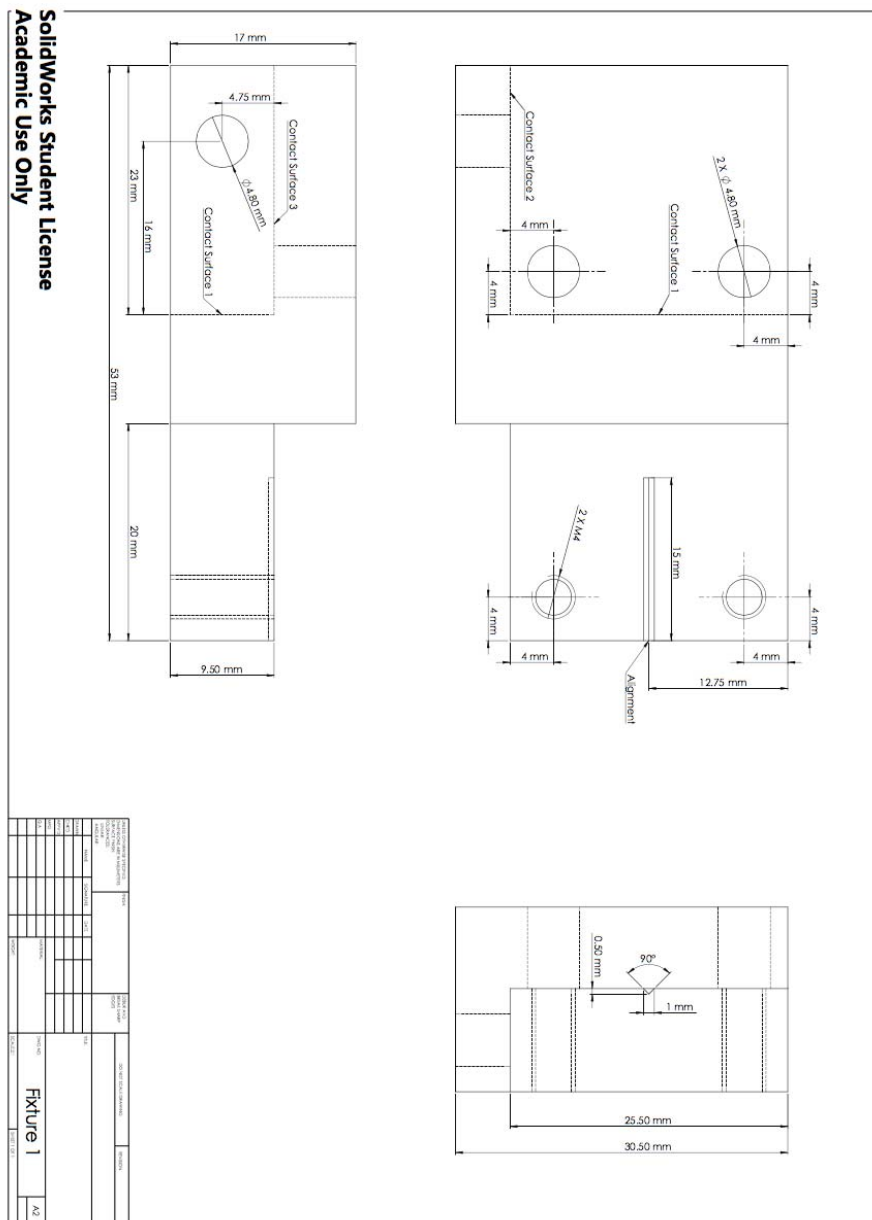
132. Chen, H., Han, J., Li, J., Li, M., "Inhomogeneous Deformation and Microstructure Evolution of Sn-Ag-Based Solder Interconnects During Thermal Cycling and Shear Testing," *Microelectronics Reliability*, Vol. 52, pp. 1112-1120, 2012.
133. Qi, L., Huang, J., Zhao, X., Zhang, H., "Effect of Thermal-Shearing Cycling on Ag₃Sn Microstructural Coarsening in SnAgCu Solder," *Journal of Alloys and Compounds*, Vol. 469, pp. 102-107, 2009.
134. Matin, M. A., Vellinga, W. P., Geers, M. G. D., "Thermomechanical Fatigue Damage Evolution in SAC Solder Joints," *Materials Science and Engineering A*, Vol. 445-446, pp. 73-85, 2007.
135. Matin, M. A., Vellinga, W. P., Geers, M. G. D., "Microstructure Evolution in a Pb-Free Solder Alloy During Mechanical Fatigue," *Materials Science and Engineering A*, Vol. 431, pp. 166-174, 2006.
136. Erinc, M., Schreurs, P. J. G., Geers, M. G. D., "Intergranular Thermal Fatigue Damage Evolution in SnAgCu Lead-Free Solder," *Mechanics of Materials*, Vol. 40, 780-791, 2008.
137. Xu, L., Pang, J. H. L., Che, F., "Impact of Thermal Cycling on Sn-Ag-Cu Solder Joints and Board-Level Drop Reliability," *Journal of Electronic Materials*, Vol. 37, pp. 880-886, 2008.
138. https://en.wikipedia.org/wiki/Scanning_electron_microscope
139. <http://www.nanoimages.com/technology/>
140. Lee, W. W., Nguyen, L. T., Selvaduray, G. S., "Solder Joint Fatigue Models: Review and Applicability to Chip Scale Packages," *Microelectronics Reliability*, Vol. 40, pp. 231-244, 2000.
141. Morrow, J., "Cyclic Plastic Strain Energy and Fatigue of Metals," *Internal Friction, Damping and Cyclic Plasticity*, pp. 45, 1965.
142. Evans, R. W., Wilshire, B., *Creep of Metals and Alloys*, the Institute of Metals, 1985.
143. Weertman, J., "Steady-State Creep through Dislocation Climb," *Journal of Applied Physics*, Vol. 28, pp. 362-366, 1957.
144. Herring, C., "Diffusional Viscosity of a Polycrystalline Solid," *Journal of Applied Physics*, Vol. 21, pp. 437-445, 1950.
145. Fix, A. R., Lopez, G. A., Brauer, I., Nuchter, W., Mittermeijer, E. J., "Microstructural Development of Sn-Ag-Cu Solder Joints," *Journal of Electronic Materials*, Vol. 34(2), pp. 137-142, 2005.
146. Porter, D. A., Easterling, K. E., *Phase Transformations in Metals and Alloys*, 2nd ed., Chapman & Hall, 1992.

147. Smallman, R. E., *Modern Physical Metallurgy*, 4th ed., Butterworth Heinemann, 1985.
148. Boistelle, R., Astier, J. P., "Crystallization Mechanisms in Solution," *Journal of Crystal Growth*, Vol. 90, pp. 14-30, 1988.
149. Dieter, G. E., *Mechanical Metallurgy*, 3rd Edition, McGraw-Hill, 1986.
150. <http://www.jr3.com/products.html>
151. Backman, M., "Motion Technology for the New Millennium," *SMMA 2000 Fall Technical Conference*, October 4-6, 2000.
152. Coffin, L. F., "A Study of the Effects of Cyclic Thermal Stresses on Ductile Metal," *ASME Transactions*, Vol. 76, pp. 931-950, 1954.
153. Manson, S. S., "Fatigue: A Complex Subject – Some SPL Approximations," *Experimental Mechanics*, Vol. 5, pp. 193-226, 1965.

APPENDIX A

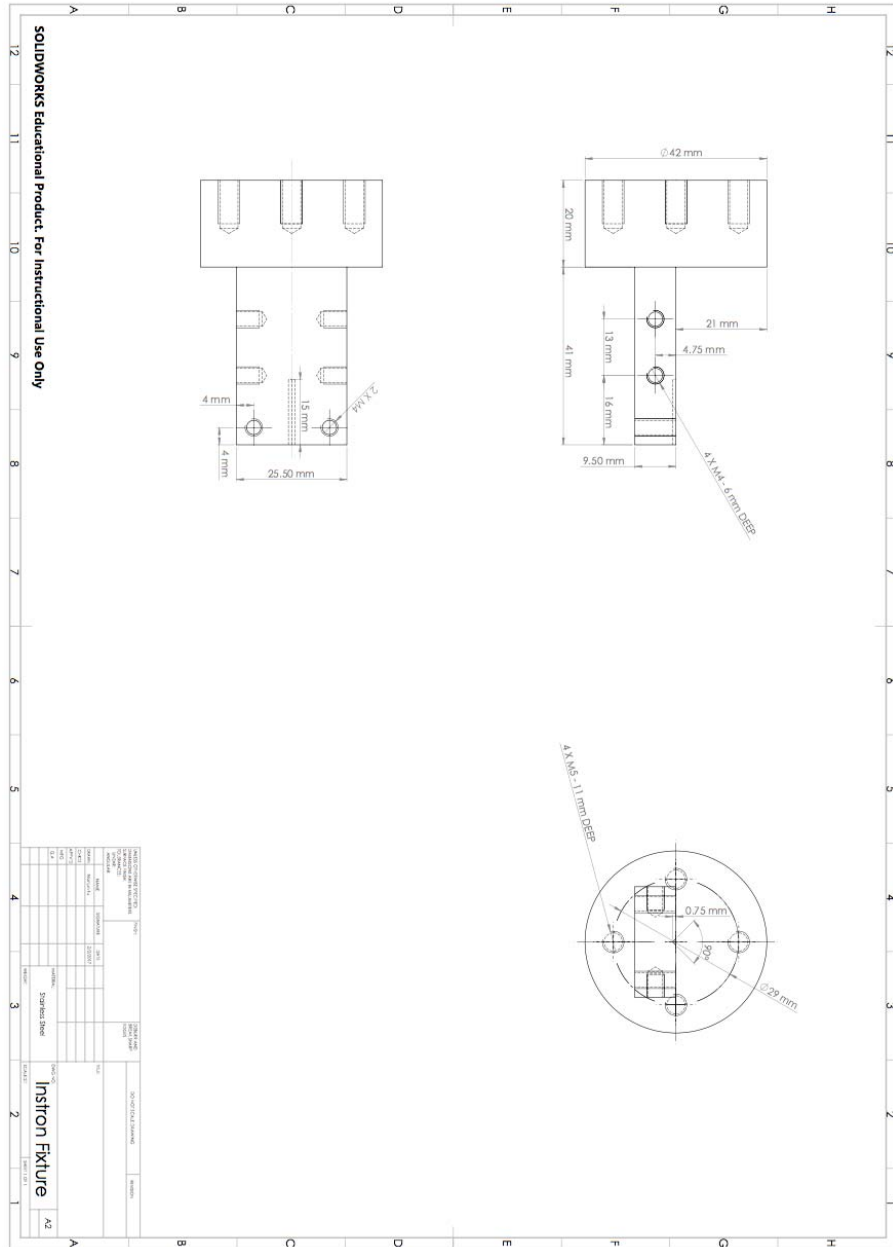
DIMENSIONAL DRAWINGS FOR DESIGNED FIXTURES

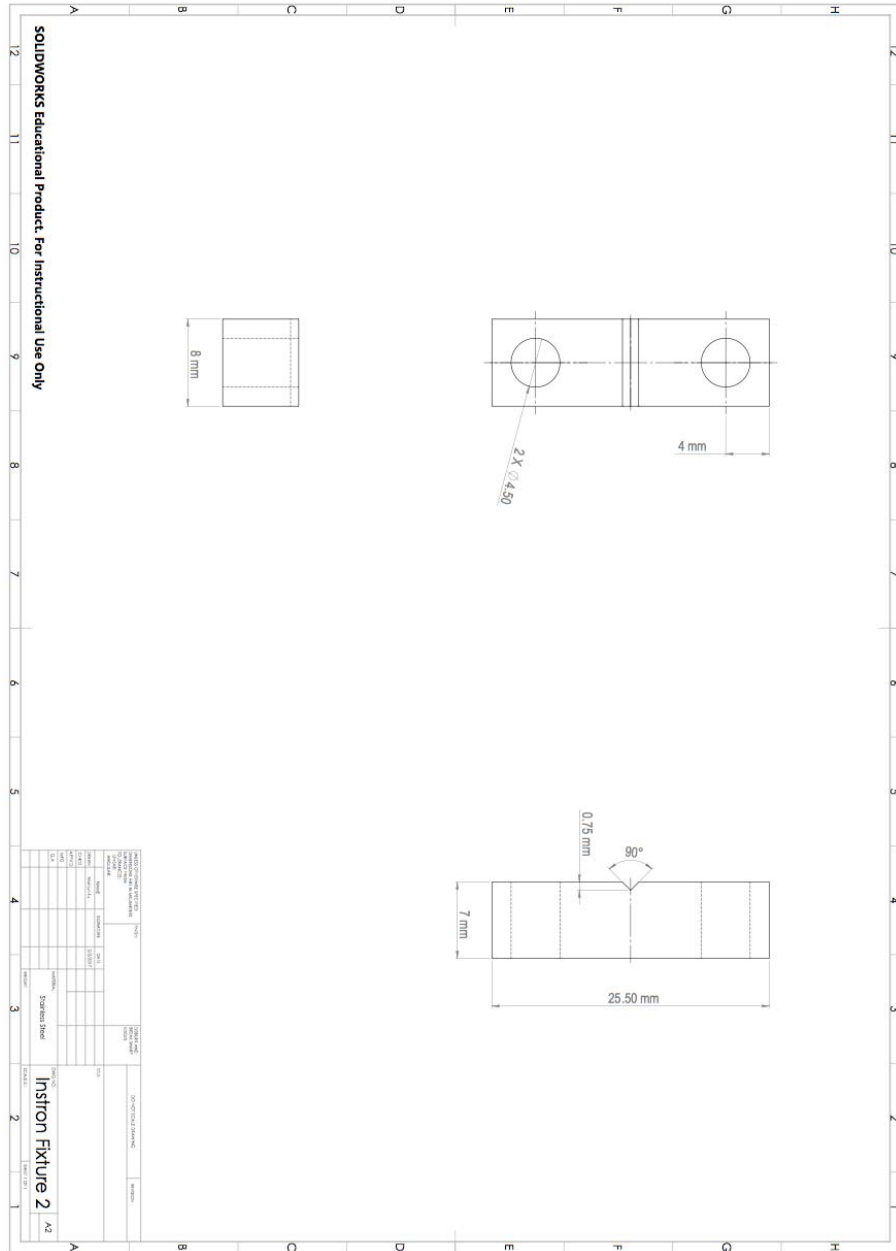
A.1 Fixtures for MT-210 Microtester



SolidWorks Student License
Academic Use Only

A.2 Fixtures for Instron 5948 Tester and New Microtester

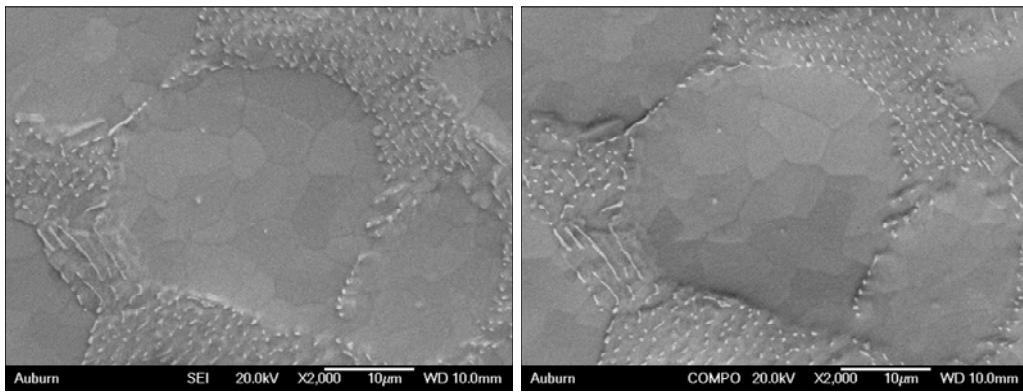




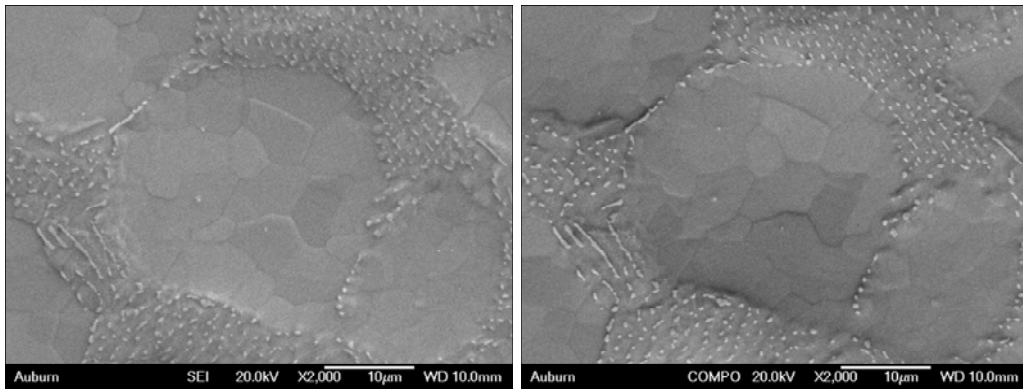
APPENDIX B

AGING INDUCED MICROSTRUCTURAL EVOLUTION IN OTHER SELECTED REGIONS

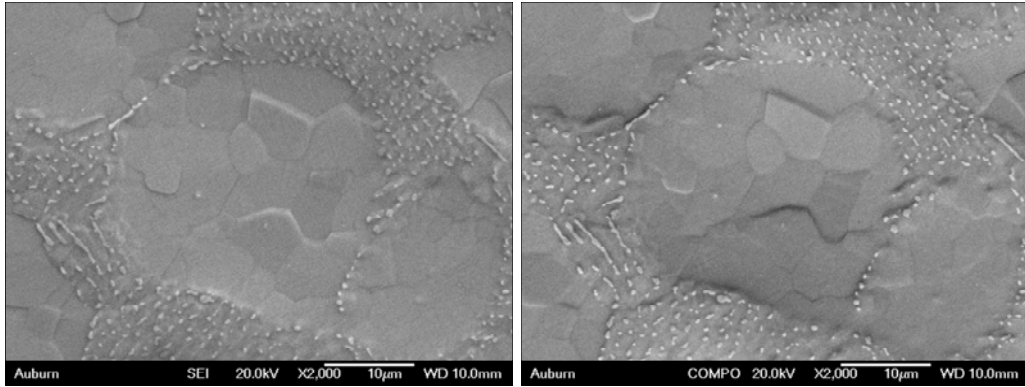
B.1 RF SAC305 (Region 2, Aging at $T = 125\text{ }^{\circ}\text{C}$)



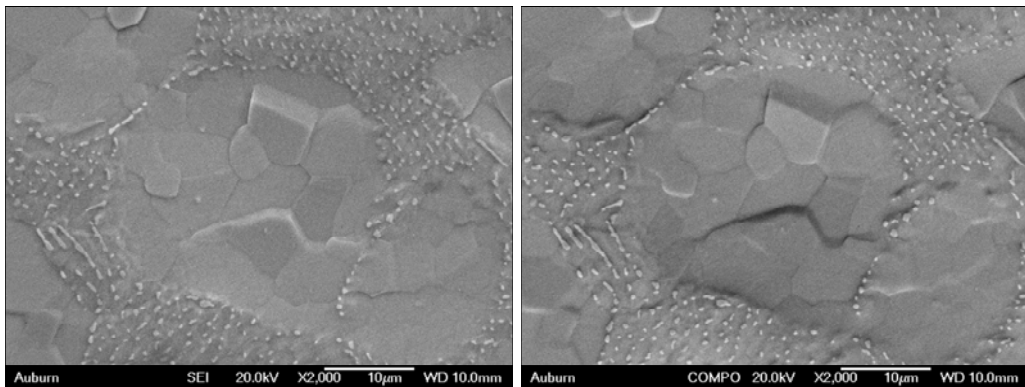
(a) No Aging (Left: SE; Right: BSE)



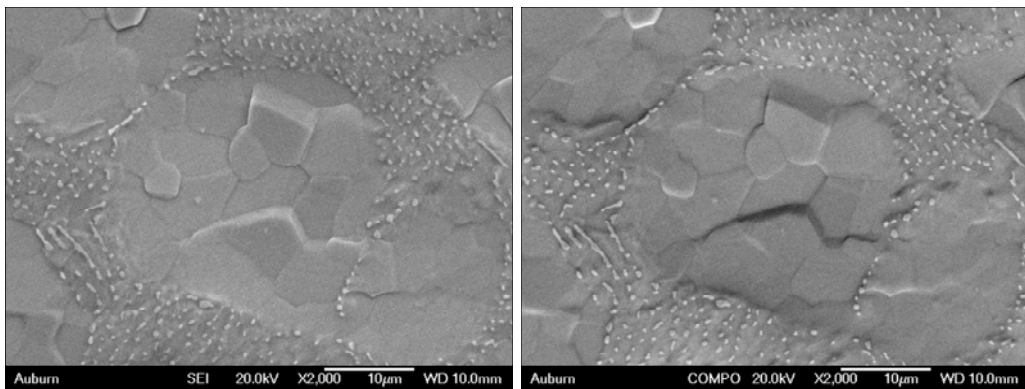
(b) 1 Hour of Aging (Left: SE; Right: BSE)



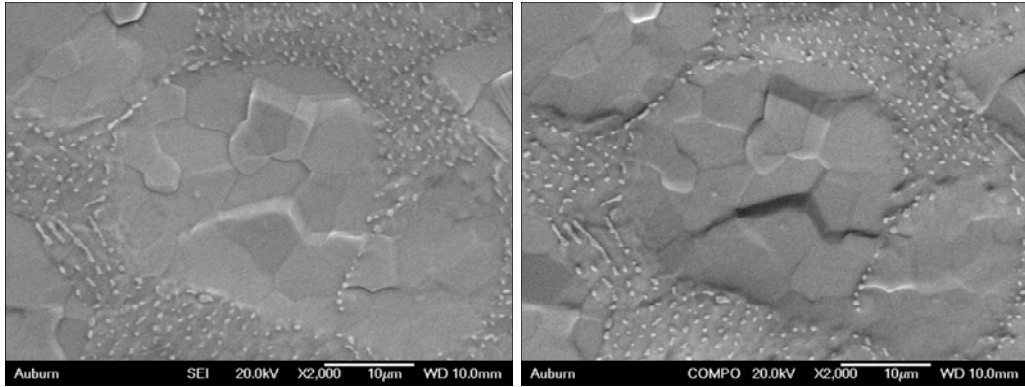
(c) 2 Hours of Aging (Left: SE; Right: BSE)



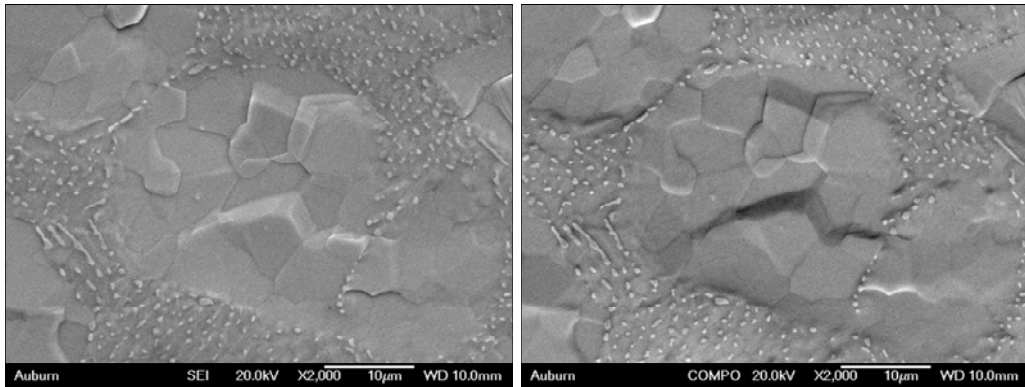
(d) 3 Hours of Aging (Left: SE; Right: BSE)



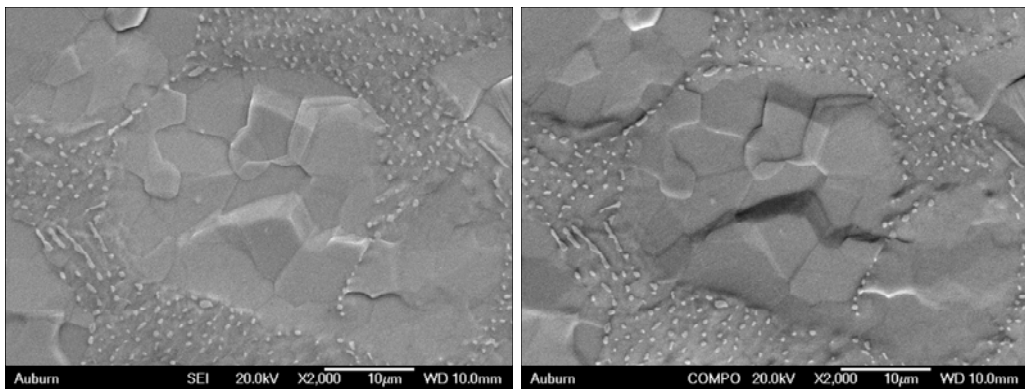
(e) 4 Hours of Aging (Left: SE; Right: BSE)



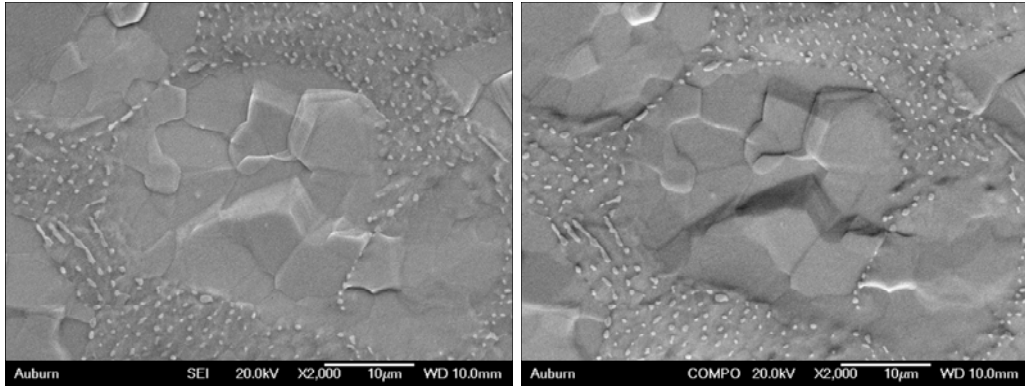
(f) 5 Hours of Aging (Left: SE; Right: BSE)



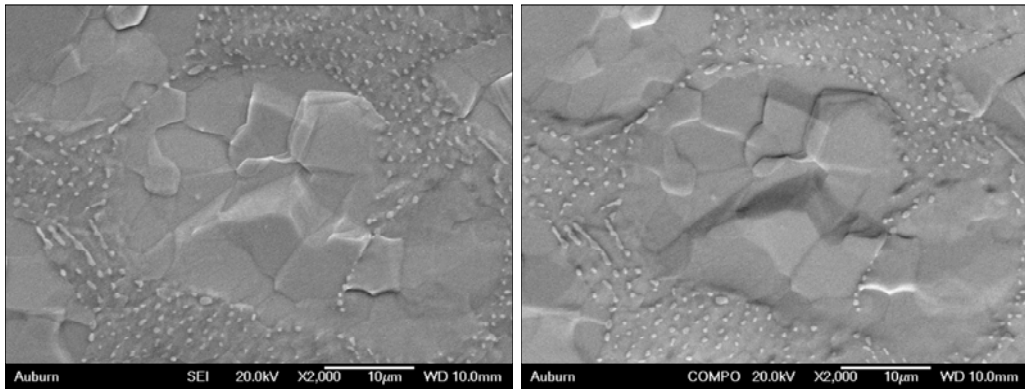
(g) 6 Hours of Aging (Left: SE; Right: BSE)



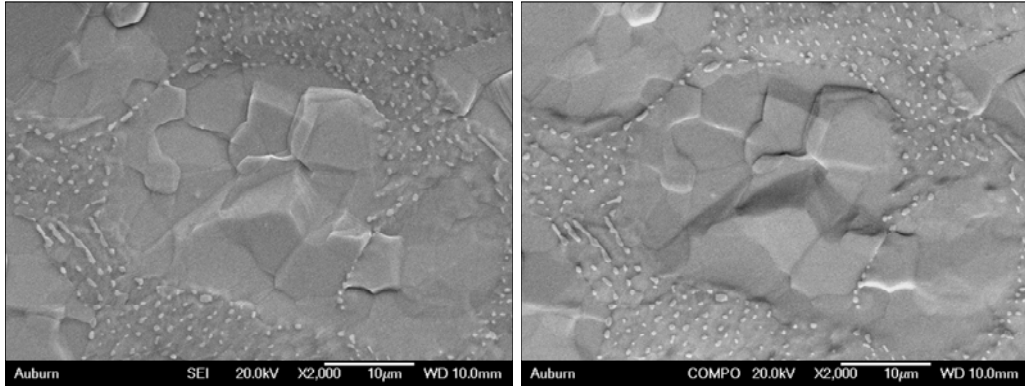
(h) 7 Hours of Aging (Left: SE; Right: BSE)



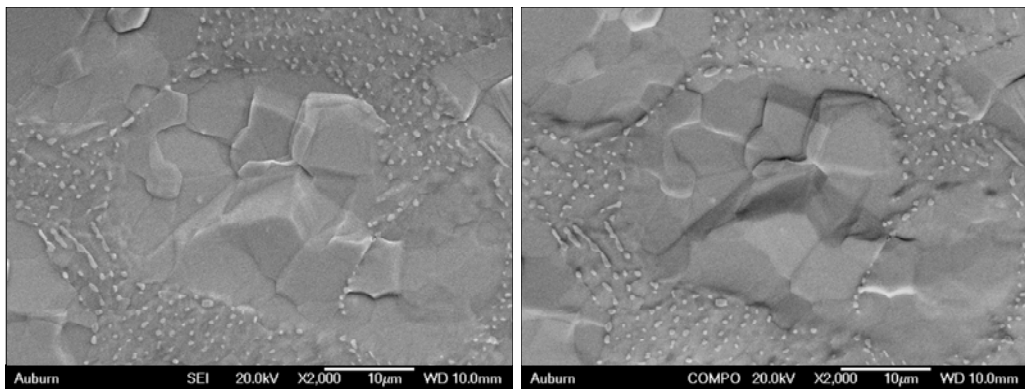
(i) 8 Hours of Aging (Left: SE; Right: BSE)



(j) 9 Hours of Aging (Left: SE; Right: BSE)

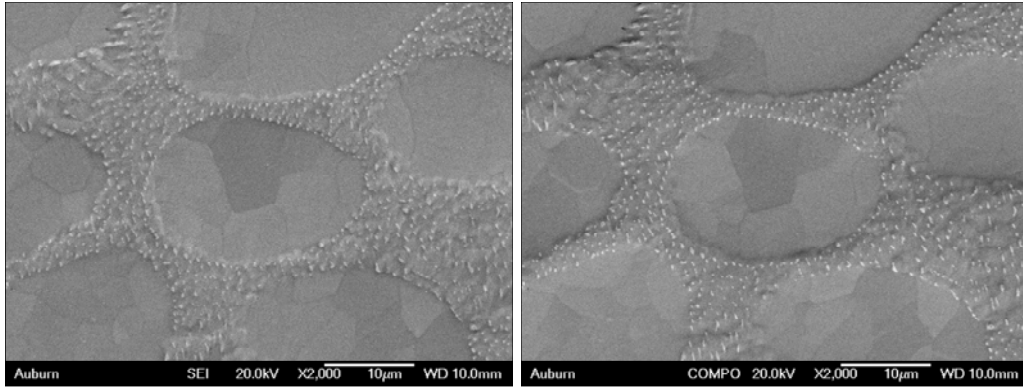


(k) 10 Hours of Aging (Left: SE; Right: BSE)

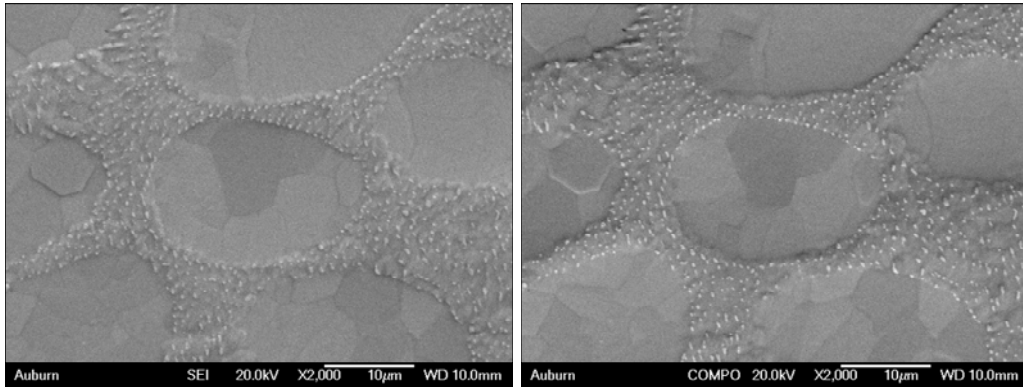


(l) 11 Hours of Aging (Left: SE; Right: BSE)

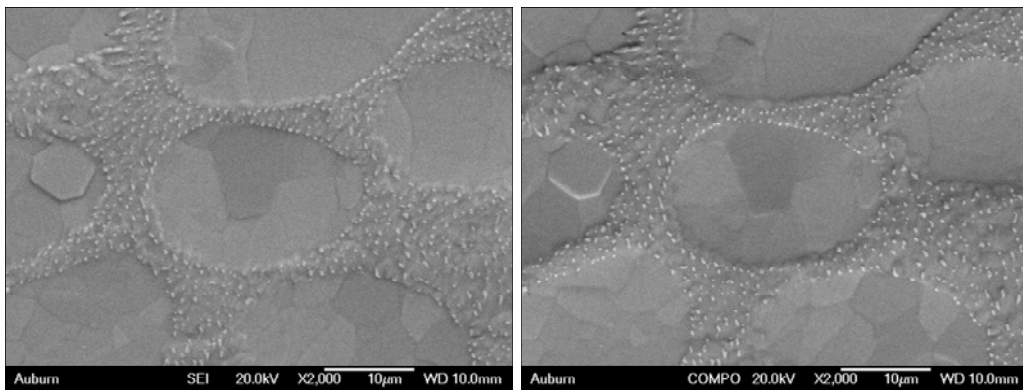
B.2 RF SAC305 (Region 3, Aging at T = 125 °C)



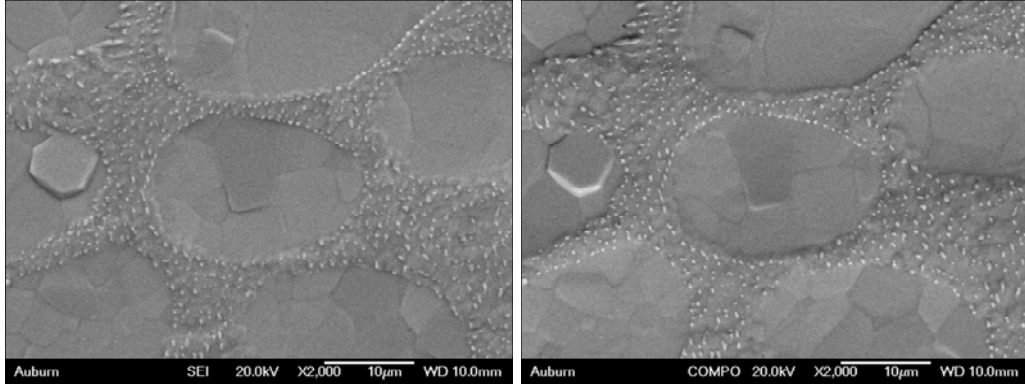
(a) No Aging (Left: SE; Right: BSE)



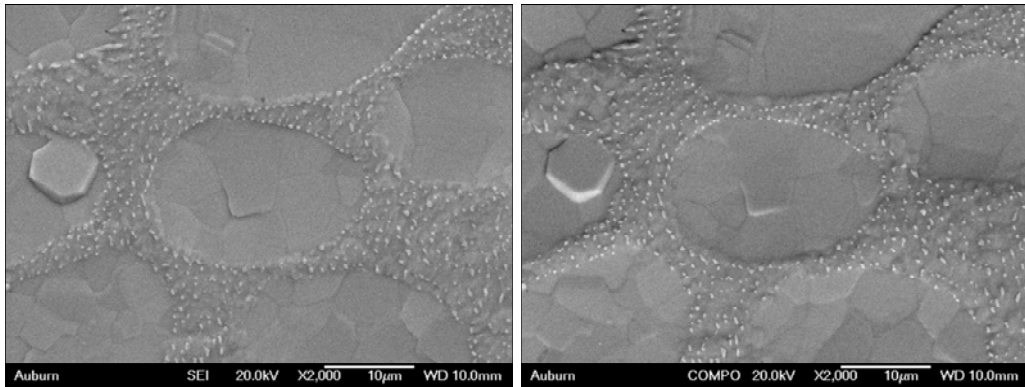
(b) 1 Hour of Aging (Left: SE; Right: BSE)



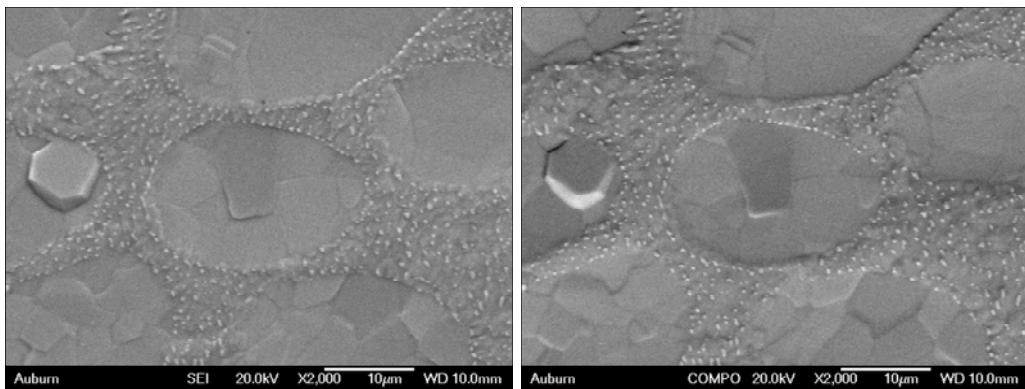
(c) 2 Hours of Aging (Left: SE; Right: BSE)



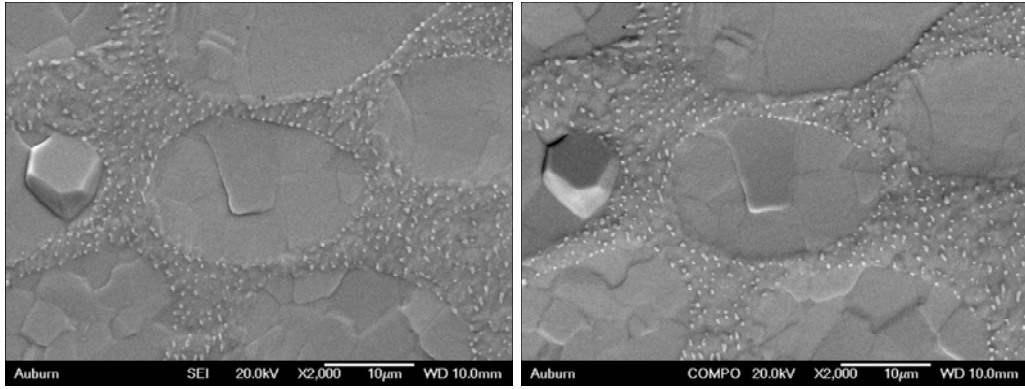
(d) 3 Hours of Aging (Left: SE; Right: BSE)



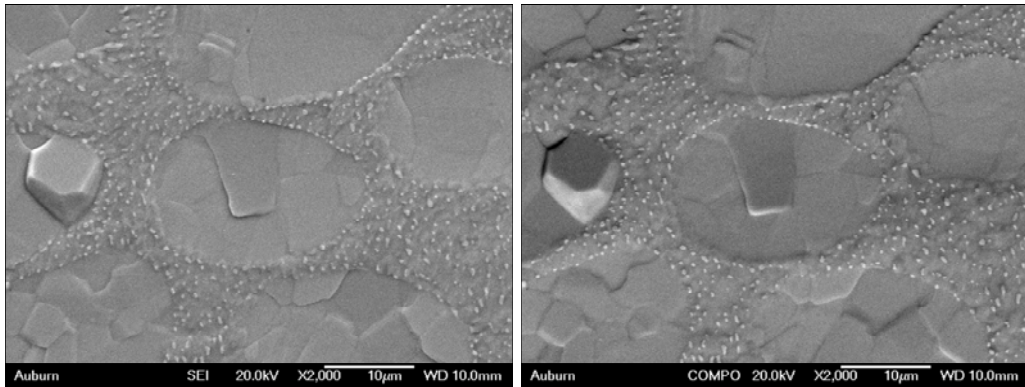
(e) 4 Hours of Aging (Left: SE; Right: BSE)



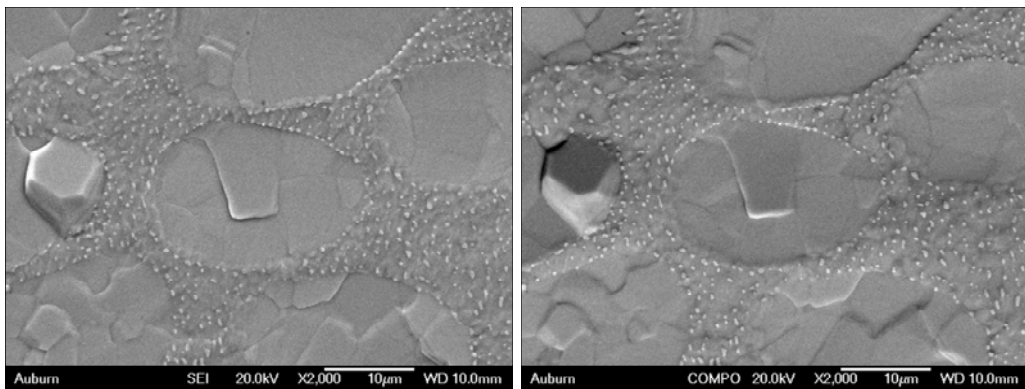
(f) 5 Hours of Aging (Left: SE; Right: BSE)



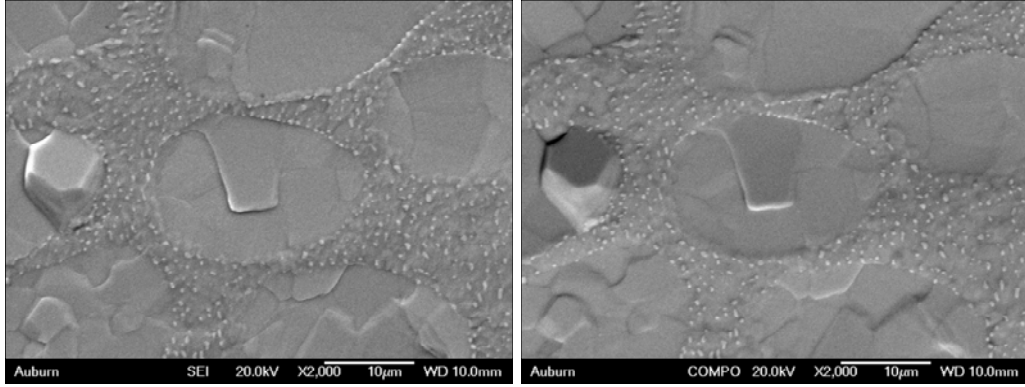
(g) 6 Hours of Aging (Left: SE; Right: BSE)



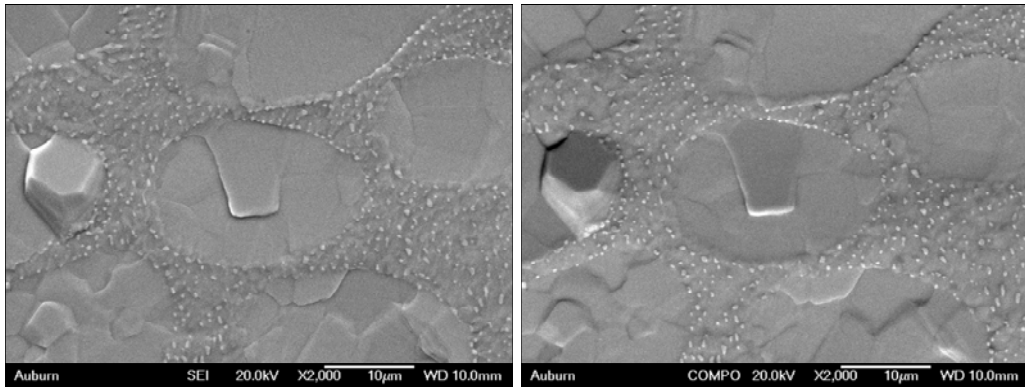
(h) 7 Hours of Aging (Left: SE; Right: BSE)



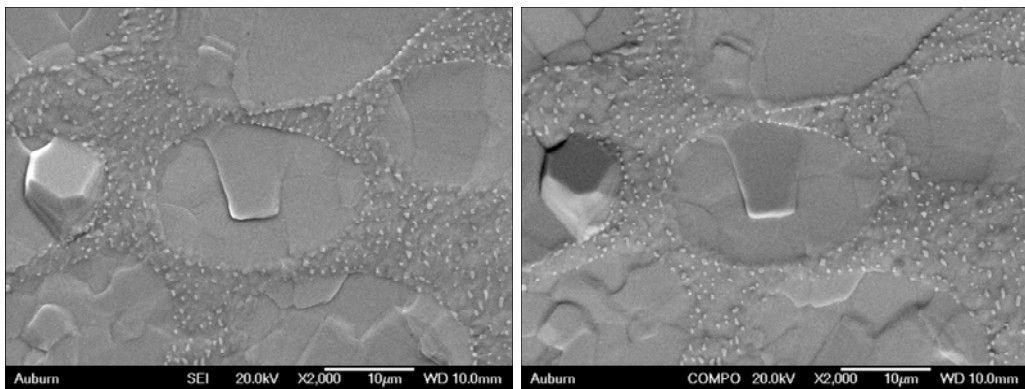
(i) 8 Hours of Aging (Left: SE; Right: BSE)



(j) 9 Hours of Aging (Left: SE; Right: BSE)

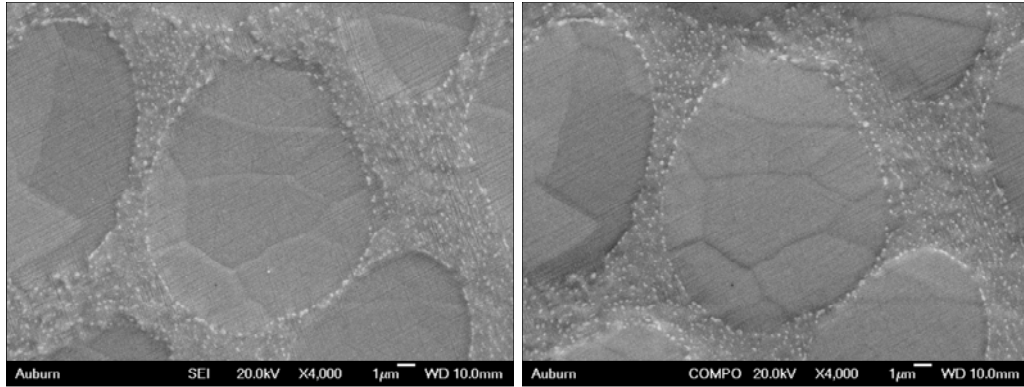


(k) 10 Hours of Aging (Left: SE; Right: BSE)

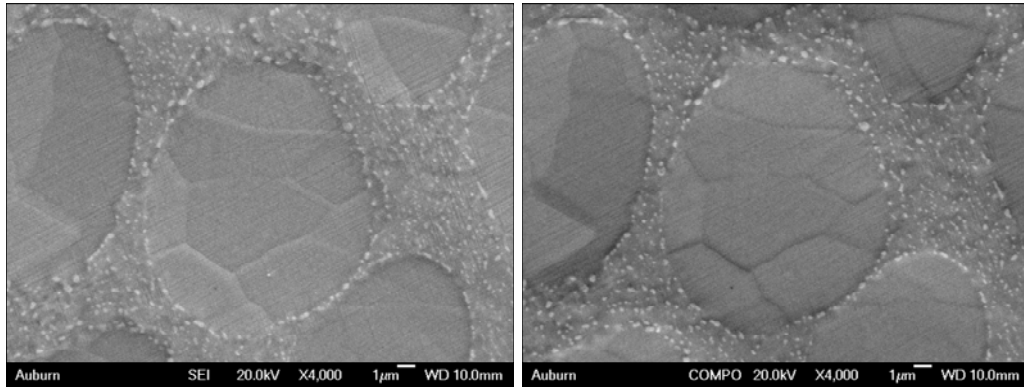


(l) 11 Hours of Aging (Left: SE; Right: BSE)

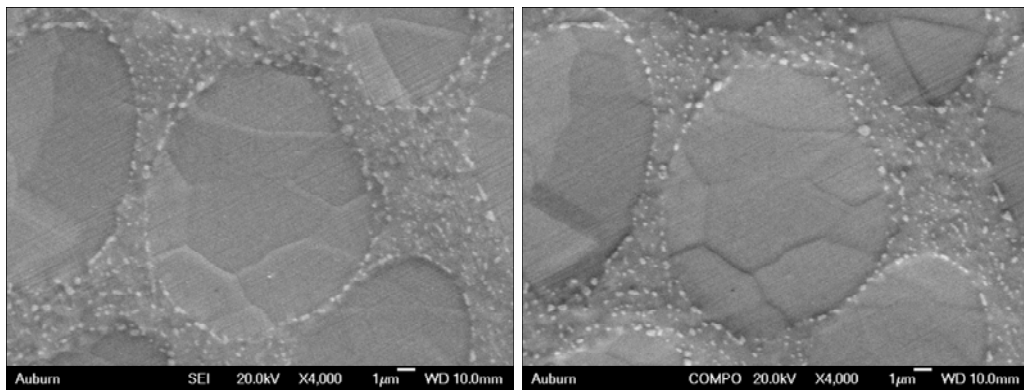
B.3 WQ SAC305 (Region 2, Aging at T = 125 °C)



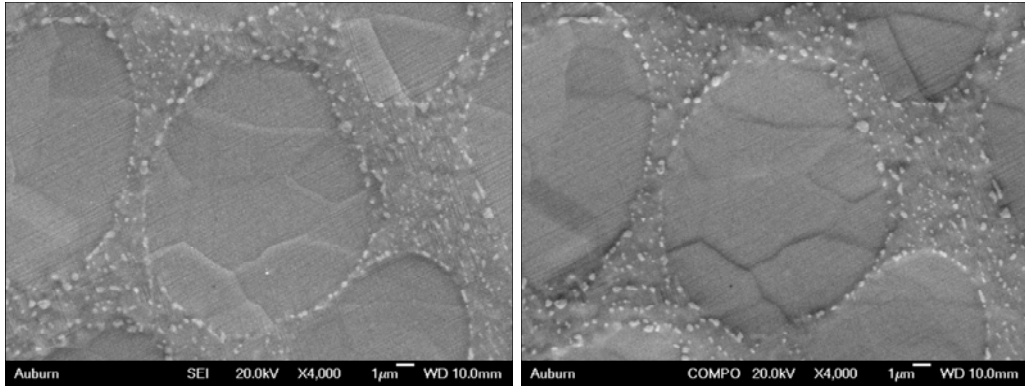
(a) No Aging (Left: SE; Right: BSE)



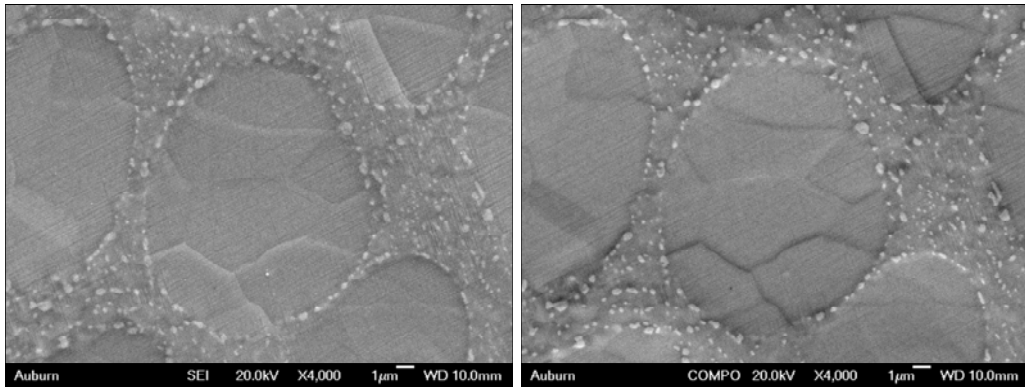
(b) 1 Hour of Aging (Left: SE; Right: BSE)



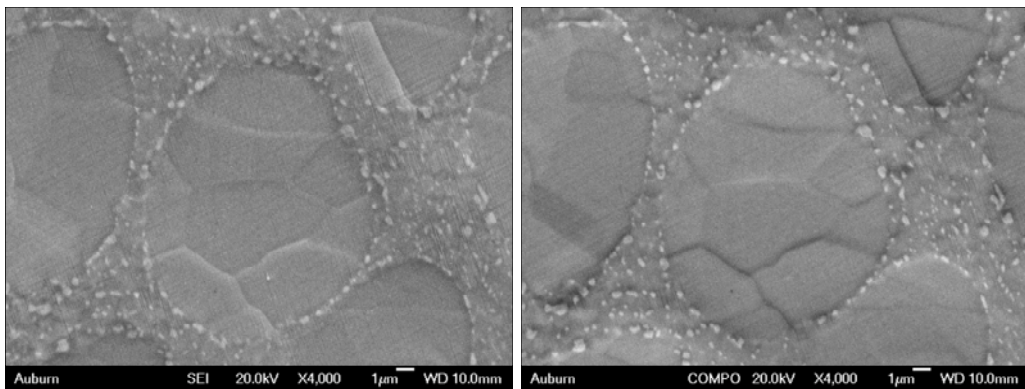
(c) 2 Hours of Aging (Left: SE; Right: BSE)



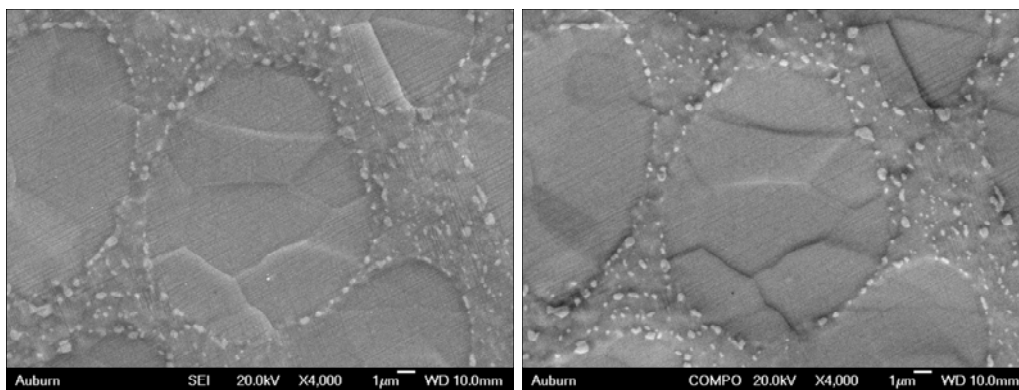
(d) 3 Hours of Aging (Left: SE; Right: BSE)



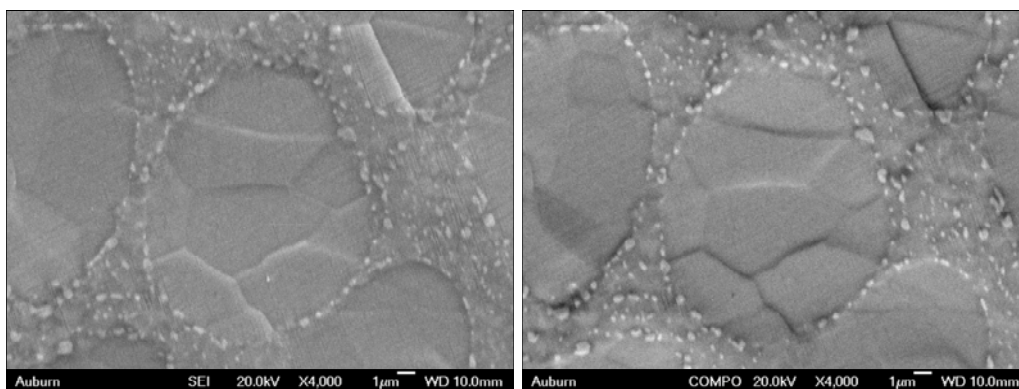
(e) 4 Hours of Aging (Left: SE; Right: BSE)



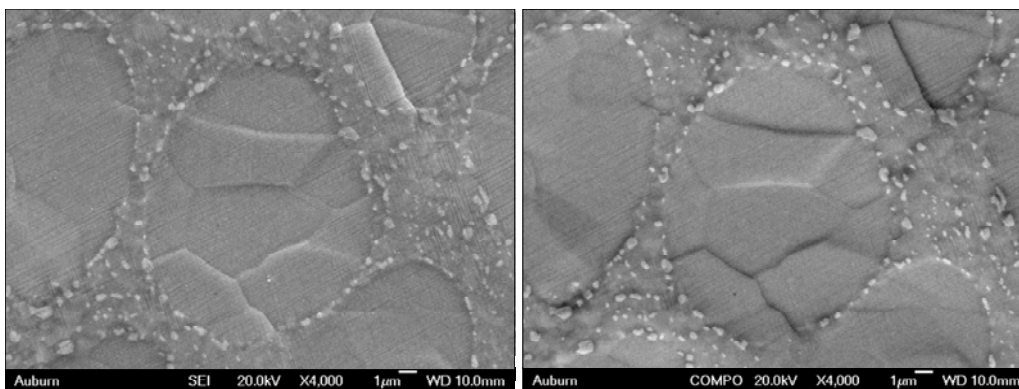
(f) 5 Hours of Aging (Left: SE; Right: BSE)



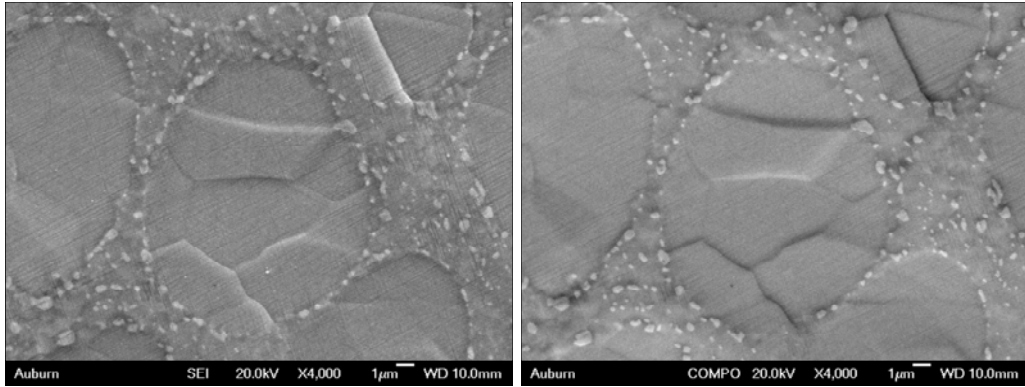
(g) 6 Hours of Aging (Left: SE; Right: BSE)



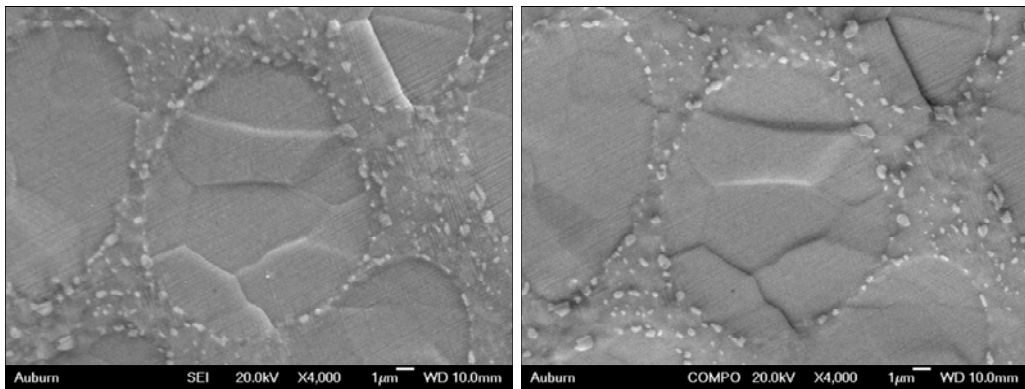
(h) 7 Hours of Aging (Left: SE; Right: BSE)



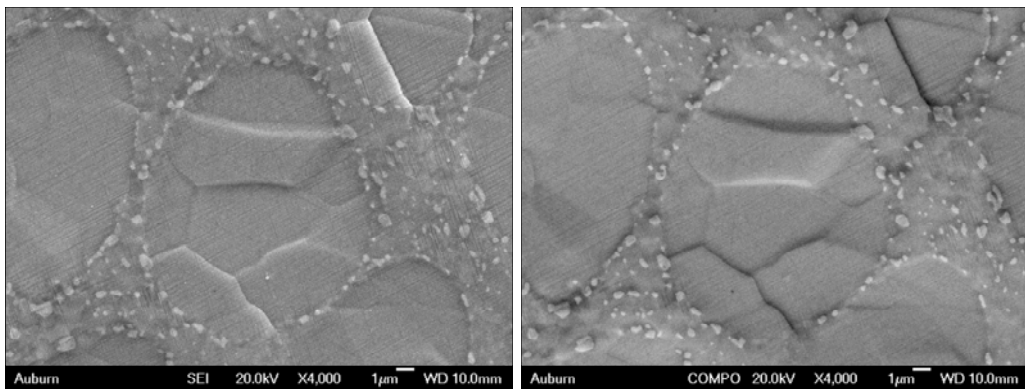
(i) 8 Hours of Aging (Left: SE; Right: BSE)



(j) 9 Hours of Aging (Left: SE; Right: BSE)



(k) 10 Hours of Aging (Left: SE; Right: BSE)



(l) 11 Hours of Aging (Left: SE; Right: BSE)